Fakultät für Elektrotechnik und Informationstechnik
Technische Universität München

Towards Safe Human-Robot Collaboration Oriented to Collision Handling

Zengjie Zhang

Vollständiger Abdruck der von der Fakultät für Elektrotechnik und Informationstechnik der Technischen Universität München zur Erlangung des akademischen Grades eines

Doktor-Ingenieurs (Dr.-Ing.)

genehmigten Dissertation.

Vorsitzender:
Prof. Dr.-Ing. Bernhard Seeber

Prüfende der Dissertation:
1. Priv.-Doz. Dr.-Ing. -habil. Dirk Wollherr
2. Prof. Dr.-Ing. Sami Haddadin

Die Dissertation wurde am 29.09.2020 bei der Technischen Universität München eingereicht und durch die Fakultät für Elektrotechnik und Informationstechnik am 19.03.2021 angenommen.

Foreword

This dissertation summarizes my research conducted at the Chair of Automatic Control Engineering (LSR), at the Technical University of Munich (TUM), Germany. I am always grateful for the skills and experience I have obtained in this chair, where I have been allowed to freely study interesting topics and collaborate with talented colleagues for valuable research results. I would like to seize this opportunity to thank all the people who have offered me great support and assistance during my stay in this chair.

First of all, I would like to sincerely thank my advisor Dr. Dirk Wollherr for his kind and patient supervision on my academic training. His continuous trust and support sustainably encourage me to overcome the challenges when seeking for novel methods for specific research problems. I am always benefiting from his helpful suggestions to improve my reports and presentations. Collaborating with him greatly broadens my horizons in various research fields. I appreciate all his valuable contributions to my work. I would also like to thank the head of the chair, Prof. Martin Buss, for the opportunity to work as an associate in his team with excellent researchers and his valuable suggestions on my research presentations. I am also grateful to all my kind cooperators, Dr. Marion Leibold, Dr. Fangzhou Liu, and Yongchao Wang in LSR, Prof. Björn Schuller in Imperial College London, Dr. Kun Qian in the University of Tokyo, and Dr. Yiyong Sun in China Aerospace Science and Technology Corporation, who greatly contributed to my research work published in LSR. My collaboration with them is pleasant and enjoyable.

I thank the whole team at LSR and ITR for all your valuable support and help. A specially warm thank goes to my colleagues from the Siemens team and the HR-Recycler team who have become my beloved friends: Dr. Özgür Ögüz, Gerold Huber, Volker Gabler, Khoi Hoang, Salman Bari, and Sebastian Kerz. Life would be tougher without your generous and selfless help. I also thank all my other friends and colleagues that are not enumerated above: Tim Brüdigam, Yingwei Du, Zhehua Zhou, Tong Liu, Ni Dang, Cong Li, Yuhong Chen, our alumni who offered me great help: Ken Friedl, Stefan Friedrich, Shushu Ma, Alexander Pekarovsky, Heiko Stüber, Dr. Xuelian Zang, Dr. Markus Schill, and Dr. Annemarie Turnward, and all our secretaries and technicians who have greatly assisted my work in LSR. Special thanks go to Dr. Qingchen Liu, Dr. Xianwei Li, and Dr. Yi Ren in the Chair of Information-oriented Control (ITR) who helped me so much with my academic career.

Most importantly, I would like to thank my parents and my grandmother for their continuous care and support. I thank my grandfather in heaven for his spiritual encouragement. My enthusiasm and confidence originate from the unlimited love of my entire family.

Munich, September 2020 Zengjie Zhang

Abstract

This dissertation is motivated by the growing demand for the safety of Human-Robot Collaboration (HRC) applications. Different from the isolation-based safety regulations for the conventional robot platforms, HRC requires a more flexible and adaptive safety mechanism to tolerate the threats to the coexistence of humans and robots. For example, a human-robot collision is not necessarily recognized as dangerous to humans but should be handled according to its effects. This motivates the studies on collision handling, an important aspect of safe HRC. In this dissertation, we propose a novel framework for safe HRC which focuses on implementing a reliable collision handling pipeline. Different from the conventional work, the proposed framework fills the gap towards robust safe HRC in uncertain environments, with partial measurement, incomplete signals, hard constraints, and external disturbances. Firstly, we propose a novel integral sliding mode observer to precisely estimate the collision forces, for which we eliminate the conventional restricted assumptions, including the requirement of velocity measurement, the system continuity, and the boundedness of disturbance derivatives. Secondly, we develop a novel online collision detection and identification scheme for robot manipulators to rapidly detect a collision and identify its type with incomplete signals. We use supervised learning methods to develop a collision classifier and use the Bayesian decision theory to improve its accuracy for incomplete collision signals. Thirdly, we design a robust safe controller with adaptive parameters for robot manipulators. The controller ensures precise tracking of the desired trajectory with external disturbances. It also avoids collisions by restricting the robot motion within predefined hard safety constraints. The effectiveness and applicability of the proposed methods have been validated by simulation and experiments on robot manipulators.

Although intended for robot manipulators, the proposed HRC safety paradigm is targeted to a step forward towards a generic safe HRC framework for various robot platforms. Especially, collision handling is required to be accurate, responsive, and reliable even in uncertain environments. In theory, this dissertation solves several critical problems concerned with environmental uncertainties based on rigorous mathematical paradigms, which is hardly discussed in previous work. In practice, experimental validations reveal that the proposed methods show great potential to solve important engineering problems. Thus, the work in this dissertation does not only provide a theoretic framework for reliable HRC in uncertain environments but also shows great potential in practical applications. Moreover, the proposed safety paradigm provides a new perspective to view and implement safe HRC by combining various methodologies in different research fields, including observation theory, machine learning, Bayesian inference, and control theory.

Zusammenfassung

Die Motivation dieser Dissertation stellt die wachsende Nachfrage nach Sicherheit in Mensch-Roboter Kollaboration (MRK) -Anwendungen dar. Im Gegensatz zu den herkömmlichen Sicherheitsbestimmungen für Roboterplattformen, die sich durch strikte Abgrenzung vom Menschen auszeichnen, erfordert MRK einen flexibleren und anpassungsfähigeren Sicherheitsmechanismus, welcher eine direkte Zusammenarbeit von Menschen und Robotern erlaubt. Beispielsweise stellt nicht jeder physische Kontakt von Mensch und Maschine zwangsläufig eine direkte Bedrohung für den Menschen dar, sondern sollte unter Berücksichtigung seiner Auswirkungen auf den Menschen entsprechend ausgewertet werden, woraus sich die Forschungsfrage der Kollisionsauswertung ergibt. In dieser Dissertation schlagen wir ein neuartiges Entwicklungsframework für sicheres MRK vor, das sich auf eine zuverlässige Pipeline für die Kollisionsbehandlung konzentriert und auf der Zusammenfassung der konventionellen MRK -Paradigmen in verwandten Arbeiten basiert. Anders als bei herkömmlichen Arbeiten füllt das vorgeschlagene Framework die Lücke zu robusten sicheren Objekten für unsichere Umgebungen mit Teilmessungen, unvollständigen Signalen, harten Einschränkungen und externen Störungen. Erstens schlagen wir eine neuartige Methode zur Schätzung externer Störungen unter Verwendung eines integrierten Sliding-Mode Beobachters vor, um die Kollisionskräfte präzise abzuschätzen. Wir eliminieren die herkömmlich verwendeten Annahmen, nämlich Geschwindigkeitsmessung, Systemkontinuität und Begrenzung der Störungsableitung. Zweitens wird ein neuartiges Online-Schema für Robotermanipulatoren entwickelt, um eine Kollision schnell zu erkennen und ihren Typ mit unvollständigen Signalen zu identifizieren. Ein Kollisionsklassifikator wird unter Verwendung von überwachten Lernmethoden entwickelt. Zudem wird die Bayes'sche Entscheidungstheorie verwendet, um die Genauigkeit des Kollisionsklassifikators bei unvollständigen Kollisionssignalen zu verbessern. Drittens entwickeln wir auch eine robuste sichere Regelungsmethode mit adaptiven Parametern für Robotermanipulatoren. Der Regler gewährleistet eine präzise Verfolgung der Solltrajektorie bei externen Störungen. Er vermeidet auch Kollisionen, indem er die Roboterbewegung innerhalb vordefinierter harter Sicherheitsbedingungen einschränkt. Die Wirksamkeit und Anwendbarkeit der vorgeschlagenen Methoden wurden durch Simulationen und Experimente an Robotermanipulatoren validiert.

Obwohl ursprünglich für Robotermanipulatoren gedacht, zielt das vorgeschlagene Sicherheitsparadigma MRK auf einen Fortschritt hin zu einem generischen sicheren MRK -Framework für verschiedene Roboterplattformen mit präziser, reaktionsschneller und zuverlässiger Kollisionsbehandlung in unsicheren Umgebungen ab. Aus theoretischer Sicht lösen wir mehrere kritische Probleme mit Umweltunsicherheiten, auf der Grundlage strenger mathematischer Paradigmen, was in vorherigen Arbeiten kaum behandelt wurde. Aus praktischer Sicht bestätigt die gute Leistung der vorgeschlagenen Meth-

oden, die sich aus Simulations- und Versuchsergebnissen ergibt, die Anwendbarkeit des vorgeschlagenen Sicherheitsparadigmas in der Praxis. Somit bietet die Arbeit in dieser Dissertation nicht nur einen theoretischen Rahmen für zuverlässige MRK in unsicheren Umgebungen, sondern zeigt auch ein großes Potential in praktischen Anwendungen. Durch die Kombination der Methoden in verschiedenen Forschungsbereichen, einschließlich Beobachtungstheorie, maschinellem Lernen, Bayes'scher Inferenz und Steuerungstheorie, bietet das in dieser Dissertation vorgestellte Sicherheitsparadigma eine neue Perspektive für die Betrachtung und Implementierung von safe MRK.

Contents

List of Figures

List of Tables

Acronyms

AHRC	the Arts and Humanities Research Council.
AI	Artificial Intelligence.
CDI	Collision Detection and Identification.
Cobot	Collaborative robot.
DM^2	Distributed Macro-Mini actuation.
DoF	Degree-of-Freedom.
EPSRC	the Engineering and Physical Sciences Research Council.
FDI	Fault Detection and Isolation.
FNN	Feedforward Neural Network.
GMM	Gaussian Mixture Model.
HCI	Human-Computer Interaction.
HIC	Human Injury Criterion.
HMM	Hidden Markov Model.
HRC	Human-Robot Collaboration.
HRI	Human-Robot Interaction.
kNN	k-Nearest Neighbors.
LDA	Linear Discriminant Analysis.
MIMO	Multi-Input Multi-Output.
MPC	Model Predictive Control.
MRK	Mensch-Roboter Kollaboration.
ODE	Ordinary Differential Equation.
PbD	Programming by Demonstration.
pHRI	physical Human-Robot Interaction.
RoA	Region of Attraction.
RRT	Rapidly exploring Random Tree.
SISO	Single-Input Single-Output.
SVM	Support Vector Machine.
UTAUT	Unified Theory of Acceptance and Use of Technology.
WAM	Whole-Arm Manipulation.

Symbols

$\mathbb{R}$	Real scalars.
$\mathbb{R}^+$	Real positive scalars.
$\mathbb{R}^n$	n-dimensional real vectors.
$\mathbb{C}$	The complex domain.
$\boldsymbol{I}_n$	n-dimensional identity matrix.
$\mathbf{0}$	Zero vectors with appropriate dimensions.
$\boldsymbol{q}$	Joint position of a robot.
$\dot{\boldsymbol{q}}$	Joint velocity of a robot.
$\ddot{\boldsymbol{q}}$	Joint acceleration of a robot.
$\boldsymbol{q}_\mathrm{d}$	Desired joint position of a robot.
$\dot{\boldsymbol{q}}_\mathrm{d}$	Desired joint velocity of a robot.
$\ddot{\boldsymbol{q}}_\mathrm{d}$	Desired joint acceleration of a robot.
$\boldsymbol{q}_\mathrm{r}$	Reference joint position of a robot.
$\dot{\boldsymbol{q}}_\mathrm{r}$	Reference joint velocity of a robot.
$\ddot{\boldsymbol{q}}_\mathrm{r}$	Reference joint acceleration of a robot.
$\boldsymbol{M}$	Inertia/Mass matrix of a robot.
$\boldsymbol{C}$	Coriolis and centrifugal matrix of a robot.
$\boldsymbol{G}$	Gravity vector of a robot.
$\boldsymbol{F}$	Fractional vector of a robot.
$\boldsymbol{\tau}_\mathrm{c}$	Commanded torque of a robot.
$\boldsymbol{\tau}_\mathrm{d}$	External torque of a robot.
$\hat{\boldsymbol{\tau}}_\mathrm{d}$	Estimation of the external torque.
$\hat{\boldsymbol{M}}$	Identified inertia/mass matrix.
$\hat{\boldsymbol{C}}$	Identified Coriolis and centrifugal matrix.
$\hat{\boldsymbol{G}}$	Identified gravity vector.
$\hat{\boldsymbol{F}}$	Identified fractional vector.
$\tilde{\boldsymbol{M}}$	Identification error of the inertia/mass matrix.
$\tilde{\boldsymbol{C}}$	Identification error the Coriolis and centrifugal matrix.
$\tilde{\boldsymbol{G}}$	Identification error the gravity vector.
$\tilde{\boldsymbol{F}}$	Identification error of the fractional vector.
$\boldsymbol{x}_1$	State variable of the observer subsystem 1.
$\boldsymbol{x}_2$	State variable of the observer subsystem 2.
$\boldsymbol{d}$	External disturbance of the robot system in regular form.
$\boldsymbol{\eta}_o$	System uncertainty for observer dynamics.
$\boldsymbol{v}_1$	Observer input of subsystem 1.
$\boldsymbol{v}_2$	Observer input of subsystem 2.

$\boldsymbol{v}_{2\mathrm{eq}}$	Equivalent control of input $\boldsymbol{v}_2$.
$\boldsymbol{v}_n$	Nominal observer input.
$\boldsymbol{v}_s$	Sliding mode observer input.
$\hat{\boldsymbol{x}}_1$	Estimation of the state variable of subsystem 1.
$\hat{\boldsymbol{x}}_2$	Estimation of the state variable of subsystem 2.
$\boldsymbol{e}_1$	Observation error $\hat{\boldsymbol{x}}_1 - \boldsymbol{x}_1$.
$\boldsymbol{e}_2$	Observation error $\hat{\boldsymbol{x}}_2 - \boldsymbol{x}_2$.
$\overline{m}$	The upper boundary scalar of $\boldsymbol{M}$.
$\overline{c}$	The upper boundary scalar of $\boldsymbol{C}$.
$\overline{g}$	The upper boundary scalar of $\boldsymbol{G}$.
$\overline{k}$	The upper boundary of the kinematic energy of the robot.
$\overline{\tau}$	The upper boundary of $\boldsymbol{\tau}$.
$\overline{\eta}_o$	The upper boundary of the uncertainty $\boldsymbol{\eta}_o$.
$\boldsymbol{\Gamma}_1$	Gain matrix of the observer.
$\boldsymbol{\Gamma}_2$	Gain matrix of the observer.
$\boldsymbol{s}$	Sliding mode variable for the observer.
α_s	The gain scalar for the switching term.
ϵ_s	The gain scalar for the switching term.
ϱ_s	The gain scalar for the switching term.
ϵ_0	Constant parameter for the observer.
ϱ_0	Constant parameter for the observer.
t_1	Lower boundary of the convergence time.
t_2	Lower boundary of the convergence time.
τ_f	Time scalar of the low-pass filter.
V_s	Lyapunov function of the sliding mode variable.
V_s^*	An upper bounding function for V_s.
V_e	Lyapunov function of the observation error.
V_1	Lyapunov function of the observation error $\boldsymbol{e}_1$.
V_1^*	An upper bounding function for V_1.
V_2	Lyapunov function of the observation error $\boldsymbol{e}_1$.
V_2^*	An upper bounding function for V_2.
δ_e	Scalar for the boundary layer of $\boldsymbol{e}_1$.
δ_s	Scalar for the boundary layer of $\boldsymbol{s}$.
δ_u	Scalar for the boundary layer of $\boldsymbol{v}_1$.
$\boldsymbol{k}_{\mathrm{pos}}$	Constant vector scaling the desired trajectory.
$\boldsymbol{k}_{\mathrm{dst}}$	Constant vector scaling the disturbance.
$\boldsymbol{e}_{\mathrm{d}}$	Trajectory tracking error $\boldsymbol{q} - \boldsymbol{q}_{\mathrm{d}}$.
$\boldsymbol{e}_{\mathrm{r}}$	Trajectory tracking error $\boldsymbol{q} - \boldsymbol{q}_{\mathrm{r}}$.
$\boldsymbol{K}_P$	The proportional gain matrix of the PD controller.
$\boldsymbol{K}_D$	The derivative gain matrix of the PD controller.
$\boldsymbol{K}_p$	The proportional gain matrix of the admittance controller.
$\boldsymbol{K}_d$	The derivative gain matrix of the admittance controller.
$\boldsymbol{F}_m$	The external force wrench.

$\boldsymbol{J}$	The Jacobian matrix of the robot.
$\boldsymbol{\tau}_m$	The measured external torque.
$\boldsymbol{T}$	The coordinate transformation matrix.
$\mathcal{T}$	The signal segment of the collision forces.
κ^*	The collision detection and classification result.
ι	The confidence index of the diagnosis result.
f_s	The sampling frequency.
$\bar{\mathcal{T}}$	The mean value of $\mathcal{T}$.
$\mathrm{Var}(\mathcal{T})$	The variance of $\mathcal{T}$.
$\mathrm{Skew}(\mathcal{T})$	The skewness of $\mathcal{T}$.
$\mathrm{Kurt}(\mathcal{T})$	The kurtosis of $\mathcal{T}$.
$\mathrm{Rng}(\mathcal{T})$	The extreme range value of $\mathcal{T}$.
$\mathrm{Dev}(\mathcal{T})$	The extreme deviation value of $\mathcal{T}$.
$E_I(\mathcal{T})$	Energy increasing index for signal segment $\mathcal{T}$.
$\mathcal{F}$	Frequency points of the Fourier transformation of signal segment $\mathcal{T}$.
$\mathcal{C}$	Complex spectrum of the Fourier transformation of signal segment $\mathcal{T}$.
$\bar{f}$	Mean frequency.
f^*	Fundamental frequency.
f_c	Band frequency.
F_crest	Crest factor.
E_rms	Average signal energy.
$E_\mathrm{rt}^{f_\mathrm{c}}$	Sub-band energy ratio with respect to band frequency f_c.
$\mathcal{X}^+$	The full feature set.
$\mathcal{X}^*$	The selected feature set.
$\mathcal{X}^-$	The minimum feature set.
$\mathcal{R}$	The observation series of classification results.
C	The collision classes.
$\mathcal{H}$	The admissible constraint set.
$h_i(\boldsymbol{q}, \dot{\boldsymbol{q}})$	State-dependent constraint functions.
c	The sliding mode coefficient (scalar).
$\boldsymbol{c}$	The sliding mode coefficients (vector).
$\boldsymbol{u}$	The control input.
$\boldsymbol{\eta}_c$	System uncertainty for the control model.
$\bar{\eta}_c$	The upper boundary of $\boldsymbol{\eta}_c$.
$\boldsymbol{e}$	The tracking error of the super-twisting controller.
$\boldsymbol{\sigma}$	The sliding mode variable super-twisting controller.
$\boldsymbol{A}$	The gain matrix for the super-twisting controller.
$\boldsymbol{\Gamma}$	The gain matrix for the super-twisting controller.
α_i	An auxiliary scalar to determine ϱ_i.
γ_i	The adaptive gain of the sliding mode controller.
ϱ_i	The gain scalar for the adaptive law.
$\bar{\gamma}_i$	An auxiliary scalar to determine ϱ_i.
γ_i^*	An ideal selection of γ_i.

$\tilde{\gamma}_i$	The adaptation errors $\gamma_i - \gamma_i^*$.
$\epsilon(\bar{\gamma}_i)$	An auxiliary scalar dependent on $\bar{\gamma}_i$ to determine ϱ_i.
V_i	The Lyapunov function of σ_i.
$\boldsymbol{z}^i$	An auxiliary vector variable for the stability proof.
z_2^i	The component of $\boldsymbol{z}^i$.
z_1^i	The component of $\boldsymbol{z}^i$.
$\boldsymbol{\Lambda}_i$	The auxiliary constant matrices for the stability proof.
ζ_i	An auxiliary variable for the stability proof.
ε_i	An auxiliary variable for the stability proof.
$\boldsymbol{P}_i$	An auxiliary constant matrix for the stability proof.
$\boldsymbol{Q}_i$	Auxiliary constant matrices.
β_i	An auxiliary constant for the stability proof.
t_c	The upper boundary of the convergence time.
$\mathcal{S}$	The invariant set.
$\partial\mathcal{S}$	Boundary of invariant set $\mathcal{S}$.
$\text{int}(\mathcal{S})$	Interior of invariant set $\mathcal{S}$.
s_i	The invariant functions.
t_0^+	The right neighborhood of t_0.
$\mathcal{Q}_0$	The admissible trajectory set at time t_0.
Δt	A small time domain in the neighborhood of t_0.
$\boldsymbol{\Omega}$	The coefficient matrix for the linear constraints.
$\boldsymbol{\Omega}_1$	The coefficient matrix for the linear constraints.
$\boldsymbol{\Omega}_2$	The coefficient matrix for the linear constraints.
$\bar{\boldsymbol{\omega}}$	The coefficient vector for the linear constraints.
$\boldsymbol{\delta}^\omega$	The coefficient vector for the linear constraints.
$\boldsymbol{q}_0$	The constant vector scaling the desired trajectory.
δ_1	A scalar to tolerate the constraint violation.
δ_2	A scalar to tolerate the constraint violation.
κ	The decaying factor of the adaptive law.

Notations

$\mathcal{A}$	Sets
$\mathcal{A} \vee \mathcal{B}$	The union of sets $\mathcal{A}$ and $\mathcal{B}$
$\overline{\mathcal{A}}$	The compliment of set $\mathcal{A}$
a	Scalars
$\dot{a}$	Time derivative of scalar a
$\ddot{a}$	Second-order derivative of scalar a
$a^{(i)}$	The i-order derivative of scalar a
$[a]$	Rounding real scalar a to an integer
$\text{sgn}(a)$	The sign function of scalar a
$\inf_{\mathcal{A}} a$	The inferior boundary of scalar a in the range $a \in \mathcal{A}$, ($\mathcal{A}$ is a continuous set)
$\sup_{\mathcal{A}} a$	The superior boundary of scalar a in the range $a \in \mathcal{A}$, ($\mathcal{A}$ is a continuous set)
$\min_{\mathcal{A}} a$	The minimal value of scalar a in the range $a \in \mathcal{A}$, ($\mathcal{A}$ is a discrete set)
$\max_{\mathcal{A}} a$	The maximal value of scalar a in the range $a \in \mathcal{A}$, ($\mathcal{A}$ is a discrete set)
$\boldsymbol{a}$	Vectors
$\dot{\boldsymbol{a}}$	Time derivative of vector $\boldsymbol{a}$
$\ddot{\boldsymbol{a}}$	Second-order derivative of vector $\boldsymbol{a}$
$\boldsymbol{a}^{(i)}$	The i-order derivative of vector $\boldsymbol{a}$
$\boldsymbol{a}^\top$	Transpose of vector $\boldsymbol{a}$
$\boldsymbol{a}_i$	The i-th element of vector $\boldsymbol{a}$
$\|\boldsymbol{a}\|$	The 2-norm of vector $\boldsymbol{a}$
$\text{sgn}(\boldsymbol{a})$	The element-wise sign function of vector $\boldsymbol{a}$
$\text{diag}(\boldsymbol{a})$	The diagonal matrix composed by the elements of vector $\boldsymbol{a}$
$\boldsymbol{A}$	Matrices
$\dot{\boldsymbol{A}}$	Time derivative of matrix $\boldsymbol{A}$
λ_A^i	The i-th eigenvalue of matrix $\boldsymbol{A}$
$\lambda_{\min}(\boldsymbol{A})$	The minimal eigenvalue of matrix $\boldsymbol{A}$
$\lambda_{\max}(\boldsymbol{A})$	The maximal eigenvalue of matrix $\boldsymbol{A}$
$\sigma(\boldsymbol{A})$	The singular value of matrix
$\|\boldsymbol{A}\|$	The 2-norm of matrix $\boldsymbol{A}$
$\boldsymbol{A}^\top$	Transpose of matrix $\boldsymbol{A}$
$\boldsymbol{A}_{i,j}$	The i-th row and j-th column element of matrix $\boldsymbol{A}$
$\boldsymbol{L}_A$	The Cholesky decomposition of matrix $\boldsymbol{A}$
C	Complex numbers

$\|C\|$	Amplitude of complex number C
$\phi(C)$	Phase angle of complex number C

1 Introduction

In recent years, robots are swarming into human society and people's daily lives, thanks to the rapid progress in computer science, mechanical manufacturing, and communication technology. They have been widely applied to various jobs with tedious tasks, repeated procedures, or hazardous environmental conditions. In the meantime, humanoid robots with service or performance purposes are widely applied in tourist spots, airports, stations, and even restaurants to serve the visiting people. The advantages of the robots, including fast speed, high precision, low uncertainty, and long durability, satisfy the growing demands for precise and standardized services. Different from the conventional industrial-oriented robot platforms that are isolated from humans, the new generation of robots are required to share the same workspace with and conduct interactive tasks with humans, which motivates the development of Human-Robot Interaction (HRI) technology [6]. By *interaction*, it usually means joint attention, verbal communication, telepresence, physical contacts, or other sorts of exchanges of information and energy between robots and humans. Especially, for those scenarios where physical contacts are demanded, physical Human-Robot Interaction (pHRI) concerns [7]. In general, most of the HRI applications are intended for a cooperative framework under which robots and humans smoothly transmit forces, signals, and information to accomplish a joint task, which is interpreted as HRC [8]. For example, on a joint assembly line of a certain mechanical device, robots and human workers are required to handover uncompleted workpieces to each other by physical contacts and then accomplish the assembly of the workpieces according to their task scripts. It is known that robots are specifically designed for precise, fast, and regulated operations, while humans are adept at flexible and creative skills. Therefore, the major motivation behind HRC is to combine these advantages to benefit the accomplishment of a comprehensively complicated task that is not possible to be conducted by a robot alone. This chapter gives an introduction of the motivation, considered topics, and contributions of this dissertation. Reviews of the fundamental work on HRI or HRC can be referred to in [6, 8–11].

1.1 Motivation and Overview

In a typical HRC scenario, the robots are usually in proximity to humans or even conduct physical contact with humans. During such an interactive process, unexpected physical contacts, or *collisions*, may potentially cause injuries to human bodies. The occurrence of collisions increases the threats to the security of the humans in an HRC system. The desire to defend humans against these threats motivates the investigation of safe HRC. It should be noted that the conventional safety standards for isolated robots no longer apply to HRC systems since humans and robots are required to share an overlapped

workspace. Instead, the safe mechanism for HRC should fully tolerate the coexistence of humans and the robot when appropriately handling potential threats. To resolve this issue, various safety frameworks for HRC systems are developed based on the studies in different research fields.

1.1.1 Objectives

The major objective of safe HRC is to prevent or mitigate the negative influences of security threats to humans. Initially, HRC safety is mainly concerned with the handling of human-robot collisions, including the detection, identification, recovery, and avoidance of collisions, which composes a collision-handling pipeline [5]. The solutions are inherited from the conventional robot platforms with additional safety regulations on proximity, velocity limits, or responsiveness requirements [12]. Meanwhile, most of the HRC safety regulations serve as exception monitoring routines intended to properly handle collisions to reduce physical injuries. Recent work also considers task errors and psychological influences as threatening factors in HRC. Although the inclusions of safe HRC are becoming more affluent and comprehensive, a universal safety framework for a generic HRC scenario still lacks. One of the challenges is that the current safe HRC frameworks do not ensure robust safety against environmental uncertainties, including partial measurements, system discontinuities, incomplete signals, and constraint violation due to external disturbances. Improving the robustness of safe HRC to uncertainties is the main goal of this dissertation.

1.1.2 Considered Topics

In this dissertation, we are concerned with the handling of human-robot collisions, a typical type of security threats of HRC. The main task of HRC collision handling is to prevent potential injuries or damages caused by accidental collisions. The collision handling mechanism, also known as a collision handling pipeline [5], typically contains two procedures, namely the pre-collision [13] and the post-collision ones [10]. The development of such a pipeline involves various research topics, including collision force estimation [303,304], collision diagnosis [13,14], collision reaction strategy design [15,16], and collision avoidance [17–19]. These topics are intended for different components in the pipeline. In this dissertation, we focus on three essential collision-handling problems, namely collision force estimation, Collision Detection and Identification (CDI), and collision avoidance control. The relationship between these topics is illustrated in Fig. 1.1, where the solid white blocks represent the pre- and post-collision pipelines, the gray blocks are considered topics in this dissertation, the dashed blocks are topics not discussed, and the arrows denote the flow of time or information. The details of these topics are specifically interpreted as follows.

1.1.2.1 Collision Force Estimation

The physical forces between humans and the robot during a collision, known as the collision forces, indicate the occurrence of a collision and its strength. Although the

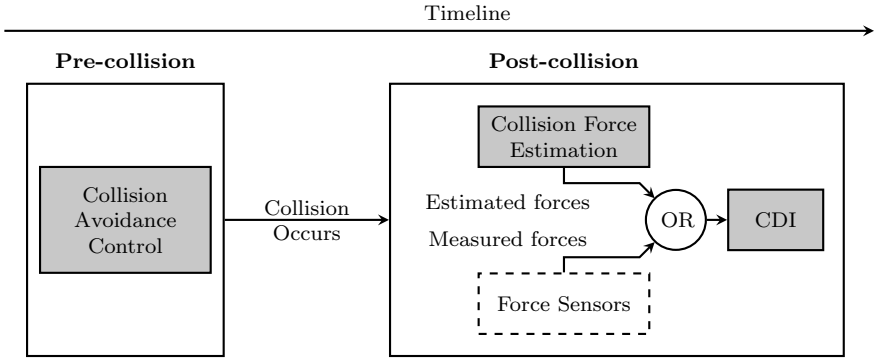

Figure 1.1: The three considered topics investigated in this dissertation.

collision forces can be accurately measured by extrinsic force sensors installed on the end-effector or joints of the robot, the force sensors with high measurement precision are usually expensive, and do not apply to robot platforms with low expense and compact structures in complicated environments. Under this condition, the collision forces can be estimated using analytical-redundancy-based methods [7, 20], for which the robot dynamic models are needed. As part of the post-collision handling pipeline, estimation of collision forces using dynamic models renders an unknown-input observation problem, for which the estimation precision is the main performance metric. Our studies on this topic is interpreted in Chapter 3.

1.1.2.2 Collision Detection and Identification

Another important procedure for post-collision handling is to detect the occurrence of a collision and identify its type, by analyzing the collision force signals. The signals are estimated forces based on analytical-redundancy, or measured forces using extrinsic force sensors, depending on specific applications. The results are used to trigger the corresponding recovery routines to reduce the potential influence of collisions. CDI for HRC requires fast and accurate classification of collision force signals between *accidental collisions* and *intentional contacts*. Here, an *accidental collision* is an unexpected physical contact that is featured with swift force changes. On the contrary, an *intentional contact* is a planned human-robot physical contact that indicates a smooth transmission of forces and energy. The former is dangerous to humans, while the latter is safe [21]. Therefore, the CDI process renders a classification problem that can be solved by supervised learning methods. However, different from the conventional classification problems, CDI for HRC should be conducted online, during the nominal task executions. This means that the diagnosis of collisions can only rely on the history signals, while the signals in the future are unknown for the current moment. The uncertainty of unknown future signals results in a classification problem with incomplete collision information. This challenge is overcome in our work presented in Chapter 4.

1.1.2.3 Collision Avoidance Control

As an important aspect of a pre-collision handling pipeline, collision avoidance is dedicated to achieving safe motion planning or control schemes for robots to prevent collisions with static and dynamic obstacles. In a well-modeled environment, the obstacles are represented as a set of safety constraints [22] or artificial potential fields [23]. The workspace confined by the constraints is the safe region for the robot motion, in which collisions can be avoided. The constraints are referred to as *hard*, since by no means the robot is expected to collide with the obstacles. To achieve a collision-free task scenario for HRC, the robot is intended to execute the task script when it is within the safe region, while adjusting its motion to prevent collisions when the task script violates the safety constraints. Various safe control methods have been applied to solve safe control problems for robot systems, including invariant control [24, 25], model predictive control [26, 27], and the barrier-function-based control [28, 28–30]. However, the conventional methods do not fully consider the influence of an uncertain environment containing the unmodeled dynamics and the external disturbances, which may lead to violation of the safety constraints. To solve this problem, we propose a robust collision avoidance control method in Chapter 5.

1.1.3 Related Research Fields

Safe HRC is a comprehensive research topic that involves multi-disciplinary concerns. Therefore, its solutions usually originated from the following various research fields. Understanding the connection of HRC to these fields benefits the improvement and generalization of current safe HRC paradigms. Following the interpretation of the related fields, we also reveal the current gaps between these fields and safe HRC, in preparation for our contributions in Sec. 1.2.

1.1.3.1 Fault Detection and Isolation

The Fault Detection and Isolation (FDI) theory is the main technology used for monitoring and diagnosis of mechatronic systems. Conventionally, FDI is considered as a significant capability of an industrial control system, especially those not accessible for humans, such as space-crafts, underwater vehicles, and remote-control robots. It enables the system to conduct self-diagnosis and self-recovery without the involvement of manual operations. Once a fault is detected, a fault-tolerant system should be able to adjust itself according to the type of the fault, and eventually initiate the fault-recovery routine to maintain the normal functions of the system. A typical FDI solution is usually analytical-redundancy-based [20], including hardware redundancy [31] and software redundancy [32]. Early work on FDI of industrial platforms and process control can be found in [33, 34], where essential model-based methods are provided. A recent survey of FDI methods can be referred to in [35].

The FDI theory relies on reconstruction and analysis of *residuals*, signals that indicate the occurrence of faults [36, 37]. A residual signal is usually equal to zero in normal cases and becomes non-zero values when a certain fault occurs. Given a certain residual

signal, a decision-making method is applied to detect the occurrence of a fault and identify its type. Therefore, the methods for FDI can be explicitly transformed to safe HRC, by recognizing the collision forces between humans and robots as residual signals. However, different from the ordinary faults in mechatronic systems, collision forces are usually featured with fast changes and short periods, which are known as instantaneous anomalies [38]. The online diagnosis of such residual signals is still a challenging work in FDI.

1.1.3.2 Robotics

The study on safe HRC originates from the desire of a smooth joint-task execution between humans and robots, where essential robotic concepts and paradigms are adopted. For example, kinematic and dynamic models of robots are utilized to implement analytical-redundancy-based FDI methods for HRC systems [39, 40]. Besides, the proxemic models are developed to regulate the distance and relative velocity between humans and mobile robots [41, 42]. Similarly, legibility [43] and human-likeness [44] are also introduced to produce human-acceptable motions for robots in safe HRC.

From the perspective of robotics, challenges still exist for a generic safe HRC framework. The main challenge is that most of the current FDI methods for HRC are not sufficiently robust to the uncertainties in unknown environments. Although various methods are proposed to model the unknown environments, it is still not possible to eliminate the modeling uncertainties. If not fully considered, these modeling uncertainties may bring down the performance of HRC systems, or even trigger dangerous events like collisions. In this dissertation, we are mainly concerned with a novel safety paradigm for HRC with an enhanced robustness against environmental uncertainties.

1.1.3.3 Control Theory

Most analytical-redundancy-based safe HRC methods are supported by control theory that provides a rigorous framework for the design of disturbance observers [45–49] and precise tracking controllers [50–54] for robot systems. The disturbance observer is used for the generation of residual signals, while the controllers are designed for a reliable task execution scheme. In this dissertation, we mainly focus on the control and observation of Euler-Lagrangian systems, i.e., rigid robot manipulators. Different from other types of nonlinear systems, the Euler-Lagrangian systems own a special passivity property inherited from the conversation-of-energy feature of mechatronic systems. Such a passive property is frequently applied to control and observation of robot systems [55]. From the perspective of control theory, the collision forces are external disturbances fed forward to the system inputs, and residual generation of robot manipulators can be formulated as an unknown-input observation problem for Euler-Lagrangian systems.

The main challenge of safe HRC in control theory is that the discontinuity of mechatronic systems, mainly caused by the viscous friction effects, is not reflected by the conventional continuous system models based on the Lipschitz condition. Thus, the approximation using continuous models leads to less rigorousness in theory and produces

filtering effects in practice. This brings down the bandwidth of the closed-loop dynamics. The sliding mode theory, supported by the discontinuous system theory [56], can be applied to resolve this issue, which is also one of the main methodologies used in this dissertation.

1.1.3.4 Signal Processing

Apart from residual generation, the diagnosis of residual signals is also an essential technology of FDI, where the signal processing methods are applied. Firstly, the identification of the collision types renders an online classification problem between accidental collisions and intentional contacts. Secondly, to develop an accurate and reliable classifier, features are generated taking full consideration of the properties of the collision signal waveform. During the development of the classifier, segmentation is a very important concern for online signal processing of the collision residual signals. Different from the conventional fault residuals considered in most FDI scenarios, collisions only last for a short period with fast changes, and vanish when the physical interaction is finished, leading to a narrow waveform with a summit shape. Therefore, to achieve accurate classification, the signal segments used for online diagnosis should contain sufficient collision information. The conventional methods usually include the entire collision waveform in the signal segments, which is an effective manner in offline applications, such as the post-fault analysis and diagnosis, but does not apply to online scenarios. However, classification based on complete collision waveform, in an online application, means that an accurate diagnosis can only be produced when the collision vanishes, which is not practical for a safe HRC system. In fact, for an HRC system with high safety requirements, the robot should be able to react to a collision in a very early stage, such that potential injuries and damages are prevented. Such a gap renders a new challenge that has not been fully investigated in related work, that is, to achieve the accurate and reliable classification of collision signals with incomplete waveform. Resolving this issue is one of the main targets of this dissertation.

1.1.3.5 Psychology and Sociology

Beyond collision handling, recent work also takes psychological and sociological factors into the consideration of safe HRC, to ensure a comfortable and acceptable interaction environment for humans, which is also known as *psychological safety* [10]. Popular psychological safety paradigms for HRC include human trust [57, 58] and social norms [10, 59], which are extensions of human-human interaction models in psychology and sociology. The analysis and construction of these models are mainly based on the validation of hypotheses by user study methods [60]. Besides, mathematical models with fundamental sociological supports, such as the proxemics model [61] and the virtual force model [62], are also used to depict the kinematic relationship between humans and robots. Although psychological safety is beyond the scope of this dissertation, a brief overview benefits the integrity of our proposed safe HRC paradigm. The related work of the psychological safety of HRC can be referred to in Chapter 2.

1.2 Contributions

In this dissertation, we investigate the safety solutions for an HRC system with collision handing as the main concern, including collision force estimation, collision detection and isolation, and collision avoidance control. Beyond the scope of the conventional methods, the following questions are considered.

Question 1. How to precisely estimate the collision forces for discontinuous systems with partial measurement?

Question 2. How to accurately classify accidental collisions from intentional contacts with incomplete collision waveform?

Question 3. How to avoid constraint violation in a tracking control task with system uncertainties?

The three questions are corresponding to the three considered topics introduced in Sec 1.1.2. **Question 1** is intended to reconstruct the collision forces online without using extrinsic torque sensors. *Online* means that the estimation results are only dependent on the current system state and the essential prior knowledge on the system and the estimation routine is executed during the task processes. **Question 2** is to online detect the occurrence of a collision and identify its type, either an *accidental collision* or an *intentional contact*, using the measured or estimated collision force signals. **Question 3** is dedicated to achieving a robust constraint-violation-free controller for robots to prevent the occurrence of collisions with static obstacles. *Robustness* indicates that the safety constraints are not violated with the existence of system uncertainties.

1.2.1 Challenges

Although the past two decades have witnessed the fast development of HRC technology, a generic safety framework for HRC systems is still missing. One of the gaps is that the current safety paradigms do not ensure sufficient safety for HRC in uncertain environments. The uncertainties include partial state measurement, incomplete sensory signals, unmodeled dynamics, and external disturbances. A collision handling mechanism fully considering these uncertainties covers the main scope of this dissertation. In the following, we specifically interpret the challenges from the perspective of each concerning research topic mentioned in Sec. 1.1.2.

Question 1: Collision Force Estimation

The collision force estimation methods based on analytical-redundancy have been intensively investigated for robot systems, including unknown input-output observer [63], nonlinear disturbance observer [64, 65], Luenberger observer [45, 46], sliding mode observers [47–49], [303], high gain observer [66], filter-based observer [67] and general momentum observers [68]. However, the application of these conventional methods is still confined in well-modeled environments since they greatly rely on the assumptions of system continuity, full-state measurement, and bounded disturbance derivatives. These impractical assumptions render uncertainties to the applications of conventional methods in practice. Acknowledging these assumptions leads to the filtering effect on the

estimation results, which brings down the estimation precision. Therefore, an applicable collision force estimator in practice has to be built on the elimination of these assumptions.

Question 2: Collision Detection and Isolation

CDI of HRC systems is conventionally formulated as a classification problem and solved by filter-based methods [14, 21] and machine-learning-based methods [69, 70]. Most of the conventional CDI methods rely on the classification of signal samples with complete waveform. Thus, they can only provide an accurate CDI result after the entire information of the collision is obtained, i.e., when the collision vanishes. These methods usually lead to impractical results in the context of safe HRC, since a collision or a contact has already occurred and negative consequences may have already been caused when the collision vanishes. Therefore, a practically applicable CDI scheme should be able to accurately identify a collision in its early stage, with incomplete collision waveform, such that potential human injuries can be prevented or reduced in advance by the successive collision-reaction procedures. The main challenge in this issue is the uncertainty brought up by the unknown future signal in an online application, which we refer to as the *causality issue* (See Sec. 4.1). To overcome the challenge, novel methods should be proposed to bring down the causality uncertainties.

Question 3: Collision Avoidance Control

The safety requirements of HRC systems are typically represented as input- or state-dependent constraints that regulate the limits of the robot motions. Therefore, the task execution process of HRC with safety regulations are formulated as a tracking control problem with constraints. Although plenty of collision-avoidance planning and control methods based on potential fields [71], invariance control [24, 25], Model Predictive Control (MPC) [27], and Region of Attraction (RoA) [72, 73] are proposed in previous work, the safety constraints may still be violated due to unmodeled dynamics and external disturbances. Thus, the robustness of constraint compliance to system uncertainties is still an open problem. Additionally, even for many robust controllers [74, 75], the determination of the parameters is a challenging work. Thererfore, a robust safe controller with an adaptive parameter tuning mechanism is desired.

1.2.2 Approaches

Currently, there are mainly three methodologies applied to the development of HRC systems, namely the physical-model-based, the hypothesis-model-based, and the data-driven-based methods. The physical-model-based methods formulate an HRC task with safety requirements as a control or planning problem confined by physical models and input- or state-dependent constraints. Physical models are typically explicit to obtain and easy to verify, by which the safe solutions can be obtained by solving a mathematical problem [76]. The hypothesis-model-based methods are usually focusing on verifying or

testing certain assumed hypotheses concerning supposed safety principles, logic or distributions, case or user studies [77]. Differently, the data-driven-based methods directly compose safety schemes by inferring the implicit laws, patterns, and relations from the collected data [78]. Typically, different safety issues require various methodologies. The problems in lower-levels of HRC systems, such as disturbance estimation and safety control, are mostly solved by physical-model-based methods [79,80]. The higher-level issues, such as the monitoring of task errors, usually rely on data-driven-based methods that enable the robots to learn the script from recorded data to allow enhanced adaptability and generalizability. A typical example is the construction of robot skills using Programming by Demonstration (PbD) [81, 82]. Hypothesis-model-based methods are mainly applied to adopt social and psychological models to HRC [83, 84]. In this dissertation, our work is built up in a comprehensive background using both physical-model-based and data-driven-based methods. We solve the collision force estimation and collision avoidance control problems with the observation theory and the control theory, respectively, based on the physical model of Euler-Lagrangian systems. In the meantime, we design the CDI scheme using supervised learning and the Bayesian decision theory, where the data of collision signals are utilized.

1.2.2.1 Observation Theory

In this dissertation, we design an integral sliding mode observer to estimate the collision forces for robot manipulators, where observation theory is applied to Euler-Lagrangian systems. Compared to the conventional methods, the sliding mode design does not rely on the Lipschitz continuous assumptions for mechatronic systems, which improves the theoretical rigorousness of the analytical-redundancy-based methods. The dynamic collapse property of the proposed method allows precise estimation of external disturbance without the velocity measurement of the system. The high-bandwidth of the discontinuous switching mechanism does not require the boundedness of disturbance derivatives. Besides, compared to the conventional sliding-mode-based methods, the application of integral sliding mode technology ensures the robustness of the closed-loop dynamics since the initial instants.

1.2.2.2 Supervised Learning

For the design of the CDI scheme for robot manipulators, we apply supervised learning methods, including k-Nearest Neighbors (kNN), Feedforward Neural Network (FNN), Support Vector Machine (SVM), and random forest. To create a representative data set for the development of classifiers, we conduct collision experiments on a real robot platform and record the collision force signals. We segment the signals, generate features, and split them into a training set and a test set. We also determine a feature set considering both the classification accuracy and the computational load, based on the analysis of feature importance and mutual dependence. After validating and testing these models, we select an FNN classifier as our classification model.

1.2.2.3 Bayesian Decision

Similar to the conventional learning-based methods, the trained collision classifier in Sec. 1.2.2.2 does not ensure accurate classification of signal segments with incomplete collision waveform. To resolve this issue, we use the Bayesian decision theory to design an online collision diagnosis module to make the ultimate decision of the classification. Based on the assumed prior probabilities and the likelihoods obtained from the experiments, we calculate the posterior probabilities that represent the belief of the CDI diagnosis with a series of classification results. The posterior probabilities then serve as reliability indexes of the diagnosis. Thus, a collision type identification result is only reported when the reliability is high, which improves the classification accuracy for incomplete waveform compared to a simple classifier. Beyond this, we also propose a fast diagnosis algorithm without calculating the posteriors, which applies to HRC systems in practice.

1.2.2.4 Control Theory

We propose a super-twisting sliding mode controller with adaptive gains for the tracking control task of a robot manipulator, to confine the robot motion within a constraint region to avoid collisions with static objects. When the desired trajectory is safe, the controller ensures precise tracking of the desired trajectory. Otherwise, when the desired trajectory violates the constraints, the controller produces a modified reference trajectory to confine the robot motion within the safe region, such that constraint violation is avoided. Both the precise tracking and safety constraints are robustly satisfied with the existence of bounded system uncertainties. The adaptive tuning law for the controller parameters improves the flexibility of the control method with various types of uncertainties, compared to the conventional methods with manually assigned gains. The stability of the closed-loop system with adaptive controller gains is proven with a Lyapunov method.

1.2.3 Main Contribution

The main contribution in this dissertation is to provide a novel solution for safe HRC in uncertain environments. Specifically, the solution is intended for accurate, fast, and reliable handling of human-robot collisions, with partial measurement, incomplete collision waveform, system discontinuity, and external disturbances. Different from the conventional methods, our solution is targeted at improving the robustness of HRC safety against environmental uncertainties. By comprehensively applying model-based and learning-based methods, we ensure decent safety performance for HRC systems, including precise estimation of collision forces, accurate collision classification, and avoidance of constraint violation with the uncertainties of partial state measurement, system discontinuity, incomplete waveform, and external disturbances. The gaps between the desired performance and the uncertainty restrictions, and the corresponding solutions, are illustrated in Fig. 1.2, where the dotted blocks are considered questions introduced in Sec 1.2.1, the solid blocks are the desired safety performance and the main challenges, and the arrows represent the methods filling the gaps. Note that the blocks filled with

gray are the novel safety metrics and uncertainties that concern this dissertation but are not considered in the previous work. Experimental validation of the proposed methods on robot manipulators indicates that our solution applies to practical HRC systems, and the results reveal decent system performance with environmental uncertainties. Thus, the proposed solution not only provides a development paradigm for HRC in complicated environments but also shows its potential towards a generic safe HRC framework for various mechatronic systems. The specific contributions corresponding to each considered topic are interpreted as follows.

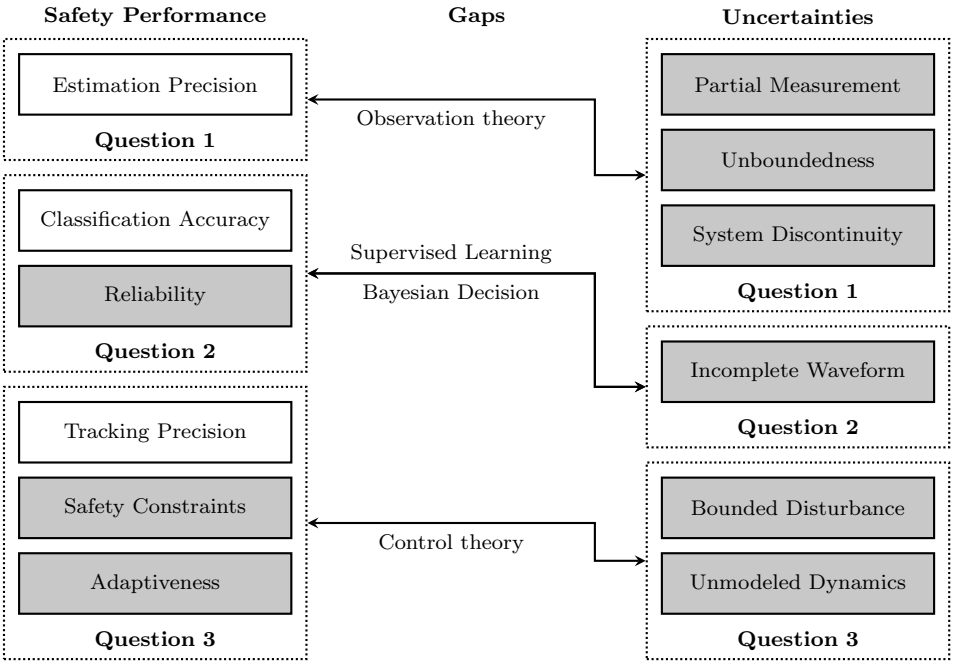

Figure 1.2: The gaps and the corresponding solutions in this dissertation.

Question 1: Collision Force Estimation

For the collision force estimation problem, the uncertainties influencing the estimation precision include partial measurement (the lack of velocity measurement), the unboundedness of disturbance derivatives, and the discontinuities of mechatronic systems. The proposed integral sliding mode observer provides a novel solution for robust disturbance estimation against these uncertainties. According to our knowledge, this is also the first unknown-input observer with the integral sliding mode technology applied.

Question 2: Collision Detection and Isolation

For collision detection and isolation, the main uncertainty is the incomplete collision waveform in online applications. In this dissertation, we use the supervised learning

methods to develop a collision signal classifier and design a Bayesian-decision-based diagnosis scheme. By achieving this, we improve the classification accuracy of the classifier with incomplete waveform and provide a belief index to represent the *reliability* of the classification result. The experimental results confirm its applicability to practical HRC systems.

Question 3: Collision Avoidance Control

For collision avoidance control, the main source of uncertainties is the constraint violation caused by unmodeled dynamics and external disturbances. Our contribution in this part is to provide a novel robust controller that satisfies precise tracking and safety constraints against the uncertainties. The application of second-order sliding mode technology eliminates the chattering phenomenon on the control output. The novel is also reflected by the adaptive parameter tuning mechanism that ensures the stability of the closed-loop system.

1.2.4 Potential Applications

The practical applicability of our methods in this dissertation is validated by a series of simulations and experiments on robot platforms. Therefore, the proposed safe HRC paradigm is promising to solve the collision handling problem for a wide range of robot systems in practice, so as to change the manner they behave in industrial manufacturing and human life. Moreover, by defining a new set of metrics measuring the safety performance of HRC systems (See Fig. 1.2), we provide a novel methodological perspective to improve the safety of robots with limited hardware resources. Some of the potential application scenarios of our safe HRC solution are illustrated as Fig. 1.3 and specifically interpreted as follows.

The first possible application of the proposed safe HRC mechanism is human-robot joint assembly, where humans and robots are required to accomplish an assembly-task sharing a common workspace [85]. In such a scenario, accidental collisions between the robot and the human body are dangerous to humans. The success of a joint assembly task has to be built on a reliable collision handling mechanism. By setting hard constraints ot keep the robot from the human-centered area and the boundaries of the workspace, our proposed safety solution enables the robot to avoid collisions with the human body and the environment. In case any collision occurs due to unexpected human motions, the robot can quickly estimate the collision forces and decide whether it is an accidental collision or an intentional contact. The advantage of our solution is reflected by its responsiveness and its reliability in uncertain environments, even without velocity and external torque measurements. Thus, our solution is promising to improve the efficiency of the joint assembly task and bring down the expenses of the system

Another potential application is the safety monitoring of bionic robots. Bionic robots mimic the appearance and structures of animals to achieve versatile dynamic properties in various environments [86]. In general, the bionic robots are designed according to specific targets and their deployed environments. Their size and weights usually have

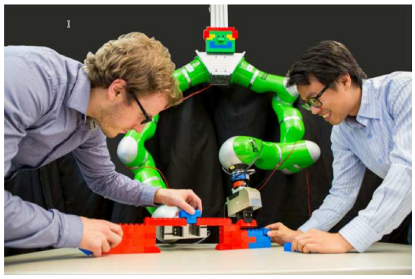

(a) Joint assembly [85].

(b) Bionic robots [86].

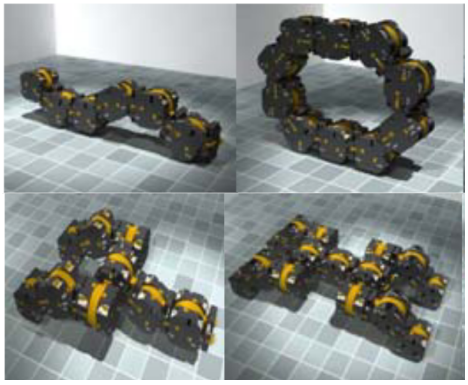

(c) Swarm robots [87].

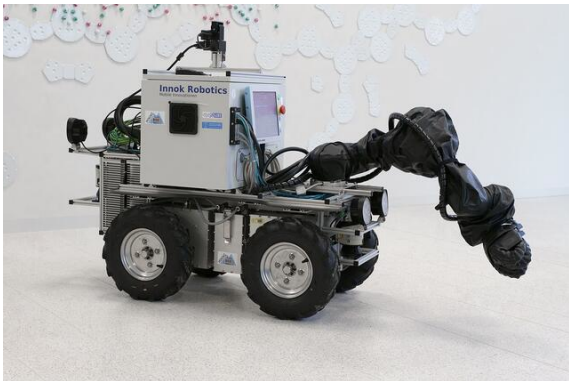

(d) Mining robots [88].

Figure 1.3: Potential applications of the proposed safe HRC paradigm.

strict restrictions. On the one hand, the bionic robots are expected to conduct versatile interactive tasks in complicated environments. On the other hand, their functionality is restricted since they can only carry a limited amount of sensory devices. Therefore, monitoring the safety of bionic robots is a challenging work due to the lack of sufficient sensory resources. The proposed collision force estimation method offers a torque-sensorless solution to detect and identify physical contacts for bionic robots. Therefore, our solution for safe HRC provides a new perspective for fault diagnosis of bionic robots.

Besides, our solution can be applied to fault detection and recovery for swarm robots. A swarm robot system is a self re-configurable robot system composed of a group of autonomous robot modules [87]. The swarm robots connect and disconnect each other to create different shapes and sizes of the entire system to meet the demands of certain tasks. The structure and functionality of each robot are usually simple, with compact structure and limited sensory devices. Similar to the bionic robots, our collision handling mechanism can be used to detect faulty events for swarm robots, such as the misconnection between the wrong pair of robots. Moreover, our methods can fully consider the mechanical discontinuity brought up by the composition and decomposition of the system. The rigid collisions can also be well reconstructed since our methods do not assume boundedness for the derivatives of the collision forces.

The last applicable scenario of our methods is the robot systems that work in complicated or hazardous environments, such as the mining robots shown in Fig. 1.3d. Robot systems easily get broken in a dangerous environment with rigid work surfaces and complicated surrounding conditions. Fragile and expensive components, such as the extrinsic sensors and cameras, are typically not installed on these robots to avoid high expenses caused by frequent consumption. Our methods are promising to provide a low-expensive and reliable FDI scheme for robot systems under such conditions. The solution tolerates the substitution of broken components since our methods are robust to system perturbations. It is also potential to be applied to a wider range of robot platforms in dangerous environments, with various structures, such as drones, vehicles, and underwater robots.

1.3 Thesis Outline

In this dissertation, Chapter 2 provides a brief overview of the previous work on safe HRC to build a connection between our work and the state of the art. Chapter 3 proposes an online collision-force estimator without assumptions on velocity measurement, system continuity, and boundedness of disturbance derivatives. The online CDI scheme is presented in Chapter 4, and the robust safe control method is discussed in Chapter 5. Finally, Chapter 6 concludes this dissertation. Before going into details, the interested readers are suggested to refer to Appendix A for the essentials of the sliding mode theory and Appendix B for the background of supervised learning and the Bayesian decision.

Related Work of Safe Human-Robot Interaction (Chapter 2)

HRC safety is a comprehensive topic containing affluent research and engineering issues from various fields, including mechanical design, control theory, signal processing, computer science, neural science, psychology, sociology, etc. For different topics, various methodologies are applied to solve problems in different forms. Therefore, the implementation of an HRC system should follow a well-organized and self-contained paradigm, such that different methodologies are properly combined. In this chapter, we provide a brief overview of the current progress of safe HRC paradigms, concerning safety factors, metrics and measures, design paradigms, and collision handling approaches. Based on this, we present our safe paradigm with a compact implementation of HRC oriented to collision handling and safe control. In such a way, we intend to construct a close connection between our solution and the previous work and outlining the advantages of our methods.

Online Collision Force Estimation (Chapter 3)

In this chapter, we propose a novel integral sliding mode observer to estimate the collision forces for robot manipulators. This method provides high-bandwidth and precise estimation results without velocity measurements, continuity assumptions, and the boundedness of disturbance derivatives. The convergence of the estimation error to zero

is theoretically in a finite time, which is proved by a direct Lyapunov method utilizing the passivity property of Euler-Lagrangian systems. An integral sliding mode manifold is designed to eliminate the reaching phase, such that the robustness of the estimation is enhanced. The method is applied to a robot manipulator to estimate the joint velocity and external contact forces in a physical human-robot task. Simulations and experiments reveal that this novel method provides fast, precise, and robust estimation results and can be used to replace the measurements of an extrinsic force sensor. The successful application of this observer to a force-sensor-less admittance controller for a manipulator contributes to the implementation of a sensor-free safety framework for HRC.

The material presented in Chapter 3 has been published in [304].

Online Collision Detection and Identification (Chapter 4)

This chapter is dedicated to developing an online CDI scheme for human-collaborative robots to detect the ocurrence of a collision and recognize its type. The scheme is composed of a signal classifier and an online diagnosor, which monitors the sensory signals of the robot system, detects the occurrence of physical human-robot interaction, and identifies its type within a short period. In the beginning, we conduct an experiment to construct a data set that contains the segmented physical interaction signals with ground truth. Then, we develop the signal classifier on the data set with the paradigm of supervised learning. To adopt the classifier to the online application with requirements on response time, an auxiliary online diagnosor is designed using Bayesian decision theory. The diagnosor provides not only a collision identification result but also a confidence index which represents the reliability of the result. Compared to the previous works, the proposed scheme ensures rapid and accurate CDI even in the early stage of physical interaction. As a result, safety mechanisms can be triggered before further injuries are caused, which is quite valuable and important towards safe HRC. In the end, the proposed scheme is validated on a robot manipulator and applied to a demonstration task with collision reaction strategies. The experimental results confirm the applicability of the scheme to collaborative robots in practice.

The material presented in Chapter 4 has been published in [305].

Adaptive and Robust Safe Tracking Control (Chapter 5)

In this chapter, we design a novel adaptive second-order sliding mode controller for Euler-Lagrangian systems with hard safety constraints. Different from the conventional sliding mode controllers, the proposed method provides adaptive controller parameters, such that the robustness of the controller is ensured for various disturbances without bringing up chattering. The controller also guarantees strict compliance with hard state-dependent inequality constraints. The asymptotic convergence of the tracking errors of the proposed controller is proven by a direct Lyapunov method. Finally, the proposed controller is validated by numerical simulation on a three-degree-of-freedom robot platform. The results confirm that the controller ensures strict constraint compliance and

precise trajectory tracking, which reveals its potential applicability to the safe control of mechatronic systems.

The material presented in Chapter 5 has been published in [306].

2 Related Work

Safety, in the context of HRC, is proposed to provide a well-defined coexistence environment for humans and robots in a collaborative task, such that physical injuries to humans are prevented or mitigated during the task execution process. Compared to the conventional robot systems, HRC systems need additional safety requirements due to the uncertainties brought up by the involvement of humans, such as constraints on robot motions and handling of accidental collisions. In recent years, the study of safe HRC is becoming a comprehensive field that involves multiple research areas including mechanical design, control theory, computer science, psychology, etc. Nevertheless, safety for HRC is still discussed in an ambiguous context, and a uniform safety framework still lacking. The target of this chapter is to provide a brief overview of the recent studies of safe HRC to build a connection between this dissertation and the related work.

2.1 Overview

The first well-known attempt to regulate robots' behaviors to protect humans is the famous Asimov-law published in the short story *Runaround* by Isaac Asimov, which is composed of the following three principles [89].

1. A robot may not injure a human being or, through inaction, allow a human being to come to harm.

2. A robot must obey the orders given it by human beings except where such orders would conflict with the First Law.

3. A robot must protect its existence as long as such protection does not conflict with the First or Second Laws.

These laws essentially formulate the basic requirements for the coexistence of robots and humans and have inspired plenty of successive variations of similar safety laws. Nevertheless, beyond the fundamental value of the Asimov-law, it is more towards a descriptive principle proposed at an abstract level. The lack of concrete definitions makes it hardly possible to be explicitly applied to practical scenarios. For example, what does it mean by *injuries* or *harms*? If the concept *protect* means an action to keep humans away from *injuries* or *harms*, what is a proper *protection* and where is the boundary? What if the *protection* of someone means *harm* to the other one? Therefore, doubts emerge to question the feasibility and applicability of the Asimov-law, due to the discrepancy of the understanding of these concepts. As a general compliment of this law, a set of five ethical *principles for designers, builders, and users of robots* is jointly published by the Engineering and Physical Sciences Research Council (EPSRC) and the Arts and Humanities Research Council (AHRC) of Great Britain in 2011, which contains the following *high-level messages* [90].

1. Robots should not be designed solely or primarily to kill or harm humans.

2. Humans, not robots, are responsible agents. Robots are tools designed to achieve human goals.

3. Robots should be designed in ways that assure their safety and security.

4. Robots are artifacts; they should not be designed to exploit vulnerable users by evoking an emotional response or dependency. It should always be possible to tell a robot from a human.

5. It should always be possible to find out who is legally responsible for a robot.

The latest internationally accepted safety standard for human-robot coexistence is [91] which provides detailed technical specifications for robot platforms with the existence of humans. Unfortunately, these laws or principles are either too generic or too specific to provide a systematic paradigm for the design of HRC systems.

For the first decade of the 21st century, safety standards and principles with precise descriptions are proposed based on previous work on the design of human-robot-coexistence systems, alongside with the rise of the studies on HRC. In [12], several quantitative requirements for human safety are presented based on the following principles.

1. A human-friendly robot must be controlled in such a way that humans and robots are able to safely share a common workspace.

2. The bandwidth of operations by a human-friendly robot must be restricted to allow a human operator to fully understand and predict the motion of the robot.

3. The collision of a human-friendly robot with a stationary person must not result in any serious injury to the person.

These principles are intended for a general class of robot systems including manipulators, mobile robots, humanoid robots, drones, etc. In this work, the significance of a *natural interface*, dedicated to implementing a reliable environmental perception, is emphasized. Especially, specific safety standards are proposed for sensory devices, which correspond to the *smooth understanding* requirement that concerns principle ***2***. These principles are validated by the experimental design of a HRC platform for a pick-and-place task. In [3], safety is interpreted as the smooth and successful execution of nominal tasks without faults or errors. It is also emphasized that physical collisions are the main threats to human safety due to high energy transference between robots and humans. Additionally, even potential collisions with large possibilities make humans feel *frightened* and do not want to work with the robots, and a reliable fault-handling mechanism is a critical technology to realize safety for HRC systems. Similar arguments are also confirmed by [9] which points out that safety means no physical contact with humans and no threats to humans, for which collisions are the main concerns. A general review of HRC applications in various fields is provided by [8], where dangerous mechanical design is also recognized as a threatening factor of HRC safety, including frictional noises, imbalance and falling, banning sharp edges or points, and accessible electric current. In [1], the relationship among *safety*, *coexistence*, and *collaboration* are interpreted as Fig. 2.1. *Safety* is the most essential and elementary aspect for all HRC systems. In this layer, lower level physical faults, such as collisions and actuator errors are concerned. *Coexistence* is mainly considered for HRC scenarios with close proximity between humans and robots. In this layer, the possibility of human coexisting with

robots is discussed, including the concerns of human acceptance. Finally, *collaboration* is the highest requirement for HRC, where humans and robots are required to jointly accomplish a task. Therefore, higher-level skills, such as coordination and task execution are demanded. This paradigm points out that the handling of collisions is a necessary procedure for HRC.

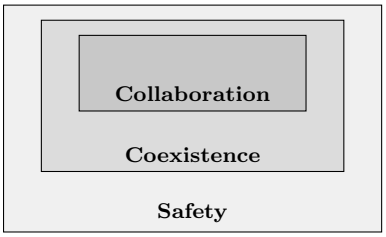

Figure 2.1: The concept diagram of safe HRC [1].

Summarizing the above mentioned previous work, we find that collision-handling is a necessary demand for HRC safety, although other factors such as mechanical design and task errors are also frequently studied. Additionally, more recent work is attempting to include psychological factors to formulate a more comprehensive HRC safety framework. For example, in [92], the psychological sense of humans is recognized as a safety factor for HRC, where the system design considering human sense is referred to as psychophysiological feedback. Also, in [10], the safety issues are generally categorized as two aspects, namely physical safety and psychological safety. Physical safety follows the conventional physical definitions mentioned above, while psychological safety focuses on producing legible, human-like and human-friendly robot motions to encourage humans to cooperate with robots.

2.2 Basic Models

The development of safe HRC systems relies on properly defined safety models. In this section, we give a brief introduction to the basic safety models applied in related work, including the main safety concerns and the development paradigms. For various safety concerns, different approaches are used, which corresponds to different components in an HRC development paradigm.

2.2.1 Safety Concerns

The HRC safety is categorized as physical safety and psychological safety. Physical safety is mainly concerned with robotic errors that might lead to robot damages or human injuries, such as collisions. Psychological safety concerns include handling human errors, legibility, trust, and social norms, which improve the acceptance of humans towards robots. These safety concerns are specifically discussed as follows.

2.2.1.1 Robotic Errors

The main functionality of the HRC safety mechanism is to properly handle robotic errors. The collision between human and robots is a representative robotic error in the lower-levels of HRC. Conventionally, errors are defined as deviations of the robot states to normal conditions. In the context of HRC, the meaning of *error* is usually twofold. Firstly, it is referred to as the *modeling errors* by early studies [93], i.e., the deviations between the actual and the nominal models of robots and the environment. Secondly, it is also used to describe the failure of a specific task or a single action [94]. For example, an error is respectively designated as the wrong dance step decision made by the human dancer and the robot partner in [95], the failure of an assembly task in [96], the inability of a robot or equipment to function normally [97], an unsafe behavior in [3], or the break down of a human-robot conversation [98]. In this dissertation, we refer to *error* following the second interpretation, while the first is interpreted as *modeling uncertainties*.

Synonyms of *error*, like *fault* and *failure*, are also frequently used, among which the distinguishment is not purposely made by early work [76,99,100]. Recent studies tend to regulate the use of these terminologies by respectively referring *error* as the disfunction in all levels of a robot system, *fault* as a lower-level error, and *failure* as a fatal error. For example, in [101], some *error*-related concepts are defined as follows.

- *Fault*: an unpermitted deviation of at least one characteristic property or parameter of the system from the acceptable, usual, or standard conditions;
- *Failure*: a permanent interruption of a system's ability to perform a required function under specified operating conditions;
- *Malfunction*: an intermittent irregularity in the fulfillment of a system's desired function;
- *Error*: a deviation between a measured or computed value (of an output variable) and the true, specified or theoretically correct value;
- *Disturbance*: an unknown (and uncontrolled) input acting on a system;
- *Perturbation*: an input acting on a system, which results in a temporary departure from the current state.

Similarly, [102] remarks that *fault* is the subset of *error* which usually happens in the lower-levels of HRC and indicates the failure of physical components such as actuators and sensors. In [94], HRC errors are classified into the following four types according to the motivation and recoverability of the system.

- *Anticipated errors*: the deviation of the motion can be *tracked back* and replanning is not necessary;
- *Exceptional errors*: the deviation from the given task is beyond the tolerance and a replanning mechanism is needed;
- *Irrecoverable errors*: the robot is not able to recover from the failure, and inference of humans are necessary;
- *Socially recoverable errors*: they can be fixed by other cooperating robots instead of working alone.

In [96], errors are classified into the following four types.

- *Execution error*: the abnormal situations caused by components failures on physical levels;
- *Planning error*: inaccurate parameter values during task planning, which lies mostly in a higher level;
- *Modeling error*: the deviation of nominal models and real features of the objects in the environment, which is closely connected with the term *environmental uncertainty*;
- *Sensing error*: the errors caused during the visual sensing processes.

To sum up, an HRC error can be interpreted as *the abnormal behaviors of robots and humans that deviate from the normal task scripts*, and it covers from the physical aspects to task executions. An error handling pipeline can be defined as a mechanism *that is able to detect the occurrence of errors and activate corresponding recovery strategies timely in order to reduce the loss as much as possible*, which contains the following procedures [103].

- *Error detection*: the process to recognize the occurrence of an error;
- *Error diagnosis*: the process to characterize the type of the error that has been detected;
- *Error recovery*: the process to recover the system error state to the normal state so that further damage be avoided;
- *Error avoidance*: the idea to construct an error-free system utilizing error avoidance methods;
- *Error forecasting*: the methods used to predict the possibility of the occurrence of an error in the future.

In this pipeline, *error detection*, *error diagnosis*, and *error recovery* are *post-handling* procedures, whilst *error avoidance* and *error forecasting* are *pre-handling* procedures. A collision, in this sense, can be recognized as a *fault*, an *irrecoverable error*, or an *execution error*. As a typical type of error, it is usually processed in the similar manner to an error handling pipeline, which is to be detailedly explained in Sec. 2.3. The Human Injury Criterion (HIC) index [104] is a frequently used qualitative metrics to measure the influence of a collision to humans, which are obtained using crash tests [105–107]. In the higher-levels of HRC, task errors are handled by discrete event system models [108], multi-variable analysis [109], discontinuous control [110], Hidden Markov Model (HMM) [111, 112], and the Petri-net model [113].

2.2.1.2 Human Errors

Besides robotic errors, human errors are also considered for safe HRC in related work. A safe robot is expected to be able to tolerate human errors in a collaborative task. According to the definition given by [114], a human error is any member of a set of human actions that exceed some limit of acceptability. Based on this, human error models are constructed in [115], and error-recovery strategies are studied in [116]. Meanwhile, the work in [117] proposes that human errors can be classified as *mistakes* or *slips* according to the causality contained in human mental models. Specifically, *mistakes* refer

to abnormal behaviors that are resulted by the wrong planning in mental models which are further classified as *rule-based mistakes* and *knowledge-based mistakes*, and *slips* are produced by the inference of environmental situations where the original intention consist with the desired objectives. A review of the studies on human errors can be found in [115].

2.2.1.3 Legibility and Human-Likeness

As a psychological terminology, *legibility* is conventionally recognized as the synonym of *readability* which means that a certain script or pattern is comprehensible and interesting to a human [118]. The application of legibility usually concerns the design of understandable display or signage [119, 120]. In [43], legibility is introduced in the study of HRC to produce intent-expressive robot motions. The work confirms that the terminology *legibility* and *intent-expressive* have the same meaning as *readability*, *anticipatory*, or *understandable* in the context of HRC. It also makes clear distinguishment between *legibility* and *predictability*. Specifically, *legibility* means *the quality of being easy to understand*, while *predictable* stands for *the capability of matching with the expectations*. From the motion-observer perspective of HRC, *legibility* and *predictability* are pointing to the opposite directions: the former targets to solving an observer to infer the actual motion, while the latter is dedicated to adjusting the motion to match the observations. Such difference is also emphasized in [121]. A recent work [122] also makes a comprehensive and detailed distinguishment between *explicability*, *legibility*, *redictability*, *transparency*, *privacy*, and *security*. The major motivation to introduce legibility to the development of HRC systems is that human motions are considered as *legible*, and humans tend to accept robots with higher legibility. A user study is conducted in [123] to investigate the influence of legibility on human acceptance. Therefore, the notion *legibility* is sometimes also discussed with the concept *human-likeness* [124–126] or *humanization* [127]. Approaches to implement legible or human-like robot motions include Bayesian inference [128], Gaussian Mixture Model (GMM) [129], and optimal planning based on minimum commanded torque [130] and minimum jerk [131]. Development of HRC systems to mimic human behaviors can be found in [44, 132].

2.2.1.4 Acceptance and Trust

Similar to legibility and predictability, human trust and acceptance are also applied to the design of safe HRC systems in related work. Differently, the modeling of human trust and acceptance is mainly based on hypothesis-based case studies [133, 134], while mathematical models for trust and acceptance are still lacking. The work in [135] provides a universal model for the investigation of user acceptance. The model is used to analyze human acceptance towards a robot assistant tour guide [136]. In [137], the influence of robot motions on human acceptance is investigated. It is also shown in [83] that the feeling of safety is the primary factor that influences human acceptance towards the robot partner. The Unified Theory of Acceptance and Use of Technology (UTAUT) is a popular model for the measurement of human acceptance [135], which has been

used together with a breaching experiment to analyze people's acceptance towards a public service robot in [136]. However, it is suggested in [83] that the UTAUT model is not suitable to all automatic systems, but should be adopted accordingly, especially for industrial assistant robots. The applications of human acceptance to the design of robots can be found in [138,139]. Compared to *acceptance*, *trust* is a step forward, which measures how humans psychologically rely on robots during the coexistence. The work on modeling of trust can be found in [84, 140–142]. Investigations of trust models in HRC applications can be referred in [57, 58].

2.2.1.5 Social Norms

The social norm is a social-psychological terminology that summarizes the conventional rules and principles that humans follow in social activities. People in society are confined by the constraints of social norms such that they behave in a predictable, smooth, and reliable manner [143]. In [144], the social norm is described as a set of non-written social rules or protocols. From a philosophical point of view, social norms are manners by which humans reduce or confine the uncertainties in their communications. It is within the recent decade that social norms are introduced to HRC, such that the robots are more *human-like* and *trustful* in the sense of social communications. In [145], social norm violations are defined as the deviation from the underlying social scripts of the HRC tasks and treated as higher-level errors to be distinguished from the lower-level technical failures. People are usually less willing to interact with a robot that violates basic social norms, which also confirms the argument of *psychological safety* in [10]. In [59], social norms are defined as the way how humans and robots interact with each other. The social behaviors between human-human and human-robot conversations are compared in [146]. In addition, social norms are also specified as task accomplishment [147–149], joint action [150–152], coordination [150, 153, 154], role adaptation [155, 156], and synchronization [157]. A review of the psychological measurement for HRC systems can be referred to in [60].

The modeling of social norm is usually challenging since it contains a large number of connotative rules that are not interpreted. It is also claimed in [158] that social norms may change to various tasks and scenarios. Most of the modeling studies of social norms are based on the analysis and processing of *social signals* or *social parameters*, including grip forces [159, 160], impedance [161], tactile sensory signals [162], emotions [163], gesture [164], gazing [165] body language [166], temporal and spatial features [167, 168], power and information transference [169], and other nonverbal social signals [170]. It is also argued in [158] that people who are interacting with the robots tend to reveal more social signals. A survey of social signal processing can be referred in [171]. Modeling of social norms using case studies can be found in [172].

Existing mathematical models for social norms include the proxemics model and the social force models. The proxemics model splits the surrounding area of a human into several ranges, with different ranges depicting various human acceptance towards the approaching objects [173]. The closer a robot is to a human, the more sensitive the human is to the robot motion. Therefore, the proxemics model has been applied to

HRC to steer the robot to adjust its velocities and accelerations when approaching to a human [41, 42, 61]. A survey on the proxemics theory can be found in [174]. The social force model is proposed based on the virtual force model and the molecular thermodynamic model [62, 175–178], which considers that the distribution of the social signals and parameters of humans (social distances, velocities, communications, interactions) are following the similar principles of molecular models. Applications of social norms to the development of HRC systems include [179, 180]. Similar safety concepts in HRC also include reliability [181], usefulness [182], human comfort [183], naturalness [184], friendliness [185], and etc.

2.2.2 Development Paradigms

To develop a safe HRC system, a well-organized paradigm is necessary to allocate the structure of the system and regulate the interfaces between different components. Therefore, various HRC safety paradigms are proposed in related work. This section gives a brief overview of some representative paradigms, based on which we present our collision-handling paradigm in Sec. 2.4.

Early approaches for the development of safe HRC include risk analysis, disturbance observation, compliant covering design, and residual signal processing [186], which are inherited from the conventional Human-Computer Interaction (HCI) framework. In [187], it is emphasized that the main difference between HRC and the conventional HCI framework is the physical and dynamical nature of robots. Therefore, in this work, a safety framework is developed for HRC based on the HCI pipeline with an extension of the hardware design iterations used to check the dangerous factors in mechanical design. Another HRC development pipeline is proposed in [59] which focuses on five safety aspects, namely *form* (abstract or anthropomorphic), *modality* (uni-modal or multi-modal), *social norms* (no knowledge of social norms or full knowledge of social norms), *autonomous* (no autonomy or fully autonomous), and *interactivity* (no causal behavior or fully causal behavior).

In [2], a hierarchical safety paradigm is proposed (See Fig. 2.2), which categorizes the safety design into tasks in four levels, namely *execution level*, *decision level*, and *human-aware motion planning*, and *symbolic planning*. The execution level is designed to guarantee the nominal functions of the control unit and the command interfaces. The decision level is composed of task agendas, interaction managers, and a supervision kernel to monitor the nominal task routines. The planning levels are designed to implement reliable task executions and legible motions while ensuring the compliance of social norm constraints.

A parallel-structured safety paradigm is presented in [3] with three separate routines, namely *intrinsic mechanism*, *safe control techniques* and *fault handing*, which is shown in Fig. 2.3. The intrinsic mechanism is concerned with the mechanical design to guarantee enhanced flexibility and compliance compared to the conventional isolated robots. Relevant work includes the Whole-Arm Manipulation (WAM) or back-drivable robots [188, 188], soft arms [189, 190], variant-impedance or -stiffness design for actuators [191–193], the Distributed Macro-Mini actuation (DM^2) design [194], and wearable

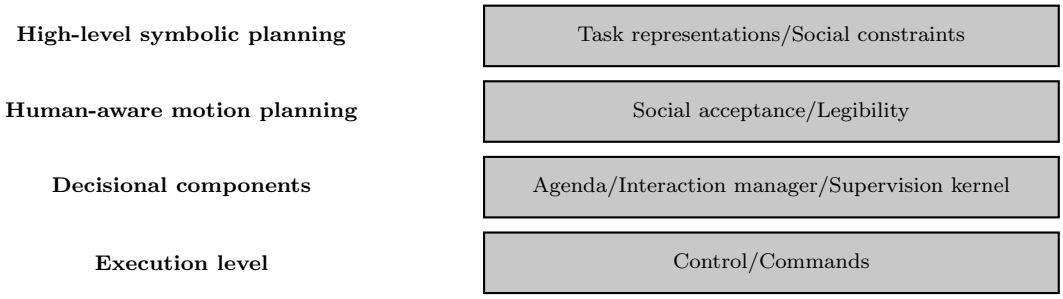

Figure 2.2: A hierarchical development paradigm [2].

devices for humans [195, 196]. The safe control techniques are targeted to implement control schemes without violating predefined safety constraints, of which the methods include invariance control [24, 25], MPC [27], and RoA based control [72, 73]. The fault handling pipeline provides a reliable routine to handle lower-level errors. Compared to the hierarchical paradigm in Fig. 2.2, this development structure treats the error handling pipeline as a separate routine from the nominal task execution. Although the errors can be handled in a manner that the nominal task is not affected, the flexibility of the handling is restricted due to lack of coupling.

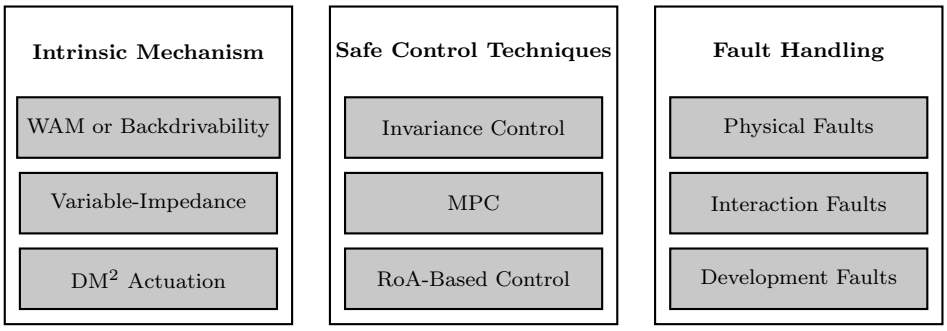

Figure 2.3: A parallel development paradigm [3].

Another hierarchical safety framework is developed in [4], which is shown in Fig. 2.4. The structure is composed of four essential levels, namely the *hardware level*, the *software level*, the *control level* and the *motion level*, with respectively the concerns of lightweight and compliant mechanical design, variable stiffness actuation, collision handling and collision avoidance planning. Compared to the hierarchical structure in Fig. 2.2, the decoupling between different levels are strengthened by regulated interfaces. Its advantage over the parallel structure in Fig. 2.3 is that error handling is integrated to the development of nominal tasks, such that the handling procedures can be flexibly designed with the tasks fully considered. This paradigm has been widely applied to the development of HRC systems [21, 197, 198].

Other HRC safety paradigms can also be found in [199, 200] with various considered safety aspects. The common ground of these safety paradigms is that the design of

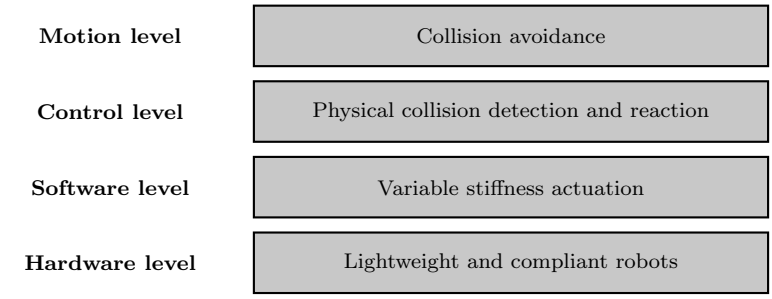

Figure 2.4: A hierarchical development paradigm [4].

HRC systems is modulized, and all modules are connected by uniform interfaces, such that different safety issues can be resolved by their corresponding methodologies without interfering the performance of the entire system.

2.3 Approaches

Collision handling for HRC is responsible for properly handling and processing human-robot collisions to protect humans from potential injuries. Therefore, it is a necessary component to achieve safe HRC. A representative collision handling pipeline is presented in [5], which is illustrated in Fig. 2.5. A complete collision handling pipeline usually contains post-handling and pre-handling pipelines, which are detailedly interpreted as follows.

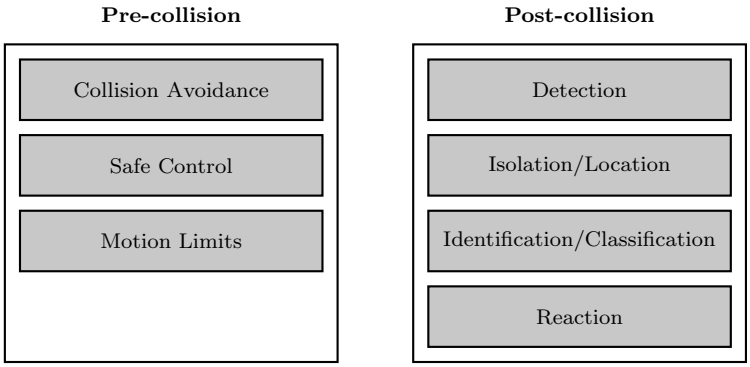

Figure 2.5: A collision handling pipeline [5].

A typical collision event handling pipeline usually contains two procedures, namely the pre-collision [13] and the post-collision ones [5, 10]. The development of such a pipeline involves various topics, including collision avoidance [17–19], collision force estimation [201, 303, 304], CDI [13, 14] and collision reaction strategy design [15, 16]. These topics are corresponding to different components in the pipeline.

2.3.1 Post-Collision Handling

A post-collision-handling procedure conducts collision force reconstruction, collision detection and identification, and collision reaction and recovery after the occurrence of a collision. The methods applied to reconstructing the collision forces include unknown input-output observer [63], nonlinear disturbance observer [64, 65], Luenberger observer [45,46], sliding mode observers [47–49,303], high gain observer [66], filter-based observer [67], general momentum observers [68], data-driven based methods [202], and learning-based methods [69, 70, 203–205]. Detection and identification of collisions are mainly conducted by classification methods [14,21,69,70]. The work in [206] pointed out a potential direction to utilize both the advantages of model-based and learning-based methods. Moreover, it is argued in [207] that an important issue for FDI applied to HRC is the unmodeled uncertainties. Reviews of applications of FDI to HRC systems can be referred in [103, 203].

2.3.2 Pre-Collision Handling

A pre-collision handling procedure is dedicated to generating or modifying the robot motions to avoid potential human-robot collisions, which is usually solved by safe control and planning methods with predefined safety conditions. The safe planning methods with human-awareness include artificial potential field [71] and Rapidly exploring Random Tree (RRT) [208]. Approaches are also proposed to consider the prediction of human motions to generate robot motions with legibility and social requirements [129,209–214]. A survey of human-aware motion planning methods for mobile robots can be referred to in [215]. Different from the safe planning methods, the safe control methods also consider the dynamic model of the system, and usually have critical online requirements. Widely applied safe control methods include the invariance control [24,25], MPC [27], PbD [82], and RoA based control [72,73]. The current challenge for safe control of HRC is that the constraint compliance with the existence of the system uncertainties, i.e., the robustness of the safety controllers, is not fully investigated. Also, self-adaptation schemes for the controller parameters are desired to improve the flexibility and adaptability of the safe control methods in various environmental conditions.

2.4 Proposed Safety Framework

In this section, we propose a novel safety paradigm for the development of HRC systems in uncertain environments, which is illustrated in Fig. 2.6. The proposed paradigm combines the advantages of the previous frameworks interpreted in Sec. 2.2.2 and contains the consideration of all safety concerns introduced in Sec. 2.2.1. This dissertation especially focuses on the implemention of a compact HRC system for collision handling, including collision force estimation, CDI, and collision avoidance control, on robot manipulators, as shown in Fig. 2.7. The compact implementation is also marked with a dotted box in Fig. 2.6. The details of the safety paradigm are explained as follows.

2.4.1 The Proposed Safety Paradigm

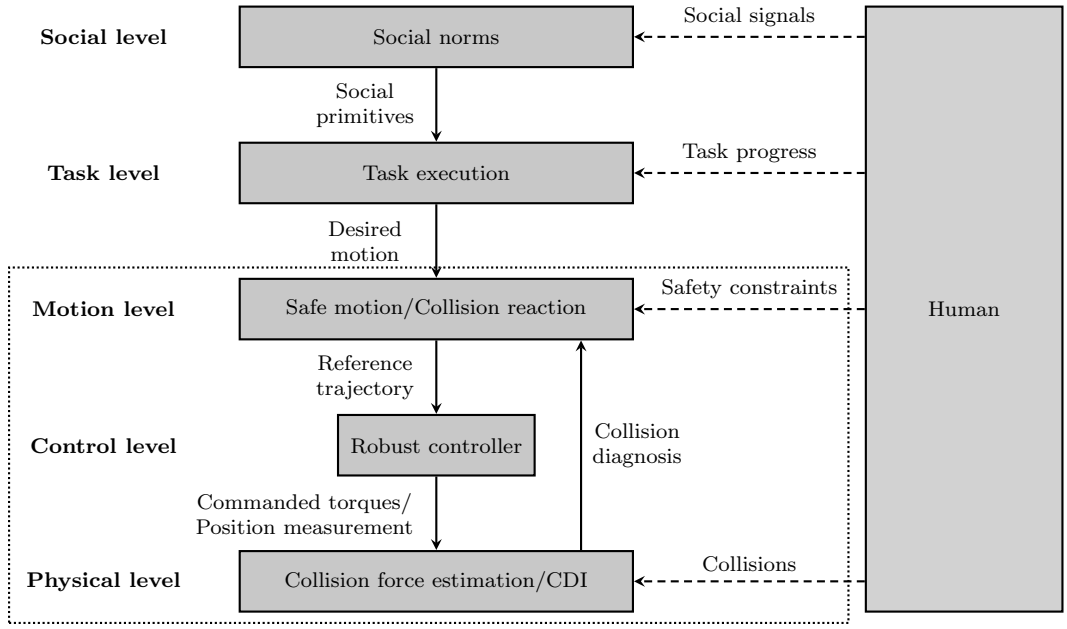

Figure 2.6: The proposed hierarchical paradigm.

As shown in Fig. 2.6, the proposed safety paradigm is concerned with the safety issues in five levels, namely *physical level*, *control level*, *motion level*, *task level*, and *social level*, from bottom to top. The five solid blocks in the middle are executable modules of the robot system in the corresponding levels. The modules communicate between different levels using predefined interfaces marked as solid arrows. The robot system also receives information from the human collaborator, which is represented as dashed arrows. The modules, interface, and perceived information at different levels are specifically interpreted as follows.

Physical Level

The *physical level* of the safety paradigm is responsible for collision force reconstruction and online CDI. From the functional point of view, it is similar to the *fault handling module* in Fig. 2.3 or the *control level* in Fig. 2.4, and corresponds to the *detection* and *classification* modules in the post-collision handling pipeline in Fig. 2.5. It takes the commanded torques and the position measurement from the system controller in the *control level*, and produces the diagnosis whether a collision occurs and what its type is to the upper-levels.

Control Level

The *control level* is intended for robust tracking of the reference trajectories provided by the higher *motion level*, which corresponds to the *execution level* in Fig. 2.2, the *safe control* routine in Fig. 2.4, or the *safe control* module in the pre-collision handling pipeline in Fig. 2.5. Its inputs are the reference trajectory and the current system state, and its output is the commanded torque to the robot joints.

Motion Level

The *motion level* is designed to generate robot motions to avoid violations of predefined safety constraints, and take reaction strategies for detected collisions. It is functionally similar to the *collision avoidance* module in the pre-collision pipeline and the *reaction* module in the post-collision pipeline in Fig. 2.5. It monitors the desired trajectory provided by the higher *task level* and produces a modified reference trajectory if the constraints are violated. It also switches the robot system to the reaction modes if a collision diagnosis is obtained.

Task Level

The *task level* monitors the progress of the joint task, and generate the desired trajectories for the robot system considering the predefined task policies and the social concerns provided by the higher *social level*. It corresponds to the *task representation* module in Fig. 2.2.

Social Level

The *social level* provides the social primitives to the robot system according to its built-in social models and the perceived social signals from humans. It is functionality similar to the *social constraints* and *social acceptance* modules in Fig. 2.2. Note that this level does not only consider social norms but also other social concerns, such as legibility and human acceptance.

Compared to the design frameworks mentioned above, our proposed safety paradigm is built on the analytical redundancy of the robot system, excluding the safety factors on mechanical design. Nevertheless, the proposed paradigm contains all safety factors listed in Sec. 2.2.1, including collisions, constraint violations, task errors, and social norms. By considering the collision handling techniques in a decoupled development structure, we combine the advantages of the previous paradigms in collision handling. Although it is still not sufficient to serve as a generic HRC safety framework, it provides a solution to include a wider range of safety concerns than the previous work.

2.4.2 A Compact Implementation

In this dissertation, we develop a compact implementation of the proposed safe HRC paradigm in Sec. 2.4.1 mainly focusing on collision handling, as shown in Fig. 2.7. The

considered partitions of the paradigm, namely the collision force estimator, the CDI scheme, and the safe control scheme, are marked by dotted boxes in Fig. 2.6, which involves the modules in the *physical*-, *control*-, and *motion*-levels. The details of the compact system are interpreted as follows.

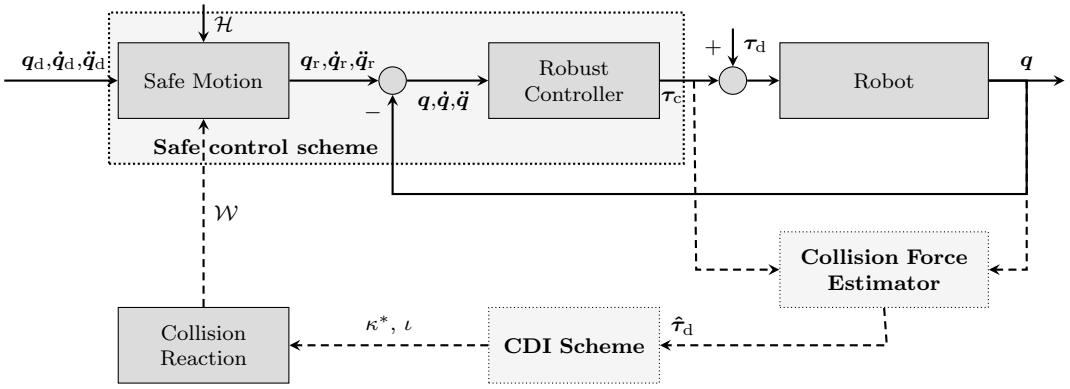

Figure 2.7: The block diagram of the proposed compact paradigm.

Currently, the compact safety paradigm is designed for robot manipulators with Euler-Lagrangian dynamics. In Fig. 2.7, the *collision force estimator* and the *CDI scheme* are corresponding to the components in the *physical level* in Fig. 2.6. $\boldsymbol{\tau}_\mathrm{d}$ represents the collision forces, and $\hat{\boldsymbol{\tau}}_\mathrm{d}$ is the estimation. $\boldsymbol{\tau}_\mathrm{c}$ and $\boldsymbol{q}$ are respectively the commanded torque and the position measurement, and κ^* and ι are respectively the classification results and the confidence index of the collision diagnosis. The robust controller forms the *control level*, and the safe motion and collision reaction modules belong to the *motion level*. $\boldsymbol{q}_\mathrm{d}$ is the desired trajectory, and $\boldsymbol{q}_\mathrm{r}$ is the reference trajectory. $\mathcal{H}$ represents the predefined constraints, and $\mathcal{W}$ is a reaction mode index to activate the corresponding reaction strategies. Besides, the modules connected by solid arrows form the inner control loop, while the dashed arrows go through the outer collision-handling loop. Note that the activation index $\mathcal{W}$ functions through a slow switching, which does not affect the stability of the system. The collision force estimator is interpreted in Chapter 3, the CDI, and the collision reaction schemes are presented in Chapter 4, and the safe control scheme, composed of the safe motion module and the robust controller, is discussed in Chapter 5.

2.5 Summary

This chapter reviews the related work in HRC on safety concerns. After a long period of development, HRC safety has been interpreted as the capability of robots to provide a harmless and comfortable joint work environment for humans. Correspondingly, the safety factors concerning the development of HRC systems are not only limited to accidental collisions but also including task errors, human errors, legibility, and psychological issues (e.g., human-trust and social norms). In the meantime, instead of simple safety regulation rules, the design paradigm for HRC systems are proposed in previous

work to include the safety concerns to the design of controllers and monitoring routines. The conventional HRC paradigms include hierarchical structures, parallel structures, and event handling pipelines. We propose a novel safe HRC framework by combining the advantages of the conventional paradigms. The proposed framework contains decoupled levels with uniform interfaces between different levels. Collision handling concerns the development of the physical level, the control level, and the motion level. Based on this paradigm, we implement a compact HRC system targeted at collision handling on a robot manipulator. For this implementation, we design a collision force estimator, an online CDI scheme, and an adaptive robust safe controller which will be specifically presented in the following chapters.

3 Online Collision Force Estimation

The primary issue to consider in our safe HRC paradigm is to obtain the physical-contact forces during the collision process. When an extrinsic force sensor is not available to provide precise measurements, the collision forces can still be reconstructed using analytical-redundancy-based methods. In this chapter, we design an online collision force estimator for robot manipulators using a novel integral sliding mode state observer, which corresponds to the *collision force estimation* module in Fig. 2.7. In theory, the observer ensures finite-time convergence of the state estimation errors to zero, which guarantees precise external force estimation. Experimental validation also confirms the decent performance and applicability of the method in practice. In general, the collision force estimation method proposed in this chapter provides a novel and reliable solution for collision reconstruction with partial state measurement, discontinuous system dynamics, and high-bandwidth disturbances. The main results of this chapter are based on the work in [304].

3.1 Overview

From a general perspective of FDI, the preliminary work before any pre- or post-processing of system faults is to obtain the *residual signals* that depict the extent of deviation from the nominal system conditions. The specific forms of residual signals may vary among different types of systems. For collision handling of HRC systems, the collision forces are usually recognized as residual signals to represent the profiles of collisions [68, 216]. The generation of residual signals with clearly defined system dynamic models renders an unknown-input observation or disturbance estimation problem.

3.1.1 Related Work

Although extrinsic force sensors provide precise measurement for collision forces [21,192], they highly restrict the size, expense, and flexibility of robot platforms. The desire of developing compact and low-expense robot platforms for highly-uncertain environments motivates our study on analytical-redundancy-based collision force reconstruction methods. As a popular approach, the disturbance estimation methods based on the observer theory are frequently used to solve FDI problems [217], especially the collision detection problem of robotic systems [216, 218]. Since no extrinsic force sensors are needed, these methods are expected to replace real force sensors in HRI tasks to achieve a sensor-less safety framework, thus bring down the cost of the robot system.

Previous work on disturbance estimation of linear systems and Euler-Lagrangian systems is vast, such as unknown input-output observer [63], nonlinear disturbance ob-

server [64, 65, 219], Luenberger observer [45, 46], sliding mode observers [47–49], high gain observer [66], filter-based observer [67] and general momentum observers [68, 201]. However, several problems or challenges still exist in these methods. First of all, the Lipschitz condition, which is a basic assumption for some previous methods [66], does not hold for practical mechatronic systems due to the existence of discontinuous friction. Second, the assumption that the derivative of the disturbance is equal to zero, which has been used in previous literature [79, 220], is not general enough to cover high-bandwidth disturbance. Third, since the position is usually the only available measurement in practice, a disturbance estimation method should not rely on velocity measurements. Instead, the velocity of the system should be estimated at the same time [221–223]. A precise velocity estimation is important to reconstruct the disturbance estimation [48].

Among the methods above, sliding mode observers solved these three problems, since they do not require the Lipschitz condition nor the disturbance derivative assumption, and they provide robust and *exact* estimation of the velocity (opposite to asymptotic). Specifically, during the sliding motion of a sliding mode observer, the state estimation is invariant from external disturbances (known as *invariance*), and the convergence of the estimation error is in a finite time (known as *exact* observation) [221, 222]. Thus the robust precision of state and disturbance estimation is guaranteed [48]. However, the invariance does not hold during the reaching phase to the sliding manifold, which means the traditional sliding mode observers are not always robust. This problem can be solved by the integral sliding mode which can theoretically eliminate the reaching phase, such that the invariance holds from the initial time instance and robustness is enhanced [224]. Even though integral sliding mode controllers are widely studied [225, 226], there has not been related work on the integral sliding mode observer for disturbance estimation of Euler-Lagrangian systems to our knowledge, whereas this enhanced robustness is worthwhile to be investigated in the fields of FDI of HRI.

3.1.2 Challenges

For the majority of the current methods, challenges still exist. Firstly, the conventional work usually constructs a disturbance observer based on the feedback linearization of continuous Euler-Lagrangian systems with the Lipschitz condition assumed, which does not coincide with the discontinuous property of mechatronic systems. Secondly, most of the existing work relies on velocity measurements of the systems which are usually obtained by difference calculation of position measurements, which naturally brings up differential noise [227–229]. On the other hand, disturbance estimation without velocity measurements renders an unknown-input observation problem with partial state measurements, which is typically challenging due to the requirement of an extra internal state reconstructor to serve as a precise differentiator. Thirdly, the previous methods mostly recognize the external disturbances as low-bandwidth or slowly changing signals by assuming a small boundary for the derivatives of the disturbance signals, which, however, does not apply to collision forces with fast changes and high-bandwidth signal components. The consequence of such an assumption is the severe filtering effect of the estimation results, where high-bandwidth signal components of the original disturbance

are lost in the estimation results, and delays are brought up. These three theoretical defects generally outline the main drawbacks of the current disturbance estimation methods in the application to safe HRC, which also forms the gap between the state of the art of FDI and the requirement of collision force reconstruction for safe HRC.

3.1.3 Contributions

The main contribution of our work in this chapter is to fill the above gap between the limitations of the current FDI methods and the desire of safe HRC, which is achieved by proposing a novel integral sliding mode observer to online estimate the external disturbances for Euler-Lagrangian systems. The adopted sliding mode paradigm provides a feasible unknown-input observation solution for discontinuous mechatronic systems. The dynamic collapse property of sliding mode produces precise differentiation of system state. Besides, the infinite-frequency switching property of sliding mode enables the capability to recover the high-bandwidth components of the collision force signals. Moreover, the sliding-mode reaching-phase of the proposed method to the integral sliding manifold is reduced compared to the conventional sliding-mode-based methods, such that the robustness is enhanced. Through these achievements, we provide a novel collision force reconstruction solution for robot systems with partial measurement, practical assumptions, higher performance standards, and severe environments.

3.1.4 Outline of the Chapter

This chapter is organized as follows. Section 3.2 briefly introduces the basic idea of integral sliding mode control and the disturbance estimation problem. The design of the integral sliding mode based observer is discussed in section 3.3 along with a finite-time stability proof. In section 3.4, a simulation is presented to show the feasibility of the integral sliding mode observer, and experiments are conducted in section 3.5 to demonstrate its performance in practical applications. Finally, section 3.6 makes a summary of the results in this chapter.

3.2 Problem Formulation

Collision force reconstruction of mechatronic systems formulates a disturbance estimation problem, and shares the same formulation as other popularly investigated problems, such as online estimation of system actuator faults [79, 230, 231], external disturbances or forces [207, 216], parametric perturbations [232] and unmodeled system dynamics [233, 234] for Euler-Lagrangian systems [68]. It is known that the analysis and diagnosis of fault signals or disturbances are critical techniques of FDI technology, especially for HRC systems [21, 106], such that robots and humans are allowed to share the same workspace and physical injuries are avoided [6, 8, 235]. More generally, disturbance estimation is also popularly studied for feed-forward disturbance compensation control [234, 236], robust control [237, 238] or fault-tolerant control [239, 240] strategies for various mechatronic systems.

3.2.1 Disturbance Estimation Problem

Consider an n-Degree-of-Freedom (DoF) Euler-Lagrangian system

$$\boldsymbol{M}(\boldsymbol{q})\ddot{\boldsymbol{q}} + \boldsymbol{C}(\boldsymbol{q}, \dot{\boldsymbol{q}})\dot{\boldsymbol{q}} + \boldsymbol{G}(\boldsymbol{q}) + \boldsymbol{F}(\dot{\boldsymbol{q}}) = \boldsymbol{\tau}_{\mathrm{c}} + \boldsymbol{\tau}_{\mathrm{d}}(t), \tag{3.1}$$

where $\boldsymbol{q}(t) \in \mathbb{R}^n$ is the vector of the generalized coordinates, $\dot{\boldsymbol{q}}(t)$ and $\ddot{\boldsymbol{q}}(t)$ are respectively the joint velocities and accelerations, $\boldsymbol{M}(\boldsymbol{q}) \in \mathbb{R}^{n\times n}$, $\boldsymbol{C}(\boldsymbol{q}, \dot{\boldsymbol{q}}) \in \mathbb{R}^{n\times n}$, $\boldsymbol{G}(\boldsymbol{q}) \in \mathbb{R}^n$ and $\boldsymbol{F}(\dot{\boldsymbol{q}}) \in \mathbb{R}^n$ are respectively the inertia matrix, Coriolis and centrifugal matrix, gravitational and frictional vectors. Note that $\boldsymbol{F}(\dot{\boldsymbol{q}})$ usually has a complicated form and contains kinematic discontinuities. $\boldsymbol{\tau}_{\mathrm{c}} \in \mathbb{R}^n$ is the commanded input, and $\boldsymbol{\tau}_{\mathrm{d}}(t)$ is the external disturbance to the system. In the case of HRI, $\boldsymbol{\tau}_{\mathrm{d}}(t)$ represents the effect of an external contact force in the joint space of a robot manipulator, which is also referred as the external torque [241]. In practice, $\boldsymbol{\tau}_{\mathrm{d}}$ can be measured by shaft torque sensors installed on the robot joints. In our work, the integral sliding mode techniques are applied to estimate $\boldsymbol{\tau}_{\mathrm{d}}$ without any extrinsic force sensors.

By defining state variables as $\boldsymbol{x}_1 = \boldsymbol{q}$, $\boldsymbol{x}_2 = \dot{\boldsymbol{q}}$, the second order system (3.1) can be written in state-space form

$$\begin{aligned} \dot{\boldsymbol{x}}_1 &= \boldsymbol{x}_2 \\ \dot{\boldsymbol{x}}_2 &= \boldsymbol{M}^{-1}(\boldsymbol{x}_1)\left(\boldsymbol{\tau} - \boldsymbol{C}(\boldsymbol{x}_1, \boldsymbol{x}_2)\boldsymbol{x}_2 - \boldsymbol{G}(\boldsymbol{x}_1) - \boldsymbol{F}(\boldsymbol{x}_2)\right) + \boldsymbol{d}(\boldsymbol{x}_1, t), \end{aligned} \tag{3.2}$$

where $\boldsymbol{d}(\boldsymbol{x}_1, t) = \boldsymbol{M}^{-1}(\boldsymbol{x}_1)\boldsymbol{\tau}_{\mathrm{d}}(t)$ is the disturbance of the system to be estimated. Note that in general, the system position $\boldsymbol{x}_1$ is directly measurable by intrinsic sensors like encoders whereas the system velocity $\boldsymbol{x}_2$ is not. In practice, $\boldsymbol{x}_2$ is usually obtained by taking the derivative of $\boldsymbol{x}_1$ and noise is involved. Note that the Lipschitz conditions can not be addressed for the dynamics (3.2) due to the discontinuity property of $\boldsymbol{F}(\boldsymbol{x}_2)$. Therefore, the target of our work in this chapter is to seek for a solution for the following problem.

Problem 1. *Given Euler-Lagrangian dynamics (3.2), reconstruct estimation $\boldsymbol{d}$ for disturbance $\boldsymbol{d}$ using only position feedback $\boldsymbol{x}_1$, such that zero is a global stability equilibrium of estimation error $\boldsymbol{d} - \hat{\boldsymbol{d}}$.*

Remark 1. *Note that in Problem 1, we do not require zero to be an asymptotic equilibrium of the estimation error, i.e., $\boldsymbol{d} - \hat{\boldsymbol{d}}$ does not have to converge to zero, due to the existence of system uncertainties. Instead, we allow a bounded perturbation of the estimation error for a given uncertainty set, to which we refer as precise estimation.*

3.2.2 Properties and Assumptions

For the Euler-Lagrangian system (3.1), it is well known that the following properties and assumptions hold.

Property 1. *[55]. The inertia matrix $\boldsymbol{M}(\boldsymbol{x}_1)$ is positive definite and its eigenvalues are bounded by $\underline{m} \leqslant \lambda_M^i(\boldsymbol{x}_1) \leqslant \overline{m}$, where $\overline{m} \in \mathbb{R}^+$, $\lambda_M^i(\boldsymbol{x}_1)$, $i = 1, 2, \cdots, n$, is the i-th*

eigenvalue of the inertia matrix $\boldsymbol{M}(\boldsymbol{x}_1)$*, and* $\underline{m}$*,* $\overline{m}$ *are respectively the minimal and maximal eigenvalues of* $\boldsymbol{M}(\boldsymbol{x}_1)$ *over all possible configurations* $\boldsymbol{x}_1$*, i.e.,*

$$\underline{m} = \inf_{\boldsymbol{x}_1} \min_{1 \leqslant i \leqslant n} \lambda_M^i(\boldsymbol{x}_1),\ \overline{m} = \sup_{\boldsymbol{x}_1} \max_{1 \leqslant i \leqslant n} \lambda_M^i(\boldsymbol{x}_1).$$

Property 2. *[55]. The Coriolis and centrifugal matrix* $\boldsymbol{C}(\boldsymbol{x}_1, \boldsymbol{x}_2)$ *is bounded by* $\|\boldsymbol{C}(\boldsymbol{x}_1, \boldsymbol{x}_2)\| \leqslant \overline{c}\|\boldsymbol{x}_2\|$*, where* $\overline{c} \in \mathbb{R}^+$*.*

Property 3. *[55]. The gravity vector is bounded by* $\|\boldsymbol{G}(\boldsymbol{x}_1)\| \leqslant \overline{g}$*, where* $\overline{g} \in \mathbb{R}^+$*.*

Property 4. *[55]. The matrix* $\dot{\boldsymbol{M}}(\boldsymbol{x}_1) - 2\boldsymbol{C}(\boldsymbol{x}_1, \boldsymbol{x}_2)$ *is skew-symmetric, i.e.,*

$$\boldsymbol{z}^\top \Big(\dot{\boldsymbol{M}}(\boldsymbol{x}_1) - 2\boldsymbol{C}(\boldsymbol{x}_1, \boldsymbol{x}_2) \Big) \boldsymbol{z} = 0,\ \forall \boldsymbol{z} \in \mathbb{R}^n,$$

where $\dot{\boldsymbol{M}}(\boldsymbol{x}_1) = \mathrm{d}\boldsymbol{M}(\boldsymbol{x}_1)/\mathrm{d}t$ *denotes the time derivative of* $\boldsymbol{M}(\boldsymbol{x}_1)$*.*

Property 5. *[47]. The Coriolis and centrifugal matrix* $\boldsymbol{C}(\boldsymbol{x}_1, \cdot)$ *satisfies,* $\forall \boldsymbol{\alpha}, \boldsymbol{\beta} \in \mathbb{R}^n$*,* $\boldsymbol{C}(\boldsymbol{x}_1, \boldsymbol{\alpha})\boldsymbol{\beta} = \boldsymbol{C}(\boldsymbol{x}_1, \boldsymbol{\beta})\boldsymbol{\alpha}$*.*

Assumption 1. *The kinetic energy of the system is bounded, i.e.,* $\boldsymbol{x}_2^\top \boldsymbol{M}(\boldsymbol{x}_1)\boldsymbol{x}_2 \leqslant \overline{k}$*, where* $\overline{k} \in \mathbb{R}^+$*.*

Assumption 2. *The external torque* $\boldsymbol{\tau}_{\mathrm{d}}(t)$ *is bounded by* $\|\boldsymbol{\tau}_{\mathrm{d}}(t)\| \leqslant \overline{\tau}$*, where* $\overline{\tau} \in \mathbb{R}^+$*.*

Remark 2. *Assumptions 1 and 2 are based on the widely accepted assumption that the kinetic energy and environmental stiffness are finite in practice. Note that we propose no assumptions on the derivative of* $\boldsymbol{\tau}_{\mathrm{d}}(t)$ *which allows our work to be applied to a wider class of systems compared to previous methods in [66, 79, 220]. Considering* $\boldsymbol{d}(\boldsymbol{x}_1, t) = \boldsymbol{M}^{-1}(\boldsymbol{x}_1)\boldsymbol{\tau}_{\mathrm{d}}(t)$ *in (3.2), we know that* $\boldsymbol{d}(\boldsymbol{x}_1, t)$ *is also bounded, i.e.,*

$$\|\boldsymbol{d}(\boldsymbol{x}_1, t)\| \leqslant \frac{\overline{\tau}}{\underline{m}}. \tag{3.3}$$

Corollary 1. *Using Assumption 1, the system velocity* $\boldsymbol{x}_2$ *is bounded by*

$$\|\boldsymbol{x}_2\| \leqslant \sqrt{\frac{\overline{k}}{\underline{m}}}.$$

Proof. Define $\boldsymbol{L}_M(\boldsymbol{x}_1)$ as the Cholesky decomposition of $\boldsymbol{M}(\boldsymbol{x}_1)$, i.e.,

$$\boldsymbol{L}_M^\top(\boldsymbol{x}_1)\boldsymbol{L}_M(\boldsymbol{x}_1) = \boldsymbol{M}(\boldsymbol{x}_1). \tag{3.4}$$

Applying Assumption 1 we have

$$(\boldsymbol{L}_M(\boldsymbol{x}_1)\boldsymbol{x}_2)^\top \boldsymbol{L}_M(\boldsymbol{x}_1)\boldsymbol{x}_2 = \boldsymbol{x}_2^\top \boldsymbol{M}(\boldsymbol{x}_1)\boldsymbol{x}_2 \leqslant \overline{k},$$

which leads to $\|\boldsymbol{L}_M(\boldsymbol{x}_1)\boldsymbol{x}_2\| \leqslant \sqrt{\overline{k}}$. Thus,

$$\|\boldsymbol{x}_2\| \leqslant \frac{\sqrt{\overline{k}}}{\inf_{\boldsymbol{x}_1} \sigma(\boldsymbol{L}_M(\boldsymbol{x}_1))} = \sqrt{\frac{\overline{k}}{\underline{m}}}, \tag{3.5}$$

where $\inf_{\boldsymbol{x}_1} \sigma(\boldsymbol{L}_M(\boldsymbol{x}_1)) = \sqrt{\underline{m}}$ is the minimal singular value of $\boldsymbol{L}_M(\boldsymbol{x}_1)$ for all $\boldsymbol{x}_1$. □

3.3 Design of Disturbance Observer

We firstly give the forms of the integral sliding mode state observer and its disturbance estimator. Then, we analyze the existence of sliding mode and the global stability of the estimation errors at zero. At the end of this section, we present the chattering reduction method for the proposed estimator in practical applications and give the derivation process of the system uncertainty term $\boldsymbol{\eta}_o(\boldsymbol{x}_1, \hat{\boldsymbol{x}}_2)$ that concerns Assumption 3.

3.3.1 Observer Formulation

The integral sliding mode state observer for Problem (1) is designed as

$$\begin{aligned}\dot{\hat{\boldsymbol{x}}}_1 =& \hat{\boldsymbol{x}}_2 - \boldsymbol{\Gamma}_1(\hat{\boldsymbol{x}}_1 - \boldsymbol{x}_1) + \boldsymbol{v}_1,\\ \dot{\hat{\boldsymbol{x}}}_2 =& \hat{\boldsymbol{M}}^{-1}(\boldsymbol{x}_1)\Big(\boldsymbol{\tau}_{\mathrm{c}} - \hat{\boldsymbol{C}}(\boldsymbol{x}_1, \hat{\boldsymbol{x}}_2)\hat{\boldsymbol{x}}_2 - \hat{\boldsymbol{G}}(\boldsymbol{x}_1) - \hat{\boldsymbol{F}}(\hat{\boldsymbol{x}}_2)\Big) + \boldsymbol{\Gamma}_2\boldsymbol{v}_1 + \boldsymbol{v}_2,\end{aligned} \tag{3.6}$$

where $\hat{\boldsymbol{x}}_1$, $\hat{\boldsymbol{x}}_2$ are the estimated system states, $\hat{\boldsymbol{M}}$, $\hat{\boldsymbol{C}}$, $\hat{\boldsymbol{G}}$, and $\hat{\boldsymbol{F}}$ are respectively the identified system parameters, $\boldsymbol{\Gamma}_1 \in \mathbb{R}^{n\times n}$ and $\boldsymbol{\Gamma}_2 \in \mathbb{R}^{n\times n}$ are positive definite matrices to be determined, and $\boldsymbol{v}_1$ and $\boldsymbol{v}_2$ are the observer inputs respectively defined as

$$\begin{aligned}\boldsymbol{v}_1(t) &= -\alpha_s \frac{\boldsymbol{e}_1(t)}{\|\boldsymbol{e}_1(t)\|} - (\varrho_s + \|\hat{\boldsymbol{x}}_2(t)\|)\frac{\boldsymbol{s}(t)}{\|\boldsymbol{s}(t)\|},\\ \boldsymbol{v}_2(t) &= \epsilon_s \frac{\boldsymbol{v}_1(t)}{\|\boldsymbol{v}_1(t)\|},\end{aligned} \tag{3.7}$$

where α_s, ϱ_s, $\epsilon_s \in \mathbb{R}^+$ are constants to be determined, $\boldsymbol{e}_1$ denotes the estimation error defined as $\boldsymbol{e}_1 = \hat{\boldsymbol{x}}_1 - \boldsymbol{x}_1$, and the switching function $\boldsymbol{s}(t)$ is defined as

$$\boldsymbol{s}(t) = \boldsymbol{e}_1(t) + \int_0^t \left(\alpha_s \frac{\boldsymbol{e}_1(\tau)}{\|\boldsymbol{e}_1(\tau)\|} + \boldsymbol{\Gamma}_1\boldsymbol{e}_1(\tau)\right)\mathrm{d}\tau - \boldsymbol{e}_1(0), \tag{3.8}$$

where $\boldsymbol{e}_1(0) = \hat{\boldsymbol{x}}_1(0) - \boldsymbol{x}_1(0)$ is the initial value of the estimation error. In this sense, the nominal control and the discontinuous control terms $\boldsymbol{v}_n$ and $\boldsymbol{v}_s$ of the observer in (3.6) are respectively

$$\boldsymbol{v}_n = \begin{bmatrix} -\boldsymbol{\Gamma}_1\boldsymbol{e}_1 \\ \boldsymbol{0} \end{bmatrix},\ \boldsymbol{v}_s = \begin{bmatrix} \boldsymbol{v}_1 \\ \boldsymbol{\Gamma}_2\boldsymbol{v}_1 + \boldsymbol{v}_2 \end{bmatrix}, \tag{3.9}$$

where $\boldsymbol{v}_n$ is the nominal continuous feedback input and $\boldsymbol{v}_s$ is the discontinuous input. The disturbance estimator for Problem 1 is determined as

$$\hat{\boldsymbol{d}} = \boldsymbol{v}_{2\mathrm{eq}}(t), \tag{3.10}$$

where $\boldsymbol{v}_{2\mathrm{eq}}(t)$ is the *equivalent control* of observer (3.6) which denotes the continuous effect of the discontinuously switching control $\boldsymbol{v}_2$ in the Filippov sense..

For convenience we also define the state estimation error $\boldsymbol{e}_2 = \hat{\boldsymbol{x}}_2 - \boldsymbol{x}_2$, where $\hat{\boldsymbol{x}}_2$ is the observed velocity. Combining the dynamics of the system (3.2) and the observer (3.6), we obtain the dynamics of the estimation errors $\boldsymbol{e}_1$ and $\boldsymbol{e}_2$ as

$$\begin{aligned}\dot{\boldsymbol{e}}_1 =& -\boldsymbol{\Gamma}_1\boldsymbol{e}_1 + \boldsymbol{e}_2 + \boldsymbol{v}_1\\ \dot{\boldsymbol{e}}_2 =& -\boldsymbol{M}^{-1}(\boldsymbol{x}_1)\left(\boldsymbol{C}(\boldsymbol{x}_1,\boldsymbol{x}_2) + \boldsymbol{C}(\boldsymbol{x}_1,\hat{\boldsymbol{x}}_2)\right)\boldsymbol{e}_2 + \boldsymbol{\Gamma}_2\boldsymbol{v}_1 + \boldsymbol{v}_2 - \boldsymbol{d}(\boldsymbol{x}_1,t) - \boldsymbol{\eta}_o(\boldsymbol{x}_1,\hat{\boldsymbol{x}}_2),\end{aligned} \tag{3.11}$$

where $\boldsymbol{\eta}_o(\boldsymbol{x}_1,\hat{\boldsymbol{x}}_2)$ is the system uncertainty caused by an inaccurate system identification, see Sec. 3.3.5 for details. Note that the solution of $\boldsymbol{e}_1$ and $\boldsymbol{e}_2$ is in the sense of Filippov but not Lipschitz [221], since (3.11) contains discontinuous inputs.

Assumption 3. *The system uncertainty $\boldsymbol{\eta}_o(\boldsymbol{x}_1,\hat{\boldsymbol{x}}_2)$ is bounded by*

$$\|\boldsymbol{\eta}_o(\boldsymbol{x}_1,\hat{\boldsymbol{x}}_2)\| \leqslant \overline{\eta} \ll \frac{\overline{\tau}}{\underline{m}}, \tag{3.12}$$

where $\overline{\eta}_o \in \mathbb{R}^+$, i.e., the system uncertainty is far smaller than the external disturbance $\boldsymbol{d}(\boldsymbol{x}_1,t)$.

Remark 3. *If the system uncertainty is far smaller than the system disturbance, then $\boldsymbol{\eta}_o(\boldsymbol{x}_1,\hat{\boldsymbol{x}}_2)$ can be ignored. This can be achieved by precise system identification.*

According to the sliding mode equivalent control theory in [48,221], if the disturbance observer (3.6) is designed in a way that the state estimation errors $\boldsymbol{e}_1$ and $\boldsymbol{e}_2$ in (3.11) converge to zero equilibrium *in finite time*, i.e.,

$$\boldsymbol{e}_1 = \boldsymbol{0},\ \dot{\boldsymbol{e}}_1 = \boldsymbol{0},\ \forall t \geqslant t_1, \tag{3.13a}$$

$$\boldsymbol{e}_2 = \boldsymbol{0},\ \dot{\boldsymbol{e}}_2 = \boldsymbol{0},\ \forall t \geqslant t_2, \tag{3.13b}$$

where $t_1,\ t_2 \in \mathbb{R}^+$, $0 < t_1,\ t_2 < +\infty$, then it is not difficult to obtain

$$\boldsymbol{v}_{2\mathrm{eq}}(t) = \boldsymbol{d}(\boldsymbol{x}_1,t) + \boldsymbol{\eta}_o(\boldsymbol{x}_1,\hat{\boldsymbol{x}}_2), \tag{3.14}$$

by substituting (3.13a) and (3.13b) into (3.11), where $\boldsymbol{v}_{2\mathrm{eq}}(t)$. Conditions (3.13a) and (3.13b) are also referred to as the *dynamics collapse* or *exact convergence* [221]. Therefore, if Assumption 3 holds, the disturbance can be approximately estimated by

It will be discussed in Sec. 3.3.2 and Sec. 3.3.3, that the proposed integral sliding mode observer ensures the exact convergence of both $\boldsymbol{e}_1$ and $\boldsymbol{e}_2$ in finite time.

Note that $\boldsymbol{v}_{2\mathrm{eq}}(t)$ cannot be computed explicitly but can be approximated by extracting the low-frequency component of $\boldsymbol{v}_2(t)$ using the following low pass filter, in practical applications, i.e.,

$$\dot{\hat{\boldsymbol{d}}} = -\frac{1}{\tau_f}\hat{\boldsymbol{d}} + \frac{1}{\tau_f}\boldsymbol{v}_2. \tag{3.15}$$

This technique is frequently used in previous work [49,221], where $\tau_f \in \mathbb{R}^+$ is the time scalar of the filter. Due to the approximation in (3.10) and the filtering in (3.15), the obtained $\hat{\boldsymbol{d}}(\boldsymbol{x}_1,t)$ is no longer a precise estimation of the disturbance $\boldsymbol{d}(\boldsymbol{x}_1,t)$, and the larger τ_f is, the more spectral component is lost. Therefore, a proper τ_f should be determined according to the practical requirements to guarantee an acceptable precision for the estimation result $\hat{\boldsymbol{d}}(\boldsymbol{x}_1,t)$.

3.3.2 Existence of the Sliding Mode Condition

In this section, we investigate the sliding mode condition of the sliding manifold. It will be shown in Sec 3.3.3, that this is a sufficient condition for the finite-time stability of the closed-loop system as in (3.11) at the zero equilibrium.

Theorem 1. *If the sliding manifold in (3.6) is designed as (3.8) and the parameter ϱ_s in (3.7) is selected such that*

$$\varrho_s \geqslant \sqrt{\overline{k}/\underline{m}} + \varrho_0, \tag{3.16}$$

where $\varrho_0 \in \mathbb{R}^+$, and $\underline{m}$, $\overline{k}$ are respectively defined in Property 1 and Assumption 1, then the following sliding mode condition holds,

$$\boldsymbol{s}(t) = \mathbf{0},\ \dot{\boldsymbol{s}}(t) = \mathbf{0},\ \forall\, t > 0. \tag{3.17}$$

Proof. By defining a Lyapunov function

$$V_s(t) = \frac{1}{2}\boldsymbol{s}(t)^\top \boldsymbol{s}(t) \tag{3.18}$$

and calculating the derivative of $\boldsymbol{s}(t)$ from (3.8)

$$\dot{\boldsymbol{s}}(t) = \dot{\boldsymbol{e}}_1(t) + \alpha_s \frac{\boldsymbol{e}_1(t)}{\|\boldsymbol{e}_1(t)\|} + \boldsymbol{\Gamma}_1 \boldsymbol{e}_1(t), \tag{3.19}$$

we obtain the derivative of $V_s(t)$ as

$$\dot{V}_s = \boldsymbol{s}^\top \dot{\boldsymbol{s}} = \boldsymbol{s}^\top \left(\dot{\boldsymbol{e}}_1 + \alpha_s \frac{\boldsymbol{e}_1}{\|\boldsymbol{e}_1\|} + \boldsymbol{\Gamma}_1 \boldsymbol{e}_1 \right).$$

For $\dot{\boldsymbol{e}}_1$ from (3.11) and $\boldsymbol{v}_1$ from (3.7), it follows that

$$\begin{aligned} \dot{V}_s &= \boldsymbol{s}^\top \left(\boldsymbol{e}_2 - (\varrho_s + \|\hat{\boldsymbol{x}}_2\|) \frac{\boldsymbol{s}}{\|\boldsymbol{s}\|} \right) = \boldsymbol{s}^\top \boldsymbol{e}_2 - (\varrho_s + \|\hat{\boldsymbol{x}}_2\|) \|\boldsymbol{s}\| \\ &\leqslant \|\boldsymbol{s}\| \|\boldsymbol{e}_2\| - (\varrho_s + \|\hat{\boldsymbol{x}}_2\|) \|\boldsymbol{s}\| \end{aligned}. \tag{3.20}$$

Since we have

$$\|\boldsymbol{e}_2\| = \|\hat{\boldsymbol{x}}_2 - \boldsymbol{x}_2\| \leqslant \|\hat{\boldsymbol{x}}_2\| + \|\boldsymbol{x}_2\| < \varrho_s + \|\boldsymbol{x}_2\|, \tag{3.21}$$

(3.20) leads to

$$\dot{V}_s \leqslant \|\boldsymbol{s}\| \|\hat{\boldsymbol{x}}_2\| + \|\boldsymbol{s}\| \|\boldsymbol{x}_2\| - \varrho_s \|\boldsymbol{s}\| - \|\hat{\boldsymbol{x}}_2\| \|\boldsymbol{s}\| = -(\varrho_s - \|\boldsymbol{x}_2\|) \sqrt{2V_s}.$$

Considering Corollary 1 and substituting (3.16), we have

$$\dot{V}_s \leqslant -\varrho_0 \sqrt{2V_s}.$$

Thus, there exists a semi-positive definite function $V_s^*(t) \in \mathbb{R}$, $V_s^*(t) \geq 0$, such that V_s is bounded by

$$0 \leqslant V_s(t) \leqslant V_s^*(t), \tag{3.22}$$

where

$$V_s^*(t) = \begin{cases} \frac{1}{2}\left(\|\boldsymbol{s}(0)\| - \varrho_0 t\right)^2, & 0 \leqslant t < \frac{1}{\varrho_s}\|\boldsymbol{s}(0)\|, \\ 0, & t \geqslant \frac{1}{\varrho_s}\|\boldsymbol{s}(0)\|. \end{cases}$$

Using (3.8), we conclude that

$$V_s^*(0) = \frac{1}{2}\boldsymbol{s}^\top(0)\boldsymbol{s}(0) = 0,$$

and finally get

$$V_s(t) = V_s^*(t) = 0, \ \forall\, t \geqslant 0. \tag{3.23}$$

Note that from (3.22) to (3.23), the comparison lemma [242] is applied, and $\dot{V}_s(t)$ and $\dot{V}_s^*(t)$ are continuous in the Filippov sense. Therefore, referring to (3.18), (3.23) leads to

$$\boldsymbol{s}(t) = 0, \ \forall t \geqslant 0, \tag{3.24}$$

which indicates a sliding mode of the dynamics (3.11) from the initial time instant $t = 0$ and the collapsed dynamics of $\boldsymbol{s}(t)$ as in (3.17) [221]. Note that $\dot{\boldsymbol{s}}(t)$ is also continuous in the sense of Filippov. □

Remark 4. *By designing the switching function (3.8) in integral form, the reaching phase is theoretically eliminated and the sliding mode exits for all $t \geqslant 0$. Thus, invariance with respect to the disturbance $\boldsymbol{d}(\boldsymbol{x}_1, t)$ holds for all $t \geqslant 0$. Note that due to the measurement uncertainties, the sliding mode condition does not strictly hold in practice and the reaching phase is not eliminated but reduced to a minimum compared to the conventional sliding mode methods.*

3.3.3 Stability Analysis

In this section, the finite-time convergence of the estimation errors $\boldsymbol{e}_1$ and $\boldsymbol{e}_2$ in (3.11) to the zero equilibrium is given by the following theorem based on the sliding mode condition (3.17) ensured by Theorem 1.

Theorem 2. *If the parameters $\boldsymbol{\Gamma}_1$, $\boldsymbol{\Gamma}_2(\hat{\boldsymbol{x}}_2)$, α_s and ϵ_s in (3.6) and (3.7) are determined such that*

$$\alpha_s > 0, \ \epsilon_s > \epsilon_0 + \overline{\eta} + \frac{\overline{\tau}}{\underline{m}}, \boldsymbol{\Gamma}_1 > 0, \ \boldsymbol{\Gamma}_2(\hat{\boldsymbol{x}}_2) > \frac{\overline{c}}{\underline{m}}\|\hat{\boldsymbol{x}}_2\|\boldsymbol{I}_n, \tag{3.25}$$

where $\epsilon_0 \in \mathbb{R}^+$, the boundary scalars $\underline{m}$, $\overline{c}$, $\overline{\tau}$, $\overline{\eta}$ are respectively defined in Properties 1, 2 and Assumptions 2, 3, and $\boldsymbol{I}_n$ is the n-dimensional identity matrix, then $\boldsymbol{e}_1(t)$ and $\boldsymbol{e}_2(t)$ converge to the zero equilibria as in (3.13a) and (3.13b) respectively in finite time t_1 and t_2, where $t_1, \ t_2 < +\infty$ are bounded by

$$t_1 < \frac{1}{\alpha_s}\|\boldsymbol{e}_1(0)\|, \ t_2 < t_1 + \frac{1}{\epsilon_s\sqrt{\underline{m}}}\|\boldsymbol{L}_M(\boldsymbol{x}_1(t))\boldsymbol{e}_2(t)\|, \tag{3.26}$$

where $\underline{m}$ is defined in Property 1, and $\boldsymbol{L}_M$ is the Cholesky matrix of $\boldsymbol{M}(\boldsymbol{x}_1)$ as in (3.4).

Proof. We define the following Lyapunov function $V_e(t) = V_1(t) + V_2(t)$, where

$$V_1(t) = \frac{1}{2}\boldsymbol{e}_1^\top \boldsymbol{e}_1,\ V_2(t) = \frac{1}{2}\boldsymbol{e}_2^\top \boldsymbol{M}(\boldsymbol{x}_1)\boldsymbol{e}_2.$$

Considering (3.17), by differentiating $\boldsymbol{e}_1$ in (3.11), we obtain

$$\dot{\boldsymbol{e}}_1 = -\alpha_s \frac{\boldsymbol{e}_1}{\|\boldsymbol{e}_1\|} - \boldsymbol{\Gamma}_1 \boldsymbol{e}_1, \tag{3.27}$$

and the derivative of V_1 reads

$$\dot{V}_1 = \boldsymbol{e}_1^\top \dot{\boldsymbol{e}}_1 = -\alpha_s \|\boldsymbol{e}_1\| - \boldsymbol{e}_1^\top \boldsymbol{\Gamma}_1 \boldsymbol{e}_1 < -\alpha_s \sqrt{2V_1}. \tag{3.28}$$

The solution of the inequality (3.28) results in $0 \leqslant V_1(t) \leqslant V_1^*(t)$, $\forall\, t \geqslant 0$, where

$$V_1^*(t) = \begin{cases} \frac{1}{2}\left(\|\boldsymbol{e}_1(0)\| - \alpha_s t\right)^2, & 0 \leqslant t < \frac{1}{\alpha_s}\|\boldsymbol{e}_1(0)\|, \\ 0, & t \geqslant \frac{1}{\alpha_s}\|\boldsymbol{e}_1(0)\|, \end{cases}$$

which leads to

$$V_1(t) = 0,\ t \geqslant t_1, \tag{3.29}$$

where t_1 is confined by

$$t_1 < \frac{1}{\alpha_s}\|\boldsymbol{e}_1(0)\| < +\infty. \tag{3.30}$$

Similar to the proof of Theorem 1, it can be concluded from (3.29) that the dynamics of $\boldsymbol{e}_1(t)$ is governed by the algebraic equations (3.13a), which indicates that the estimation error $\boldsymbol{e}_1(t)$ converges to zero in finite time and the dynamics collapse occurs afterwards. Note that $\dot{V}_1(t)$, $\dot{V}_1^*(t)$ and $\dot{\boldsymbol{e}}_1(t)$ are continuous in the sense of Filippov.

Now we consider the convergence of the velocity estimation error $\boldsymbol{e}_2(t)$. Substituting (3.11), the time derivative of $V_2(t)$ reads

$$\begin{aligned} \dot{V}_2 =& \boldsymbol{e}_2^\top \boldsymbol{M}(\boldsymbol{x}_1)\dot{\boldsymbol{e}}_2 + \frac{1}{2}\boldsymbol{e}_2^\top \dot{\boldsymbol{M}}(\boldsymbol{x}_1)\boldsymbol{e}_2 \\ =& -\boldsymbol{e}_2^\top \left(\boldsymbol{C}(\boldsymbol{x}_1, \boldsymbol{x}_2) + \boldsymbol{C}(\boldsymbol{x}_1, \hat{\boldsymbol{x}}_2)\right)\boldsymbol{e}_2 + \boldsymbol{e}_2^\top \boldsymbol{M}(\boldsymbol{x}_1)\boldsymbol{\Gamma}_2 \boldsymbol{v}_1 \\ & + \boldsymbol{e}_2^\top \boldsymbol{M}(\boldsymbol{x}_1)\left(\boldsymbol{v}_2 - \boldsymbol{d} - \boldsymbol{\eta}_o\right) + \frac{1}{2}\boldsymbol{e}_2^\top \dot{\boldsymbol{M}}(\boldsymbol{x}_1)\boldsymbol{e}_2 \\ =& \boldsymbol{e}_2^\top \left(\frac{1}{2}\dot{\boldsymbol{M}}(\boldsymbol{x}_1) - \boldsymbol{C}(\boldsymbol{x}_1, \boldsymbol{x}_2)\right)\boldsymbol{e}_2 + \boldsymbol{e}_2^\top \boldsymbol{M}(\boldsymbol{x}_1)\boldsymbol{\Gamma}_2 \boldsymbol{v}_1 \\ & + \boldsymbol{e}_2^\top \boldsymbol{M}(\boldsymbol{x}_1)\left(\boldsymbol{v}_2 - \boldsymbol{d} - \boldsymbol{\eta}_o\right) - \frac{1}{2}\boldsymbol{e}_2^\top \boldsymbol{C}(\boldsymbol{x}_1, \hat{\boldsymbol{x}}_2)\boldsymbol{e}_2. \end{aligned} \tag{3.31}$$

According to Property 4, we have

$$\boldsymbol{e}_2^\top \left(\frac{1}{2}\dot{\boldsymbol{M}}(\boldsymbol{x}_1) - \boldsymbol{C}(\boldsymbol{x}_1, \boldsymbol{x}_2)\right)\boldsymbol{e}_2 = 0. \tag{3.32}$$

Therefore, substituting (3.7) and (3.32) to (3.31), we obtain

$$\begin{aligned}\dot{V}_2 =& \boldsymbol{e}_2^\top \boldsymbol{M}(\boldsymbol{x}_1)\boldsymbol{\Gamma}_2\boldsymbol{v}_1 - \frac{1}{2}\boldsymbol{e}_2^\top(\boldsymbol{C}(\boldsymbol{x}_1,\hat{\boldsymbol{x}}_2)+\boldsymbol{C}(\boldsymbol{x}_1,\hat{\boldsymbol{x}}_2))\boldsymbol{e}_2 \\ &+ \epsilon_s \frac{\boldsymbol{e}_2^\top \boldsymbol{M}(\boldsymbol{x}_1)\boldsymbol{v}_1}{\|\boldsymbol{v}_1\|} - \boldsymbol{e}_2^\top \boldsymbol{M}(\boldsymbol{x}_1)\left(\boldsymbol{d}+\boldsymbol{\eta}_o\right).\end{aligned} \tag{3.33}$$

Substituting the collapsed dynamics of $\boldsymbol{e}_1$ in (3.13a) to $\dot{\boldsymbol{e}}_1$ in (3.11), we have

$$\boldsymbol{0} = \boldsymbol{v}_1 + \boldsymbol{e}_2,\ t \geqslant t_1, \tag{3.34}$$

which holds in the sense of Filippov. Thus, substituting (3.34) to (3.33) we have

$$\begin{aligned}\dot{V}_2 =& -\boldsymbol{e}_2^\top\left(\boldsymbol{\Gamma}_2\boldsymbol{M}(\boldsymbol{x}_1)+\frac{1}{2}\boldsymbol{C}^\top(\boldsymbol{x}_1,\hat{\boldsymbol{x}}_2)+\frac{1}{2}\boldsymbol{C}(\boldsymbol{x}_1,\hat{\boldsymbol{x}}_2)\right)\boldsymbol{e}_2 \\ &- \epsilon_s \frac{\boldsymbol{e}_2^\top \boldsymbol{M}(\boldsymbol{x}_1)\boldsymbol{e}_2}{\|\boldsymbol{e}_2\|} - \boldsymbol{e}_2^\top \boldsymbol{M}(\boldsymbol{x}_1)\left(\boldsymbol{d}+\boldsymbol{\eta}_o\right).\end{aligned} \tag{3.35}$$

Considering the selection of $\boldsymbol{\Gamma}_2$ and γ_s in (3.25), we have

$$\begin{aligned}&\boldsymbol{\Gamma}_2\boldsymbol{M}(\boldsymbol{x}_1)+\frac{1}{2}\boldsymbol{C}^\top(\boldsymbol{x}_1,\hat{\boldsymbol{x}}_2)+\frac{1}{2}\boldsymbol{C}(\boldsymbol{x}_1,\hat{\boldsymbol{x}}_2) \\ &\quad > \frac{\overline{c}\|\hat{\boldsymbol{x}}_2\|}{\underline{m}}\boldsymbol{M}(\boldsymbol{x}_1)+\frac{1}{2}\boldsymbol{C}^\top(\boldsymbol{x}_1,\hat{\boldsymbol{x}}_2)+\frac{1}{2}\boldsymbol{C}(\boldsymbol{x}_1,\hat{\boldsymbol{x}}_2) \geqslant 0,\end{aligned} \tag{3.36}$$

where Property 1 and 2 are applied. Therefore, (3.35) leads to

$$\dot{V}_2 < -\epsilon_s \frac{\boldsymbol{e}_2^\top \boldsymbol{M}(\boldsymbol{x}_1)\boldsymbol{e}_2}{\|\boldsymbol{e}_2\|} - \boldsymbol{e}_2^\top \boldsymbol{M}(\boldsymbol{x}_1)\left(\boldsymbol{d}+\boldsymbol{\eta}_o\right). \tag{3.37}$$

Substituting (3.4), we have

$$\begin{aligned}\dot{V}_2 <& -\epsilon_s \frac{\|\boldsymbol{L}_{\mathrm{M}}\boldsymbol{e}_2\|}{\|\boldsymbol{e}_2\|}\frac{\boldsymbol{e}_2^\top \boldsymbol{M}(\boldsymbol{x}_1)\boldsymbol{e}_2}{\|\boldsymbol{L}_{\mathrm{M}}\boldsymbol{e}_2\|} - (\boldsymbol{L}_M\boldsymbol{e}_2)^\top \boldsymbol{L}_M(\boldsymbol{d}+\boldsymbol{\eta}_o) \\ \leqslant& -\epsilon_s\sigma_{\min}(\boldsymbol{L}_M)\|\boldsymbol{L}_M\boldsymbol{e}_2\| + \|\boldsymbol{L}_M\boldsymbol{e}_2\|\|\boldsymbol{L}_M(\boldsymbol{d}+\boldsymbol{\eta}_o)\| \\ \leqslant& (-\epsilon_s + \|\boldsymbol{d}+\boldsymbol{\eta}_o\|)\inf\sigma(\boldsymbol{L}_M)\|\boldsymbol{L}_M\boldsymbol{e}_2\|, \\ \leqslant& (-\epsilon_s + d_O + h_O)\sqrt{\underline{m}}\,\|\boldsymbol{L}_M\boldsymbol{e}_2\|,\end{aligned}$$

Considering (3.25), we obtain

$$\dot{V}_2 < -\epsilon_0\sqrt{2\underline{m}V_2}.$$

Thus, $V_2(t)$ is bounded by $0 \leqslant V_2(t) \leqslant V_2^*(t)$, $t \geqslant t_1$, where

$$V_2^*(t) = \frac{1}{2}\left(\|\boldsymbol{L}_M\boldsymbol{e}_2(t_1)\| + \epsilon_0\sqrt{\underline{m}}\,(t_1 - t)\right)^2$$

for $t_1 \leqslant t < t_1 + \frac{1}{\epsilon_0\sqrt{\underline{m}}}\|\boldsymbol{L}_M\boldsymbol{e}_2(t_1)\|$, and $V_2^*(t) = 0$ for $t \geqslant t_1 + \frac{1}{\epsilon_0\sqrt{\underline{m}}}\|\boldsymbol{L}_M\boldsymbol{e}_2(t_1)\|$, which leads to

$$V_2(t) = 0,\ t \geqslant t_2, \tag{3.38}$$

where t_2 is confined by

$$t_2 < t_1 + \frac{1}{\epsilon_0 \sqrt{\underline{m}}} \|\boldsymbol{L}_M \boldsymbol{e}_2(t_1)\| < +\infty.$$

Therefore, $\boldsymbol{e}_2(t)$ achieves dynamics collapse within finite time t_2. Note that $\dot{V}_2(t)$, $\dot{V}_2^*(t)$ and $\dot{\boldsymbol{e}}_2(t)$ are also continuous in the sense of Filippov. □

Remark 5. *In the proof of Theorem 2, it is noticed that the dynamics collapse of $\boldsymbol{e}_1(t)$ is a necessary condition of the finite-time convergence of $\boldsymbol{e}_2(t)$. Therefore, the sliding mode of $\boldsymbol{e}_2$ is achieved only after the convergence of $\boldsymbol{e}_1$. By constructing such successive sliding modes of $\boldsymbol{s}$, $\boldsymbol{e}_1$ and $\boldsymbol{e}_2$, the proposed observer (3.6) ensures a theoretically precise estimation of the disturbance $\boldsymbol{d}$ without the velocity measurement $\boldsymbol{x}_2$.*

Different from the conventional integral sliding mode which merely ensures the asymptotic convergence of system states, the proposed observer in (3.6) guarantees the finite-time convergence of both $\boldsymbol{s}(t)$ and the estimation errors $\boldsymbol{e}_1(t)$ and $\boldsymbol{e}_2(t)$ to zero. Nevertheless, we still name the method as an *integral sliding mode observer*, since it possesses the advantage of conventional integral sliding mode, i.e., the sliding mode is achieved since the initial time instant.

3.3.4 Chattering Reduction and Filtering

Similar to the conventional sliding mode controller, chattering is a major issue for this integral sliding mode observer. The main reason for chattering is the finite switching frequency, which is confined by the sampling rate of the system. To reduce the chattering and obtain a smooth disturbance estimation, the boundary layer method is applied. We change the unit control switching function in (3.7) into the following modified form

$$\begin{aligned} \boldsymbol{v}_1 &= -\frac{\alpha_s \boldsymbol{e}_1}{\|\boldsymbol{e}_1\| + \delta_e} - (\varrho_s + \|\hat{\boldsymbol{x}}_2(t)\|) \frac{\boldsymbol{s}}{\|\boldsymbol{s}\| + \delta_s}, \\ \boldsymbol{v}_2 &= \frac{\epsilon_s \boldsymbol{v}_1}{\|\boldsymbol{v}_1\| + \delta_u}, \end{aligned} \tag{3.39}$$

and the sliding manifold $\boldsymbol{s}$ from (3.8) is also modified to

$$\boldsymbol{s} = \boldsymbol{e}_1 + \int_{t_0}^{t} \left(\frac{\alpha_s \boldsymbol{e}_1}{\|\boldsymbol{e}_1\| + \delta_e} + \boldsymbol{\Gamma}_1 \boldsymbol{e}_1 \right) \mathrm{d}\tau - \boldsymbol{e}_1(0),$$

where δ_e, δ_s, $\delta_u \in \mathbb{R}^+$ are scalars that determine the width of the boundary layers.

Note that after applying this modification, the finite-time convergence of $\boldsymbol{s}(t)$, $\boldsymbol{e}_1(t)$ and $\boldsymbol{e}_2(t)$ do not strictly hold with respect to the equilibria as in (3.17), (3.13a) and (3.13b), but only with respect to the boundary layers $\|\boldsymbol{s}(t)\| \leqslant \delta_s$, $\|\boldsymbol{e}_1(t)\| \leqslant \delta_e$ and $\|\boldsymbol{e}_2(t)\| \leqslant \delta_u$ instead. The consequence is inferior estimation precision and robustness. Therefore, a compromise has to be found between estimation performance and the chattering level, and the boundary layer parameters δ_e, δ_s and δ_u should be carefully determined according to the specific requirements of practical applications.

3.3.5 Derivation of System Uncertainty

This section provides the derivation of the error dynamics (3.11) of the proposed observer (3.6) and estimate the boundary of the system uncertainty $\boldsymbol{\eta}_o(\boldsymbol{x}_1, \hat{\boldsymbol{x}}_2)$ in Assumption 3. By combining the observer dynamics (3.6) and the original system (3.2), we obtain the form of $\boldsymbol{\eta}_o(\boldsymbol{x}_1, \hat{\boldsymbol{x}}_2)$ as

$$\begin{aligned}\dot{\boldsymbol{e}}_2 =&\boldsymbol{M}^{-1}\boldsymbol{C}(\boldsymbol{x}_1, \boldsymbol{x}_2)\boldsymbol{x}_2 - \hat{\boldsymbol{M}}^{-1}\hat{\boldsymbol{C}}(\boldsymbol{x}_1, \hat{\boldsymbol{x}}_2)\hat{\boldsymbol{x}}_2 + \boldsymbol{M}^{-1}\boldsymbol{G} - \hat{\boldsymbol{M}}^{-1}\hat{\boldsymbol{G}} \\ &+ \boldsymbol{M}^{-1}\boldsymbol{F}(\boldsymbol{x}_2) - \hat{\boldsymbol{M}}^{-1}\hat{\boldsymbol{F}}(\hat{\boldsymbol{x}}_2) - \boldsymbol{M}^{-1}\boldsymbol{\tau}_{\mathrm{c}} + \hat{\boldsymbol{M}}^{-1}\boldsymbol{\tau}_{\mathrm{c}} - \boldsymbol{d}(\boldsymbol{x}_1, t) + \boldsymbol{\Gamma}_2\boldsymbol{v}_1 + \boldsymbol{v}_2, \\ =&\boldsymbol{M}^{-1}\Big(\boldsymbol{C}(\boldsymbol{x}_1, \boldsymbol{x}_2)\boldsymbol{x}_2 - \hat{\boldsymbol{C}}(\boldsymbol{x}_1, \hat{\boldsymbol{x}}_2)\hat{\boldsymbol{x}}_2 + \tilde{\boldsymbol{G}} + \tilde{\boldsymbol{F}}\Big) \\ &+ \Big(\boldsymbol{M}^{-1} - \hat{\boldsymbol{M}}^{-1}\Big)\Big(\hat{\boldsymbol{C}}(\boldsymbol{x}_1, \hat{\boldsymbol{x}}_2)\hat{\boldsymbol{x}}_2 + \hat{\boldsymbol{G}} + \hat{\boldsymbol{F}} - \boldsymbol{\tau}_{\mathrm{c}}\Big) - \boldsymbol{d}(\boldsymbol{x}_1, t) + \boldsymbol{\Gamma}_2\boldsymbol{v}_1 + \boldsymbol{v}_2,\end{aligned} \tag{3.40}$$

where $\tilde{\boldsymbol{C}}(\boldsymbol{x}_1, \hat{\boldsymbol{x}}_2) = \boldsymbol{C}(\boldsymbol{x}_1, \hat{\boldsymbol{x}}_2) - \hat{\boldsymbol{C}}(\boldsymbol{x}_1, \hat{\boldsymbol{x}}_2)$, $\tilde{\boldsymbol{G}} = \boldsymbol{G} - \hat{\boldsymbol{G}}$, $\tilde{\boldsymbol{F}} = \boldsymbol{F}(\boldsymbol{x}_2) - \hat{\boldsymbol{F}}(\hat{\boldsymbol{x}}_2)$ are model deviations, and $\boldsymbol{x}_1$ is omitted in the inertia matrices $\boldsymbol{M}$ and $\hat{\boldsymbol{M}}$ and the gravity matrices $\boldsymbol{G}$ and $\hat{\boldsymbol{G}}$. Therefore, (3.40) results in considering that

$$\begin{aligned}&\hat{\boldsymbol{C}}(\boldsymbol{x}_1, \hat{\boldsymbol{x}}_2)\hat{\boldsymbol{x}}_2 - \boldsymbol{C}(\boldsymbol{x}_1, \boldsymbol{x}_2)\boldsymbol{x}_2 = \boldsymbol{C}(\boldsymbol{x}_1, \hat{\boldsymbol{x}}_2)\hat{\boldsymbol{x}}_2 \\ &\quad - \boldsymbol{C}(\boldsymbol{x}_1, \boldsymbol{x}_2)\boldsymbol{x}_2 + \hat{\boldsymbol{C}}(\boldsymbol{x}_1, \hat{\boldsymbol{x}}_2)\hat{\boldsymbol{x}}_2 - \boldsymbol{C}(\boldsymbol{x}_1, \hat{\boldsymbol{x}}_2)\hat{\boldsymbol{x}}_2 \\ &= \boldsymbol{C}(\boldsymbol{x}_1, \hat{\boldsymbol{x}}_2)\hat{\boldsymbol{x}}_2 - \boldsymbol{C}(\boldsymbol{x}_1, \boldsymbol{x}_2)\boldsymbol{x}_2 + \tilde{\boldsymbol{C}}(\boldsymbol{x}_1, \hat{\boldsymbol{x}}_2)\hat{\boldsymbol{x}}_2 \\ &= \boldsymbol{C}(\boldsymbol{x}_1, \hat{\boldsymbol{x}}_2)\hat{\boldsymbol{x}}_2 - \boldsymbol{C}(\boldsymbol{x}_1, \hat{\boldsymbol{x}}_2)\boldsymbol{x}_2 + \tilde{\boldsymbol{C}}(\boldsymbol{x}_1, \hat{\boldsymbol{x}}_2)\hat{\boldsymbol{x}}_2, \\ &\quad + \boldsymbol{C}(\boldsymbol{x}_1, \hat{\boldsymbol{x}}_2)\boldsymbol{x}_2 - \boldsymbol{C}(\boldsymbol{x}_1, \boldsymbol{x}_2)\boldsymbol{x}_2,\end{aligned} \tag{3.41}$$

and substituting $\boldsymbol{C}(\boldsymbol{x}_1, \hat{\boldsymbol{x}}_2)\boldsymbol{x}_2 = \boldsymbol{C}(\boldsymbol{x}_1, \boldsymbol{x}_2)\hat{\boldsymbol{x}}_2$, which is supported by Property 5, to (3.41), we have

$$\begin{aligned}&\hat{\boldsymbol{C}}(\boldsymbol{x}_1, \hat{\boldsymbol{x}}_2)\hat{\boldsymbol{x}}_2 - \boldsymbol{C}(\boldsymbol{x}_1, \boldsymbol{x}_2)\boldsymbol{x}_2 \\ &= \boldsymbol{C}(\boldsymbol{x}_1, \hat{\boldsymbol{x}}_2)\hat{\boldsymbol{x}}_2 - \boldsymbol{C}(\boldsymbol{x}_1, \hat{\boldsymbol{x}}_2)\boldsymbol{x}_2 + \tilde{\boldsymbol{C}}(\boldsymbol{x}_1, \hat{\boldsymbol{x}}_2)\hat{\boldsymbol{x}}_2, \\ &\quad + \boldsymbol{C}(\boldsymbol{x}_1, \boldsymbol{x}_2)\hat{\boldsymbol{x}}_2 - \boldsymbol{C}(\boldsymbol{x}_1, \boldsymbol{x}_2)\boldsymbol{x}_2 \\ &= \boldsymbol{C}(\boldsymbol{x}_1, \hat{\boldsymbol{x}}_2)\boldsymbol{e}_2 + \tilde{\boldsymbol{C}}(\boldsymbol{x}_1, \hat{\boldsymbol{x}}_2)\hat{\boldsymbol{x}}_2 + \boldsymbol{C}(\boldsymbol{x}_1, \boldsymbol{x}_2)\boldsymbol{e}_2.\end{aligned} \tag{3.42}$$

Therefore, substituting (3.42) to (3.40) and compare with (3.11), we figure out the expression of $\boldsymbol{\eta}_o(\boldsymbol{x}_1, \hat{\boldsymbol{x}}_2)$ as

$$\begin{aligned}\boldsymbol{\eta}_o(\boldsymbol{x}_1, \hat{\boldsymbol{x}}_2) =&\boldsymbol{M}^{-1}\Big(\tilde{\boldsymbol{C}}(\boldsymbol{x}_1, \hat{\boldsymbol{x}}_2)\hat{\boldsymbol{x}}_2 + \tilde{\boldsymbol{G}} + \tilde{\boldsymbol{F}}\Big) \\ &+ \Big(\hat{\boldsymbol{M}}^{-1} - \boldsymbol{M}^{-1}\Big)\Big(\hat{\boldsymbol{C}}(\boldsymbol{x}_1, \hat{\boldsymbol{x}}_2)\hat{\boldsymbol{x}}_2 + \hat{\boldsymbol{G}} + \hat{\boldsymbol{F}}(\hat{\boldsymbol{x}}_2) - \boldsymbol{\tau}_{\mathrm{c}}\Big) \\ =&\boldsymbol{M}^{-1}\Big(\tilde{\boldsymbol{C}}(\boldsymbol{x}_1, \hat{\boldsymbol{x}}_2)\hat{\boldsymbol{x}}_2 + \tilde{\boldsymbol{G}} + \tilde{\boldsymbol{F}}\Big) \\ &+ \Big(\hat{\boldsymbol{M}}^{-1} - \boldsymbol{M}^{-1}\Big)\Big(\hat{\boldsymbol{C}}(\boldsymbol{x}_1, \hat{\boldsymbol{x}}_2)\hat{\boldsymbol{x}}_2 + \hat{\boldsymbol{G}} + \hat{\boldsymbol{F}}(\hat{\boldsymbol{x}}_2) - \boldsymbol{\tau}_{\mathrm{c}}\Big)\end{aligned} \tag{3.43}$$

Note that the identified parametric matrices $\hat{\boldsymbol{M}}$, $\hat{\boldsymbol{C}}(\boldsymbol{x}_1, \hat{\boldsymbol{x}}_2)$, $\hat{\boldsymbol{G}}(\boldsymbol{x}_1)$ and $\hat{\boldsymbol{F}}(\hat{\boldsymbol{x}}_2)$ do not depend on the modeling deviations. Therefore, (3.43) indicates that the system uncertainty

$\boldsymbol{\eta}_o(\boldsymbol{x}_1, \hat{\boldsymbol{x}}_2)$ is linearly dependent on the deviations $\tilde{\boldsymbol{C}}(\boldsymbol{x}_1, \hat{\boldsymbol{x}}_2)$, $\tilde{\boldsymbol{G}}$ and $\tilde{\boldsymbol{F}}$. By applying precise system identification procedures, the uncertainty boundary $\|\boldsymbol{\eta}_o(\boldsymbol{x}_1, \hat{\boldsymbol{x}}_2)\|$ can be reduced.

3.4 Simulations

The proposed integral sliding mode observer has been evaluated by a simulation of a 3-DoF robot manipulator described by (3.1). In this simulation, we run the robot with a given desired trajectory and a PD tracking controller. A predefined disturbance torque $\boldsymbol{\tau}_\mathrm{d}$ is exerted on the joints during the motion of the robot. Meanwhile, the integral sliding mode observer is implemented to obtain the online estimation $\hat{\boldsymbol{\tau}}_\mathrm{d}$. Then, the observer is evaluated based on the comparison between $\boldsymbol{\tau}_\mathrm{d}$ and $\hat{\boldsymbol{\tau}}_\mathrm{d}$. The dynamic parameters of the simulated manipulator model are shown in Tab. 3.1 and Tab. 3.2, where $m_{ij}, i, j = 1, 2, 3$ are the corresponding elements in the inertia matrix $\boldsymbol{M}(\boldsymbol{q})$ and n_k, $k = 1, 2, 3$ are the elements of the Coriolis and centrifugal vector $\boldsymbol{C}(\boldsymbol{q}, \dot{\boldsymbol{q}})\dot{\boldsymbol{q}}$. For brevity, the gravity and friction terms are omitted to simulate a friction-less robot confined in the horizontal plane. The values of the parameters are listed in Tab. 3.3 and 3.4, where $q_i, \dot{q}_i \in \mathbb{R}$ respectively denote the angular position and velocity of the i-th joint. The simulation is implemented using a first-order Euler solver with a sampling rate 1 kHz, and runs for 6 s.

Table 3.1: Elements of the Inertia Matrix

Variable	Expression	Variable	Expression
m_{11}	$\alpha_1 + 2\beta_1 c_{23} + 2\beta_2 c_2 + 2\beta_3 c_3$	m_{22}	$\alpha_2 + \beta_3 c_3$
m_{12}	$\alpha_2 + \beta_1 c_{23} + \beta_2 c_2 + 2\beta_3 c_3$	m_{23}	$\alpha_3 + \beta_3 c_3$
m_{13}	$\alpha_3 + \beta_1 c_{23} + \beta_3 c_3$	m_{33}	α_3

Table 3.2: Elements of Coriolis and centrifugal vector

Variable	Expression
n_1	$\gamma_1 s_2 \dot{q}_1^2 + \gamma_2 s_{23} \dot{q}_1^2 + \gamma_3 s_2 (\dot{q}_1 + \dot{q}_2)^2 + \gamma_4 s_3 (\dot{q}_1 + \dot{q}_2)^2$ $+\gamma_5 s_{23} (\dot{q}_1 + \dot{q}_2 + \dot{q}_3)^2 + \gamma_6 s_3 (\dot{q}_1 + \dot{q}_2 + \dot{q}_3)^2$
n_2	$\gamma_1 s_2 \dot{q}_1^2 + \gamma_2 s_{23} \dot{q}_1^2 + \gamma_4 s_3 (\dot{q}_1 + \dot{q}_2)^2$ $+\gamma_6 s_3 (\dot{q}_1 + \dot{q}_2 + \dot{q}_3)^2$
n_3	$\gamma_2 s_{23} \dot{q}_1^2 + \gamma_4 s_3 (\dot{q}_1 + \dot{q}_2)^2$

Table 3.3: Trigonometric Functions

Symbol	Expression	Symbol	Expression	Symbol	Expression
c_2	$\cos(q_2)$	c_3	$\cos(q_3)$	c_{23}	$\cos(q_2+q_3)$
s_2	$\sin(q_2)$	s_3	$\sin(q_3)$	s_{23}	$\sin(q_2+q_3)$

Table 3.4: System parameters

Param	Value	Parameter	Value	Param	Value	Param	Value
α_1	1.0425	β_1	0.0405	γ_1	0.1742	γ_4	0.0281
α_2	0.4398	β_2	0.1742	γ_2	0.0405	γ_5	-0.0405
α_3	0.1788	β_3	0.0281	γ_3	-0.1742	γ_6	-0.0281

In the simulation, a sinusoidal desired trajectory $\boldsymbol{q}_\mathrm{d}(t) \in \mathbb{R}^3$ in joint space is defined as (see Fig. (3.1))

$$\boldsymbol{q}_\mathrm{d}(t) = \left(1 + \sin\left(\frac{\pi}{3}t - \frac{\pi}{6}\right)\right)\boldsymbol{k}_\mathrm{pos},\ 0 \leqslant t \leqslant 6,$$

where $\boldsymbol{k}_\mathrm{pos} = [\ 0.5\ \ 0.8\ \ 0.2\ ]^\top$ is the coefficient vector to distribute different amplitudes to each joint. The manipulator is configured with non-zero initial conditions, i.e. $\boldsymbol{q}(0) = [\ 0.25\ \ 0.4\ \ 0.1\ ]^\top$ and $\dot{\boldsymbol{q}}(0) = [\ 0.45\ \ 0.73\ \ 0.18\ ]^\top$. A PD controller is designed for the robot to track the given trajectory $\boldsymbol{q}_\mathrm{d}(t)$,

$$\boldsymbol{\tau}_\mathrm{c} = \boldsymbol{M}(\boldsymbol{q})\left(\ddot{\boldsymbol{q}}_\mathrm{d} + \boldsymbol{K}_D\dot{\boldsymbol{e}}_\mathrm{d} + \boldsymbol{K}_P\boldsymbol{e}_\mathrm{d}\right) + \boldsymbol{C}(\boldsymbol{q},\dot{\boldsymbol{q}})\dot{\boldsymbol{q}}, \tag{3.44}$$

where $\boldsymbol{e}_\mathrm{d} = \boldsymbol{q}_\mathrm{d} - \boldsymbol{q}$ and $\dot{\boldsymbol{e}}_\mathrm{d} = \dot{\boldsymbol{q}}_\mathrm{d} - \dot{\boldsymbol{q}}$ are the tracking errors, $\boldsymbol{K}_P = 200\boldsymbol{I}_3$, $\boldsymbol{K}_D = 36\boldsymbol{I}_3$ are the diagonal proportional and derivative gain matrices, and $\boldsymbol{I}_3$ is a 3×3 unit diagonal matrix.

Sinusoidal disturbance torques $\boldsymbol{\tau}_\mathrm{d}(t)$ are added to the commanded input $\boldsymbol{\tau}_\mathrm{c}$ on the three joints of the robot in the simulation which are

$$\boldsymbol{\tau}_\mathrm{d}(t) = \begin{cases} 0, & 0 \leqslant t \leqslant 2.5 \\ \sin\left(\dfrac{\pi}{2}(t-0.5)\right)\boldsymbol{k}_\mathrm{dst}, & 0.5 < t \leqslant 2.5, \\ \sin\left(\dfrac{\pi}{2}(t-4)\right)\boldsymbol{k}_\mathrm{dst}, & 4 < t \leqslant 6, \end{cases} \tag{3.45}$$

where $\boldsymbol{k}_\mathrm{dst} = [\ 15\ \ 18\ \ 12\ ]^\top$ is the coefficient vector. Similar disturbances are also used in related work, such as in [79], since they resembles the waveform of contact forces in practice.

An integral sliding mode observer in (3.6) is implemented to estimate the disturbance $\hat{\boldsymbol{\tau}}_\mathrm{d}$ in (3.45). The parameters of the observer are listed in Tab. 3.5. The initial states of the observer are set to $\hat{\boldsymbol{x}}_1(0) = \boldsymbol{0}$ and $\hat{\boldsymbol{x}}_2(0) = \boldsymbol{0}$. The evaluation of the simulation

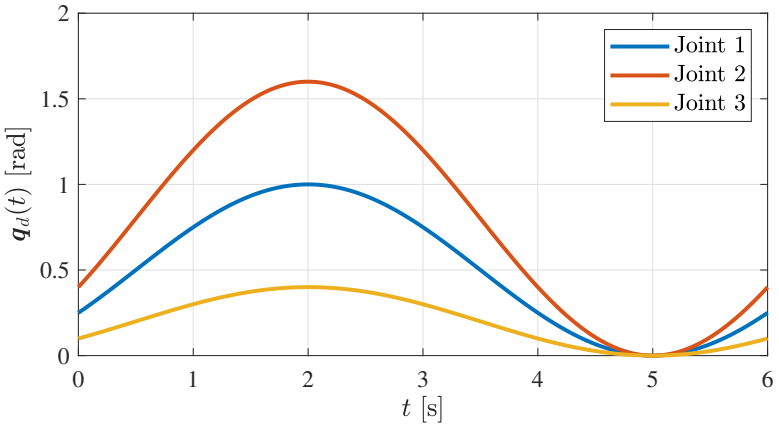

Figure 3.1: The desired trajectory of the robot manipulator.

Table 3.5: Observer parameters

Param	Value	Param	Value	Param	Value	Param	Value
ϵ_s	190	ϱ_s	240	δ_a	0.2	$\boldsymbol{\Gamma}_1$	$112\boldsymbol{I}_3$
α_s	10	δ_s	0.1	δ_u	0.3	$\boldsymbol{\Gamma}_2$	$175\boldsymbol{I}_3$

results are as follows. For brevity, only the results of the first joint are displayed, since the results on the three joints are similar.

In Fig. 3.2a, the original disturbance $\hat{\boldsymbol{\tau}}_{\mathrm{d}}(t)$ and its estimation $\hat{\boldsymbol{\tau}}_{\mathrm{d}}(t)$ are compared. It is noticed that, even though the non-zero initial conditions are given, the estimation $\hat{\boldsymbol{\tau}}_{\mathrm{d}}(t)$ precisely tracks $\hat{\boldsymbol{\tau}}_{\mathrm{d}}(t)$ after a short transient stage (approx. 0.0625s), even at the time instants where sharp changes emerge in the disturbance (e.g. 0.5s, 2.5s and 4s). This confirms the high-bandwidth feature of the integral sliding mode observer. Fig. (3.2b) shows the comparison between the measured velocity $\dot{\boldsymbol{q}}(t)$ and its estimation $\dot{\hat{\boldsymbol{q}}}(t)$ by the observer. Note that the measured velocity comes from the direct derivative of measured position $\boldsymbol{q}(t)$. Similar to the estimation of the disturbance, $\dot{\hat{\boldsymbol{q}}}(t)$ converges to $\dot{\boldsymbol{q}}(t)$ after a short transient stage (also approx 0.0625s). Fig. (3.2c) shows that the switching function $\boldsymbol{s}(t)$ is kept within the range $\|\boldsymbol{s}(t)\| < 4 \times 10^{-3}$ despite the non-zero initial condition $\boldsymbol{e}_1(0) = [-0.25 \;\; -0.4 \;\; -0.1]^\top$. This result reveals the effectiveness of the proposed integral sliding mode observer that the velocity estimation $\dot{\hat{\boldsymbol{q}}}(t)$ is always invariant from disturbance $\boldsymbol{d}(\boldsymbol{x}_1, t)$. Thus, the enhanced robustness of this novel observer is confirmed.

3.5 Experiments

In this section, the proposed observer has been applied to a robot platform (see Fig. 3.3) to evaluate its estimation performance in practice. Similar to the simulation, in

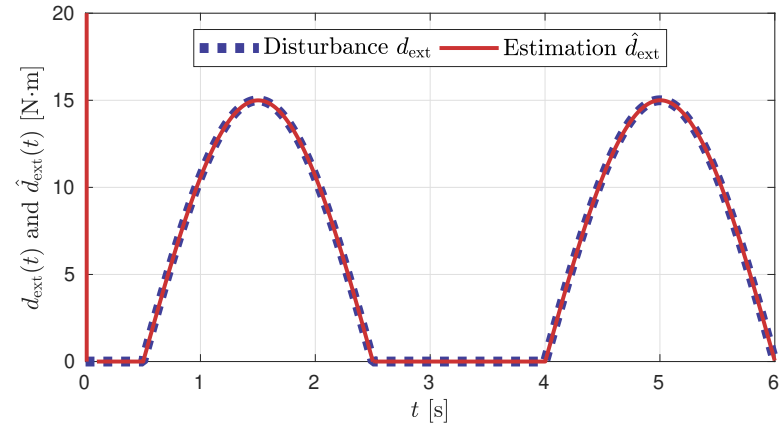

(a) The disturbance and its estimation on the first joint.

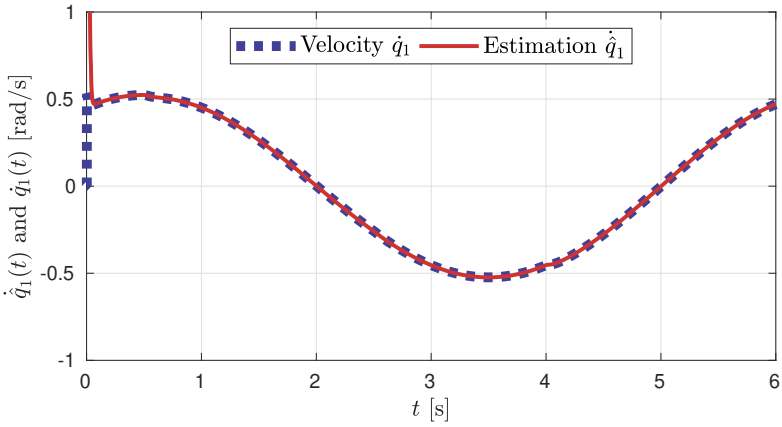

(b) The joint velocity and its estimation on the first joint.

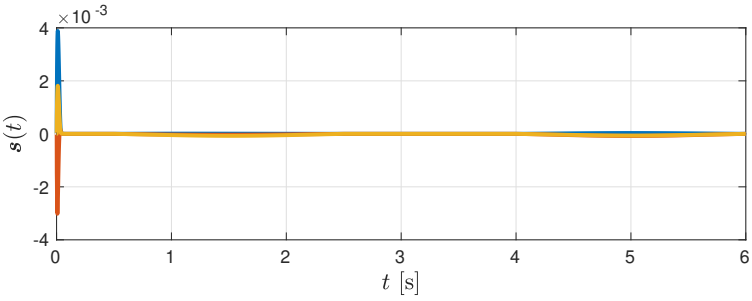

(c) The switching function of the integral sliding mode observer.

Figure 3.2: The estimation results for the sinusoidal disturbance.

this experiment, the robot is actuated by a PD controller tracking the given desired trajectory. Different types of disturbance are added to the joint actuators, and the ex-

perimental performance of the integral sliding mode observer is evaluated by comparing the predefined disturbance $\boldsymbol{\tau}_\mathrm{d}$ and its estimation $\hat{\boldsymbol{\tau}}_\mathrm{d}$.

The experiment configurations are as follows. The manipulator platform is actuated by 3 Maxon torque motors on the joints with a turn ratio of 1:100. The actuators are installed in parallel along the axes, such that the robot moves in the horizontal plane, and gravity is ignored. The incremental encoders offer the joint position measurement with a resolution of 2000. The sensors and actuators are connected with the computer using a PCI communication card. The Maxon driver is used to communicate between the executable and the robot. The executable of the algorithm is created by MATLAB 2017a in Ubuntu 14.04 LTS, with the first-order Euler solver at the sampling rate of 1 kHz, and runs for 70 s. The dynamic model of the robot is well identified.

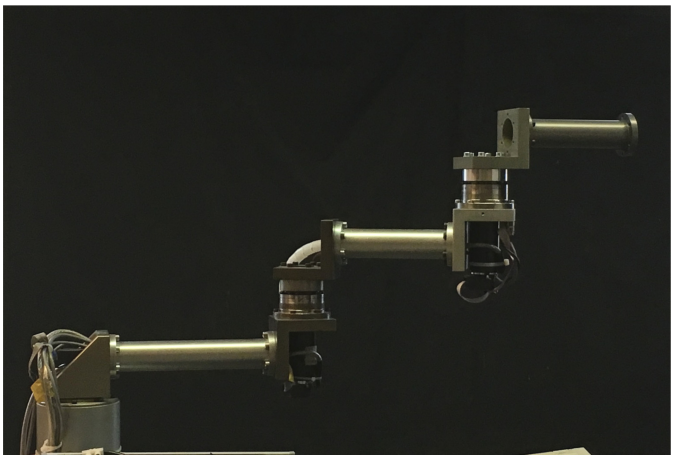

Figure 3.3: The robot manipulator platform for the experiment.

3.5.1 Estimation of Predefined Disturbances

In the first experiment, a trajectory tracking task is implemented on the robot platform. The desired trajectory $\boldsymbol{q}_\mathrm{d}(t)$ is designed as

$$\boldsymbol{q}_\mathrm{d}(t) = \left(1 - \cos\left(\frac{2\pi}{5}t\right)\right)\boldsymbol{k}_\mathrm{pos},\ 5 < t \leqslant 65. \tag{3.46}$$

which is shown in Fig. (3.4). The PD controller in (3.44) is implemented to track the given trajectory (3.46).

During the motion of the manipulator, three different kinds of predefined disturbances $\boldsymbol{d}(t)$ are inserted to the robot joint command inputs to simulate the external force, such that the comparison can be made between the estimated contact force $\hat{\boldsymbol{d}}(t)$ and the original disturbance $\boldsymbol{d}(t)$. Respectively, the sinusoidal disturbance (also used in [79]), the square form disturbance (also used in [49,207,220]) and the triangle form disturbance (also used in [48]) are used in this experiment, since they all resemble the waveform of

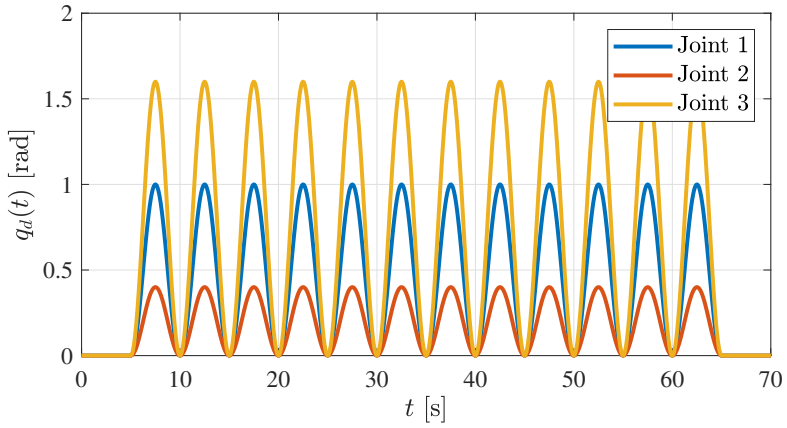

Figure 3.4: The desired trajectory for the robot manipulator.

contact force in practice which is featured with large amplitudes, short time periods and summit-shape waveform. The specific formulations are as follows:

Disturbance 1. Sinusoidal waveform

$$\boldsymbol{d}_{\sin}(t) = \begin{cases} \sin\left(\frac{\pi}{2}(t-12.5)\right)\boldsymbol{k}_{\text{dst}}, & 12.5 < t \leqslant 14.5, \\ 0, & \text{else.} \end{cases} \tag{3.47}$$

Disturbance 2. Square waveform

$$\boldsymbol{d}_{\text{sqr}}(t) = \begin{cases} \boldsymbol{k}_{\text{dst}}, & 12.5 < t \leqslant 14.5, \\ 0, & \text{else.} \end{cases} \tag{3.48}$$

Disturbance 3. Triangle waveform

$$\boldsymbol{d}_{\text{trg}}(t) = \begin{cases} (t-12.5)\boldsymbol{k}_{\text{dst}}, & 12.5 < t \leqslant 13.5, \\ (-t+14.5)\boldsymbol{k}_{\text{dst}}, & 13.5 < t \leqslant 14.5, \\ 0, & \text{else.} \end{cases} \tag{3.49}$$

An integral sliding mode observer in (3.6) is implemented on the robot platform with the same parameter selection as in Tab 3.5. The evaluation of the estimation results are as follows.

Fig. (3.5) shows the estimation results of the first robot joint with the sinusoidal disturbance from (3.47). Similar to the simulation results, the precise estimation $\hat{\boldsymbol{\tau}}_{\text{d}}(t)$ and $\dot{\hat{\boldsymbol{q}}}(t)$ of the disturbance $\boldsymbol{d}(t)$ and velocity $\dot{\boldsymbol{q}}(t)$ of the system can be respectively seen in Fig. (3.5a) and Fig. (3.5b). In Fig. (3.5c), it is obvious that the switching function remains in the region $\|\boldsymbol{s}(t)\| < 2 \times 10^{-4}$. These results have confirmed the robustness of the integral sliding mode observer.

The estimation results of the square form disturbance and the triangle form disturbance are shown in Fig. (3.6) and Fig. (3.7). Apart from the similar arguments to the above, Fig. (3.6b) especially shows the precise tracking of joint velocity even with

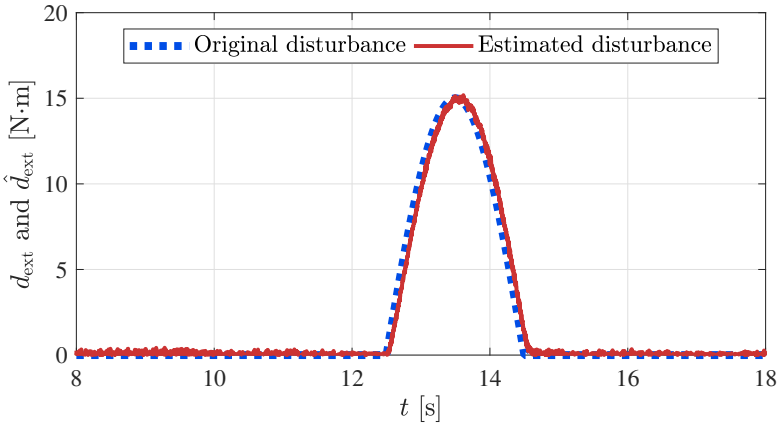

(a) The disturbance and its estimation on the first joint.

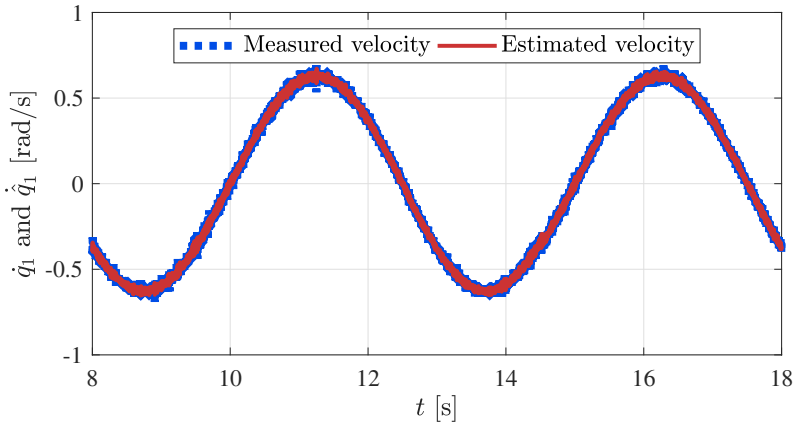

(b) The velocity and its estimation on the first joint.

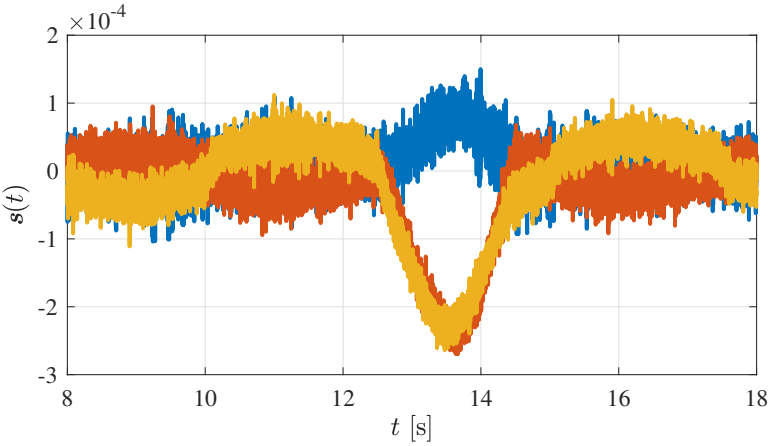

(c) The switching function of the observer.

Figure 3.5: The results of observer for sinusoidal disturbance.

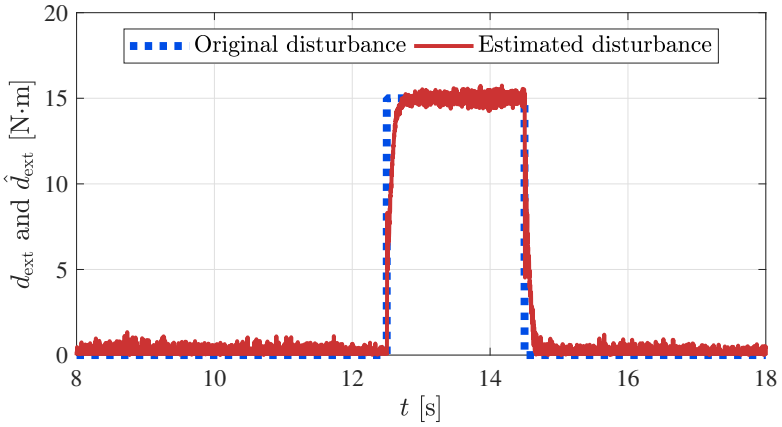

(a) The disturbance and its estimation on the first joint.

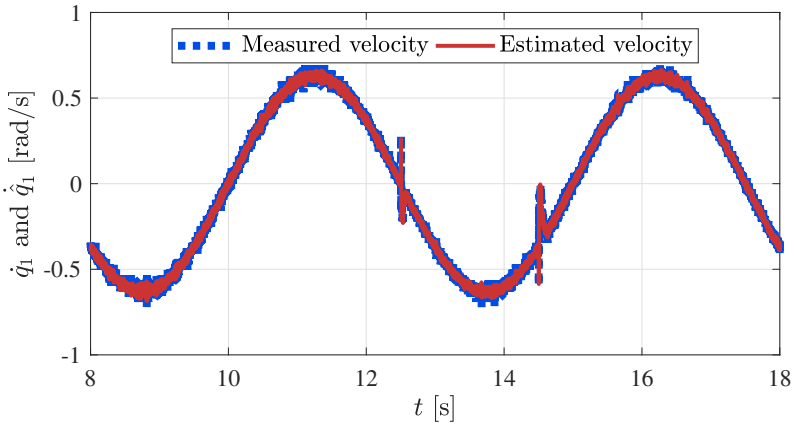

(b) The velocity and its estimation on the first joint.

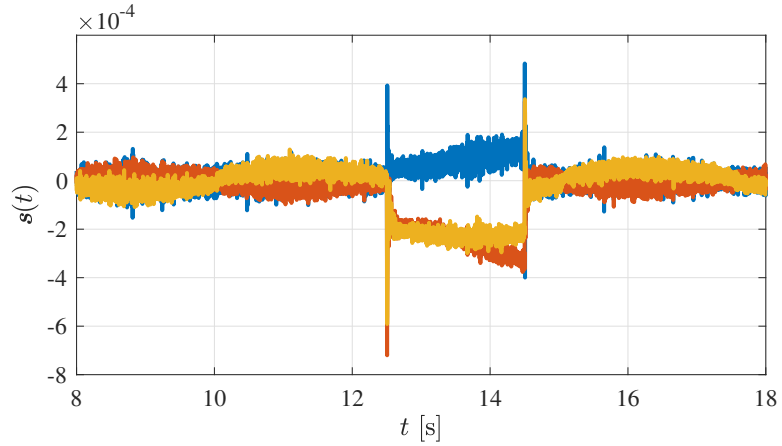

(c) The switching function of the observer.

Figure 3.6: The results of observer for square form disturbance

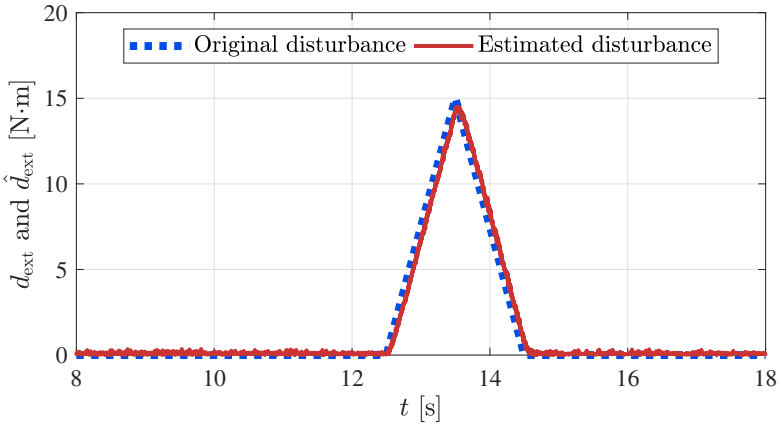

(a) The disturbance and its estimation on the first joint.

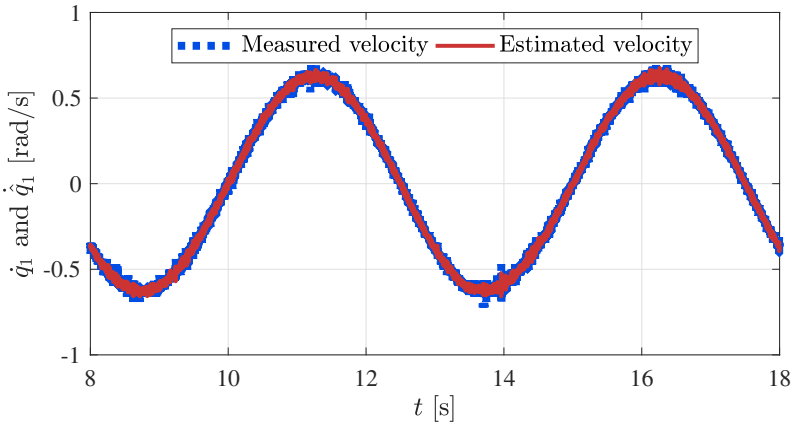

(b) The velocity and its estimation on the first joint.

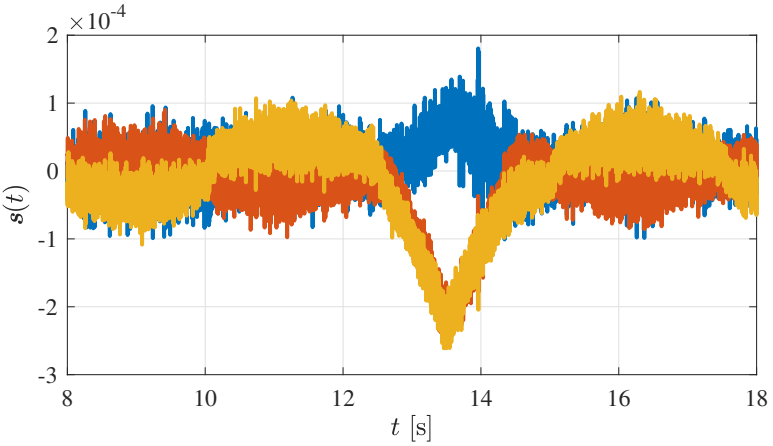

(c) The switching function of the observer.

Figure 3.7: The results of observer for triangle form disturbance

high bandwidth signal perturbations (e.g. in 12.5 s, and 14.5 s) which are caused by the jumps on the system disturbance. Thus again, the high-bandwidth and robustness of this observer are confirmed.

3.5.2 Estimation of Contact Force

In this experiment, we investigate the performance of the integral sliding mode observer which estimates the contact forces between the robot and the environment. To make a comparison, a JR3 force sensor (see Fig. (3.8a)) is installed to the end-effector of the manipulator to measure the contact forces, which provides the measurement as a wrench form in Cartesian space. A plastic attachment is fixed with the JR3 force sensor with a spherical appendix (see Fig. (3.8b)) to guarantee a firm and steady contact. A sponge fixed to a stick holder (see Fig. (3.8b)) is used to make contacts with the spherical appendix instead of human hands. The desired trajectory is given as (3.46) and the PD controller in (3.44) is used. The configuration of the integral sliding mode observer is the same as the previous experiment.

(a) **(b)**

Figure 3.8: The contact devices and the JR3 force sensor

During the motion of the manipulator, several contacts are made to the spherical appendix on the end-effector using the sponge to simulate the robot-environment contacts in a robot task. The occurrence time instances of the manual contacts are approximately 37 s, 42 s, 47 s, 52 s, 57 s, and 62 s. At the same time, the contact force is measured and recorded. Note that the measurement of JR3 is in the form of a wrench $\boldsymbol{F}_m \in \mathbb{R}^6$ in the task coordinate, whereas the estimated torque $\hat{\boldsymbol{\tau}}_\mathrm{d}$ is in the joint coordinate. Therefore, we transform the measured contact wrench into the joint space coordinate by $\boldsymbol{\tau}_m = \boldsymbol{J}^\top(\boldsymbol{q})\boldsymbol{T}(\boldsymbol{q})\boldsymbol{F}_m$, where the measured external torque $\boldsymbol{\tau}_m$ denotes the reflection of $\boldsymbol{F}_m$ in the joint coordinate, $\boldsymbol{J}(\boldsymbol{q})$ is the Jacobian matrix and $\boldsymbol{T}(\boldsymbol{q})$ is the coordinate transformation from the task coordinate to the base coordinate. The comparison be-

tween the measured external torque $\boldsymbol{\tau}_m$ and the estimated external torque $\hat{\boldsymbol{\tau}}_\mathrm{d}$ is shown in Fig. (3.9).

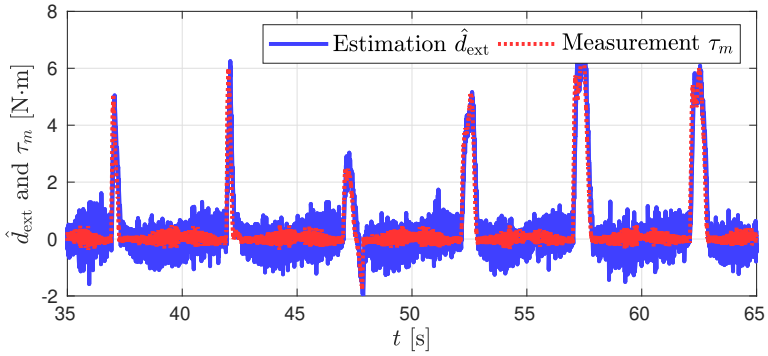

Figure 3.9: The estimated and measured collision torque on the first joint.

The results have shown that the estimation $\hat{\boldsymbol{\tau}}_\mathrm{d}$ by the observer is very close to the measured external torque $\boldsymbol{\tau}_m$ by JR3 torque sensor. Note that the waveform of the external torques possess similar features to the predefined disturbances in (3.47), (3.48) and (3.49). This confirms the estimation precision and bandwidth of the integral sliding mode observer in practical applications.

3.5.3 Application Example: Sensorless Admittance Control

The precise, high-bandwidth and robust estimation performance of the integral sliding mode observer confirmed by the above simulation and experiments reveals its potential application to safe human robot collaborations, which is investigated in this section by implementing a force-sensor-less admittance controller as an example. An admittance controller is an important component in the HRI safety framework. By modifying the reference trajectory according to the external force feedback, the robot can compliantly react to the interactive forces, such that an admittance featured motion is achieved. Usually an external force sensor, such as the JR3 torque sensor, is needed to implement an admittance controller, whereas here we use the estimated external torque $\hat{\boldsymbol{\tau}}_\mathrm{d}$ instead of the measured torque $\boldsymbol{\tau}_m$. Thus the admittance controller in this experiment is designed as follows

$$\boldsymbol{\tau}_\mathrm{c} = \hat{\boldsymbol{M}}(\boldsymbol{q})\left(\ddot{\boldsymbol{q}}_\mathrm{r} + \boldsymbol{K}_D\dot{\boldsymbol{e}}_\mathrm{r} + \boldsymbol{K}_P\boldsymbol{e}_\mathrm{r}\right) + \hat{\boldsymbol{C}}(\boldsymbol{q},\dot{\boldsymbol{q}})\dot{\boldsymbol{q}} + \hat{\boldsymbol{F}}(\dot{\boldsymbol{q}}),$$

where $\boldsymbol{q}_\mathrm{r}$, $\dot{\boldsymbol{q}}_\mathrm{r}$ and $\ddot{\boldsymbol{q}}_\mathrm{r}$ are respectively the reference position, velocity and acceleration of the robot in the joint space, $\boldsymbol{e}_\mathrm{r} = \boldsymbol{q}_\mathrm{r} - \boldsymbol{q}$ is the deviation between the reference position and the current position, $\boldsymbol{K}_D$ and $\boldsymbol{K}_P$ are the same as in (3.44). The reference trajectory $\boldsymbol{q}_\mathrm{r}$ is defined by

$$\dot{\boldsymbol{q}}_\mathrm{r} = \dot{\boldsymbol{q}}_\mathrm{d} + \boldsymbol{K}_d^{-1}\left(\boldsymbol{K}_p(\boldsymbol{q}_\mathrm{d} - \boldsymbol{q}_\mathrm{r}) + \hat{\boldsymbol{\tau}}_\mathrm{d}\right), \tag{3.50}$$

where $\boldsymbol{K}_p = 50\boldsymbol{I}_3$ and $\boldsymbol{K}_d = 50\boldsymbol{I}_3$ respectively define the stiffness and damp of the admittance behavior. Note that different from the simulation and the experiments above, the estimated disturbance $\hat{\boldsymbol{\tau}}_\mathrm{d}$ is applied to the closed-loop control, see (3.50). The motion

of the robot with this force-sensor-less admittance controller is shown in Fig. (3.10). Initially, the robot stays in a static position (see Fig. (3.10a)). When an object makes a contact with the end-effector (see Fig. (3.10b)), an admittance reaction behaviour is achieved (see Fig. (3.10c)). After the contact vanishes, the robot returns to the original configuration. Note that due to the approximation from (3.10), the filter (3.15) and the boundary layer techniques (3.39), $\hat{\boldsymbol{\tau}}_{\mathrm{d}}$ is not exactly equal to $\boldsymbol{\tau}_{\mathrm{d}}$. As a result, the closed-loop stability of the admittance controller does not hold for all possible values of K_d and K_p as in (3.50). Large values of τ and the boundary layers may lead to small feasible sets of control parameters K_d and K_p.

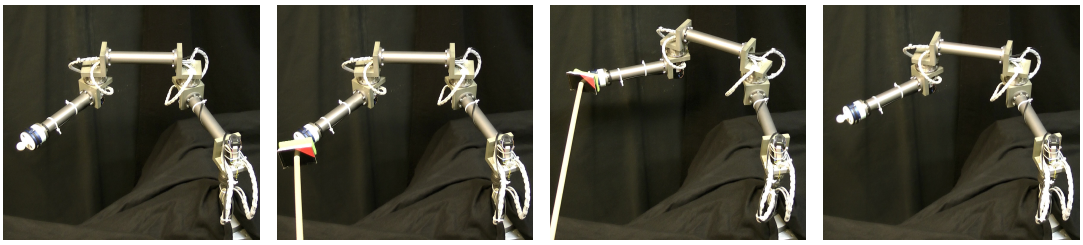

(a) **(b)** **(c)** **(d)**

Figure 3.10: The reactive motion of force-sensor-less admittance controller

As shown in the example demonstration above, the force-sensor-less admittance controller reveals an expected compliance behavior when physical contact is exerted on the end-effector, which justifies the applicability of the integral sliding mode observer to practical HRC scenarios. Thus, a safe compliance-controller can be designed without expensive force sensory devices. The disadvantage is, however, the resulting control precision is inferior to the control schemes using force sensors due to applying the filter and boundary layer techniques. Therefore, this force-sensor-less application is suitable to the low-cost robot platforms which do not have strict requirements on the force control precision.

3.6 Summary

In this chapter, we present a novel collision force estimator and apply it to a robot manipulator. The usage of a novel integral sliding mode observer for Euler-Lagrangian systems ensures precise estimation of the collision forces without the conventional assumptions, namely system continuity, velocity measurement, and boundedness of the disturbance derivative. Results of the simulation and experiments have shown the high precision, bandwidth, and robustness of this novel method. It is worth mentioning that our method is effective for various disturbances, including sinusoidal, square, and triangle disturbances that represent the most collision forces in practice. The experimental comparison with sensory measurements reveals that it is possible to replace a real force sensor in practice. The implementation of a force-sensor-less admittance controller lights up the ambition to achieve a sensor-free and low-cost safety framework for

human-friendly collaborative robots. Therefore, our method for collision force estimation of Euler-Lagrangian systems provides a high-performance solution for HRC with application values. Its practical potential is validated by successful implementation on real robots, which proposes a positive answer to **Question 1** raised in Sec. 1.2. Nevertheless, it should be noted that the experimental results are obtained on a well-identified robot manipulator platform. The actual estimation precision of the method in practise may be reduced if unmodeled dynamics exist.

4 Online Collision Detection and Identification

Once the collision forces are measured or reconstructed, the *CDI* module in the collision handling pipeline takes in the force signals and produces a diagnosis result indicating whether a collision occurs and what type the collision is, as shown in Fig. 2.7. As part of the post-collision procedure, a CDI scheme is intended to monitor the sensory signals, detect the occurrence of a physical contact and identify whether it is an accidental collision or an intentional contact. The results of CDI will be given to the *collision reaction* procedure, where the corresponding safe strategy is enabled to avoid further harms [5]. In this chapter, we present an online CDI scheme using supervised learning methods and Bayesian decision theory. Different from the conventional methods, the proposed scheme is able to provide an accurate diagnosis result in the early stage of a collision, such that severe injuries or damages can be prevented in advance. The experimental validation confirms the applicability of the proposed scheme in practice. The results of this chapter are based on the work in [305].

4.1 Overview

The work in this chapter is motivated by the desire of handling different types of physical contacts that exert various impacts on humans. The intentional contacts desired by the cooperative tasks, such as the human teaching processes, are usually quite safe. On the contrary, the accidental collisions, which may lead to unexpected injuries or damages, are often dangerous to humans. As pointed out by many surveys on the safety of human-robot collaboration [243, 244], the accidental collisions are inevitable in pHRI and should be carefully handled. Especially, the reaction strategy for the accidental collisions should be distinguished from the intentional contacts since they tend to cause opposite consequences. In this chapter, without causing ambiguity and confusion, we refer to the dangerous accidental collisions as *collisions*, the safe intentional contacts as *contacts*, and their summary as pHRI.

As claimed in [5], accidental collisions and intentional contacts possess distinguishable properties, which are reflected in the features of the sensory signals. Considering this, one can formulate robot CDI as a multi-class classification problem, with *collision*, *contact*, and *free* respectively denoting the accidental collisions, intentional contacts and the nominal cases where no pHRI occurs. Then, the main target of CDI becomes to develop a pHRI signal classifier using a data set that contains the pHRI waveform. In general, this proposes a classification problem for time series.

4.1.1 Related Work

Conventionally, CDI for robot systems has been recognized as an engineering-oriented problem and is mainly solved by simple threshold logic or hypothesis testing based methods [14, 101], where the filter-based techniques are widely applied [21]. More recent work tends to formulate CDI as a classification problem for segmented time series. Similar work can be found in relevant fields, such as speech recognition [245], snoring identification [246], bird sound recognition [247] and fault identification of mechatronic systems [248–250]. The common ground of these applications is that the segmented time series, either acoustic signals or sensory streams, are expected to be classified as a certain type. In [251], the classification of time series is generally investigated by applying various data sets. In [252], a deep neural network is constructed to detect the system faulty status. In [253], various classifiers are developed and tested using the recorded signal samples. Similar work also includes [204, 205], where neural network is constructed to monitor the grasping slippages and colliding torques, and [69, 70], where SVM classifiers are developed to detect external collisions. Based on the mentioned work, a mature development framework for time series has been well-formed. However, such a framework is confronted with challenges when applied to CDI for robot systems with pHRI tasks, since the prediction results are only available after the collision vanishes or the entire pHRI waveform is segmented. Therefore, these methods are not suitable for human-robot collaboration with high requirements on human safety.

As alternatives, the probabilistic series-models, such as the HMM [254] and the Gaussian Mixture Model (GMM) [255] are also applied to CDI by exploiting the dependence properties of time series. In [256], an HMM is developed to detect exceptional events in an object-alignment robot task, where the measured torques and their derivatives are used. The work in [257] also develops an HMM model to realize a fault detection scheme for a feeding-assistant robot using multi-sensor signals. In [258], probabilistic support vector machine is used to detect online anomalies. Nevertheless, these series models require artificially assigned prior knowledge on the distributional dependence of the raw signals. In most practical scenarios, such knowledge is challenging to acquire, especially in a complicated environment where the distribution of the disturbance and noise is not treated as Gaussian.

4.1.2 Challenges

Generally, an important technique in the classification problem for time series is the segmentation of raw signals, since classifiers can not process series with infinite length. In a conventional paradigm of classifier development, the raw signals are segmented before predictions are conducted, even for the online applications. In the context of CDI, the conventional solutions typically design some detection logic, such as a signal threshold, to approximately mark the starting instant of a pHRI, and segment the online signals after observing the entire pHRI waveform, before producing a prediction result using a trained classier. As a result, an accurate prediction result can only be produced when the pHRI *almost* vanishes. By *almost* we mean that the pHRI waveform is contained

in the signal segments as much as a correct identification result can be produced. Such a method, however, usually leads to a useless result in the context of safe human-robot collaboration, since a collision or a contact has already occurred and negative consequences may have already been caused. Intuitively speaking, a prediction result of the classifier does not really *predict* the occurrence of a collision. The reason for this issue is that the signal values in the future are not available for the segment at the current time, due to the causality of online time-series.

Nevertheless, this is a significant issue for safe human-robot collaboration, since A CDI scheme that can be practically applied is expected to accurately report the pHRI in its early stage, definitely before it vanishes, such that potential injuries can be prevented in advance. Unfortunately, such a valuable topic has attracted very little attention, probably due to the following two challenges. Firstly, accurate prediction results should be produced even when the segmented pHRI waveform is incomplete. From a general perspective, this introduces inconsistency between the distribution of the training data and that of the predicted samples, if the classifier is developed on the signal segments with complete pHRI waveform. This indicates that the identification result in the early stage of a pHRI is very likely to be incorrect. Secondly, an accidental collision is usually referred to as an *instantaneous anomaly* [259], which occurs unexpectedly and only lasts for a short period of time. Thus, it is more difficult to be identified than the other anomalies that are featured with low bandwidth and steady changes [260, 261]. The main target of our work is to fill these gaps by proposing a novel online CDI scheme that ensures both high accuracy and fast response.

4.1.3 Contributions

The main contribution of this work is to develop an online CDI scheme for safe human-robot collaboration. The major advantage of this novel scheme over the conventional methods is to produce fast and accurate CDI in the early stage of pHRI. Apart from the identification result, it also provides a confidence index to indicate how much the result can be trusted, which benefits the design of a flexible collision handling pipeline in future work. Moreover, the scheme does not require extra detection logic and any prior knowledge on the dependence of pHRI signals. Therefore, no heuristic thresholds or distribution assumptions are needed. Another contribution of this work is to provide a pHRI data set with manual labels specifically for the CDI usage, which is still lacking in the literature. Different from most of the previous work where the torque sensors are installed on the end-effectors, the signal data we used in this work is from the torque sensors on the robot joints, which can even detect pHRIs on robot links. On the other hand, the data set contains more interfering signals due to coupled mechanical vibrations and strong current noise on the sensors, which leads to a larger challenge to the development of the CDI scheme. From another perspective, however, our work reflects the complicated conditions in practice, which provides an outcome truly with application values.

4.1.4 Outline of the Chapter

The main content of this chapter is organized as follows. Sec. 4.1.1 summarizes the related work and clarifies the main contributions of this work. Sec. 4.2 introduces the overall structure of the scheme and the collection process of the pHRI data set. The development of two important components of the scheme, the signal classifier, and the online diagnosor, is respectively presented in Sec. 4.3 and Sec. 4.4. In section 4.5, the proposed CDI scheme is validated on a seven-degree-of-freedom (DoF) KUKA robot. The decent performance of the CDI scheme revealed by the experimental validation confirms its applicability in practice. Finally, section 4.6 summarizes this chapter.

4.2 Scheme Overview and Data Acquisition

In this section, we introduce the overall structure of the proposed CDI scheme. To develop this scheme, we conducted a data collection experiment with manual collisions and contacts to construct a pHRI data set. The data comes from the segmentation of the external torques that are measured by shaft-mounted torque sensors installed on the robot joints.

4.2.1 Scheme Overview

The general structure of the proposed online CDI scheme and the development flowchart of each component are illustrated in Fig. 4.1, where $\boldsymbol{\tau}_\mathrm{d}$ is the measured torque signal, $\mathcal{T}$ is the signal segment, r is the prediction result of the signal classifier, and κ^*, ι are respectively the ultimate diagnosis result and its confidence index. During an online execution, the CDI routine takes the torque signal τ and segment it recurrently. Then, the features extracted from the signal segment $\mathcal{T}$ are given to the classifier which produces a prediction result r among *collision*, *contact* and *free*. Based on a series of prediction results, the online diagnosor offers a CDI diagnosis result κ^* and a confidence index ι. In this framework, no heuristic threshold values are needed to mark the occurrence time of the pHRI.

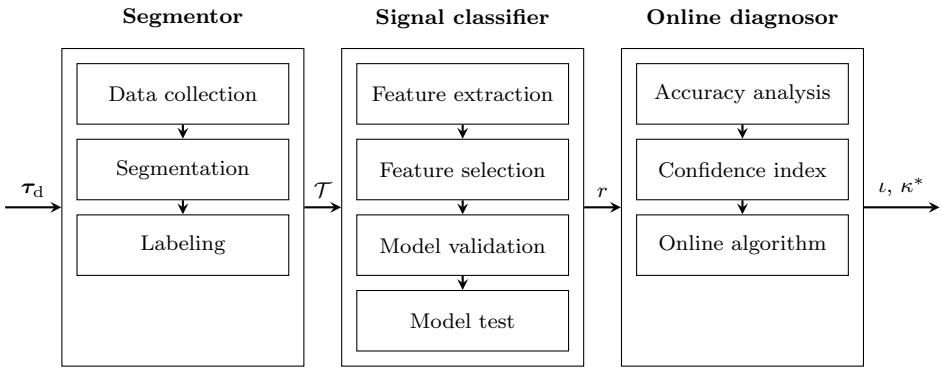

Figure 4.1: Overview of the proposed scheme and its development flowcharts

4.2.2 Data Collection

To construct the pHRI data set for the development of the signal classifier, we conduct a collection experiment using a seven DoF KUKA LWR4+ robot manipulator [262], which is firmly mounted onto a fixed platform. During the experiment, different types of physical interaction in various strengths and directions is manually exerted on the robot end-effector by seven subjects hired for this experiment, aiming to include individual uncertainties in the collected data, so as to ensure the generalization ability of the data set. In the experiment, accidental *collisions* are created using a soft hammer with fast hand speed and tough strength, whilst intentional *contacts* are made by gloved hands with compliant forces. A spherical plastic end-effector is specially designed to bear the contact forces from arbitrary directions.

Note that the pHRI is exerted during the movement of the robot, such that the measured signals contain drifts and noise caused by the joint motions. It is worth mentioning that the drifts and noise are also affected by the direction of the joint motion. Considering this, we apply several different robot trajectories that are assigned with the same starting position but different ending positions, such that both positive and negative motion directions are covered for each joint. The trajectories are designed in the joint space and interpolated by sinusoidal functions to ensure smooth motion. All these experiment configurations are intended to ensure a representative data distribution, which is important to ensure a high generalization ability to the classifier.

The motion of the robot is controlled by a trajectory tracking program that implements a continuous reciprocating motion of the manipulator between the starting position and each ending position. The program also reads the measured torque signals and records them as seven-dimensional time-series with a sampling period of 1 ms. During the motion of the robot, one experimenter exerts an accidental *collision* or an intentional *contact* on the end-effector. At the same time, the other experimenter notes down the occurrence instant and the type of the pHRI. To obtain a balanced data set between *collisions* and *contacts*, we try to produce an equal amount of samples for these two classes.

4.2.3 Signal Segmentation and Sample Labeling

After collecting the raw pHRI signals, we conduct segmentation to split the signals into segments with fixed-length. Let us denote the width of the segments as l and the bias as b, with the unit of ms. By bias we mean the time period between the occurrence instant of a pHRI and the ending instant of the segment, where we have $0 \leqslant b \leqslant l$. In general, l determines how much signal information is included in the segments, whilst b adjusts the proportion of the pHRI waveform in the segment. If the ending instant of the segment represents the current time, b denotes the period after the occurrence of the corresponding pHRI. Therefore, the segmentation scheme is well determined by the two parameters l and b. For the data set, the segment bias is typically set as $b = l$, since the torque values before the pHRIs are irrelevant to the classification. The determination of segment width l is mainly based on the engineering experience. Usually, it should be large enough to contain sufficient information of the pHRI waveform. On the other

hand, an overlarge width may involve irrelevant signals and lead to poor generalization ability.

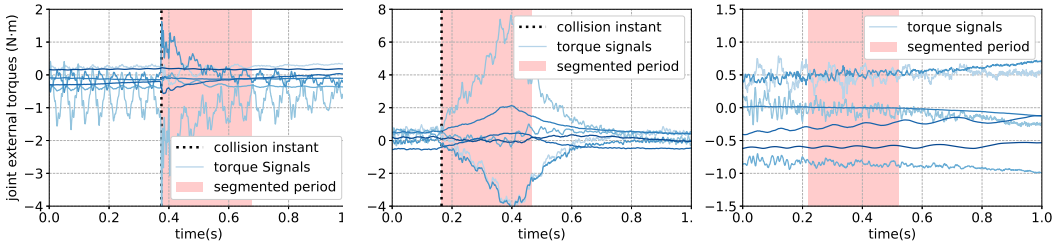

(a) Waveform of *collision* **(b)** Waveform of *contact* **(c)** Waveform of *free*

Figure 4.2: The waveform of physical contacts on the seven joints.

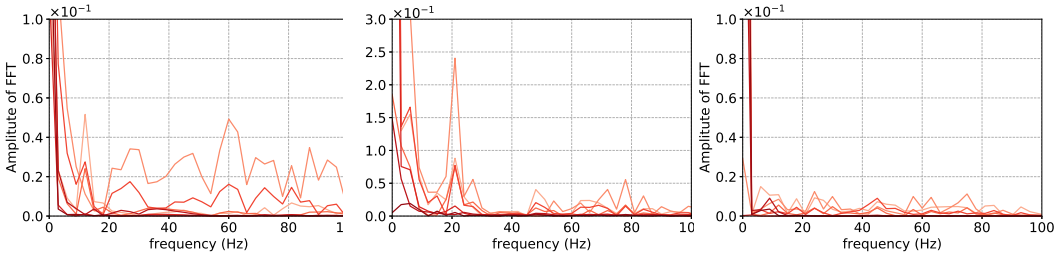

(a) Spectrum of *collision* **(b)** Spectrum of *contact* **(c)** Spectrum of *free*

Figure 4.3: The spectrum of signal segments.

To determine the value of l, we inspect the waveform of the pHRI signals presented in Fig. 4.2, where the segmented partitions are marked with colored areas. We notice that the average width of a *contact* is approximately 400ms, whilst that of a *collision* is less than 200ms. This also applies to most of the recorded pHRI signals. Therefore, we set the segment width as $l = b = 300$(ms), as a balanced result. Then, we label the two types of segment samples respectively as *collision* (Fig. 4.2a) and *contact* (Fig. 4.2b). The segmented parts of the raw signals are marked by colored areas in Fig. 4.2. During the segmentation, invalid data due to storage damages or unrecognizable pHRI waveforms are eliminated. As a result, we obtain 6718 *collisions* and 7346 *contacts*, which is approximate to a balanced radio 1:1. We also create signal segments without any pHRI waveform and label them as *free*. However, the number of *free* samples should not be equal to the other two classes since the frequency of contact-less cases is usually higher than pHRI. In practice, both *collisions* and *contacts* are positive instances which will call the corresponding safety mechanism, whilst *frees* are negative instances which do not trigger the safety mechanism. Therefore, a reasonable idea would be to keep a balance between the *free* samples and the summary of all pHRI samples, i.e., a scale ratio 1:1:2

between *collision*, *contact* and *free*. Therefore, we take the *free* segments respectively in the front, rear and middle of the pHRI segments in the raw signals, and finally obtain 13633 of them.

Until now, a data set containing the pHRI signal segments is constructed. We randomly shuffle all the samples and split them into a training set and a test set with the partition ratio 3:1. The training set will be applied to feature engineering and model selection, whilst the test set will be used to evaluate the trained model.

4.3 Development of the Signal Classifier

In this section, we develop the signal classifier component in the CDI scheme. As explained in Sec. 4.1.1, we do not consider the probabilistic series-models to avoid prior knowledge on the distributional dependence of the raw signals. Additionally, although the end-to-end learning mechanisms, such as the convolutional neural network (CNN) and recurrent neural network (RNN), have drawn much attention and made great achievements in image recognition and model-free planning, they still suffer from the lack of explainability and high dependence on complex manually designed structures. Therefore, in this work, we develop the signal classifier based on the paradigm of supervised learning, by which we assume that the samples in the data set are independent of each other. In this section, the *scikit-learn* machine learning tool-kit is used to train and test the classifier [263].

4.3.1 Feature Extraction

To form a feature set that benefits the signal classification, we consider both the properties of pHRI signals and the successful experience in previous work [253, 264]. From Fig. 4.2, we can conclude that the waveform of *collisions* (Fig. 4.2a) has sharp shapes and fast amplitude changes, while the waveform of *contacts* (Fig. 4.2b) changes more gently and lasts for a longer time. We also investigate the spectrum of the signal segments in Fig. 4.2 and shown it in Fig. 4.3. Compared to the *free* sample, the *collision* and *contact* possess more components in all frequency ranges. Especially, the *collision* shows a large amplitude in the frequency interval 10 - 20 Hz, whist the *contact* in 0 - 10 Hz. Therefore, distinguishable properties between the two classes are found in both time-domain and frequency-domain. Based on this, we initially extract 18 features in both domains. Most of these features also have achieved success in previous work [264].

4.3.1.1 Features in the Time Domain

The time domain features are frequently used in the fields like signal processing and pattern recognition [265, 266]. Since each sample is naturally a segmented time series $\mathcal{T} = \{\tau_1, \tau_2, \cdots, \tau_l\}$, the time-domain features can be represented as the functions of $\mathcal{T}$. Here, we mainly select features that are concerned with the amplitude changes of the signals. First of all, the 1st to 4th order statistical moments, namely the mean value $\bar{\mathcal{T}}$,

the variance $\mathrm{Var}(\mathcal{T})$, the skewness $\mathrm{Skew}(\mathcal{T})$ and the kurtosis $\mathrm{Kurt}(\mathcal{T})$ of samples $\mathcal{T}$ are applied to depict the stochastic properties of the signal segment, where

$$\begin{aligned} \bar{\mathcal{T}} &= \frac{1}{l}\sum_{i=1}^{l}\tau_i, \quad \mathrm{Kurt}(\mathcal{T}) = \frac{1}{l}\mathrm{Var}(\mathcal{T})^{-2}\sum_{i=1}^{l}\left(\tau_i-\bar{\mathcal{T}}\right)^4-3, \\ \mathrm{Var}(\mathcal{T}) &= \frac{1}{l}\sum_{i=1}^{l}\left(\tau_i-\bar{\mathcal{T}}\right)^2, \quad \mathrm{Skew}(\mathcal{T}) = \frac{1}{l}\mathrm{Var}(\mathcal{T})^{-\frac{3}{2}}\sum_{i=1}^{l}\left(\tau_i-\bar{\mathcal{T}}\right)^3. \end{aligned} \tag{4.1}$$

The median value $\tilde{m}_\tau$, the extreme range $\mathrm{Rng}(\mathcal{T})$ and the extreme deviation $\mathrm{Dev}(\mathcal{T})$ of $\mathcal{T}$ are also used as supplementary, where $\mathrm{Rng}(\mathcal{T}) = \max_i|\tau_i| - \min_i|\tau_i|$ and $\mathrm{Dev}(\mathcal{T}) = \max_i|\tau_i| - \bar{\mathcal{T}}$, for $1 \leqslant i \leqslant l$. Additionally, we propose the energy increasing rate $E_I(\mathcal{T})$ as

$$E_I(\mathcal{T}) = \frac{1}{2}\lg\left(\sum_{i=[n/2]}^{n}\tau_i^2 \Big/ \sum_{i=1}^{[n/2]}\tau_i^2\right) \tag{4.2}$$

to represent the temporal change of signal energy within a segment, where the ratio is made between the squared signal sums within the two halves of the segment. Here, $[\cdot]$ rounds a real number to integer.

4.3.1.2 Features in the Frequency Domain

The frequency domain features are commonly applied to depict the spectral profiles of signals [14, 267], which are mostly calculated by fast Fourier transformation (FFT). The FFT of a signal sequence $\mathcal{T}$ includes a sampled frequency sequence $\mathcal{F} = \{f_1, f_2, \cdots, f_m\}$ with the frequency sampling interval f_s/m, and the corresponding complex spectrum sequence $\mathcal{C} = \{C(f_1), C(f_2), \cdots, C(f_m)\}$. The length of the spectrum sequence m is usually equal to l. The frequency domain features are mainly concerned with the amplitudes and phase angles of the signal spectrum in different frequency intervals, such as the mean frequency $\bar{f}$, the fundamental frequency f^* and their corresponding spectral amplitudes $|S(\bar{f})|$, $|C(f^*)|$ and phase angles $\phi(S(\bar{f})), \phi(C(f^*))$, where $|\cdot|:\mathbb{C}\to\mathbb{R}$ and $\phi(\cdot):\mathbb{C}\to\mathbb{R}$ respectively denote the amplitudes and phase angles. The mean frequency $\bar{f}$ is defined as $\bar{f} = \sum_{i=1}^{m} f_i|C(f_i)|/\sum_{i=1}^{m}|C(f_i)|$ and the fundamental frequency f^* is the frequency point such that $C(f^*)$ is the spectrum summit. The crest factor F_{crest}, the average signal energy E_{rms} and the sub-band energy ratio $E_{\mathrm{rt}}^{f_c}$ are respectively defined as $F_{\mathrm{crest}} = |C(f^*)|/\sqrt{\frac{1}{m}\sum_{i=1}^{m}|C(f_i)|^2}$, $E_{\mathrm{rms}} = \sqrt{\frac{1}{m}\sum_{i=1}^{m}|C(f_i)|^2}$, $E_{\mathrm{rt}}^{f_c} = \frac{1}{2}\lg(\sum_{f_i=f_c}^{f_s}|C(f_i)|^2/\sum_{f_i=0}^{f_c}|C(f_i)|^2$ for band frequencies $f_c = 10,\ 20\,\mathrm{Hz}$. These features are also widely used in [264, 265, 268] to depict the energy properties of signals. The crest factor F_{crest}, also known as peak-to-average ratio, represents the significance of the signal peak. The average energy E_{rms} denotes the average signal power level, and the sub-band energy ratio $E_{\mathrm{rt}}^{f_c}$ reflect the relative energy proportion on the two sides of the sub-band frequency f_c. Here, we define two sub-band energy indexes. The corresponding sub-band frequencies 10Hz and 20Hz are determined according to the distinguishable spectral features of *collisions* and *contacts*.

In summary, we extract the following features $\mathcal{X}^+ = \{\bar{\mathcal{T}}, \mathrm{Var}(\mathcal{T}), \mathrm{Skew}(\mathcal{T}), \mathrm{Kurt}(\mathcal{T}), \bar{m}_\tau, \mathrm{Rng}(\mathcal{T}), \mathrm{Dev}(\mathcal{T}), E_I(\mathcal{T}), f^*, |C(f^*)|, \phi(C(f^*)), \bar{f}, |S(\bar{f})|, \phi(S(\bar{f})), F_{\mathrm{crest}}, E_{\mathrm{rms}}, E_{\mathrm{rt}}^{10}, E_{\mathrm{rt}}^{20}\}$, where $\mathcal{X}^+$ denotes a *full* feature set. For brevity, we order these features and number them from #1 to #18. Note that the signals have 7 dimensions corresponding to the 7 robot joints. Therefore, in total 126 features are generated.

4.3.2 Feature Selection

To select the beneficial features for the classification, we use the Spearman correlation analysis and the Relieff algorithm to evaluate the 126 features in $\mathcal{X}^+$. The former inspects the dependence between any two features, whilst the latter calculates weights for the features which are recognized as their *importance* to the classification. Features with high dependence on the others or low *importance* are eliminated after the analysis. Note that we only use the data in the training set during the entire feature selection procedure.

4.3.2.1 Dependence Analysis

High dependence among features brings redundancy to the model training, which potentially causes a poor generalization ability to the classifier. Therefore, we analyze the Spearman correlation between the features to investigate their dependence. The Spearman rank correlation analysis is an efficient tool to describe the general monotonic relationship between two stochastic variables, which applies not only to linear dependence, but also the nonlinear cases. Given the values of two features $X = \{X_1, X_2, \cdots, X_m\}$ and $Y = \{Y_1, Y_2, \cdots, Y_m\}$, where m is the size of the data set, the Spearman correlation coefficient $\rho_{X,Y}$ is calculated by

$$\rho_{X,Y} = \frac{\sum_{i=1}^{m} (x_i - \bar{x})(y_i - \bar{y})}{\sqrt{\sum_{i=1}^{m} (x_i - \bar{x})^2 \sum_{i=1}^{m} (y_i - \bar{y})^2}}, \tag{4.3}$$

where $x = \{x_1, x_2, \cdots, x_m\}$ and $y = \{y_1, y_2, \cdots, y_m\}$ are the ranks of features X and Y, and $\bar{\cdot}$ denotes the mean value [269]. Ranging from -1 to 1, the coefficient $\rho_{X,Y}$ depicts the dependence between X and Y, of which the sign denotes whether the relationship of the two variables are proportional (when positive) or inversely proportional (when negative), and the absolute value indicates the extent of dependence. We apply the Spearman correlation analysis to all 126 features in $\mathcal{X}^+$. The results are illustrated in Fig. 4.4 by colored matrices. Each micro square block represents the correlation coefficients between the corresponding two features, of which the values are marked by colors. Dark red indicates highly positive dependence and dark blue means the opposite.

Fig. 4.4a displays the dependence between all 126 features which are grouped by the joint numbers. Each square block (surrounded by black dashed lines) on the diagonal represents the self-feature- dependence of each joint, i.e., the dependence between the features of the same joint. Meanwhile, the blocks off the diagonal indicate the dependence among the features of different joints. It is noticed that the the blocks on the

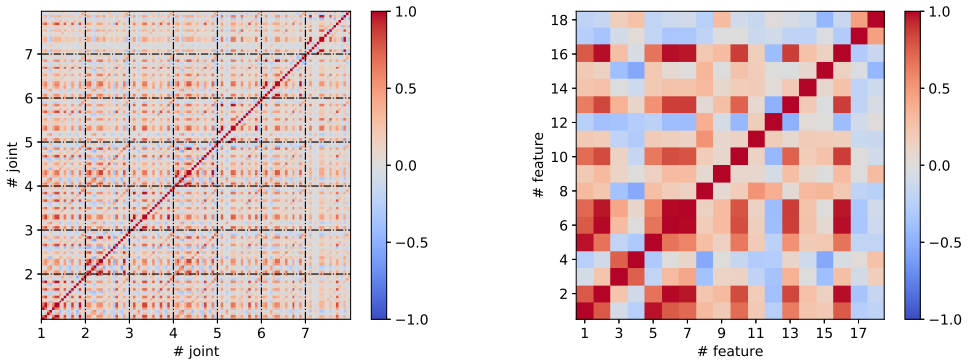

(a) The spearman correlation between the 126 features.

(b) The spearman correlation between the 18 features on joint #1.

Figure 4.4: The Spearman correlation analysis of the features.

diagonal are highly similar to each other, which indicates that the features on all robot joints possess similar self-dependence properties. Therefore, it is reasonable to only investigate the analysis result of a single joint and selected or eliminated the features in batches in the unit of joint.

The correlation analysis of all 18 features on joint #1, which is corresponding the block in the down-left corner in Fig. 4.4a, is illustrated in Fig. 4.4b. The results reveal that features #1 ($\bar{\mathcal{T}}$) and #5 ($\bar{m}_\tau$) show high dependence, so do features #2 ($\mathrm{Var}(\mathcal{T})$), #6 ($\mathrm{Rng}(\mathcal{T})$), #7 ($\mathrm{Dev}(\mathcal{T})$) and #16 ($E_{\mathrm{rms}}$). Therefore, these features are preferably considered to be eliminated from $\mathcal{X}^+$, yet their *importance* to the classification still needs to be considered.

4.3.2.2 Importance Analysis

After analyzing the dependence of the features, we apply the Relieff algorithm to the 126 features in $\mathcal{X}^+$ to evaluate their *importance*. As a popular feature engineering technique used in the previous work [264], it provides a weight for each feature to depict its *importance* to the classification, which is independent of the classifier models. The predecessor of Relieff, known as Relief, is originally proposed in [270] for binary classification problems. Its main idea is to recursively and randomly select a sample x from the data set and find out its closest samples with the same and different labels (respectively referred as the near-hit z^+ and the near-miss z^-). For the i-th feature of sample x, x_i, its weight w_i is iteratively updated by the following law,

$$w_i = w_i - \left(x_i - z_i^+\right)^2 + \left(x_i - z_i^+\right)^2,$$

where z_i^+ and z_i^- are the i-th features of z^+ and z^-. The weight w_i depicts the reward (if w_i is positive) or punishment (if w_i is negative) of the i-th feature to the classifica-

tion, and a larger w_i indicates higher *importance*. Relieff is adapted from Relief as the extension to multi-class problems [271].

On the training set, we calculate the weights, or importance of all 126 features using Relieff and illustrate the results in Fig. 4.5, grouping them respectively by the feature number (see Fig. 4.5a) and joint number (see Fig. 4.5b). The results indicate that the feature importance varies among both features and joints. In Fig. 4.5a, the feature $\#\,2$ ($\mathrm{Dev}(\mathcal{T})$) shows the lowest *importance* (0.49), followed by $\#\,4\,(\mathrm{Kurt}(\mathcal{T}))$, $\#\,5\,(\bar{m}_\tau)$, $\#\,9\,(f^*)$, and $\#\,13\,(S|(\bar{f})|)$. In Fig. 4.5b, the feature weights on joint $\#\,1$, $\#\,2$ and $\#\,4$ are higher than the other joints.

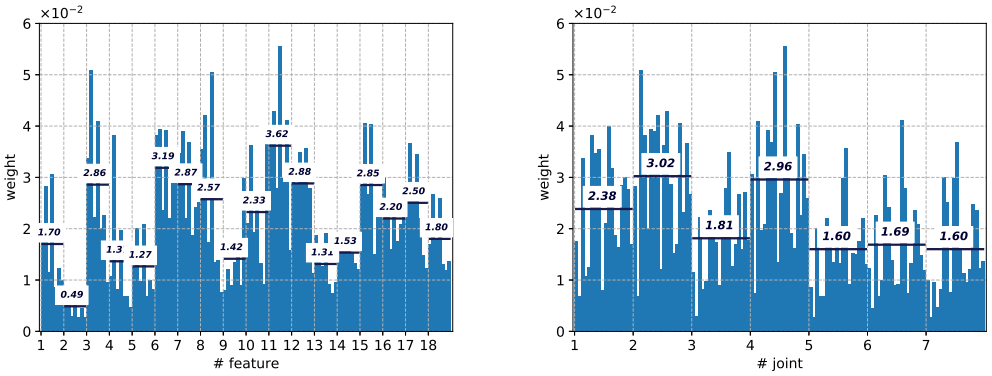

(a) Feature weights grouped by feature numbers. The averaged weight over all 7 joints is marked for each feature.

(b) Feature weights grouped by joint numbers. The averaged weight over all features is marked for each joint.

Figure 4.5: The weights of the features obtained by Relieff algorithm.

Since the classifier is supposed to function in a online scheme, we are quite concerned with the computational load of the features. Therefore, we tend to form a small feature set, while maintaining a decent classification accuracy. Considering both high dependence and low *importance*, we eliminate features $\#\,2$ ($\mathrm{Dev}(\mathcal{T})$), $\#\,4\,(\mathrm{Kurt}(\mathcal{T}))$ and $\#\,5\,(\bar{m}_\tau)$. Features $\#\,6\,(\mathrm{Rng}(\mathcal{T}))$ and $\#\,16\,(E_{\mathrm{rms}})$ are also eliminated due to their strong relationship with $\#\,7\,(\mathrm{Dev}(\mathcal{T}))$, as well as $\#\,18\,(E_{\mathrm{rt}}^{20})$ due to its redundancy to $\#\,17\,(E_{\mathrm{rt}}^{10})$. Additionally, we remove the features of the joints $\#\,3$, $\#\,5$, $\#\,6$ and $\#\,7$ due to their low importance. Therefore, we determine the feature set for the development of the signal classifier as $\mathcal{X}^* = \{\bar{\mathcal{T}}, \mathrm{Skew}(\mathcal{T}), \mathrm{Dev}(\mathcal{T}), E_I(\mathcal{T}), f^*, |C(f^*)|, \phi(C(f^*)), \bar{f}, |S(\bar{f})|, \phi(S(\bar{f})), F_{\mathrm{crest}}, E_{\mathrm{rt}}^{10}\}_{1,2,4}$ which contains 36 features, where the subscript denotes the joints. To evaluate $\mathcal{X}^*$, we also define a minimum set $\mathcal{X}^- = \{\bar{\mathcal{T}}, \mathrm{Skew}(\mathcal{T}), \mathrm{Dev}(\mathcal{T}), E_I(\mathcal{T}), f^*, |C(f^*)|, \phi(C(f^*)), \bar{f}, |S(\bar{f})|, \phi(S(\bar{f})), F_{\mathrm{crest}}, E_{\mathrm{rt}}^{10}\}_1$, which only includes 12 feature on joint $\#\,2$. We will evaluate the three feature sets $\mathcal{X}^+$, $\mathcal{X}^*$ and $\mathcal{X}^-$ and select the best when determining the classifier models. Note that such development procedure is justified since the entire feature selection process is independent from the classification models.

4.3.3 Model Validation

After determining the feature sets $\mathcal{X}^+$, $\mathcal{X}^*$ and $\mathcal{X}^-$, we are ready to select the model for the signal classifier. Since a large number of models are used in the literature for the classification of time series, enumerating all of them for the best one is a tedious and unnecessary process. Instead, we assign several popular models with representative properties as candidates, and validate these candidate models using the training set, before selecting the best one. In our work, we determine the candidate models based on three factors, namely the pHRI signal properties, engineering experience in the previous work and the values of models in practice. Thus, four classifier models, namely a Linear Discriminant Analysis (LDA) model, kNN model, an SVM model, and a FNN model are chosen as candidate models, due to their simple structures and successful applications in the previous work [264]. These four models are featured with various properties and essentially cover most representative classifier structures. Specifically, the LDA model is well known for its high efficiency and stable performance, and is able to achieve high prediction accuracy for the linearly classifiable data sets. The kNN model is supported by well-developed theoretical foundations and is easy to be extended to a larger scale database in future work. The SVM model shows the excellent ability of generalization. The NN model, as a powerful and comprehensive approximator, has strong adaptability and flexibility for various data sets. In this work, we only consider the NN model with one hidden layer. Note that simple structures are always preferred in practice since the reliability of the system tends to decrease when the system becomes more complicated. To evaluate the four classifier models on the training set with the feature sets $\mathcal{X}^+$, $\mathcal{X}^*$ and $\mathcal{X}^-$, we use a ten-fold cross-validation method and calculate the mean values of the ten validation scores which are briefly referred to as *score*. We also apply a grid search method to seek for the best hyper-parameters of the models. The models and the corresponding grid values of their hyper-parameters are shown in Tab. 4.1.

Table 4.1: Hyper-Parameters for Grid-Searching Validation

Models	Hyper-params	Grid values
LDA	solver	'svd', 'lsqr', 'eigen'
kNN	k value	$2, 3, \cdots, 80$
	distance metrics	'canberra', 'chebyshev', 'euclidean', 'manhattan', 'minkowski'
SVM	C value	$10^{-3}, 10^{-2.8}, \cdots, 10^{3}$
	kernel function	'linear', 'rbf', 'sigmoid'
FNN	hidden neurons	$2, 4, \cdots, 100$
	activation function	'identity', 'logistic', 'tanh', 'relu'

The four models and the corresponding hyper-parameter values achieving the best scores in the validation are listed in Tab. 4.2, where the hyper-parameter values are in the same order as the hyper-parameters in Tab. 4.1. The validation scores of the models trained with various feature sets are presented in the *score* columns, $\mathcal{X}^+$, $\mathcal{X}^*$ and X^-, respectively, which show that all four models achieve satisfactory scores, with the FNN model showing the highest (96.6%). Thus, we select FNN with 48 hidden-layer neurons, with 'logistic' activation function as the model for the signal classifier of the CDI scheme. In the meantime, the results also reveal that the scores using $\mathcal{X}^*$ are close to that using the full feature set $\mathcal{X}^+$ for all models, despite of slight decreases. On the contrary, the scores of the minimum feature set $\mathcal{X}^-$ drastically drop compared to $\mathcal{X}^+$ $\mathcal{X}^*$. Therefore, we determine $\mathcal{X}^*$ as the feature set to train the FNN model, since it achieves similar scores to the full feature set $\mathcal{X}^+$ with a greatly reduced number of features.

Table 4.2: The Model Configurations with Best Validation Scores

Models	Hyper-parameters	score($\mathcal{X}^+$)	score($\mathcal{X}^*$)	score($\mathcal{X}^-$)
LDA	'svd'	94.8%	92.4%	82.2%
kNN	5, 'canberra'	97.5%	96.3%	88.0%
SVM	63.1, 'linear'	97.3%	96.0%	86.4%
FNN	48, 'logistic'	96.8%	96.6%	89.7%

4.3.4 Model Test

After determining the model for the signal classifier (FNN, 48 hidden-layer neurons, 'logistic' activation function), we train the model using all samples in the training set with the feature set $\mathcal{X}^*$ and evaluate its prediction accuracy using the test set. The tested accuracy score, 96.5%, is generally comparable with the score 96.6% in the model validation in Sec. 4.3.3, which indicates that the signal classifier possesses a satisfactory ability of generalization. The confusion matrix of the test is presented in Fig. 4.6, where the prediction accuracy for *collisions*, *contacts* and *free* respectively achieves as high as 95.6%, 93.7% and 98.4%, showing a decent performance of the classifier. Especially, the higher accuracy rate of *collisions* than *contacts* reveals that the classifier is more sensitive to accidental *collisions*, which is reasonable since *collisions* are more dangerous to humans than *contacts*. The high accuracy score for *free* means that the classifier hardly produces false-positive results.

4.4 Design of the Online Diagnosor

Although the signal classifier shows high accuracy for samples with complete pHRI waveform, the same performance is not likely to be ensured in the early stage of a pHRI

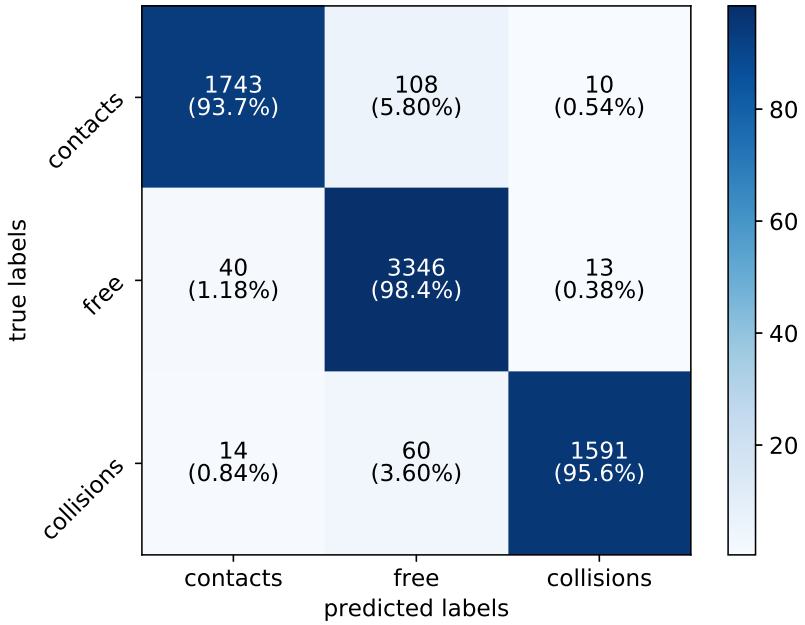

Figure 4.6: The confusion matrix in the test with the trained classifier.

in online applications, since the segmented waveform is incomplete. As discussed in Sec. 4.1, the main reason is the distribution inconsistency between the training set and the segmented online signals, such that a single prediction result of the classifier does not guarantee a reliable CDI before the pHRI vanishes. To resolve this issue, we design an additional online diagnosor for the CDI scheme to produce online decisions based on a series of prediction results, which is proven to be more reliable than using a single result.

4.4.1 Prediction Analysis of Incomplete Waveforms

As the first step of designing the online diagnosor, we investigate the prediction accuracy of the signal classifier for signal samples with incomplete pHRI waveform. We create several test sets from the raw signals with various b values which represent the segmented online signals with different proportion of pHRI waveform, and use them to evaluate the prediction accuracy of the signal classifier. Note that all the test sets are of the same size as the one in Sec. 4.3.4. The accuracy scores with different b values are illustrated in Fig. 4.7.

As a general tendency, the prediction accuracy increases when the segment bias b becomes larger. An intuitive explanation is that more useful information on the pHRI waveform naturally leads to higher accuracy scores. Within the interval $b \leqslant 50$, the prediction accuracy is lower than 77.3%, which indicates that a prediction result within 50 ms after the pHRI is very likely to be incorrect. In contrast, when $b > 200$, the

accuracy is higher than 93.0%, which reveals that an accurate result is only possible after 200 ms. Apparently, a single prediction result of the signal classifier does not offer a reliable CDI decision in the early stage of pHRI.

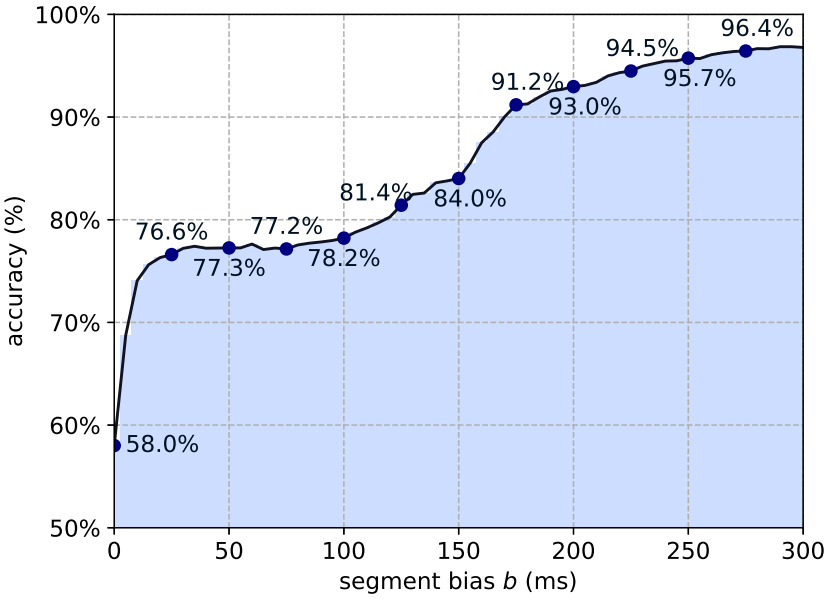

Figure 4.7: The accuracy scores of the classifier for various bias values.

4.4.2 Diagnosis Using Confidence Indexes

Our solution to this problem is to extend the decision horizon, such that the CDI result κ^* is produced based on a series of successive prediction results. Moreover, a quantified metric is need to depict the reliability of the CDI result. Let us assume that the pHRI occurs at time t_0. At a certain time instant $t_1 = t_0 + b$, a segmented torque signal $\mathcal{T}_1$ is given to the signal classifier which then reports a prediction r_1. The value of the prediction result r_1 can be -1, 0 or 1 which corresponds to *collision*, *contact* and *free*. Here, r_1 is not directly used to make the decision κ^*. Instead, we postpone s sampling intervals until we obtain s signal segments $\mathcal{T}_1, \mathcal{T}_2, \cdots, \mathcal{T}_s$ and a series of prediction results $\mathcal{R} = \{r_1, r_2, \cdots, r_s\}$. Here, we refer to $\mathcal{R}$ as an *observation* series with the window size s. According to the Bayesian decision theory, the posterior probability of the class $C = \{-1, 0, 1\}$ based on the observation series $\mathcal{R}$ with parameter b reads

$$p(C|\mathcal{R}, b) = \frac{p(C|b)p(\mathcal{R}|C, b)}{p(\mathcal{R}|b)}, \tag{4.4}$$

where $p(C|b)$ is the prior knowledge of proportions of the data set, $p(\mathcal{R}|C, b)$ is the likelihood of class C and $p(\mathcal{R}|b)$ is the evidence that adjusts the weight of the posterior

probabilities, where $p(\mathcal{R}|b) = \sum_C p(C|b)p(\mathcal{R}|C,b)$. As mentioned in the beginning of Sec. 4.3, the signal segments $\boldsymbol{\tau}_1, \boldsymbol{\tau}_2, \cdots, \boldsymbol{\tau}_s$ are independent from each other, so are the prediction results $r_1, r_2, \cdots, r_s$. Therefore, the likelihood $p(\mathcal{R}|C,b)$ can be calculated by the following product

$$p(\mathcal{R}|C,b) = \prod_{j=1}^{s} p(r_j|C,b_j), \tag{4.5}$$

where for each r_j, $j = 1, 2, \cdots, s$, $p(r_j|C,b_j)$ represents the likelihood of a single prediction result r_j with given pHRI class C. The parameter b_j is the bias of segment $\boldsymbol{\tau}_j$, reflecting a hidden condition that r_j is the j-th element of $\mathcal{R}$. The likelihood $p(r_j|C,b_j)$ depicts the probability that the classifier predicts a sample labeled C as r_j, which depends on the capability of the classifier.

Here, the posterior probability $p(C|\mathcal{R},b)$ serves as a confidence index for decision C given observation series $\mathcal{R}$. It indicates the belief on the classifier to produce an accurate diagnosis result within b ms after the occurrence of the pHRI. A larger value of $p(C|\mathcal{R},b)$ corresponds to a more trustful decision C. Therefore, the decision law for the online diagnosor can be designed as

$$\kappa^* = i, \text{ if } p(C^{[i]}|\mathcal{R},b) = \max_C p(C|\mathcal{R},b), \ i = -1, 0, 1, \tag{4.6}$$

where κ^* is the diagnosis result ($\kappa^* = -1$ for *contacts*, $\kappa^* = 1$ for *collisions* and $\kappa^* = 0$ for *free*) and $C^{[i]}$ represents the event $C = i$ for brevity. The confidence index for decision κ^* is $\iota_{\mathcal{R}}^{\kappa^*} = p(\kappa^*|\mathcal{R},b)$.

To calculate the posterior probabilities, the likelihoods $p(r_j|C,b_j)$ for all $r_j = \{-1, 0, 1\}$ and $C = \{-1, 0, 1\}$ can be approximated by experimental methods similar to that in Sec. 4.4.1. The difference is that the calculation of the likelihoods requires the values in the confusion matrices, rather than the overall accuracy scores. Such approximation is justified by the large number principle. The observation window size s can be determined accordingly. A wider window leads to a higher resolution of the confidence index and provides more flexibility to the collision handling pipeline, which on the other hand, involves more computational load. Note that the value b, as a parameter to be assigned, represents a conservative estimation, rather than the true diagnosis delay. A reliable CDI diagnosis is guaranteed in the early stage of a pHRI, as long as a high confidence index is obtained for even small values of b. Therefore, in the practical design of the CDI scheme, b can be heuristically determined as a reference reaction time. By designing the decision law (4.6) with the confidence index ι, the collision handling pipeline can be implemented in a more flexible manner.

4.4.3 A Fast Online Diagnosis Algorithm

The decision law in (4.6) requires the calculation of the posterior probabilities for every observation series $\mathcal{R}$, which is not suitable for online applications due to the large computational load. Here, we propose a fast online diagnosis algorithm (as Algorithm 1) that only involves simple comparison logic but ensures high reliability. In the algorithm,

the observation window size is set as $s = 5$. The main routine of the algorithm is to compare the observation $\mathcal{R}$ with two reference events $\mathcal{R}_l^4$ and $\mathcal{R}_t^2$, where $\mathcal{R}_l^4$ means that at least 4 *collisions* are observed in $\mathcal{R}$, and $\mathcal{R}_t^2$ represents at least 2 *contacts* are witnessed. To evaluate the reliability of Algorithm 1, we calculate its posterior probabilities, $p(C^{[1]}|\mathcal{R}_l^4, b)$, $p(C^{[1]}|\mathcal{R}_t^2, b)$ and $p(C^{[1]}|\mathcal{R}_f, b)$ with $b = 50$, where $\mathcal{R}_f$ denotes $\overline{\mathcal{R}_l^4 \vee \mathcal{R}_t^2}$, i.e., neither a *collision* nor a *contact* occurs. Here, $\vee$ denotes the union of two events and $\overline{(\cdot)}$ represents the compliment of a event. Therefore, the posterior $p(C^{[1]}|\mathcal{R}_l^4, b)$ represents the confidence index of Algorithm 1 when making a decision $C = 1$ given $\mathcal{R} \in \mathcal{R}_l^2$, $p(C^{[1]}|\mathcal{R}_l^4, b)$ is for decision $C = -1$ with $\mathcal{R}_t^2$, and the else is depicted by $p(C^{[0]}|\mathcal{R}^f, b)$ which describes the reliability of the algorithm in *free* cases.

Algorithm 1 The Fast Online Diagnosor

Input: $\mathcal{R} = \{r_1, r_2, r_3, r_4, r_5\}$
Output: κ^*
1: **if** $\mathcal{R} \in \mathcal{R}_{\text{cls}}^4$ **then**
2: $\quad \kappa^* = 1$;
3: **else if** $\mathcal{R} \in \mathcal{R}_{\text{ctc}}^2$ **then**
4: $\quad \kappa^* = -1$;
5: **else**
6: $\quad \kappa^* = 0$;
7: **end if**

Table 4.3: The confusion matrices of signal classifier with test set $b = 50$ms (I).

$p(r\|C)$	$r^{[1]}$	$r^{\overline{[1]}}$	$p(r\|C)$	$r^{[-1]}$	$r^{\overline{[-1]}}$
$C^{[1]}$	1207 (72.5%)	458 (27.5%)	$C^{[-1]}$	593 (31.9%)	1268 (68.1%)
$C^{\overline{[1]}}$	13 (0.25%)	5247 (99.7%)	$C^{\overline{[-1]}}$	419 (8.27%)	4645 (91.8%)

Table 4.4: The confusion matrices of signal classifier with test set $b = 50$ms (II).

$p(r\|C)$	$r^{[0]}$	$r^{[-1]}$	$r^{[1]}$
$C^{[0]}$	3376 (99.4%)	20 (5.89%)	3 (0.09%)
$C^{\overline{[0]}}$	1317 (37.4%)	992 (28.2%)	1217 (34.6%)

To calculate the posteriors, we firstly use (4.5) to calculate the following likelihoods,

$$p(\mathcal{R}_l^4|C^i, b_j^{[50]}) = \sum_{\mathcal{R}\in\mathcal{R}_l^4} \prod_{j=1}^{s} p(r_j|C^i, b_j^{[50+j]}),\ i = [1], \overline{[1]},$$

$$p(\mathcal{R}_t^2|C^i, b_j^{[50]}) = \sum_{\mathcal{R}\in\mathcal{R}_t^2} \prod_{j=1}^{s} p(r_j|C^i, b_j^{[50+j]}),\ i = [-1], \overline{[-1]},$$

$$p(\mathcal{R}_f|C^i, b_j^{[50]}) = \sum_{\mathcal{R}\in\mathcal{R}_f}\prod_{j=1}^{s} p(r_j|C^i, b_j^{[50+j]}),\ i = [0], \overline{[0]},$$

where $b^{[50]}$ means $b = 50$ and $C^{\overline{[1]}}$ denotes the event that $C \neq 1$, i.e., $C^{\overline{[1]}} = C^{[-1]} \vee C^{[0]}$, while similar is $C^{\overline{[-1]}}$. Such a compact form is for the purpose of brevity. We assume that $p(r_j|C^{[1]}, b_j^{[50+j]}) \approx p(r_j|C^{[1]}, b_j^{[50]})$, for all $j = 1, 2, \cdots, 5$, considering a high sampling rate of the system. Therefore, the likelihoods are calculated by follows,

$$p(\mathcal{R}_l^4|C^i) = p(r^{[1]}|C^i)^5 + 5p(r^{[1]}|C^i)^4 p(r^{\overline{[1]}}|C^i), \tag{4.7a}$$

$$p(\mathcal{R}_t^2|C^i) = 1 - p(r^{\overline{[-1]}}|C^i)^5 - 5p(r^{\overline{[-1]}}|C^i)^4 p(r^{[-1]}|C^i), \tag{4.7b}$$

$$\begin{aligned} p(\mathcal{R}_f|C^i) =& p(r^{[0]}|C^i)^5 + 5p(r^{[0]}|C^i)^4 p(r^{[1]}|C^i) \\ &+ 10p(r^{[0]}|C^i)^3 p(r^{[1]}|C^i)^2 + 10p(r^{[0]}|C^i)^2 p(r^{[1]}|C^i)^3 \\ &+ 5p(r^{[-1]}|C^i) \times \Big(p(r^{[0]}|C^i)^4 + 4p(r^{[0]}|C^i)^3 p(r^{[1]}|C^i) \\ &+ 6p(r^{[0]}|C^i)^2 p(r^{[1]}|C^i)^2 + 4p(r^{[0]}|C^i) p(r^{[1]}|C^i)^3 \Big), \end{aligned} \tag{4.7c}$$

respectively for $i = [1], \overline{[1]}$, $i = [-1], \overline{[-1]}$ and $i = [0], \overline{[0]}$, where $b^{[50]}$ and the subscript j for r_j are omitted for brevity. Similar to above, we use $r^{[1]}$ and $r^{\overline{[1]}}$ to represent $r = 1$ and $r \neq 1$. To obtain the values of the single-prediction likelihoods on the right sides of (4.7), we evaluate the signal classifier using the test set with $b = 50\,(\text{ms})$ and calculate the confusion matrix which is decomposed to three matrices in Tab. 4.3, respectively for the calculation of (4.7a), (4.7b) and (4.7c). The rows of Tab. 4.3 $C^{[i]}$, $i = -1, 0, 1$ represent the ground truth, whilst the columns $r^{[i]}$ denote the predicted classes. In each block, both the number of samples and the accurate scores are presented, which explicitly corresponds to the values of the likelihoods $p(r|C)$. For example, the value of $p(r^{[1]}|C^{[1]})$ is approximated as 0.73 corresponding to the value in $C^{[1]}$, $r^{[1]}$.

Checking the values in Tab. 4.3 and using (4.7), we calculate the values of the likelihoods as

$$\begin{aligned} p(\mathcal{R}_l^4|C^{[1]}) = 0.87,\ p(\mathcal{R}_l^4|C^{\overline{[1]}}) = 9.80 \times 10^{-5}, \\ p(\mathcal{R}_t^2|C^{[-1]}) = 0.51,\ p(\mathcal{R}_t^2|C^{\overline{[-1]}}) = 6.74 \times 10^{-2}, \\ p(\mathcal{R}_f|C^{[0]}) = 0.99,\ p(\mathcal{R}_f|C^{\overline{[0]}}) = 0.52, \end{aligned}$$

Here, we set the prior probabilities as $p(C^{[0]}) = 0.5$, $p(C^{[1]}) = p(C^{[-1]}) = 0.25$, according to the proportion of samples in the data set. Therefore, according to the Bayes law in (4.5), we calculate the confidence indexes for Algorithm 1 as follows,

$$p(C^{[1]}|\mathcal{R}_l^4) = \frac{p(C^{[1]})p(\mathcal{R}_l^4|C^{[1]})}{\sum_{i=[1]}^{\overline{[1]}} p(C^i)p(\mathcal{R}_l^4|C^i)},$$

$$p(C^{[-1]}|\mathcal{R}_t^2) = \frac{p(C^{[-1]})p(\mathcal{R}_t^2|C^{[-1]})}{\sum_{i=[-1]}^{\overline{[-1]}} p(C^i)p(\mathcal{R}_t^2|C^i)},$$

$$p(C^{[0]}|\mathcal{R}_f) = \frac{p(C^{[0]})p(\mathcal{R}_f|C^{[0]})}{\sum_{i=[0]}^{\overline{[0]}} p(C^i)p(\mathcal{R}_f|C^i)},$$

which leads to $p(C^{[1]}|\mathcal{R}_l^4) = 0.99$, $p(C^{[-1]}|\mathcal{R}_t^2) = 0.72$ and $p(C^{[0]}|\mathcal{R}_f) = 0.66$.

The results of the posterior probabilities indicate that Algorithm 1 produces high confidence on its diagnosis for *collisions* ($\iota_{\mathcal{R}}^1 = 0.99$) and *contacts* ($\iota_{\mathcal{R}}^{-1} = 0.72$) with given observation series $\mathcal{R}$. A larger value of $p(C^{[1]}|\mathcal{R}_l^4)$ than $p(C^{[-1]}|\mathcal{R}_t^2)$ means that the diagnosor is more sensitive to *collisions* than *contacts*. The confidence index $\iota_{\mathcal{R}}^0 = 0.66$ for *free* reveals that the diagnosor is also trustful for avoiding false detection. Due to the fact that $p(C^{[1]}|\mathcal{R}_l^4) = \max_C p(C|\mathcal{R}_l^4)$, $p(C^{[-1]}|\mathcal{R}_t^2) = \max_C p(C|\mathcal{R}_t^2)$ and $p(C^{[0]}|\mathcal{R}_f) = \max_C p(C|\mathcal{R}_f)$, Algorithm 1 is consistent with the decision law in (4.6). Therefore, the confidence index ι can be explicitly obtained without calculation, which leads to a faster and easier implementation for online applications.

4.4.4 Comparison with the Single Prediction

To justify the advantage of the online diagnosor using observation series instead of a single prediction result, we also calculate the confidence indexes for the latter for comparison. The confidence index for class C^i, with a single observation r^i, is calculated by

$$p(C^i|r^i) = \frac{p(C^i)p(r^i|C^i)}{\sum_{k=i}^{\bar{i}} p(C^k)p(r^k|C^k)},\ i = [-1], [0], [1].$$

Checking the likelihoods in Tab. 4.3, we obtain $p(C^{[-1]}|r^{[-1]}) = 0.57$, $p(C^{[0]}|r^{[0]}) = 0.75$, $p(C^{[1]}|r^{[1]}) = 0.99$. The results show that such a scheme ensures a low reliability on identifying *contacts* (0.57), i.e., the diagnosor is sensitive to *collisions* but quite dull to *contacts*, which shows a inferior performance than Algorithm 1.

4.5 Experiments

4.5.1 Accuracy Evaluation

In this section, we evaluate the performance of the proposed CDI scheme in terms of both the identification accuracy and the responsiveness by applying it to an online validation on the recorded raw signals. These signals contain 242 collisions and 225 contacts and have never been used during the development of the signal classifier. The torque signal is sequentially sampled at the rate of 1 kHz and recursively segmented as new samples for the signal classifier. The online diagnosor is equipped with the fast online diagnosor in Algorithm 1 to provide online diagnosis. Note that the evaluation method and metrics in this experiment are different from the model test in Sec. 4.3.4. For the classifier development, the accuracy scores are calculated based on the number of signal segments containing the pHRI waveform, while in a human-robot collaboration, a CDI scheme focuses more on the number of correctly identified *collisions* or *contacts*. The

main difference is that the pHRI, in an online application, usually produces several segments with various b values, corresponding to the signals segmented in different sampling instants. Therefore, for the experimental validation, we must clarify that we evaluate the performance of the CDI scheme with respect to the entire pHRI, rather than its segments. We recognize that the pHRI is accurately identified, if the scheme proposes a correct diagnose before it vanishes.

During the experiment, 240 out of 242 collisions and all 225 interactions are correctly identified, with 2 collisions misclassified as 1 contact and 1 free, achieving an overall accuracy 99.6%. Some identification instances are shown in Fig. 4.8, which illustrates the accuracy and responsiveness of the scheme. It is noticed that most of the diagnosis results are correctly produced in the early stages of the pHRI, which confirms the high accuracy of the online CDI scheme. The fast response of the scheme is also clearly reflected in Fig. 4.9 with both instances of a *collision* and a *contact*. The two pHRI are all correctly identified within 20ms after their occurrence, which confirms the responsiveness of the scheme.

4.5.2 A Simple Collision Reaction Scheme

To demonstrate the applicability of the proposed online CDI scheme in a practical task, we implement it on the Kuka LWR4+ robot platform (as shown in Fig. 4.10) together with a collision reaction routine. The script of the task is to implement a cyclic motion by steering the manipulator to track a desired sinusoidal trajectory $\boldsymbol{q}_{\mathrm{d}}(t)$. During this process, we manually exert a collision or a contact to the robot endeffector. Then, the CDI scheme monitors the external torques on the robot joints, detects any pHRI and activate the collision reaction routine which modifies the desired trajectory to enable the corresponding reaction mode. The reaction strategy is, if a *collision* is detected (as Fig. 4.10a), an emergency stop is triggered and the robot holds on the current position until the safety alarm is deactivated (as Fig. 4.10b). If a *contact* is detected (as Fig. 4.10c), the robot enables its gravity compensation mode such that the human can conduct active guidance on the robot (as Fig. 4.10d). The reaction strategy can be represented as follows.

$$\boldsymbol{q}_{\mathrm{r}}(t) = \begin{cases} \boldsymbol{q}_{\mathrm{c}}, & \kappa^* = 1, \\ \boldsymbol{q}(t), & \kappa^* = -1, \\ \boldsymbol{q}_{\mathrm{d}}(t), & \kappa^* = 0, \end{cases}$$

where $\boldsymbol{q}_{\mathrm{r}}(t)$ is the modified reference trajectory, $\boldsymbol{q}_{\mathrm{c}}$ is the fixed current position which represents an emergency stop, $\boldsymbol{q}(t)$ is the actual robot state which indicates a gravity compensation, and $\boldsymbol{q}_{\mathrm{r}}(t) = \boldsymbol{q}_{\mathrm{d}}(t)$ denotes the nominal task.

During the operation of the robot, the CDI scheme correctly detects and identifies most of the pHRI and enables the corresponding reaction procedure, although some week contacts and collisions fail to be detected. When the robot is smoothly moving, the false diagnosis of collisions and contacts is hardly witnessed. Nevertheless, a false diagnosis occurs when the robot motion shows large vibrations due to fierce motion or bad controller design. Therefore, a smooth functioning condition is still necessary. As for the responsiveness, the diagnosis delay is basically not obviously perceivable experimenters,

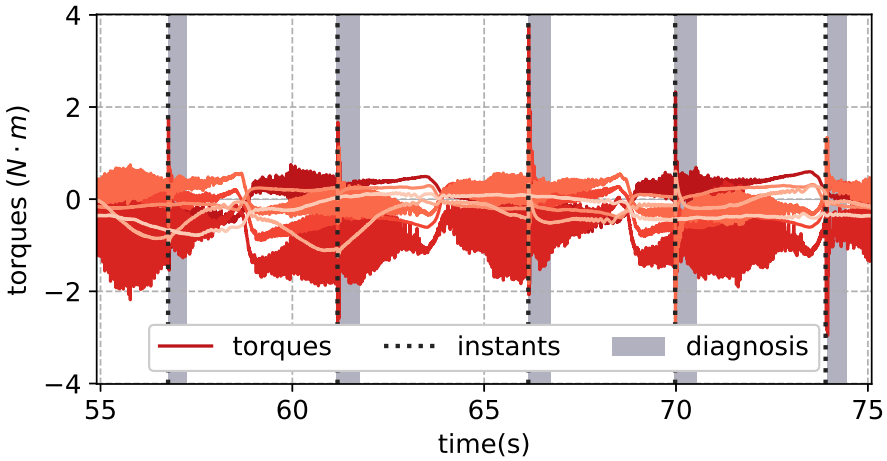

(a) The CDI diagnosis of collisions. The red solid lines are the raw signals, the black dot lines are the occurrence instants of the collisions and the grey regions represent the time intants when collisions are detected and identified.

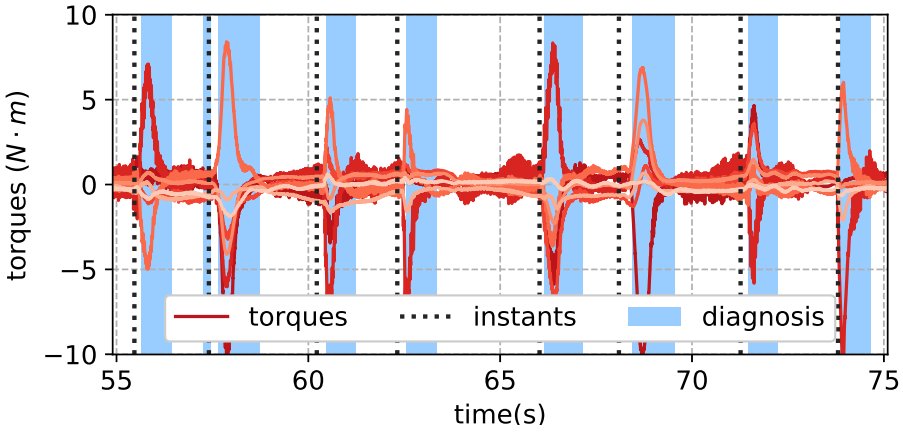

(b) The CDI diagnosis of contacts. The red solid lines are the raw signals, the black dot lines are the occurrence instants of the contacts, and the blue regions represent the time intants when contacts are detected and identified.

Figure 4.8: The experiment results of the online scheme.

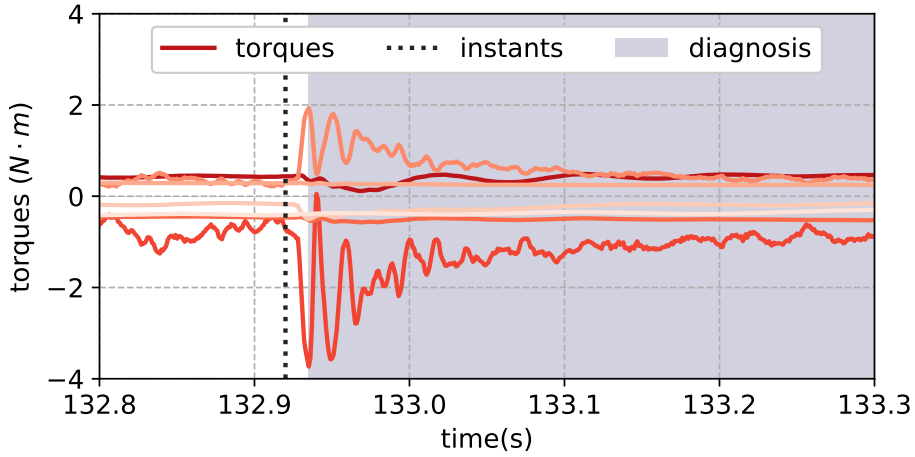

(a) The CDI diagnosis of a collision. The red solid lines are the raw signals, the black dot lines are the occurrence instants of the collisions and the grey regions represent the time intants when collisions are detected and identified.

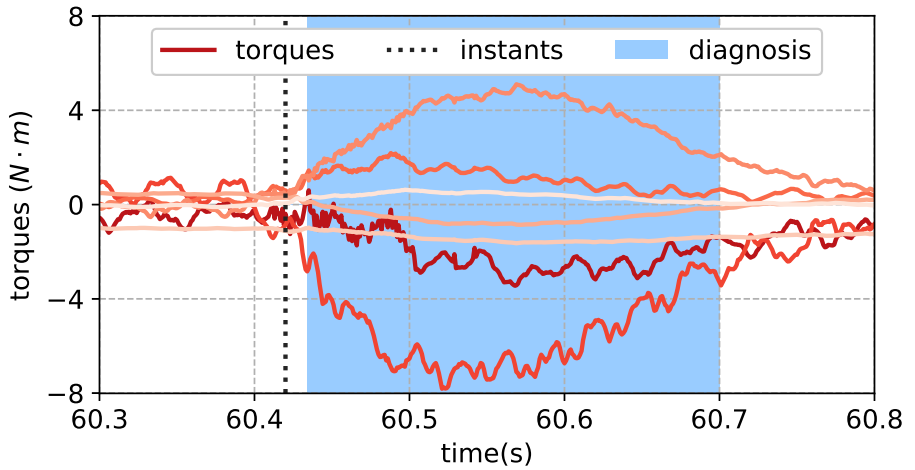

(b) The CDI diagnosis of a contact. The red solid lines are the raw signals, the black dot lines are the occurrence instants of the contacts, and the blue regions represent the time intants when contacts are detected and identified.

Figure 4.9: The diagnosis results of a collision and a contact.

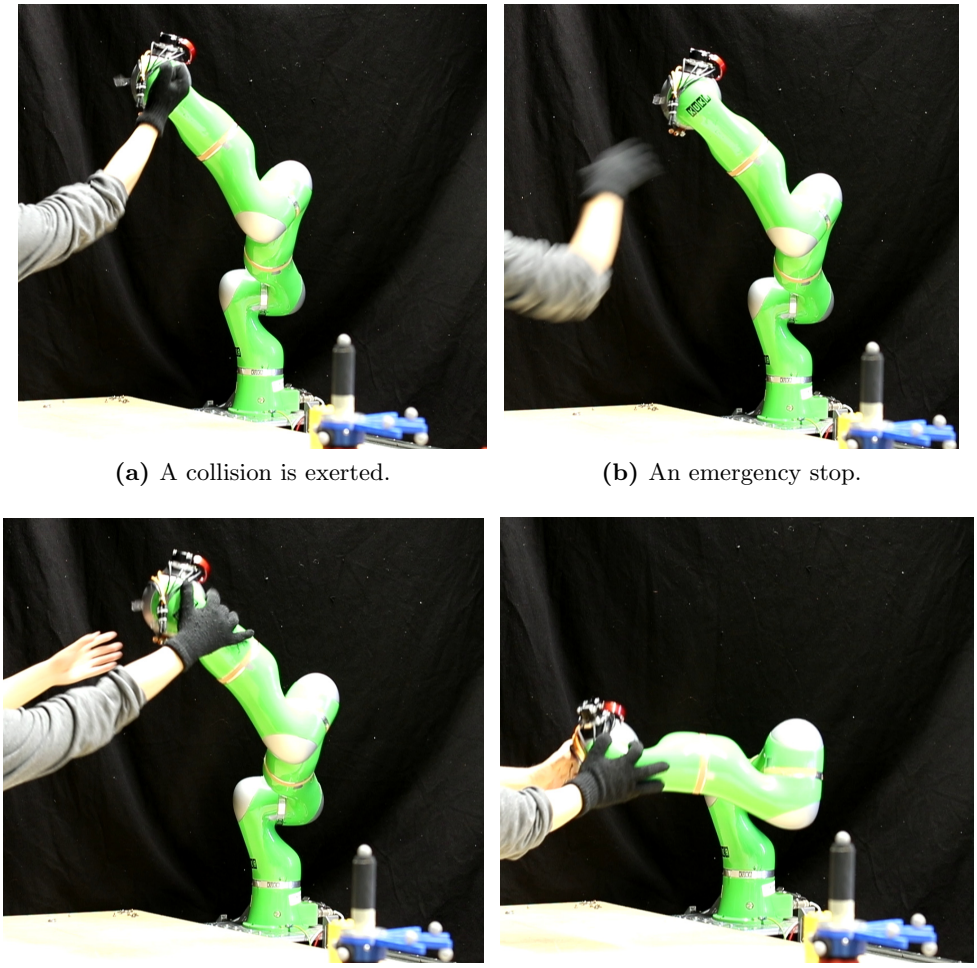

(a) A collision is exerted. **(b)** An emergency stop.

(c) An interaction is exerted. **(d)** The guidance mode.

Figure 4.10: The application demonstration of the online scheme.

which is acceptable in a typical human-robot collaborative task. Therefore, the demonstration confirms the performance of the proposed CDI and indicates its applicability to human-robot collaboration tasks in practice.

4.6 Summary

In this chapter, we develop a novel online CDI scheme for robot manipulators using supervised learning and the Bayesian decision theory. During the data collection process, we try to cover various execution conditions of the robot to ensure a representative data set. After carefully investigating the properties of the pHRI signals, we extract and select the features by analyzing their dependence and importance. As a result, the signal classifier presents excellent predictability and generalization ability. Based on this, we

propose a fast and simply implementable online diagnosor with a quantified confidence index to depict the reliability of the diagnosis result based on the Bayesian decision theory. Examined by both theoretical analysis and experimental validation, the proposed CDI scheme shows a promising value to improve the safety of human-robot collaboration systems. It should be noted that the development of the CDI scheme, including the procedures of the data collection, feature engineering, and the model training, is conducted on a specific robot platform. Thus, the applicability of the developed CDI scheme to different platforms needs further investigations. In general, our work ensures rapid and accurate detection and identification of accidental collisions in their early stages. As a result, a collision is *predicted* before it vanishes, such that further damages or injuries can be avoided. The common ground of our work and the probabilistic-series-model-based methods is to make a decision using the observation series. Nevertheless, the proposed CDI scheme is more suitable to be widely applied in practice since it does not require prior knowledge of the signal dependence and assumptions on the data distribution. Therefore, our CDI scheme in this chapter provides a decent solution to **Question 2** raised in Sec. 1.2.

5 Collision Avoidance Control

Post-handling of collisions does not guarantee the absolute safety of HRC systems due to modeling uncertainties and misclassification. Therefore, pre-handling of collisions such as safe control and planning methods targeted to collision avoidance is necessary for a collision handling pipeline. In this chapter, we design a trajectory tracking controller for robot manipulators satisfying strict safety constraints, corresponding to the robust controller module in Fig. 2.7. These constraints are represented as a set of unilateral state-dependent inequalities to regulate the feasible configuration space for robot motions, such that the robot is kept away from static objects in the environment. In this work, besides confined trajectory tracking errors and avoidance of constraint violations, we are also concerned with the robustness and adaptiveness of the controller. Environmental results indicate that the controller produces decent tracking precision with bounded disturbances and adaptive controller parameters. The robot motion is strictly confined within the safe region even the desired trajectory violates the safety constraints. The proposed method provides a novel solution to safe control of HRC with environmental uncertainties, flexible control structures, and hard safety requirements. The main results of this chapter are based on the work in [306].

5.1 Overview

Precise tracking control of mechatronic systems in the free space or with equality constraints has been well studied in the past several decades. However, the conventional formulations are mainly concerned with reducing the tracking errors for desired trajectories. As a result, most of the existing control methods do not ensure safety for the system when the desired trajectory violates the predefined constraints. For example, in an HRC task, the robot is required to comply with certain proximity rules or speed limitations to avoid collisions with humans. When the desired trajectory violates these requirements, additional methods should be taken to confine the robot within safe conditions. In general, this renders a control problem for Euler-Lagrangian systems with unilateral state-dependent constraints, which is not fully investigated by previous work.

5.1.1 Related Work

Different from the control problem in free space or equality constraints, control with unilateral constraints usually corresponds to a state-dependent switching scheme. Fundamental work on control of mechatronic systems with unilateral constraints is introduced in [272], where an essential switching control law design framework is constructed for measure differential equation systems. The work in [273] is among the earliest ones

to demonstrate the constrained control problems under the framework of positively invariant set. This inspires the invariance control based methods [24, 25] which has been applied to a wide range of systems, such as rollovers [274], legged robot [275], manipulators [276] and collaborative robots [277]. [274, 277]. Other popular methods for constrained control include model predictive control [26, 27] and the barrier-function-based methods [28,28–30]. From the perspective of robot motion planning or navigation, where system kinematics and a global path are concerned, this problem corresponds to trajectory modification or replanning [278–283]. For these methods, however, the safety constraints may be violated when disturbances or unmodeled dynamics exist in the system. Therefore, the robustness of the control methods with unilateral constraints is still a challenging problem.

In this work, we apply the sliding mode control method due to its excellent robustness for mechatronic systems. The super-twisting algorithm, as a second-order sliding mode controller, is popular for robot manipulators [74] benefiting the reduced chattering level. Towards a balance between the robustness and chattering, controllers with adaptive gains are proposed [284] and [285]. As a result, the robustness of the system is ensured without manually assigning the controller parameters, which greatly improves the conventional sliding mode controllers. For the safety of systems, sliding mode controllers with hard state-dependent constraints are also investigated [286, 287]. However, robust controllers with both adaptive parameters and hard-constraint compliance are still lacking.

5.1.2 Challenges

The major gap between the current control methods and safe control of HRC is the lack of robustness to system uncertainties and the adaptiveness of controller parameters. The system uncertainties, such as unmodeled dynamics or external disturbances, may cause deviations to system states and lead to constraint violations. Therefore, a safe control method for HRC systems has to ensure that the robot motions are still confined within the feasible space with the existence of uncertainties. Besides, the determination of controller parameters is usually a challenging and tedious work for practical systems, and an adaptive parameter tuning law is always preferred to enhance the flexibility of the control method. Thus, the main challenge in this work is to provide a theoretical framework for robust safe control of HRC satisfying the following three essential requirements against system uncertainties: task execution (trajectory tracking precision), safety (violation avoidance of predefined constraints), and adaptiveness (adaptive parameter tuning).

To overcome this challenge, we apply a second-order sliding mode control method. In the conventional invariant-set based methods [274, 277], an invariant controller is designed to confine the system state within $\inf(\mathcal{S})$ by triggering a switching-law when the system attempts to cross the invariant-set boundary $\partial\mathcal{S}$. For sliding-mode-based control methods, however, switching on the boundary $\partial\mathcal{S}$ may break the sliding mode and affect the robust tracking performance of the controller. Therefore, we propose a novel sliding-mode based invariant controller by modifying the sliding mode manifold, such that the safety constraints are satisfied while the robustness is retained. Note that,

by *invariance*, we mean the controller ensures $\mathcal{S}$ to be a CPI set for the closed-loop system.

5.1.3 Contributions

The major contribution of our work is to propose a novel adaptive super-twisting-based sliding mode controller for robot manipulators with hard safety constraints. The sliding mode mechanism ensures high tracking performance of desired trajectories with bounded uncertainties. An online trajectory modification scheme confines system states within the predefined constraint set. An adaptive law is designed to automatically tune the controller parameters. The global convergence of tracking errors to zero is proven by a Lyapunov method. In general, our method provides a safe, efficient, robust, and flexible solution to HRC safe control.

5.1.4 Outline of the Chapter

The chapter is organized as follows. Sec. 5.2 formulates the problem to be investigated. The adaptive super-twisting-based tracking controller is presented in Sec. 5.3, and improved in Sec. 5.3.2 for the constraint compliance. In Sec. 5.5, the proposed method is validated by the simulation on a three-Degree-of-freedom (DoF) robot manipulator. Finally, Sec. 5.6 summarizes our work in this chapter.

5.2 Problem Formulation

The dynamic model of an n-DoF Euler-Lagrangian system is formed as (3.1). The nominal task of the manipulator is to ensure the precise tracking of a desired trajectory $\boldsymbol{q}_{\mathrm{d}}(t)$, $\dot{\boldsymbol{q}}_{\mathrm{d}}(t)$, $\ddot{\boldsymbol{q}}_{\mathrm{d}}(t) \in \mathbb{R}^n$, such that the tracking errors $\boldsymbol{e}_{\mathrm{d}}(t) = \boldsymbol{q}(t) - \boldsymbol{q}_{\mathrm{d}}(t)$ converge to zeros. In this chapter, we consider a scenario where the system state is strictly confined within a feasible set rendered by several unilateral constraints, to avoid potential human-robot collisions. When the desired trajectory $\boldsymbol{q}_{\mathrm{d}}(t)$ is within the feasible set, the nominal tracking task is accomplished. On the contrary, when $\boldsymbol{q}_{\mathrm{d}}(t)$ violates the constraints, a modified desired trajectory is provided such that the system state is kept within the constrained set. Note that these requirements should be satisfied with the existence of external disturbances $\boldsymbol{\tau}_{\mathrm{d}}$ (See Sec. 3.2.1) and the unmodeled dynamics (See Sec. 3.3.5).

5.2.1 Safe Control

To ensure safety, the system is confined by a set of hard kinematic constraints which are depicted by state-dependent inequalities $h_i(\boldsymbol{q}, \dot{\boldsymbol{q}}) \leq 0$, $i = 1, 2, \cdots, p$, where $h_i : \mathbb{R}^n \times \mathbb{R}^n \to \mathbb{R}$ are sufficiently smooth functions and p is the number of the inequality constraints. The set of the system state in which all the constraints are complied with is referred to as the *admissible set* $\mathcal{H} \subseteq \mathbb{R}^n \times \mathbb{R}^n$,

$$\mathcal{H} = \{(\boldsymbol{q}, \dot{\boldsymbol{q}}) | h_i(\boldsymbol{q}, \dot{\boldsymbol{q}}) \leq 0, \forall\, i = 1, 2, \cdots, p\}\,, \tag{5.1}$$

and the system state $(\boldsymbol{q}, \dot{\boldsymbol{q}}) \in \mathcal{H}$ is called an *admissible state*. Therefore, the system state $(\boldsymbol{q}(t), \dot{\boldsymbol{q}}(t))$ should be guaranteed admissible for all $t > 0$, by which we formulate the following constrained control problem for system (3.1).

Problem 2. *For system (3.1), design a state-feedback controller $\boldsymbol{\tau}_{\mathrm{c}}(\boldsymbol{q}, \dot{\boldsymbol{q}})$, such that the following conditions hold for any initial condition $(\boldsymbol{q}(0), \dot{\boldsymbol{q}}(0)) \in \mathcal{H}$ and bounded disturbance $\boldsymbol{\tau}_{\mathrm{d}}(t)$.*

(a). The system state is confined by $(\boldsymbol{q}(t), \dot{\boldsymbol{q}}(t)) \in \mathcal{H}$, $\forall\, t > 0$.

(b). The tracking error $\boldsymbol{e}_{\mathrm{d}}(t)$ converges to zero, if (a) holds.

5.2.2 Invariant Set

In this work, the *invariant-set* theory is used to integrate the unilateral constraints to the sliding mode control framework. Here, we give a brief interpretation of the invariant-set theory.

Definition 1. *(adapted from [273]): The set $\mathcal{S} \subseteq \mathbb{R}^n \times \mathbb{R}^n$ is said controlled positively invariant (CPI) for system (3.1), if there exists a continuous feedback control law $\boldsymbol{u}(\boldsymbol{q}, \dot{\boldsymbol{q}})$, such that for any initial condition $(\boldsymbol{q}(0),\, \dot{\boldsymbol{q}}(0)) \in \mathcal{S}$, $(\boldsymbol{q}(t),\, \dot{\boldsymbol{q}}(t)) \in \mathcal{S}$ holds for all $t > 0$.*

The CPI-set is an important concept for control problems with state-dependent inequality constraints. The admissible-state set in (5.1) is not violated for all $t > 0$, if there exists a CPI set $\mathcal{S} \subseteq \mathcal{H}$, where $(\boldsymbol{q}(0), \dot{\boldsymbol{q}}(0)) \in \mathcal{S}$. Therefore, the target of Problem 1-(a) is to define a subset $\mathcal{S}$ of the admissible state set $\mathcal{H}$ and seek for a corresponding feedback control law $\boldsymbol{u}(\boldsymbol{q}, \dot{\boldsymbol{q}})$, such that $\mathcal{S}$ is a CPI set. For $\mathcal{S}$, we assume that the following conditions hold.

Assumption 4. *The CPI set $\mathcal{S}$ is the convex intersection of r unilateral constraints represented by the following inequalities,*

$$s_i(\boldsymbol{q}, \dot{\boldsymbol{q}}) \leq 0,\ \ i = 1, 2, \cdots, r, \tag{5.2}$$

where $s_i \colon \mathbb{R}^n \times \mathbb{R}^n \to \mathbb{R}$ is a continuously differentiable function.

We define $\partial\mathcal{S}$ as the boundary of $\mathcal{S}$ and $\mathrm{int}(\mathcal{S})$ as the interior of $\mathcal{S}$. Under the conditions in Assumption 4, $\partial\mathcal{S}$ is continuous and piece-wisely continuously differentiable. For any system state $(\boldsymbol{q},\, \dot{\boldsymbol{q}}) \in \partial\mathcal{S}$, there exists at least one i, $1 \leq i \leq r$, such that

$$s_i(\boldsymbol{q}, \dot{\boldsymbol{q}}) = 0,\ \ 1 \leq i \leq r. \tag{5.3}$$

Although the CPI set $\mathcal{S}$ can be selected the same as $\mathcal{H}$, the boundary of $\mathcal{H}$ is not necessarily piece-wise continuously differentiable. Therefore, $\mathcal{S}$ is usually determined as a conservative subset of the admissible-state set $\mathcal{H}$.

5.2.3 Admissible Trajectory

Based on the invariant-set theory, we define the *admissible trajectory* for the CPI set $\mathcal{S}$ which is the basis of our safe control method.

Definition 2. *For a continuous function $\boldsymbol{q}(t)$, if there exist $t_0 > 0$, such that $(\boldsymbol{q}(t_0), \dot{\boldsymbol{q}}(t_0)) \in \partial\mathcal{S}$, and its right-hand derivatives $\dot{\boldsymbol{q}}(t_0^+)$ and $\ddot{\boldsymbol{q}}(t_0^+)$ exist, then $\boldsymbol{q}(t)$ is an admissible trajectory, if for all $i = 1, 2, \cdots, r$,*

$$\dot{s}_i(t_0^+) = \frac{\partial s_i}{\partial \boldsymbol{q}^\top}\dot{\boldsymbol{q}}(t_0^+) + \frac{\partial s_i}{\partial \dot{\boldsymbol{q}}^\top}\ddot{\boldsymbol{q}}(t_0^+) \leq 0, \text{ if } s_i(t_0) = 0. \tag{5.4}$$

The set of all admissible trajectories for t_0 is represented as $\mathcal{Q}_0$.

Remark 6. *An admissible trajectory $\boldsymbol{q}(t)$ moves along the direction to which the functions $s_i(\boldsymbol{q}(t), \dot{\boldsymbol{q}}(t))$ decrease for all active constraints, in the right neighborhood of t_0, $[t_0, t_0 + \Delta t)$, where $\Delta t > \mathbb{R}^+$ is a sufficiently small interval, such that the system shows a tendency to move into* $\mathrm{int}(\mathcal{S})$.

From the definition of the sliding mode variable $\boldsymbol{\sigma}(t)$ in (5.8), we have

$$\boldsymbol{\sigma}(t) = (\boldsymbol{q}(t) + c\dot{\boldsymbol{q}}(t)) - (\boldsymbol{q}_\mathrm{d}(t) + c\dot{\boldsymbol{q}}_\mathrm{d}(t)),$$

and precise tracking of $\boldsymbol{q}_\mathrm{d}(t)$ is achieved by forcing $\boldsymbol{\sigma}(t)$ to zero. Therefore, constraints $(\boldsymbol{q}, \dot{\boldsymbol{q}}) \in \mathcal{S}$ are violated if the desired trajectory $\boldsymbol{q}_\mathrm{d}(t) \notin \mathcal{Q}_0$. This problem can be solved by seeking for a modified reference trajectory $\boldsymbol{q}_\mathrm{r}(t)$, such that $\boldsymbol{q}_\mathrm{r}(t) \in \mathcal{Q}_0$. The robustness of the tracking controller ensures $\boldsymbol{q}(t)$ to converge to $\boldsymbol{q}_\mathrm{r}(t)$ within a finite time and thus also becomes admissible. Note that such admissible trajectory solutions are not unique, since (5.4) is confined by inequalities instead of equations. Nevertheless, it is straightforward to select a $\boldsymbol{q}_\mathrm{r}(t)$ that is closest to the original desired trajectory $\boldsymbol{q}_\mathrm{d}(t)$. Based on this idea, we formulate a specified equivalent of Problem 2-(a).

Problem 3. *For a piece-wise continuously differential function $\boldsymbol{q}_\mathrm{d}(t)$, if there exists $t_0 > 0$, such that $(\boldsymbol{q}_\mathrm{d}(t_0), \dot{\boldsymbol{q}}_\mathrm{d}(t_0)) \in \partial\mathcal{S}$ and $\boldsymbol{q}_\mathrm{d}(t) \notin \mathcal{Q}_0$, solve the following minimization problem,*

$$\min_{t \in [t_0, t_0 + \Delta t)} \|\boldsymbol{q}_\mathrm{r}(t) - \boldsymbol{q}_\mathrm{d}(t)\|, \text{ s.t. } \boldsymbol{q}_\mathrm{r}(t_0) = \boldsymbol{q}_\mathrm{d}(t_0), \tag{5.5a}$$

$$\dot{s}_i(t_0^+) \leq 0, \text{ if } s_i(t_0) = 0, \ 1 \leq i \leq r. \tag{5.5b}$$

Remark 7. *In Problem 3, (5.5a) aims to find the closest solution of an admissible trajectory $\boldsymbol{q}_\mathrm{r}(t)$ to the original inadmissible trajectory $\boldsymbol{q}_\mathrm{d}(t)$. The terminal condition confines that the system trajectory $\boldsymbol{q}(t)$ is continuous. The constraints in (5.5b) require that $\boldsymbol{q}_\mathrm{r}(t)$ is admissible, corresponding to the condition (5.4).*

5.3 Adaptive Robust Tracking Control

In this section, we present the super-twisting-based robust tracking controller with adaptive gains for Problem 3-(b) without considering the unilateral constraints. The stability of the tracking error dynamics is proven by a direct Lyapunov method. The integration of safety concerns will be discussed in Sec. 5.4.

5.3.1 Robust Controller for Mechatronic Systems

For robust tracking control of system (3.1) with desired trajectory $\boldsymbol{q}_{\mathrm{d}}(t)$, we design the following controller,

$$\boldsymbol{\tau} = \hat{\boldsymbol{M}}(\boldsymbol{q})(\ddot{\boldsymbol{q}}_{\mathrm{d}} - c\dot{\boldsymbol{e}} + \boldsymbol{u}) + \hat{\boldsymbol{C}}(\boldsymbol{q}, \dot{\boldsymbol{q}})\dot{\boldsymbol{q}} + \hat{\boldsymbol{G}}(\boldsymbol{q}) + \hat{\boldsymbol{F}}(\dot{\boldsymbol{q}}), \tag{5.6}$$

where $\hat{\boldsymbol{M}}(\boldsymbol{q})$, $\hat{\boldsymbol{C}}(\boldsymbol{q}, \dot{\boldsymbol{q}})$, $\hat{\boldsymbol{G}}(\boldsymbol{q})$ and $\hat{\boldsymbol{F}}(\dot{\boldsymbol{q}})$ are the identified system parameters, $c \in \mathbb{R}^+$ is a convergence coefficient to be determined and $\boldsymbol{u}(t) \in \mathbb{R}^n$ is a second-order sliding mode controller in the form of

$$\boldsymbol{u}(t) = -\boldsymbol{A}|\boldsymbol{\sigma}(t)|^{\frac{1}{2}}\mathrm{sgn}(\boldsymbol{\sigma}(t)) - \boldsymbol{\Gamma}\int \mathrm{sgn}(\boldsymbol{\sigma}(t))\mathrm{d}t, \tag{5.7}$$

where $\boldsymbol{A} = \mathrm{diag}(\alpha_1, \alpha_2, \cdots, \alpha_n)$ and $\boldsymbol{\Gamma} = \mathrm{diag}(\gamma_1, \gamma_2, \cdots, \gamma_n)$ are gain parameters to be determined, $\boldsymbol{\sigma}(t) \in \mathbb{R}^n$ is the sliding mode variable defined as

$$\boldsymbol{\sigma}(t) = \dot{\boldsymbol{e}}(t) + c\boldsymbol{e}(t), \tag{5.8}$$

where $\boldsymbol{e}(t) = \boldsymbol{q}(t) - \boldsymbol{q}_{\mathrm{d}}(t)$ is the trajectory tracking error, and $\mathrm{sgn}(\cdot)$ is the element-wisely defined sign function. Note that the operator $|\cdot|^{\frac{1}{2}}\mathrm{sgn}(\cdot) : \mathbb{R}^n \to \mathbb{R}^n$ is also defined in an element-wise manner, i.e.,

$$\Big(|\boldsymbol{\sigma}|^{\frac{1}{2}}\mathrm{sgn}(\boldsymbol{\sigma})\Big)_i = |\sigma_i|^{\frac{1}{2}}\mathrm{sgn}(\sigma_i),\ \forall \boldsymbol{\sigma} \in \mathbb{R}^n,$$

where $(\cdot)_i$ denotes the i-th element of a vector. Substituting (5.6) and (5.7) to the system model (3.1), we obtain

$$\ddot{\boldsymbol{q}} = \boldsymbol{M}^{-1}\hat{\boldsymbol{M}}(\ddot{\boldsymbol{q}}_{\mathrm{d}} - c\dot{\boldsymbol{e}} + \boldsymbol{u}) + \boldsymbol{M}^{-1}\Big(\boldsymbol{\tau}_{\mathrm{d}} - \tilde{\boldsymbol{C}}\dot{\boldsymbol{q}} - \tilde{\boldsymbol{G}} - \tilde{\boldsymbol{F}}\Big), \tag{5.9}$$

where $\tilde{\boldsymbol{M}}(\boldsymbol{q}) = \boldsymbol{M}(\boldsymbol{q}) - \hat{\boldsymbol{M}}(\boldsymbol{q})$, $\tilde{\boldsymbol{C}}(\boldsymbol{q}, \dot{\boldsymbol{q}}) = \boldsymbol{C}(\boldsymbol{q}, \dot{\boldsymbol{q}}) - \hat{\boldsymbol{C}}(\boldsymbol{q}, \dot{\boldsymbol{q}})$, $\tilde{\boldsymbol{G}}(\boldsymbol{q}) = \boldsymbol{G}(\boldsymbol{q}) - \hat{\boldsymbol{G}}(\boldsymbol{q})$ and $\tilde{\boldsymbol{F}}(\dot{\boldsymbol{q}}) = \boldsymbol{F}(\dot{\boldsymbol{q}}) - \hat{\boldsymbol{F}}(\dot{\boldsymbol{q}})$ are the unmodeled dynamics. Then, we take the time derivative of the sliding function $\boldsymbol{\sigma}(t)$ in (5.8) and obtain

$$\dot{\boldsymbol{\sigma}}(t) = \boldsymbol{u}(t) - \boldsymbol{\eta}_c(t), \tag{5.10}$$

where $\boldsymbol{\eta}_c = \hat{\boldsymbol{M}}^{-1}(\tilde{\boldsymbol{M}}\ddot{\boldsymbol{q}} + \tilde{\boldsymbol{C}}\dot{\boldsymbol{q}} + \tilde{\boldsymbol{G}} + \tilde{\boldsymbol{F}} - \boldsymbol{\tau}_{\mathrm{d}})$ is the system uncertainty term including the unmodeled dynamics and the external disturbances. For the system uncertainties, we propose the following assumption.

Assumption 5. *The time derivative of $\boldsymbol{\eta}_c(t)$ is bounded, i.e., $\|\boldsymbol{\eta}_c(t)\| \leq \bar{\eta}_c$, $\exists\ \bar{\eta}_c \in \mathbb{R}^+$.*

Note that the boundedness of the system uncertainties is a basic assumption popularly used in related works, such as [288, 289].

5.3.2 Adaptive Super-twisting Algorithm

Deriving from (5.10), the dynamics of sliding function $\boldsymbol{\sigma}(t)$ in each dimension reads $\dot{\sigma}_i(t) = u_i(t) - \eta_i(t)$, $i = 1, 2, \cdots, n.$, where u_i and η_i are respectively the i-th element of $\boldsymbol{u}$ and $\boldsymbol{\eta}_c$. Substituting (5.7) to it, we have

$$\dot{\sigma}_i = -\alpha_i |\sigma_i|^{\frac{1}{2}} \mathrm{sgn}(\sigma_i) - \gamma_i \int \mathrm{sgn}(\sigma_i) \mathrm{d}t - \eta_i. \tag{5.11}$$

Although the determination of the parameters α_i and γ_i are theoretically provided by the existing framework [286, 289], selecting a proper integral coefficient γ_i, is a challenging work in practical applications. In this chapter, we propose an adaptive tuning law for γ_i which is given by the following theorem.

Theorem 3. *For the dynamics of $\sigma_i(t)$ in (5.11), $i = 1, 2, \cdots, r$, if Assumption 5 is ensured and $\alpha_i > 0$, then $\sigma_i(t)$ asymptotically converges to zero within a finite time $t_c < \infty$, with the following adaptive tuning law,*

$$\dot{\gamma}_i = \varrho_i \, \mathrm{sgn}(\sigma_i) \int \mathrm{sgn}(\sigma_i) \mathrm{d}t, \tag{5.12}$$

where $\varrho_i > 2\bar{\gamma}_i - \alpha_i^2/2$, with $\bar{\gamma}_i \in \mathbb{R}^+$ being a scalar such that

$$\frac{\alpha_i^3}{\epsilon(\bar{\gamma}_i) + \sqrt{2\epsilon(\bar{\gamma}_i)^2 + 4\alpha_i^2}} + \bar{\eta}_c \sqrt{\alpha_i^2 + 1} = \frac{\alpha_i}{2}, \tag{5.13}$$

where $\epsilon(\bar{\gamma}_i)$ is defined as

$$\epsilon(\bar{\gamma}_i) = 2\bar{\gamma}_i + \alpha_i^2 - 1. \tag{5.14}$$

Proof. Let us assume that $\gamma_i^* > 0$ is an ideal parameter selection of γ_i, such that the dynamics of $\sigma_i(t)$ in (5.11) is stable if $\gamma_i = \gamma_i^*$. Therefore, the sliding dynamics in (5.11) can be represented as

$$\dot{\sigma}_i = -\alpha_i |\sigma_i|^{\frac{1}{2}} \mathrm{sgn}(\sigma_i) - (\tilde{\gamma}_i + \gamma_i^*) \int \mathrm{sgn}(\sigma_i) \mathrm{d}t - \eta_i, \tag{5.15}$$

where $\tilde{\gamma}_i = \gamma_i - \gamma_i^*$ denotes the error of the parameter tuning. By defining an auxiliary variable

$$\varepsilon_i = -\gamma_i^* \int \mathrm{sgn}(\sigma_i) \mathrm{d}t - \eta_i, \tag{5.16}$$

we formulate the closed-loop dynamics in (5.15) as follows,

$$\begin{aligned} \dot{\sigma}_i &= -\alpha_i |\sigma_i|^{\frac{1}{2}} \mathrm{sgn}(\sigma_i) - \tilde{\gamma}_i \int \mathrm{sgn}(\sigma_i) \mathrm{d}t + \varepsilon_i, \\ \dot{\varepsilon}_i &= -\gamma_i^* \mathrm{sgn}(\sigma_i) - \dot{\eta}_i. \end{aligned} \tag{5.17}$$

Note that similar techniques are also used in [290] and [289]. Let us define $z_2^i = |\sigma_i|^{\frac{1}{2}}\mathrm{sgn}(\sigma_i)$, $z_1^i = \varepsilon_i$ and represent (5.17) as $\dot{z}_1^i = \frac{1}{2}|\sigma_i|^{-\frac{1}{2}}\dot{\sigma}_i$, $\dot{z}_2^i = \dot{\varepsilon}_i$, which then leads to

$$\begin{aligned}\dot{z}_1^i &= |\sigma_i|^{-\frac{1}{2}}\left(-\frac{\alpha_i}{2}|\sigma_i|^{\frac{1}{2}}\mathrm{sgn}(\sigma_i) - \frac{\tilde{\gamma}_i}{2}\int \mathrm{sgn}(\sigma_i)\mathrm{d}t + \frac{z_2^i}{2}\right),\\ \dot{z}_2^i &= -\gamma_i^*\mathrm{sgn}(\sigma_i) - \dot{\eta}_i.\end{aligned}$$

Substituting the functions of σ_i with z_1^i and z_2^i, we obtain

$$\begin{aligned}\dot{z}_1^i &= -\frac{\alpha_i}{2}|\sigma_i|^{-\frac{1}{2}}z_1^i + \frac{1}{2}|\sigma_i|^{-\frac{1}{2}}z_2^i - \frac{\tilde{\gamma}_i}{2}|\sigma_i|^{-\frac{1}{2}}\int \mathrm{sgn}(\sigma_i)\mathrm{d}t,\\ \dot{z}_2^i &= -\gamma_i^*|\sigma_i|^{-\frac{1}{2}}z_1^i - \dot{\eta}_i,\end{aligned}$$

and further we have

$$\dot{\boldsymbol{z}}_i = -|\sigma_i|^{-\frac{1}{2}}\boldsymbol{\Lambda}_i\boldsymbol{z}_i - \boldsymbol{\zeta}_i(\sigma_i)\tilde{\gamma}_i - \dot{\boldsymbol{\eta}}_i, \tag{5.18}$$

where $\boldsymbol{z}_i = \begin{bmatrix} z_1^i & z_2^i \end{bmatrix}^\top$, $\boldsymbol{\zeta}_i(\sigma_i) = \begin{bmatrix} \zeta_i(\sigma_i) & 0 \end{bmatrix}^\top$, $\boldsymbol{\eta}_i = \begin{bmatrix} 0 & \eta_i \end{bmatrix}^\top$, $\boldsymbol{\Lambda}_i = \begin{bmatrix} \frac{\alpha_i}{2} & -\frac{1}{2} \\ \gamma_i^* & 0 \end{bmatrix}$, and $\zeta_i(\sigma_i)$ $= \frac{1}{2}|\sigma_i|^{-\frac{1}{2}}\int \mathrm{sgn}(\sigma_i)\mathrm{d}t$. To investigate the stability of $\boldsymbol{z}_i$ at the zero equilibrium, we define the following Lyapunov function

$$V_i = \frac{1}{2}\boldsymbol{z}_i^\top\boldsymbol{P}_i\boldsymbol{z}_i + \frac{1}{2}\tilde{\gamma}_i^2,\ \boldsymbol{P}_i = \begin{bmatrix} 2\gamma_i^* + \frac{1}{2}\alpha_i^2 & -\frac{1}{2}\alpha_i \\ -\frac{1}{2}\alpha_i & 1 \end{bmatrix} \tag{5.19}$$

where $\boldsymbol{P}_i$ is a positive definite matrix. Taking the derivative of V_i, we have $\dot{V}_i = \boldsymbol{z}_i\boldsymbol{P}_i\dot{\boldsymbol{z}}_i + \tilde{\gamma}_i\dot{\gamma}_i$. Substituting $\dot{\boldsymbol{z}}_i$ in (5.18) and $\dot{\gamma}_i$ in (5.12) to it, we obtain

$$\begin{aligned}\dot{V}_i =& -\frac{1}{2}|\sigma_i|^{-\frac{1}{2}}\boldsymbol{z}_i^\top\boldsymbol{Q}_i\boldsymbol{z}_i - \boldsymbol{z}_i^\top\boldsymbol{P}_i\dot{\boldsymbol{\eta}}_i - \boldsymbol{z}_i^\top\boldsymbol{P}_i\boldsymbol{\zeta}_i(\sigma_i)\tilde{\gamma}_i + \tilde{\gamma}_i\varrho_i\mathrm{sgn}(\sigma_i)\int \mathrm{sgn}(\sigma_i)\mathrm{d}t\\ =& -\frac{1}{2}|\sigma_i|^{-\frac{1}{2}}\boldsymbol{z}_i^\top\boldsymbol{Q}\boldsymbol{z}_i - \boldsymbol{z}_i^\top\boldsymbol{P}_i\dot{\boldsymbol{\eta}}_i + \frac{\alpha_i}{2}\varepsilon_i\tilde{\gamma}_i\zeta_i(\sigma_i) + \left(\varrho_i - 2\gamma_i^* - \frac{1}{2}\alpha_i^2\right)\tilde{\gamma}_i\\ &\times \mathrm{sgn}(\sigma_i)\int \mathrm{sgn}(\sigma_i)\mathrm{d}t,\end{aligned} \tag{5.20}$$

where

$$\boldsymbol{Q}_i = \boldsymbol{P}_i\boldsymbol{\Lambda}_i + \boldsymbol{\Lambda}_i^\top\boldsymbol{P} = \frac{1}{2}\alpha_i\begin{bmatrix} 2\gamma_i^* + \alpha_i^2 & -\alpha_i \\ -\alpha_i & 1 \end{bmatrix}.$$

Therefore, the eigenvalues of $\boldsymbol{Q}_i$, $\lambda_1(\boldsymbol{Q}_i)$ and $\lambda_2(\boldsymbol{Q}_i)$, satisfy that $\lambda_1(\boldsymbol{Q}_i) + \lambda_2(\boldsymbol{Q}_i) = \alpha_i\gamma_i^* + \frac{1}{2}\alpha_i^3 + \frac{1}{2}\alpha_i$, $\lambda_1(\boldsymbol{Q}_i)\lambda_2(\boldsymbol{Q}_i) = \frac{1}{2}\alpha_i^2\gamma_i^*$, which indicates that $\boldsymbol{Q}_i$ is positive definite if $\alpha_i, \gamma_i^* > 0$ holds. Meanwhile, since γ_i^* is an ideal parameter selection, (5.16) denotes an ideal sliding mode and we have $\varepsilon_i = 0$ in the sense of Filippov. Substituting $\varepsilon_i = 0$ to (5.20), we obtain

$$\begin{aligned}\dot{V}_i \leq& -\frac{1}{2}|\sigma_i|^{-\frac{1}{2}}\lambda_{\min}(\boldsymbol{Q}_i)\|\boldsymbol{z}_i\|^2 + \|\boldsymbol{z}_i\|\|\boldsymbol{P}_i\dot{\boldsymbol{\eta}}_i\|\\ &+ \left(\varrho_i - 2\gamma_i^* - \frac{1}{2}\alpha_i^2\right)\tilde{\gamma}_i\mathrm{sgn}(\sigma_i)\int \mathrm{sgn}(\sigma_i)\mathrm{d}t,\end{aligned} \tag{5.21}$$

where $\|\boldsymbol{P}_i\dot{\boldsymbol{\eta}}_i\| = \left\|[\,-\alpha_i/2\ 1\,]^\top\dot{\eta}_i\right\| \leq \bar{\eta}_c\sqrt{\alpha_i^2/4+1}$ and $\lambda_{\min}(\boldsymbol{Q}_i)$ is the minimal eigenvalue of $\boldsymbol{Q}_i$,

$$\lambda_{\min}(\boldsymbol{Q}_i) = \min(\lambda_1(\boldsymbol{Q}_i), \lambda_2(\boldsymbol{Q}_i)) = \frac{\alpha_i}{2}\left(1 - \frac{\alpha_i^2}{\epsilon(\gamma_i^*) + \sqrt{2\epsilon(\gamma_i^*)^2 + 4\alpha_i^2}}\right),$$

where the scalar function $\epsilon(\cdot)$ is defined as in (5.14). Note that $\lambda_{\min}(\boldsymbol{Q}_i)$ is a function of γ_i^* for given α_i. Therefore, we represent $\lambda_{\min}(\boldsymbol{Q}_i)$ as $\bar{\lambda}(\gamma_i^*)$. Considering $|\sigma_i|^{\frac{1}{2}} = |z_1^i| \leq \|\boldsymbol{z}^i\|$, we have $-|\sigma_i|^{-\frac{1}{2}} \leq -\|\boldsymbol{z}_i\|^{-1}$, which leads (5.21) to

$$\begin{aligned}\dot{V}_i \leq& -\frac{1}{2}\bar{\lambda}(\gamma_i^*)\|\boldsymbol{z}_i\| + \|\boldsymbol{z}_i\|\|\boldsymbol{P}_i\dot{\boldsymbol{\eta}}_i\| + \left(\varrho_i - 2\gamma_i^* - \frac{1}{2}\alpha_i^2\right)\tilde{\gamma}_i\,\mathrm{sgn}(\sigma_i)\int\mathrm{sgn}(\sigma_i)\mathrm{d}t \\ =& -\frac{1}{2}\|\boldsymbol{z}_i\|\left(\bar{\lambda}(\gamma_i^*) - \bar{\eta}_c\sqrt{\alpha_i^2+4}\right) + \left(\varrho_i - 2\gamma_i^* - \frac{1}{2}\alpha_i^2\right)\tilde{\gamma}_i\,\mathrm{sgn}(\sigma_i)\int\mathrm{sgn}(\sigma_i)\mathrm{d}t.\end{aligned} \tag{5.22}$$

Note that (5.22) also holds in the Filippov sense. From (5.13), it is known that $\bar{\gamma}_i$ satisfies $\bar{\lambda}(\bar{\gamma}_i) - \bar{\eta}_c\sqrt{\alpha_i^2+4} = 0$, and for any $\gamma_i^* > \bar{\gamma}_i$, we have

$$\bar{\lambda}(\gamma_i^*) - \bar{\eta}_c\sqrt{\alpha_i^2+4} > 0. \tag{5.23}$$

Note that for any $\varrho_i > 2\gamma_i^* - \alpha_i^2/2$, there exists $\gamma_i^* > \bar{\gamma}_i$, such that (5.23) and $\varrho_i - 2\gamma_i^* - \frac{1}{2}\alpha_i^2 = 0$ holds, which leads to

$$\dot{V}_i \leq -\frac{1}{2}\|\boldsymbol{z}_i\|\left(\bar{\lambda}(\gamma_i^*) - \bar{\eta}_c\sqrt{\alpha_i^2+4}\right) < 0.$$

Therefore, $\boldsymbol{z}_i$ converges to zero and γ_i converges to γ_i^* asymptotically. It is worth mentioning that such an ideal value γ_i^* is not unique but belongs to a half-closed set $\gamma_i^* > \bar{\gamma}_i$. Therefore, γ_i will finally reaches an ideal value γ_i^*, such that $\tilde{\gamma}_i = 0$ holds. In this sense, from (5.19), we obtain $V_i = \boldsymbol{z}_i^\top\boldsymbol{P}_i\boldsymbol{z}_i/2$, which leads to $\|\boldsymbol{z}_i\| \geq \sqrt{2V_i/\lambda_{\max}(\boldsymbol{P}_i)}$, where $\lambda_{\max}(\boldsymbol{P}_i)$ is the minimum eigenvalue of $\boldsymbol{P}_i$. For any positive scalar $\beta_i \in \mathbb{R}^+$ satisfying $\bar{\lambda}(\gamma_i^*) - \bar{\eta}_c\sqrt{\alpha_i^2+4} > \beta_i$, we have

$$\dot{V}_i \leq -\beta_i\sqrt{V_i/2\lambda_{\max}(\boldsymbol{P}_i)}. \tag{5.24}$$

According to the finite-time convergence property of sliding mode [56], (5.24) indicates that the convergence of $\boldsymbol{z}_i$ is within a finite time

$$t_c = \frac{2}{\beta_i}\sqrt{\lambda_{\max}(\boldsymbol{P}_i)\boldsymbol{z}_{i,0}^\top\boldsymbol{P}_i\boldsymbol{z}_{i,0}} = \frac{2}{\beta}\lambda_{\max}(\boldsymbol{P}_i)\|\boldsymbol{z}_{i,0}\|,$$

where $\boldsymbol{z}_{i,0}$ is the initial value of $\boldsymbol{z}_i$ when γ_i reaches γ_i^*. According to the definition of $\boldsymbol{z}_i$, $\boldsymbol{\sigma}_i(t)$ and $\dot{\boldsymbol{\sigma}}_i(t)$ also converge to zeros within finite time t_c. □

Remark 8. *Theorem 3 indicates that $\boldsymbol{\sigma}_i(t)$, $\dot{\boldsymbol{\sigma}}_i(t)$ converge to zero within a finite time for all $i = 1, 2, \cdots, n$, which ensures that the tracking error $\boldsymbol{e}(t)$ asymptotically converge to zero. Therefore, the controller (5.6) designed for system (3.1) guarantees robust trajectory tracking for the system uncertainty $\boldsymbol{\eta}_c(t)$.*

It is noticed that the update of $\boldsymbol{\gamma}$ in (5.12) involves twice-integration which may produce an over-large control gain $\boldsymbol{\gamma}$, which leads chattering to the control input $\boldsymbol{u}(t)$. To avoid this, we modify the tuning law in (5.12) as follows

$$\dot{\gamma}_i = \begin{cases} \varrho_i \operatorname{sgn}(\sigma_i) \int \operatorname{sgn}(\sigma_i) \mathrm{d}t, & \|\boldsymbol{\sigma}\| \geq \sigma_0, \\ -\kappa \gamma_i, & \|\boldsymbol{\sigma}\| < \sigma_0, \end{cases} \tag{5.25}$$

where $\kappa > 0$ is a decaying factor for γ_i and $\sigma_0 > 0$ is a boundary layer scalar for $\boldsymbol{\sigma}(t)$. Therefore, the self-tuning of γ_i is only activated when $\boldsymbol{\sigma}(t)$ exceeds the boundary layer, and decays when $\boldsymbol{\sigma}(t)$ is within the boundary layer. As a result, the unlimited growing of γ_i is avoided, and $\boldsymbol{\sigma}(t)$ is confined within the boundary layer, such that the robustness of the closed-loop system is ensured without bringing up chattering.

5.4 Integration of Unilateral Constraints

In this section, we solve Problem 2-(a) by integrating the unilateral constraints $(\boldsymbol{q}(t)\ \dot{\boldsymbol{q}}(t)) \in \mathcal{H}$, $\forall\, t > 0$, in the robust tracking controller (5.6). To achieve this, we firstly solve its equivalent, Problem 3.

5.4.1 Problem Simplification

We take the Taylor expansion of $\boldsymbol{q}_{\mathrm{r}}(t)$ and $\boldsymbol{q}_{\mathrm{d}}(t)$ in the neighborhood of t_0, and (5.5a) is equivalent to

$$\min_{\boldsymbol{q}_{\mathrm{r}} \in \mathcal{Q}_0} \lim_{\Delta t \to 0} \sum_{i=0}^{\infty} \frac{(\Delta t)^i}{i!} \left\| \boldsymbol{q}_{\mathrm{r}}^{(i)}(t_0^+) - \boldsymbol{q}_{\mathrm{d}}^{(i)}(t_0^+) \right\|, \tag{5.26}$$

where $(\cdot)^{(i)}$ is the i-th order derivative of $(\cdot)$. Since the higher-order derivatives of $\boldsymbol{q}_{\mathrm{r}}(t)$ for $i > 2$ do not show up in the formulation (5.5), they can be neglected. Then, the formulated problem in (5.5a) is simplified as

$$\min_{\boldsymbol{q}_{\mathrm{r}}^{(i)}(t_0) \in \mathbb{R}^n} \left\| \boldsymbol{q}_{\mathrm{r}}^{(i)}(t_0) - \boldsymbol{q}_{\mathrm{d}}^{(i)}(t_0) \right\|^2, \ \forall\, i = 0, 1, 2. \tag{5.27}$$

Here, we formulate (5.27) as a quadratic form. Note that solving Problem 3 only ensures that the constraints are complied with in the neighborhood $[t_0, t_0 + \Delta t)$. To guarantee safety in a continuous period of time $T \gg \Delta t$, Problem 3 should be solved for all $t \in (t_0, t_0 + T)$. Therefore, the sliding-mode-based invariance controller is similar to (5.6), with $\boldsymbol{q}_{\mathrm{d}}(t)$ substituted by $\boldsymbol{q}_{\mathrm{r}}(t)$, i.e.,

$$\boldsymbol{\tau} = \hat{\boldsymbol{M}}(\boldsymbol{q})(\ddot{\boldsymbol{q}}_{\mathrm{r}} - c\dot{\boldsymbol{e}}_{\mathrm{d}} + \boldsymbol{u}) + \hat{\boldsymbol{C}}(\boldsymbol{q}, \dot{\boldsymbol{q}})\dot{\boldsymbol{q}} + \hat{\boldsymbol{G}}(\boldsymbol{q}) + \hat{\boldsymbol{F}}(\dot{\boldsymbol{q}}) \tag{5.28}$$

which ensures asymptotic convergence of the tracking error $\boldsymbol{e}_{\mathrm{r}}(t) = \boldsymbol{q}(t) - \boldsymbol{q}_{\mathrm{r}}(t)$ to zero.

It is worth mentioning that, when a modified reference trajectory $\boldsymbol{q}_{\mathrm{r}}(t)$ is solved, the continuity of $\boldsymbol{q}_{\mathrm{r}}(t)$ is always guaranteed by the terminal conditions (5.5b), but not necessarily for $\dot{\boldsymbol{q}}_{\mathrm{r}}(t)$ and $\ddot{\boldsymbol{q}}_{\mathrm{r}}(t)$, which leads to a new transient stage to the sliding mode. Nevertheless, since $\boldsymbol{q}_{\mathrm{r}}(t)$ lies on $\partial\mathcal{S}$ and $\partial\mathcal{S}$ is piece-wisely continuously differentiable, a new sliding mode can still be achieved if the finite convergence time of the sliding mode is sufficiently small, such that the robust stability of the system is not affected. However, due to the transient stages, the constraints $(\boldsymbol{q}(t), \dot{\boldsymbol{q}}(t)) \in \mathcal{S}$ may be violated for a short period of time. Therefore, a more conservative CPI set $\mathcal{S}$ should be determined for the hard constraint set $\mathcal{H}$ to tolerate possible violations.

5.4.2 Control with Linear Holonomic Constraints

Problem 3 formulates a minimization problem (5.27) with constraints (5.5b), which usually requires numerical methods for solutions. However, analytical solutions can be obtained for linear holonomic constraints which are frequently used in practice. Consider system (3.1) with the following position-dependent holonomic constraints,

$$h_i(\boldsymbol{q}) = \boldsymbol{\omega}_i^{\top}\boldsymbol{q} + \bar{\omega}_i \leq 0,\ \forall\, 1 \leq i \leq r,$$

where $\boldsymbol{\omega}_i \in \mathbb{R}^n$ is the constant coefficient and $\bar{\omega}_i \in \mathrm{R}$ is a constant bias. We determine a CPI set $\mathcal{S}$ as follows,

$$s_i(\boldsymbol{q}) = \boldsymbol{\omega}_i^{\top}\boldsymbol{q} + \bar{\omega}_i + \delta_i^{\omega} \leq 0,\ \forall\, 1 \leq i \leq r, \tag{5.29}$$

where $\delta_i^{\omega} \geq 0$, $i = 1, 2, \cdots, r$, is the scalar for the tolerance of the constraint violation due to the transient stages. For given $t_0 > 0$, such that $(\boldsymbol{q}(t_0), \dot{\boldsymbol{q}}(t_0)) \in \partial\mathcal{S}$, there exist $1 \leq l_1 < l_2 < \cdots < l_m \leq r$, such that

$$\boldsymbol{\omega}_i^{\top}\boldsymbol{q} + \bar{\omega}_i + \delta_i^{\omega} = 0,\ \forall\, i = l_1, l_2, \cdots, l_m, \tag{5.30}$$

where m is the number of active constraints. We represent (5.30) as the following matrix form

$$\boldsymbol{s}(\boldsymbol{q}) = \boldsymbol{\Omega}^{\top}\boldsymbol{q} + \bar{\boldsymbol{\omega}} + \boldsymbol{\delta}^{\omega} = 0,$$

where $\boldsymbol{s} = [\, s_{l_1}\ s_{l_2}\ \cdots\ s_{l_m}]^{\top}$, $\boldsymbol{\Omega} = [\, \boldsymbol{\omega}_{l_1}\ \boldsymbol{\omega}_{l_2}\ \cdots\ \boldsymbol{\omega}_{l_m}]$, $\bar{\boldsymbol{\omega}} = [\, \bar{\omega}_{l_1}\ \bar{\omega}_{l_2}\ \cdots\ \bar{\omega}_{l_m}]^{\top}$ and $\boldsymbol{\delta}^{\omega} = \left[\, \delta_{l_1}^{\omega}\ \delta_{l_2}^{\omega}\ \cdots\ \delta_{l_m}^{\omega}\right]^{\top}$. Then, the solution to Problem 2 of $\boldsymbol{q}_{\mathrm{r}}(t)$ at the neighborhood $[t_0, t_0 + \Delta t)$ is

$$\boldsymbol{q}_{\mathrm{r}}(t) = \begin{cases} \boldsymbol{\Omega}_1\boldsymbol{q}_{\mathrm{d}}(t) + \bar{\boldsymbol{\omega}}_1, & \text{if } \boldsymbol{q}_{\mathrm{d}}(t) \notin \mathcal{Q}_0, \\ \boldsymbol{q}_{\mathrm{d}}(t), & \text{if } \boldsymbol{q}_{\mathrm{d}}(t) \in \mathcal{Q}_0. \end{cases} \tag{5.31}$$

where $\boldsymbol{\Omega}_1 = \boldsymbol{I}_{l_m} - \boldsymbol{\Omega}\big(\boldsymbol{\Omega}^{\top}\boldsymbol{\Omega}\big)^{-1}\boldsymbol{\Omega}^{\top}$, $\bar{\boldsymbol{\omega}} = \boldsymbol{\Omega}\big(\boldsymbol{\Omega}^{\top}\boldsymbol{\Omega}\big)^{-1}(\bar{\boldsymbol{\omega}} + \boldsymbol{\delta}^{\omega})$, and $\boldsymbol{I}_{l_m}$ is the identity matrix. It is straight forward to verify that, for $\boldsymbol{q}_{\mathrm{r}}(t)$,

$$\dot{\boldsymbol{s}}(\boldsymbol{q}_{\mathrm{r}}(t)) = \boldsymbol{\Omega}^{\top}\dot{\boldsymbol{q}}_{\mathrm{r}}(t) = 0,\ \text{if } \boldsymbol{q}_{\mathrm{d}}(t) \notin \mathcal{Q}_0, \tag{5.32}$$

which satisfies the admissible condition (5.5b). Therefore, $\boldsymbol{q}_{\mathrm{r}}(t)$ is an admissible trajectory for t_0.

It is worth mentioning that (5.32) indicates $\boldsymbol{q}_{\mathrm{r}}(t) \subseteq \partial\mathcal{S}$ for $\boldsymbol{q}_{\mathrm{d}}(t) \notin \mathcal{Q}_0$, i.e., $\boldsymbol{q}_{\mathrm{r}}(t)$ lies on the boundary of the CPI set $\mathcal{S}$ when $\boldsymbol{q}_{\mathrm{d}}(t)$ violates the constraints. Additionally, (5.31) shows that $\boldsymbol{q}_{\mathrm{r}}(t) \equiv \boldsymbol{q}_{\mathrm{d}}(t)$, if $\boldsymbol{q}_{\mathrm{d}}(t) \in \mathcal{Q}_0$. Therefore, $\boldsymbol{q}_{\mathrm{r}}(t)$ is also piece-wise continuously differentiable, which means that a new sliding mode is achievable after every switching of (5.31), if the convergence time of the sliding mode is sufficiently small. Thus, both robustly precise tracking and hard constraint compliance are guaranteed.

5.5 Simulations

In this section, we evaluate the proposed controller by a numerical simulation on a 3-DoF manipulator in MATLAB 2019a. The detailed model information of the robot can be referred to Sec. 3.4. The simulation runs from 0s to 70s at a sampling rate 1kHz, and starts at the zero initial condition $\boldsymbol{q}(0) = \dot{\boldsymbol{q}}(0) = \boldsymbol{0}$. The desired trajectory $\boldsymbol{q}_{\mathrm{d}}(t)$ for the system is designed as,

$$\boldsymbol{q}_{\mathrm{d}}(t) = \begin{cases} -2\cos\left(\frac{\pi}{8}(t-3)\right)\boldsymbol{q}_0, & \text{if } 11 < t \leq 59, \\ 0, & \text{if } t \leq 3 \text{ or } t > 67, \\ \left(1-\cos\left(\frac{\pi}{8}(t-3)\right)\right)\boldsymbol{q}_0, & \text{else}, \end{cases}$$

where $\boldsymbol{q}_0 = [\,1.5 \;\; 0.6 \;\; 0.9\,]^\top$. A tracking controller as in (5.6) and (5.7) is implemented with strict compliance with the following constraints,

$$-3 \leq s(\boldsymbol{q}(t)) \leq 3, \tag{5.33}$$

where $s(\boldsymbol{q}(t)) = q_1(t) + q_2(t) + q_3(t)$ is the invariant function, $q_1(t)$, $q_2(t)$ and $q_3(t)$ are respectively the angular positions of the three joints. We define the CPI set $\mathcal{S}$ as

$$\begin{aligned} s_1(\boldsymbol{q}) &= \boldsymbol{\omega}_1^\top \boldsymbol{q}(t) - 3 + \delta_1 \leq 0, \\ s_2(\boldsymbol{q}) &= \boldsymbol{\omega}_2^\top \boldsymbol{q}(t) - 3 + \delta_2 \leq 0, \end{aligned} \tag{5.34}$$

where $\boldsymbol{\omega}_1 = [\,1 \;\; 1 \;\; 1\,]^\top$, $\boldsymbol{\omega}_2 = [\,-1 \;\; -1 \;\; -1\,]^\top$, and $\delta_1 = \delta_2 = 0.1$ denotes the violation tolerance. The controller parameters are selected as $c = 50$, $\kappa = 0.01$, $\alpha_i = 2$, $\varrho_i = 50$, $\forall\, i = 1, 2, 3$, $\sigma_0 = 0.2$. For the CPI set $\mathcal{S}$ in (5.34), the admissible trajectory $\boldsymbol{q}_{\mathrm{r}}(t)$ is determined as

$$\boldsymbol{q}_{\mathrm{r}}(t) = \begin{cases} \boldsymbol{\Omega}_1 \boldsymbol{q}_{\mathrm{d}}(t) + \bar{\boldsymbol{\omega}}_1, & \text{if } \boldsymbol{\omega}_1^\top \boldsymbol{q}_{\mathrm{d}}(t) \geq 2.9, \\ \boldsymbol{\Omega}_2 \boldsymbol{q}_{\mathrm{d}}(t) + \bar{\boldsymbol{\omega}}_2, & \text{if } \boldsymbol{\omega}_2^\top \boldsymbol{q}_{\mathrm{d}}(t) \geq 2.9, \\ \boldsymbol{q}_{\mathrm{d}}(t), & \text{if } \boldsymbol{q}_{\mathrm{d}}(t), \dot{\boldsymbol{q}}_{\mathrm{d}}(t) \in \mathrm{int}(\mathcal{S}). \end{cases}$$

where $\boldsymbol{\Omega}_1 = \boldsymbol{\omega}_1(\boldsymbol{\omega}_1^\top\boldsymbol{\omega}_1)^{-1}\boldsymbol{\omega}_1^\top + \boldsymbol{I}$, $\boldsymbol{\Omega}_2 = \boldsymbol{\omega}_2(\boldsymbol{\omega}_2^\top\boldsymbol{\omega}_2)^{-1}\boldsymbol{\omega}_2^\top + \boldsymbol{I}$, $\bar{\boldsymbol{\omega}}_1 = -2.9 + \boldsymbol{\omega}_1(\boldsymbol{\omega}_1^\top\boldsymbol{\omega}_1)^{-1}$, and $\bar{\boldsymbol{\omega}}_2 = -2.9 + \boldsymbol{\omega}_2(\boldsymbol{\omega}_2^\top\boldsymbol{\omega}_2)^{-1}$.

The reference trajectory $\boldsymbol{q}_{\mathrm{r}}(t)$ on the three robot joints is shown in Fig. 5.1 and is compared with the original desired trajectory $\boldsymbol{q}_{\mathrm{d}}(t)$. It is noticed that $\boldsymbol{q}_{\mathrm{r}}(t)$ deviates from $\boldsymbol{q}_{\mathrm{d}}(t)$ when $\boldsymbol{q}_{\mathrm{d}}(t)$ violates the constraint (gray area). Fig. 5.2 clearly shows that the system trajectory $\boldsymbol{q}(t)$ is confined within the constraints (5.33), even though the

desired trajectory $\boldsymbol{q}_{\mathrm{d}}(t)$ exceeds the constraints. The trajectory tracking error $\boldsymbol{e}_{\mathrm{r}}(t)$ is illustrated in Fig 5.3, which indicates that the proposed controller provides precise tracking performance for the reference trajectory $\boldsymbol{q}_{\mathrm{r}}(t)$. The value of the adaptive gain $\boldsymbol{\gamma}$ of the proposed controller (5.28), shown in Fig. 5.4, reveals the success of the adaptive parameter tuning law. Therefore, the simulation results confirm that the proposed controller provides robustly precise tracking of the reference trajectories and complies with hard safety constraints.

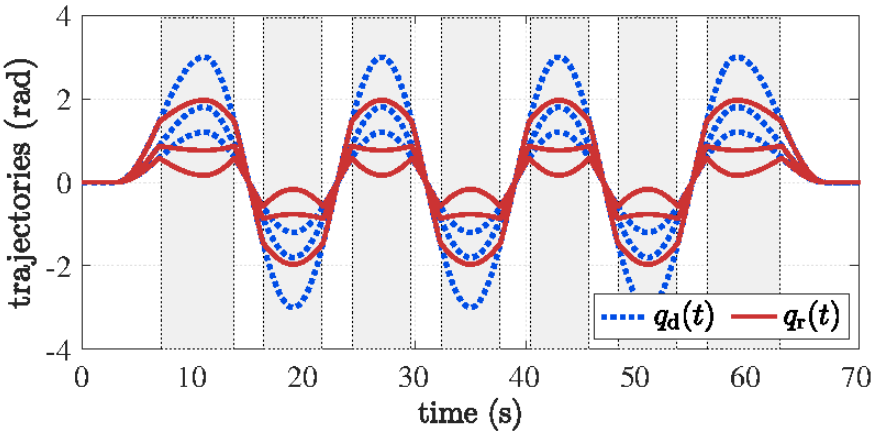

Figure 5.1: The desired trajectory and the modified reference trajectory.

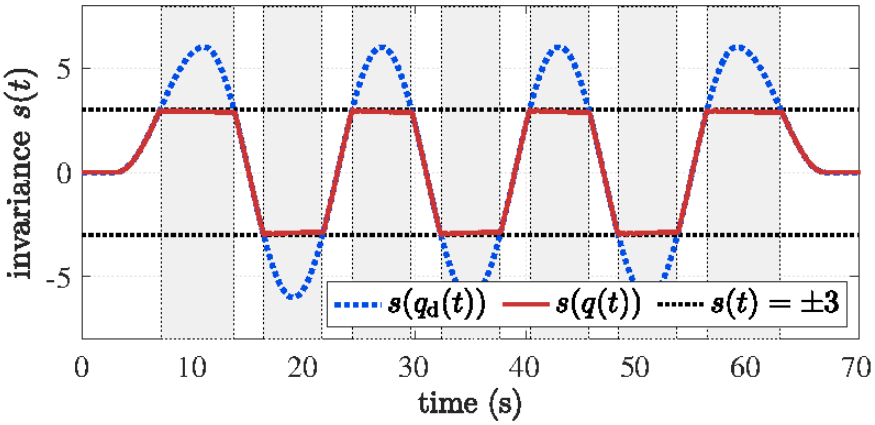

Figure 5.2: The invariance functions.

5.6 Summary

In this chapter, we propose a novel adaptive second-order sliding mode controller for Euler-Lagrangian systems with inequality constraints. Different from the conventional

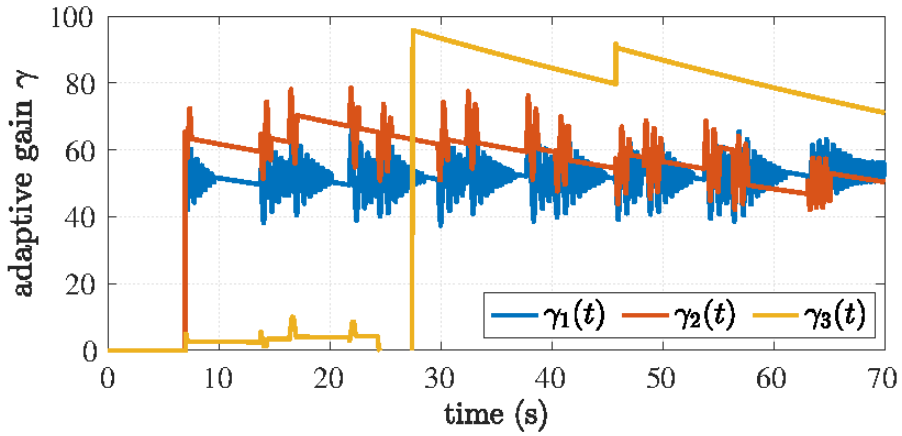

Figure 5.3: The adaptive gains.

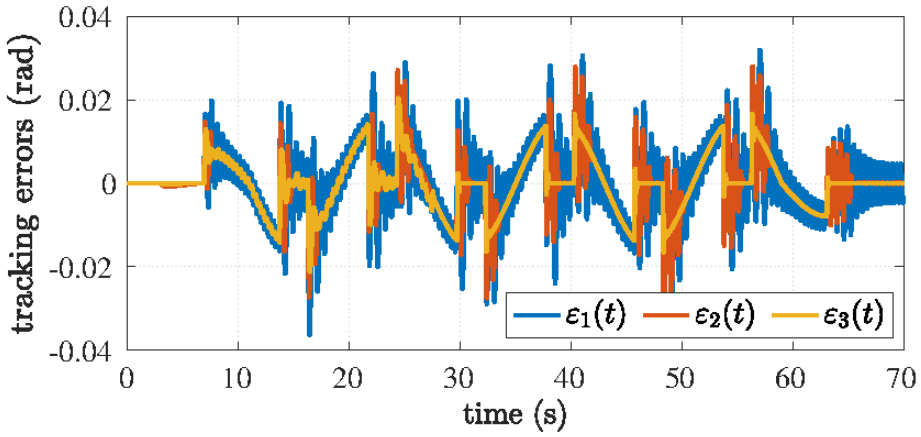

Figure 5.4: The tracking error on the three joints.

tracking control methods, the proposed controller ensures both precise trajectory tracking and invariance to the safety constraint set. By applying the adaptive tuning law for the controller gain, manual parameter assignment is avoided and robustness to system uncertainties is ensured without causing chattering. The convergence of the tracking error is guaranteed by a rigorous Lyapunov-based stability proof. The simulation validation indicates that the method has promising potential in the application to safe HRC. Therefore, the proposed safe control scheme ensures tracking precision, safe constraints, and adaptiveness for the robot manipulator systems, which provides a novel solution for Question 3 raised in Sec. 1.2.

6 Conclusion and Future Work

In this dissertation, we provide a novel solution for safe HRC oriented to collision handling in an uncertain environment. In the beginning, we take an overview of the essential concepts, concerning factors, development paradigms, and approaches for safe HRC in previous work. Based on this, We propose a five-level safe HRC paradigm that contains the handling mechanism for a wide range of unsafe factors, including collisions, constraint violation, task errors, and social norm violation. We validate the feasibility of this paradigm through a compact implementation, including a collision force estimator, an online CDI scheme, and an adaptive robust safe controller which forms a collision handling pipeline, on robot manipulators. As an attempt to fill the gap between the state of the art and the desire for a robust safe HRC with uncertainties, our work is targeted to achieve an accurate, responsive, reliable, and generalizable collision handling mechanism by eliminating conventional assumptions, redefining collision handling metrics, and improving the robustness and adaptability of the system.

6.1 Conclusions

By proposing novel methods for our safe HRC paradigm based on multi-disciplinary approaches and validating them in simulations and experiments, we provide reliable and applicable solutions to the three questions raised in Sec. 1.2. The correspondence between our solutions and the questions is specifically interpreted as follows.

Solution to question 1: How to precisely estimate the collision forces for discontinuous systems with partial measurement?

In Chapter 3, we propose a novel disturbance estimation method to solve this question. We argue that the estimated collision forces using analytical-redundancy-based methods can be used to replace the measurements by extrinsic torque sensors in low-expense robot platforms. We also consider that the conventional assumptions required by the previous methods, namely system continuity, velocity measurement, and boundedness of disturbance derivative, are the main reason to restrict the precision of the estimation results. By designing a novel integral sliding mode observer, the proposed collision force estimation method ensures a precise estimation result without the continuity assumption. The high-gain switching inputs applied in the method releases the requirement on the disturbance derivative. Through achieving the full-dynamic-collapse of the estimation errors with a finite convergence time, the system velocity is also precisely estimated. Thus, velocity measurement is not needed for the proposed collision force estimator. The experimental results have confirmed the estimation precision of the proposed method and verified its applicability to replace a torque sensor. It is validated

that the proposed method is effective for various types of disturbances including the sinusoidal, the square, and the triangle disturbances. The success of the proposed method is mainly due to the elimination of conventional assumptions. Note that the fewer assumptions or preconditions are required, the easier the method can be generalized to other robot platforms. Therefore, the proposed method can be recognized as a step towards a generic collision force reconstruction framework for various robot platforms. Moreover, an applicable FDI scheme without using force sensors can be developed based on the proposed method for robot systems with low expense, compact structure, and complicated environment, such as those mentioned in Sec. 1.2.4.

Solution to question 2: How to accurately classify accidental collisions from intentional contacts with incomplete collision waveform?

In Chapter 4, we solve this problem by developing a novel online CDI scheme with redefined functionalities. Different from the conventional CDI methods that analyze a collision waveform after it vanishes, the proposed online CDI scheme can accurately detect a collision and identify its type in its early stage, such that the collision reaction mechanism can be activated to prevent further injuries. The major challenge to achieve such responsiveness is to ensure high accuracy for signal samples with incomplete collision waveforms. We resolve this issue by inferring the posterior of the decision using a series of classification results. The posterior serves as a confidence index to indicate the *reliability* of the decision. The experimental results show that the proposed scheme achieves high diagnostic accuracy and short detection time, which confirms the application potential of the proposed method in practice. Therefore, our solution to use a series of classification results to improve the diagnosis accuracy with incomplete collision waveform is confirmed to be successful. Similar technology can be applied to the monitoring of a wider class of faults using incomplete environmental knowledge, such as task error detection or social norm violation in uncertain environments.

Solution to question 3: How to avoid constraint violation in a tracking control task with system uncertainties?

In Chapter 5, we are concerned with the safety of HRC in an uncertain environment, for example, with the existence of disturbances or unmodeled system dynamics. The influence of the environmental uncertainties on system performance is twofold. Firstly, the system tracking errors may not converge to zero due to unmodeled dynamics. Secondly, safety constraints may be violated under the effect of disturbances. To resolve these issues, we design a robust trajectory tracking controller using a second-order sliding mode controller. The controller is able to online modify the desired trajectory when the predefined safety constraints are violated. It also ensures robust tracking of the modified reference trajectory to bounded uncertainties. Also, we design an adaptive tuning law for the control parameters to adapt to the varying uncertainties. Simulation results confirm the applicability of the proposed control method. The robustness, flexibility, and adaptability of the controller provide a generic solution for the safe control of robot systems in uncertain environments.

In summary, by developing a collision-handling-oriented safety mechanism for robot manipulators, this dissertation provides a novel perspective to define and implement safe HRC tolerating environmental uncertainties. The elimination of the conventional assumptions, the definition of new metrics, and the enhancement of system robustness solve the critical problems in practice (See Sec. 1.2). The proposed methods indicate potential applicability to various practical scenarios (See Sec. 1.2.4) and contribute to a step forward towards a generic safe HRC framework. Nevertheless, there are still several issues that are not perfectly solved in this dissertation, which will be detailedly interpreted in Sec 6.2, with an outlook of the possible improvements.

6.2 Improvements and Future Research Directions

While the proposed development paradigm provides a novel perspective to regard and redefine safe HRC, it also leaves several open problems for potential improvements. Some of the major concerns are specifically discussed as follows.

Generalization of the Proposed Safety Paradigm

Towards a generic safe HRC framework, the application of the proposed safety paradigm to various robot platforms has to be considered beyond of this dissertation. The main challenge is that other types of robots may not have an Euler-Lagrangian physical model similar to robot manipulators. Therefore, the generalization of the safety paradigms should seriously consider the applicability of the methods to different robot physical models. It is worth mentioning that the proposed safety paradigm presents superior generalizability compared to conventional methods, due to fewer assumptions and enhanced robustness to system uncertainties. Improvements include the investigation of the feasibility to extend the proposed HRC paradigm to different robot platforms, such as unicycle robots, drones, and multi-agent systems.

Handling of Higher-Level Errors

As mentioned in Sec. 2.2.1, higher-level errors, such as task errors and social norm violation, are also recognized as unsafe factors for HRC. Thus, possible improvement can also consider the handling of these higher-level errors using mathematical or psychologic methodologies. Different from the physical models applied to collision-handling, task and social models will be considered. The main focus of the improvement is the adaptation of the approaches and metrics used in the proposed paradigm to the higher-level errors.

Generalization of the Collision Force Estimation Method

The collision force estimation method proposed in this dissertation is designed for rigid robot manipulators with Euler-Lagrangian system models. To generalize the method to various robot platforms, such as mobile robots, drones, and flexible robots, the proposed collision force estimation methods should be adapted to the unicycle model and Elastic

joint models. The main challenges include the underactuation and compliant dynamics which raise the difficulty of the design of the disturbance observers. Additional state estimators may be required to reconstruct the internal dynamics of these systems.

Extension of the Collision Detection and Identification Scheme

In this dissertation, the entire development process of the online CDI scheme, including data acquisition, signal segmentation, feature extraction and evaluation, and classifier training and validation, is conducted on one robot manipulator. Thus, the main challenge to extend the CDI scheme to a generic safe HRC is to ensure similar accuracy and responsiveness on other robot platforms. Methods like transfer learning and generative adversarial nets can be used to generate samples for different robot platforms. Another interesting topic is to compensate for the effects of the varying robot loads, which can be solved by dynamic model-based disturbance estimation methods, such as the disturbance estimation method developed in Chapter. 3.

Safe Control for Time-Variant Constraints

The major remaining issue for the proposed safe control method is that time-variant constraints are not considered. In practice, the motion of humans and dynamic objects render the modeling of time-variant constraints which increase the difficulty for online motion generation. Improvement of the work can consider the solution of safe control for time-variant safety constraints in uncertain environments. Besides, the slight constraint violation caused by the transient phase of sliding mode will be eliminated by applying the integral sliding mode methods. In the meantime, the control method can be extended to a wider range of robot systems, such as under-actuated robots and manipulators with flexible joints.

A Sliding Mode Control

Sliding mode control, also known as *variable structure control*, has been widely applied to precise control of mechatronic systems due to its advantage of high robustness to matched system uncertainties. Based on the discontinuous system theory by Filippov, sliding mode control decouples the controller design for mechatronic systems into two separate procedures: definition of a state-dependent sliding mode variable and selection of a discontinuous switching control law. Therefore, the controller design process is simplified by reducing the dimensions of the system. The result is that the system state is steered to a sliding mode manifold on which the system is dominated by an equivalently desired stable dynamics. The feasibility of such separation is guaranteed by the finite-time convergence of the system state from an arbitrary initial condition to the sliding mode manifold. The modal in which the system evolves on the sliding mode manifold is referred to as *sliding mode* which does not hold in the conventional Lipschitz sense but in the Filippov discontinuity sense, based on the assumption of infinite-frequency discontinuous switching of the control law. In the *sliding mode*, the system dynamics is dominated by the sliding mode motion, and the disturbance and unmodeled dynamics are compensated by the fast switching control law. Therefore, the system dynamics are not affected by system uncertainties and robustness is ensured, which is referred to as the *invariance* property of sliding mode. However, since infinite-frequency switching is impractical, the switching control law in applications can only be implemented by finite switching frequencies, which results in *chattering* phenomenon and potential system damages. Therefore, a major direction of the research work on sliding mode control lies in the investigation of chattering reduction or attenuation schemes. In this dissertation, the sliding mode theory has been applied to the design of the collision-force estimator and the robust safe controller due to its *invariance* feature. The following contents give a brief introduction to the sliding mode control theory, which is sufficient to support the understanding of the work in this dissertation. Further knowledge of advanced sliding mode control can be found in the references recommended at the end of each following section.

A.1 Essentials of Sliding Mode

Consider a Single-Input Single-Output (SISO) nonlinear system $\dot{\boldsymbol{x}} = \boldsymbol{f}(\boldsymbol{x}) + \boldsymbol{G}(\boldsymbol{x})u$ with the following control-affine form

$$\begin{aligned} \dot{\boldsymbol{x}}_1 &= \boldsymbol{f}_1(\boldsymbol{x}_1, \boldsymbol{x}_2), \\ \dot{x}_2 &= f_2(\boldsymbol{x}_1, \boldsymbol{x}_2) + g(\boldsymbol{x})u \end{aligned} \tag{A.1}$$

where $\boldsymbol{x} = [\boldsymbol{x}_1^\top \ x_2]^\top \in \mathbb{R}^n$ is the system state, $\boldsymbol{x}_1 \in \mathbb{R}^{n-1}$, $x_2 \in \mathbb{R}$ are subsystem state variables, $u \in \mathbb{R}$ is the control input, $\boldsymbol{f}_1 : \mathbb{R}^n \to \mathbb{R}^{n-1}$ and $f_2 : \mathbb{R}^n \to \mathbb{R}$ are smooth vector fields, $g(\boldsymbol{x}) \in \mathbb{R}$ is a non-singular gain matrix, $\boldsymbol{f} = [\boldsymbol{f}_1^\top \ f_2]^\top$, and $\boldsymbol{G} = [\boldsymbol{0}^\top \ g(\boldsymbol{x})]^\top$. The form of the system in (A.1) is also referred to as the *regular form*. A typical sliding mode control law for $u(\boldsymbol{x})$ is given by

$$u(\boldsymbol{x}) = \begin{cases} u^+(\boldsymbol{x}), & s(\boldsymbol{x}) > 0, \\ u^-(\boldsymbol{x}), & s(\boldsymbol{x}) < 0. \end{cases} \tag{A.2}$$

where $u^+, u^- : \mathbb{R}^n \to \mathbb{R}$ are scalar functions of $\boldsymbol{x}$, and $s : \mathbb{R}^n \to \mathbb{R}$ is the *sliding-mode variable* or *switching function* defined as the following linear form

$$s(\boldsymbol{x}) = \boldsymbol{x}_2 + \boldsymbol{c}^\top \boldsymbol{x}_1,$$

where $\boldsymbol{c} \in \mathbb{R}^{n-1}$ is a predefined constant vector. The target of the control law $u(\boldsymbol{x})$ is to confine the system state to the hyperplane in the state space $s(\boldsymbol{x}) = 0$, which is referred to as the *sliding mode manifold*. In this situation, the algebraic relationship $\boldsymbol{x}_2 + \boldsymbol{c}^\top \boldsymbol{x}_1 = 0$ holds, and the system dynamics becomes

$$\dot{\boldsymbol{x}}_1 = \boldsymbol{f}_1(\boldsymbol{x}_1, -\boldsymbol{c}^\top \boldsymbol{x}_1). \tag{A.3}$$

Note that the order of this subdynamics is reduced to $n-1$, which is referred to as the *partial dynamic collapse*. The stability of the full-order system is then determined by the $n-1$ order dynamics (A.3). Therefore, the design of the sliding mode control law (A.2) is composed of the following two steps. Firstly, define a proper state-dependent sliding-mode variable $s(\boldsymbol{x})$ which regulates the desired state dynamics. Secondly, design a proper switching control law $u(\boldsymbol{x})$. It is usually assumed that the switching of $u(\boldsymbol{x})$ can be infinitely fast.

A.1.1 Filippov Discontinuity and Equivalent Control

Due to the discontinuity brought up by the switching control law (A.2) which lies on the right-hand side of the nonlinear system (A.1), the rendered closed-loop dynamics of the system does not formulate an Ordinary Differential Equation (ODE) that holds in the conventional Lipschitz sense. Therefore, the analysis of the sliding mode solution follows a different principle, which is usually conducted using the *Filippov method* or the *equivalent control* method.

The Filippov method recognizes that the state derivative $\dot{\boldsymbol{x}}$, dominated by the discontinuous switching law $u(\boldsymbol{x})$, as the weighted average of two vector fields $\boldsymbol{f}^+ = \boldsymbol{f}(\boldsymbol{x}) + \boldsymbol{G}(\boldsymbol{x})u^+(\boldsymbol{x})$ and $\boldsymbol{f}^- = \boldsymbol{f}(\boldsymbol{x}) + \boldsymbol{G}(\boldsymbol{x})u^-(\boldsymbol{x})$, i.e.,

$$\dot{\boldsymbol{x}} = \mu \boldsymbol{f}^+ + (1-\mu)\boldsymbol{f}^- \tag{A.4}$$

where

$$\mu = \frac{(\nabla s)^\top \boldsymbol{f}^-}{(\nabla s)^\top (\boldsymbol{f}^- - \boldsymbol{f}^+)}, \ \nabla s = \frac{\partial s(\boldsymbol{x})}{\partial \boldsymbol{x}}.$$

It is noted that the equality in (A.4) only holds when the switching between $\boldsymbol{f}^+$ and $\boldsymbol{f}^-$ is infinitely fast such that it is equivalent to a continuous dynamics, which is referred to as the *Filippov sense*.

The equivalent control method considers that there exists a continuous control input $u_{\text{eq}}(\boldsymbol{x})$, where $u_{\text{eq}}(\boldsymbol{x}) = u(\boldsymbol{x})$ holds in the Filippov sense, such that the system dynamics corresponds to the following *sliding mode condition*,

$$s(\boldsymbol{x}) = 0,\ \dot{s}(\boldsymbol{x}) = 0, \tag{A.5}$$

for any initial system state $\boldsymbol{x}_0$ on the sliding mode manifold. Taking the derivative of $s(t)$ and substituting $u_{\text{eq}}(\boldsymbol{x}) = u(\boldsymbol{x})$ to it, we have

$$\dot{s} = \dot{x}_2 + \boldsymbol{c}^\top \boldsymbol{f}_1(\boldsymbol{x}) + f_2(\boldsymbol{x}) + g(\boldsymbol{x})u_{\text{eq}}$$

and the equivalent control can be solved as

$$u_{\text{eq}} = -\frac{\dot{x}_2 + \boldsymbol{c}^\top \boldsymbol{f}_1(\boldsymbol{x}) + f_2(\boldsymbol{x})}{g(\boldsymbol{x})},$$

Therefore, both the Filippov method and the equivalent control method are trying to formulate the discontinuous dynamics of the original system to an equivalent continuous dynamics, such that further analysis of the system can be built on the conventional Lipschitz continuous sense. It is proven that both methods produce the same closed-loop solution for the system with a regular form as (A.1) [56].

A.1.2 Robustness and Invariance

Consider that the system is steered by the uncertainty term $d((\boldsymbol{x}), t)$ as

$$\begin{aligned} \dot{\boldsymbol{x}}_1 &= \boldsymbol{f}_1(\boldsymbol{x}_1, \boldsymbol{x}_2), \\ \dot{x}_2 &= f_2(\boldsymbol{x}_1, \boldsymbol{x}_2) + g(\boldsymbol{x})u + d(\boldsymbol{x}, t), \end{aligned} \tag{A.6}$$

where $d(\boldsymbol{x}, t)$ is bounded by $\|d(\boldsymbol{x}, t)\| \leqslant \bar{d}$, $\bar{d} \in \mathbb{R}^+$. Then, the state derivative in the Filippov sence becomes

$$\dot{\boldsymbol{x}} = \mu \boldsymbol{f}^+ + (1-\mu)\boldsymbol{f}^- + [\boldsymbol{0}^\top\ 1]^\top d(\boldsymbol{x}, t). \tag{A.7}$$

Therefore, the state derivative $\dot{\boldsymbol{x}}$ is influenced by the uncertainty term $d(\boldsymbol{x}, t)$. On the other hand, the influence of $d(\boldsymbol{x}, t)$ can be reduced or even eliminated by adjusting the value of μ, which is achieved by setting proper values of $u^+(\boldsymbol{x})$ and $u^-(\boldsymbol{x})$. In this sense, the derivative of the sliding mode variable becomes

$$\dot{s} = \dot{x}_2 + \boldsymbol{c}^\top \boldsymbol{f}_1(\boldsymbol{x}) + f_2(\boldsymbol{x}) + g(\boldsymbol{x})u_{\text{eq}} + d(\boldsymbol{x}_1, t),$$

and the equivalent control is

$$u_{\text{eq}} = -\frac{\dot{x}_2 + \boldsymbol{c}^\top \boldsymbol{f}_1(\boldsymbol{x}) + f_2(\boldsymbol{x}) + d(\boldsymbol{x}_1, t)}{g(\boldsymbol{x})}.$$

This indicates that the switching control $u(\boldsymbol{x})$ is able to cover the uncertainty term $d(\boldsymbol{x}, t)$. As a result, the equivalent dynamics A.3 is not affected by $d(\boldsymbol{x}, t)$. Such a property is referred to as *invariance* of sliding mode, which depicts the robustness of sliding mode controllers to bounded uncertainties. Note that the *invariance* property only holds on the assumption of infinitely-fast switching of the control law $u(\boldsymbol{x})$.

A.1.3 Extension to Multi-Input Multi-Output Systems

The sliding mode control law in (A.2) can be extended to Multi-Input Multi-Output (MIMO) systems. The regulation form of a MIMO system is formulated as

$$\begin{aligned} \dot{\boldsymbol{x}}_1 &= \boldsymbol{f}_1(\boldsymbol{x}), \\ \dot{\boldsymbol{x}}_2 &= \boldsymbol{f}_2(\boldsymbol{x}) + \boldsymbol{G}_1(\boldsymbol{x})\boldsymbol{u}, \end{aligned} \tag{A.8}$$

where $\boldsymbol{x}_1 \in \mathbb{R}^{n-m}$, $\boldsymbol{x}_2 \in \mathbb{R}^n$ are state variables of subsystems, $\boldsymbol{u} \in \mathbb{R}^m$ is the system input, $\boldsymbol{f}_1 : \mathbb{R}^n \to \mathbb{R}^{n-m}$, $\boldsymbol{f}_2 : \mathbb{R}^n \to \mathbb{R}^m$ are continuous vector fields, $\boldsymbol{G}_1(\boldsymbol{x}) \in \mathbb{R}^{m\times m}$ is a non-singular matrix. The vector-form of sliding mode control input $\boldsymbol{u}$ is

$$u_i(\boldsymbol{x}) = \begin{cases} u_i^+(\boldsymbol{x}), & s(\boldsymbol{x}) > 0, \\ u_i^-(\boldsymbol{x}), & s(\boldsymbol{x}) < 0, \end{cases} \tag{A.9}$$

where $u_i(\boldsymbol{x})$ is the i-th element of $\boldsymbol{u}(\boldsymbol{x})$, $u_i^+(\boldsymbol{x}), u_i^-(\boldsymbol{x}) \in \mathbb{R}$ are constant scalars for each $i = 1, 2, \cdots, m$ and the sliding mode variable is defined as

$$\boldsymbol{s}(\boldsymbol{x}) = \boldsymbol{x}_2 + \boldsymbol{c}^\top \boldsymbol{x}_1,$$

where $\boldsymbol{c} \in \mathbb{R}^{n-m}$ is a predefined constant vector. Another form of MIMO sliding mode control takes the following form,

$$u(\boldsymbol{x}) = \rho(\boldsymbol{x}, t)\frac{(\nabla \boldsymbol{s}\boldsymbol{G}(\boldsymbol{x}))^\top \boldsymbol{s}(\boldsymbol{x})}{\| (\nabla \boldsymbol{s}\boldsymbol{G}(\boldsymbol{x}))^\top \boldsymbol{s}(\boldsymbol{x})\|}, \ \nabla \boldsymbol{s} = \frac{\partial \boldsymbol{s}}{\partial \boldsymbol{x}}.$$

Taking the derivative of $\boldsymbol{s}(\boldsymbol{x})$, we obtain

$$\dot{\boldsymbol{s}}(t) = \dot{\boldsymbol{x}}_2 + \boldsymbol{c}^\top \boldsymbol{f}_1(\boldsymbol{x}) + \boldsymbol{f}_2(\boldsymbol{x}) + \boldsymbol{G}(\boldsymbol{x})\boldsymbol{u}_{\text{eq}},$$

for which the equivalent control $\boldsymbol{u}_{\text{eq}}(\boldsymbol{x})$ can be solved as

$$\boldsymbol{u}_{\text{eq}} = -\boldsymbol{G}^{-1}(\boldsymbol{x})\left(\boldsymbol{c}^\top \boldsymbol{f}_1(\boldsymbol{x}) + \boldsymbol{f}_2(\boldsymbol{x})\right).$$

A.2 Advanced Sliding Mode Control

For arbitrary initial conditions, the system state does not necessarily lie on the sliding mode manifold. Therefore, a *reaching phase* is usually inevitable which denotes the process that the system evolves from the initial state to the sliding mode manifold. Note that the invariance property does not hold during the reaching phase. Thus, the

integral sliding mode control method is brought up to eliminate the reaching phase to ensure robustness throughout, which is briefly introduced in Sec. A.2.1. The readers can also refer to [224] (Chapter 7) for details. Another critical issue of the essential sliding mode is the chattering phenomenon on the system state due to the discontinuous control input with finite sampling frequency. The boundary-layer method and second-order sliding mode control are two main solutions to attenuate chattering, which are respectively interpreted in Sec. A.2.2 and Sec. A.2.3.

A.2.1 Integral Sliding Mode Control

This section gives a short introduction of the theory of integral sliding mode. Consider a multi-input multi-output (MIMO) control affine system

$$\dot{\boldsymbol{x}} = \boldsymbol{f}(\boldsymbol{x}) + \boldsymbol{G}(\boldsymbol{x})\left(\boldsymbol{u} + \boldsymbol{d}(\boldsymbol{x}, t)\right), \tag{A.10}$$

where $\boldsymbol{x}(t) \in \mathbb{R}^n$ is the state vector of the system, $\boldsymbol{f}(\boldsymbol{x}) \in \mathbb{R}^n$ is a smooth vector field, $\boldsymbol{G}(\boldsymbol{x}) \in \mathbb{R}^{n\times m}$ is a m-rank smooth matrix, $\boldsymbol{u}(t) = [u_1,\ u_2,\ \cdots,\ u_m]^T$ is the m-dimensional input vector, and $\boldsymbol{d}(\boldsymbol{x}, t) \in \mathbb{R}^m$ is the state and time dependent system disturbance which is assumed to be bounded by

$$\|\boldsymbol{d}(\boldsymbol{x}, t)\| \leqslant \delta_d,\ \delta_d \in \mathbb{R}^+.$$

Note that all norms $\|\cdot\|$ in this paper denote 2-norms. For system (A.10), an integral sliding mode controller that guarantees the asymptotic stability of the of the equilibrium $\boldsymbol{x} = 0$ is designed as

$$\boldsymbol{u}(t) = \boldsymbol{u}_n + \boldsymbol{u}_s, \tag{A.11}$$

where $\boldsymbol{u}_n$ is a controller that stabilizes the nominal system and $\boldsymbol{u}_s$ is the discontinuous control input that compensates for the disturbance $\boldsymbol{d}(\boldsymbol{x}, t)$

$$\boldsymbol{u}_s = -M_s \frac{\boldsymbol{s}(\boldsymbol{x}, t)}{\|\boldsymbol{s}(\boldsymbol{x}, t)\|}, \tag{A.12}$$

where $M_s \in \mathbb{R}^+$ is a properly selected input gain and the switching function, and

$$\boldsymbol{s}(\boldsymbol{x}, t) = \boldsymbol{s}^*(\boldsymbol{x}) + \boldsymbol{z}(t) \tag{A.13}$$

is the sum of a conventional sliding manifold $\boldsymbol{s}^*(\boldsymbol{x}) \in \mathbb{R}^n$ and an additional integral term $\boldsymbol{z}(t) \in \mathbb{R}^n$, where $\boldsymbol{s}^*(\boldsymbol{x})$ and $\boldsymbol{z}(t)$ respectively satisfy

$$\operatorname{rank}\left(\frac{\partial \boldsymbol{s}^*(\boldsymbol{x})}{\partial \boldsymbol{x}}\right) = m$$

and

$$\dot{\boldsymbol{z}} = -\frac{\partial \boldsymbol{s}^*(\boldsymbol{x})}{\partial \boldsymbol{x}}\left(\boldsymbol{f}(\boldsymbol{x}) + \boldsymbol{G}(\boldsymbol{x})\boldsymbol{u}_n\right),\ \boldsymbol{z}(0) = -\boldsymbol{s}^*(\boldsymbol{x}(0)),$$

where $\boldsymbol{x}(0)$ is the initial condition of the system state. Note that the control in (A.12) is referred to as *unit vector control* [221] and guarantees the following sliding mode condition

$$\boldsymbol{s}(\boldsymbol{x}, t) = 0, \ \forall \ t \geqslant 0. \tag{A.14}$$

As a result, the system state $\boldsymbol{x}$ is confined to the sliding manifold (A.13), and the equivalent sliding mode dynamics is

$$\dot{\boldsymbol{x}} = \boldsymbol{f}(\boldsymbol{x}) + \boldsymbol{G}(\boldsymbol{x})\boldsymbol{u}_n$$

which does not depend on the system disturbance $\boldsymbol{d}(\boldsymbol{x}, t)$, if $\boldsymbol{d}(\boldsymbol{x}, t)$ is matched [291] as in (A.10). This feature has been called *invariance* in sliding mode control, since the system behavior is invariant to $\boldsymbol{d}(\boldsymbol{x}, t)$. Different from the conventional sliding mode control, integral sliding mode control can theoretically eliminate the reaching phase to the sliding manifold of the system. As a result, the invariance of integral sliding mode control holds for all times.

A.2.2 Boundary-Layer Method

The main source of the chattering phenomenon is the discontinuous switching of control law $u(\boldsymbol{x})$. In practice, infinitely fast switching is impossible, finite switching frequency brings latency to the switching and produces chattering. Therefore, an explicit solution to chattering is to modify the hard discontinuous switching to sort of continuous functions. For example, a continuous adaptation of the discontinuous control law (A.2) can be formulated as

$$u(\boldsymbol{x}) = M\text{sat}\left(\frac{s(\boldsymbol{x})}{\epsilon}\right)$$

where $\text{sat}(\cdot)$ is the saturation defined as

$$\text{sat}(z) = \begin{cases} 1, & x > 1, \\ x, & -1 < x \leqslant 1, \\ -1, & x \leqslant -1, \end{cases} \tag{A.15}$$

and $\epsilon \in \mathbb{R}^+$ is a sufficiently small scalar. The region $-\epsilon < s < \epsilon$ is referred to as the *boundary layer*. On the one hand, the control law in (A.15) allows the system state derivative $\dot{\boldsymbol{x}}$ to continuously change, which leads to a smooth motion of the sliding variable s in the boundary layer. On the other hand, the sliding mode variable s is confined within the boundary layer, but the sliding mode condition (A.5) does not strictly hold. As a result, the robustness of the closed-loop system is sacrificed for the reduced chattering. Therefore, the boundary layer should be carefully selected to maintain a balance between robustness and chattering reduction. Other continuous functions used for boundary-layer method can also be found in [292, 293].

A.2.3 Second-Order Sliding Mode Control

Another popular method to solve the chattering attenuation problem is the higher-order sliding mode control. By design a control law such that the discontinuous terms emerge in higher-order derivatives of the sliding mode variable, the chattering phenomenon can be eliminated in theory. The most popularly applied higher-order sliding mode control method in mechatronic systems is the *super-twisting algorithm* which is a second-order sliding mode control method. For a SISO control system with the following form

$$\dot{x} = f(x) + g(x)u, \tag{A.16}$$

where $x \in \mathbb{R}$ is the system state, $u \in \mathbb{R}$ is the system input, $f : \mathbb{R} \to \mathbb{R}$ is a smooth vector field, and $g(x) \in \mathbb{R}$ is a continuous function. A super-twisting algorithm controller is formulated as follows [294],

$$u = -\alpha|\sigma(\tau)|^{\frac{1}{2}}\mathrm{sgn}(\sigma(\tau)) - \int_0^t \gamma\mathrm{sgn}(\sigma(\tau))\mathrm{d}\tau,$$

where $\sigma(t) = \dot{x} + cx$ is the higher-order sliding mode variable, and $\alpha, \gamma, c \in \mathbb{R}^+$ are parameters to be determined. substituting the system dynamics (A.16) to $\sigma(t)$, we obtain

$$\sigma(t) = cx + f(x) + g(x) - \alpha|\sigma(\tau)|^{\frac{1}{2}}\mathrm{sgn}(\sigma(\tau)) + \int_0^t \gamma\mathrm{sgn}(\sigma(\tau))\mathrm{d}\tau.$$

It is not difficult to verify that $\sigma(t)$ does not contain discontinuous terms, which avoids the occurrence of chattering phenomenon. More details on higher-order sliding mode controllers can be found in [294–296].

B Supervised Learning Methods

Supervised learning is a type of machine learning tasks that try to approximate a function using a provided set of data. The data set is composed of labeled samples with input-output pairs that reveal the mapping between two variables. The input variable is typically referred to as a *sample*, while the output variable is called a *label*. The process of using a mathematical model to fit the training data with a tolerable level of errors is referred to as *training*, while applying the trained model to decide the label of a given vector is called *prediction*. Supervised learning can be used to solve a *classification* problem, where the label-space is discrete, or a *regression* problem, of which the label-space is continuous. In the following, we provide a brief introduction of the Bayesian decision theory and some non-parametric classification models that we used to construct our CDI scheme.

B.1 Bayesian Decision Theory

The Bayesian decision theory is a stochastic method of the decision theory that utilizes the Bayesian probability to estimate the expected values of all actions according to given observations. It is also widely applied to classification problems, which is known as the *Naive Bayesian* classifier. In this dissertation, we apply the Bayesian decision theory as an auxiliary scheme to strengthen the reliability of the proposed CDI scheme using a series of observations. In general, this still renders a classification problem, although the training process sequentially online proceeds, and its training data is obtained from an existing classifier. In the following, we give a brief introduction to the basic ideas of the Bayesian decision theory, part of which is referred to [297], Chapter 3.

Suppose that we are expected to make a decision from r classes, $C_1, C_2, \cdots, C_r$, based on m observed results $\mathcal{X} = \{x_1, x_2, \cdots, x_m\}$, where $x_j \in \Omega$, $j = 1, 2, \cdots, m$, and Ω is the observation vector space. Then, the posterior probability $p(C_i|\mathcal{X})$ for each class C_i, $i = 1, 2, \cdots, r$, based on the observation series $\mathcal{X}$, is calculated by

$$p(C_i|\mathcal{X}) = \frac{p(C_i|\mathcal{X})p(C_i)}{p(\mathcal{X})}, \tag{B.1}$$

where $p(C_i)$ is the *prior probability* for each class C_i that stands for a previous belief on the class distribution; $p(x|C_i)$ is the *class likelihood* that represents the conditional probability of the observation $\mathcal{X}$ with given class C_i, and $p(\mathcal{X})$ is the *evidence*, the marginal probability of observation $\mathcal{X}$. The prior $p(C_i)$ is usually manually assigned according to experience, which indicates a subjective preference or belief. The likelihood $p(\mathcal{X}|C_i)$ serves as the modification of the posterior based on new observations. If the

observed results are assumed as independent from each other, then the likelihood further reads

$$p(\mathcal{X}|C_i) = \prod_{j=1}^{m} p(x_j|C_i), \tag{B.2}$$

where for every $x_j \in \Omega$, $p(x_j|C_i)$ is a likelihood whose value can be obtained offline using experimental methods. The marginal $p(\mathcal{X})$ serves as a normalization factor to ensure that the posterior $p(C_i|\mathcal{X})$ is probability, i.e., $\sum_{j=1}^{r} p(C_i|\mathcal{X}) = 1$. It is calculated by

$$p(\mathcal{X}) = \sum_{i=1}^{m} p(\mathcal{X}|C_i)p(C_i).$$

Therefore, the main idea of Bayesian decision theory revealed by (B.1) is to use the new observations to modify the prior belief, such that subjective bias can be corrected by new data. After calculating posterior probabilities $p(C_i|\mathcal{X})$ for all classes C_i, the decision is made based on the maximum posterior, i.e.,

$$C = \arg\max_i p(C_i|\mathcal{X}),$$

where C is the ultimate decision result. Taking the logarithm of the posterior, the decision mechanism can also be represented as

$$C = \arg\max_i \ln p(C_i|\mathcal{X}) = \arg\max_i \left(\sum_{j=1}^{m} \ln p(x_j|C_i) + \ln p(C_i) \right) - \ln p(\mathcal{X}),$$

considering the independent property of the observations (B.2). Thus, if the prior distribution is set as even, i.e., $p(C_1) = p(C_2) = \cdots = p(C_n)$, then the decision is only dependent on the likelihood correction term $\sum_{j=1}^{m} \ln p(x_j|C_i)$. It indicates that similar observation results accumulate the likelihood values, and strengthen the preference of the posterior towards its correlated class, which is exactly the reason why the Bayesian decision theory is applied in this dissertation.

B.2 Classification Models

For a classification problem, the output of the training process is a *discriminant*, a vector function that determines the class of the sample to be tested. The prediction is conducted usually by explicitly applying the discriminant. A classification model is referred to as a *parametric* method if its discriminant depends on a parameterized probabilistic distribution. The training of parametric models renders an estimation problem for the distribution parameters, where statistic methods are used. Otherwise, the classification model is called a *non-parametric* method, where the discriminant is obtained by solving an optimization problem. In this section, we present the essentials of four non-parametric models, namely LDA, kNN, SVM, and FNN that we apply in Chapter 4. Part of the contents in this section is referred to in [298]

B.2.1 Linear Discriminant Analysis

Linear Discriminant Analysis (LDA) is a popular dimensionality reduction technique applied to classification problems. LDA attempts to maximize the variance between different classes while minimizing the variance within each class, such that the optimal separation between different classes is achieved. Different from the Principal Component Analysis method, LDA is a supervised model that fully considers the labels of different classes. Therefore, LDA can be directly applied to a classification problem as a supervised learning method. The essential principle of LDA is interpreted as follows.

Given a data set with m samples, $\mathcal{D} = \{(x_1, y_1), (x_2, y_2), \cdots, (x_m, y_m)\}$, for all $i = 1, 2, \cdots, m$, $x_i \in \mathbb{R}^n$, $y_i \in \{C_1, C_2, \cdots, C_n\}$ is the label of x_i. For a two-class problem, i.e., $r = 2$, the target of LDA is to seek for a coefficient vector $w \in \mathbb{R}^n$, such that the following index is maximized,

$$w^* = \arg\max_{w} \frac{w^\top S_b w}{w^\top S_w w}, \tag{B.3}$$

where w^* is the optimal projection direction, the within-class scatter S_w and between-class scatter S_b are defined as

$$S_w = \Sigma_1 + \Sigma_2,\ S_b = (\mu_1 - \mu_2)(\mu_1 - \mu_2)^\top,$$

and for each class C_j, $j = 1, 2$, the mean value μ_j and variance Σ_j are respectively calculated by

$$\mu_j = \frac{1}{N_j} \sum_{\forall y_i = C_j} x_i,\ \Sigma_j = \sum_{\forall y_i = C_j} (x_i - \mu_j)(x_i - \mu_j)^\top,$$

where N_j is the number of samples belonging to class C_j. In LDA, the scatters S_w and S_b are used for the maximization of separation between different classes. It is known that the maximum value of the criteria (B.3) is the maximum eigenvalue of $S_w^{-\frac{1}{2}} S_b S_w^{-\frac{1}{2}}$, and the corresponding optimal solution w^* is the eigenvector corresponding to this eigenvalue. In general, LDA is seeking for an optimal projection direction for the two-class sets. For a multi-class problem, where $r > 2$, the optimization criteria is

$$W^* = \arg\max_{W \in \mathbb{R}^{n \times d}} \frac{\prod\limits_{\text{diag}} W^\top S_b W}{\prod\limits_{\text{diag}} W^\top S_w W},$$

where $\prod\limits_{\text{diag}} (\cdot)$ denotes the product of the diagonal elements of a matrix, W is the projection matrix, and d is the dimensionality of the hyperplane to which the samples are projected. The scatters S_w and S_b are redefined as

$$S_w = \sum_{j=1}^{r} \sum_{\forall y_i = C_j} (x_i - \mu_j)(x_i - \mu_j)^\top,\ S_b = \sum_{j=1}^{r} N_j (\mu_j - \mu)(\mu_j - \mu)^\top,$$

where μ is the mean value of all samples.

After the optimal projection vector w^* is obtained, transformations can be performed on the samples, and Euclidean distance can be used to classify the test samples based on a nearest-distance principle. The applicable solvers for the LDA problem (B.3) include *svd*, *lsqr*, and *eigen*, which can be referred to in [299].

B.2.2 k-Nearest Neighbor

The k-nearest neighbor method is a classical non-parametric approach for classification or regression. It is especially suitable for a naive classification problem with little prior knowledge of the distribution of the data. The main advantage of k-nearest neighbor is that no training process is required. For the prediction of a test sample, the k-nearest-neighbor classifier calculates the distance between a test sample and the training samples. Given a data set with m samples, $\mathcal{D} = \{(x_1, y_1), (x_2, y_2), \cdots, (x_m, y_m)\}$, for all $i = 1, 2, \cdots, m$, $x_i \in \mathbb{R}^n$, $y_i \in \{C_1, C_2, \cdots, C_n\}$ is the label of x_i. Let $x \in \mathbb{R}^n$ be a test sample, the distance between samples x and x_i, $i = 1, 2, \cdots, n$, under the Euclidean metric is

$$d(x, x_i) = \sqrt{\|x - x_i\|^2}.$$

Therefore, the prediction is made according to the minimum distance principle, i.e., the label of the test sample follows the majority of its nearest neighbors. In an extreme scenario, where the 1-nearest neighbor rule is applied, the test sample is labeled with the class of its nearest training sample.

There are mainly two hyper-parameters that are frequently used to adjust the performance of the k-nearest neighbor method. The first is the value of k, namely how many nearest neighbors should be considered to predict the test sample. A larger value for k tends to oversimplify the classifier model, while a smaller value may cause the overfitting problem. Both cases bring down the prediction accuracy of the k-nearest neighbor classifier. The second hyper-parameter is the distance metric that can be determined as *Euclidean*, *Canberra*, *Chebyshev*, *Manhattan*, and *Minkowski*. The distance metrics perform nonlinear transformations on the samples and should be carefully selected according to the distributional properties of data.

B.2.3 Support Vector Machine

Support Vector Machine (SVM) is another non-parametric classifier with an excellent capability of generalization. From a geometric point of view, SVM creates a pair of hyperplane for each two-class data set. The training process of the classifier tends to create the widest separation between the hyperplane pair. As a result, SVM is quite insensitive to the distribution of the data set since its structure only depends on a small cluster of training samples. Nonlinear kernel functions allow the mapping of samples into higher-dimensional spaces, such that linearly inseparable problems can be solved.

Given a data set with m samples, $\mathcal{D} = \{(x_1, y_1), (x_2, y_2), \cdots, (x_m, y_m)\}$, for all $i = 1, 2, \cdots, m$, $x_i \in \mathbb{R}^n$, $y_i \in \{C_1, C_2, \cdots, C_n\}$ is the label of x_i. For a two-class problem which confines the label between 1 and -1, the label of a test sample $x \in \mathbb{R}^n$ is

determined by

$$y = \begin{cases} 1, & g(x) > 0 \\ -1, & g(x) < 0, \end{cases}$$

where $g(x)$ is the discriminant in the following form

$$g(x) = \sum_{i=1}^{m} \alpha_i y_i K(x_i, x) + \beta,$$

where $\alpha_i \in \mathbb{R}$, $i = 1, 2, \cdot, m$, for each x_i, is a coefficient, $\beta \in \mathbb{R}$ is the bias, and $K(\cdot, \cdot)$ is the kernel function of two samples. The coefficients $\alpha_1, \alpha_2, \cdots, \alpha_m$ are the solution of the following optimization problem

$$\begin{aligned} \alpha^* &= \arg\min_{\alpha} \left(-\frac{1}{2} \sum_{i=1}^{m} \sum_{j=1}^{m} \alpha_i \alpha_j y_i y_j K(x_i, x_j) + \sum_{i=1}^{m} \alpha_i \right), \\ \text{s.t.} &\sum_{i=1}^{m} \alpha_i y_i = 0,\ 0 \leqslant \alpha_i \leqslant C, \forall i = 1, 2, \cdots, m, \end{aligned} \tag{B.4}$$

which formulates the training process of a SVM classifier with $\mathcal{D}$, where α^* is the optimal solution of (B.4). Depending on the geometric relationship, the coefficients of the training samples are valued as

$$\alpha_i \begin{cases} = 0, & y_i g(x_i) > 1 \\ < C \text{ and } > 0, & y_i g(x_i) = 1 \\ = C, & y_i g(x_i) < 1, \end{cases}$$

where $C \in \mathbb{R}^+$ is a useful hyper-parameter to punish the misclassified samples. The sample x_i is referred to as a *support vector*, if it lies on the hyperplane pair $|g(x)| = 1$, i.e., $y_i g(x_i) = 1$. Thus, the geometric properties of the SVM are only dependent on the distribution of the support vectors that only account for a small proportion of the data set, which offers SVM a decent ability of generalization. The kernel functions $K(\cdot, \cdot)$ is also a manually assigned hyper-parameter to specify the mapping of samples to higher-dimensional spaces. Popular kernel functions include the *linear kernel*, the *radial basis function kernel*, and the *sigmoid kernel* which can be referred in [300].

B.2.4 Feedforward Neural Network

The feedforward neural network (FNN) is the simplest neural network structure that has been widely used for classification problems. An artificial neural network is an operation model composed of a cluster of self-connected neurons. In an FNN, each neuron contains a linear structure $z = w^\top x + b$ and an activation function $y = f(z)$, where $x \in \mathbb{R}^n$ is the input of the neuron, $w \in \mathbb{R}^n$ is the weight vector, $b \in \mathbb{R}$ is the bias, $z \in \mathbb{R}$ is an auxiliary variable, and $y \in \mathbb{R}$ is the output of the neuron. The activation function $f : \mathbb{R} \to \mathbb{R}$ serves as a nonlinear mapping from the linear output z to the class space. The input of each neuron is connected only with the neuron in its fore-layers and only produces an output to those in its back-layers. No feedback exists in an FNN.

In a multi-layer FNN, the neurons between the inputs and outputs are referred to as the *hidden neurons* which form the *hidden layer*. The hidden layer is recognized as a *feature detector* to serve as an alternative of feature extraction. Therefore, the hidden layers usually dominate the performance of the FNN. The number of hidden layers, the number of neurons in each hidden layer, and the activation functions of each hidden neuron are useful hyper-parameters to adjust the performance of the classification. Popular activation functions for FNN include *logistic sigmoid function*, *hyperbolic tan function*, and the *rectified linear unit function* which can be referred to in [301].

Given a data set with m samples, $\mathcal{D} = \{(x_1, y_1), (x_2, y_2), \cdots, (x_m, y_m)\}$, for all $i = 1, 2, \cdots, m$, $x_i \in \mathbb{R}^n$, $y_i \in \{C_1, C_2, \cdots, C_n\}$ is the label of x_i. The prediction of a test sample $x \in \mathbb{R}^n$ is conducted by feeding it to the input of an FNN and calculate the output using the trained configuration. For a two-class problem, the classification result is explicitly provided by the output layer of the FNN. Nevertheless, for a multi-class problem, the result is obtained through the softmax discriminant function. The training of an FNN with data set $\mathcal{D}$ is based on the *back propagation* technology which iteratively corrects the weight of each neuron according to the classification error originated from the output. Note that backpropagation does not certainly ensure the convergence of the training, nor provides a clearly defined terminating principle. However, some heuristic principles can be used to guarantee the convergence of the classification error of the training samples and terminate the training process [302].

Bibliography

[1] F. Flacco and A. De Luca. Safe physical human-robot collaboration. In *2013 IEEE/RSJ International Conference on Intelligent Robots and Systems*, pages 2072–2072. IEEE, 2013.

[2] R. Alami, A. Clodic, V. Montreuil, E. A. Sisbot, and R. Chatila. Task planning for human-robot interaction. In *Proceedings of the 2005 joint conference on Smart objects and ambient intelligence: innovative context-aware services: usages and technologies*, pages 81–85, New York, NY, USA, 2005. Association for Computing Machinery.

[3] A. De Santis, B. Siciliano, A. De Luca, and A. Bicchi. An atlas of physical human–robot interaction. *Mechanism and Machine Theory*, 43(3):253 – 270, 2008.

[4] A. De Luca and F. Flacco. Integrated control for phri: Collision avoidance, detection, reaction and collaboration. In *Proc. IEEE Biomedical Robotics and Biomechatronics*, pages 288–295, Roma, Italy, Nov 2012.

[5] S. Haddadin, A. De Luca, and A. Albu-Schäffer. Robot collisions: A survey on detection, isolation, and identification. *IEEE Trans. Robot.*, 33(6):1292–1312, Dec 2017.

[6] M. A. Goodrich and A. C. Schultz. Human-robot interaction: a survey. *Foundations and trends in human-computer interaction*, 1(3):203–275, 2007.

[7] A. De Santis, B. Siciliano, A. De Luca, and A. Bicchi. An atlas of physical human–robot interaction. *Mechanism and Machine Theory*, 43(3):253–270, Mar 2008.

[8] A. Bauer, D. Wollherr, and M. Buss. Human–robot collaboration: a survey. *Int J Humanoid Robotics*, 5(01):47–66, Apr 2008.

[9] A. Pervez and J. Ryu. Safe physical human robot interaction-past, present and future. *Journal of Mechanical Science and Technology*, 22(3):469, 2008.

[10] P. A. Lasota, T. Fong, J. A. Shah, et al. A survey of methods for safe human-robot interaction. *Foundations and Trends® in Robotics*, 5(4):261–349, 2017.

[11] P. Tsarouchi, S. Makris, and G. Chryssolouris. Human–robot interaction review and challenges on task planning and programming. *International Journal of Computer Integrated Manufacturing*, 29(8):916–931, 2016.

[12] J. Heinzmann and A. Zelinsky. Quantitative safety guarantees for physical human-robot interaction. *Int J Robotics Research*, 22(7-8):479–504, July 2003.

[13] D. Kulić and E. Croft. Pre-collision safety strategies for human-robot interaction. *Autonomous Robots*, 22(2):149–164, 2007.

[14] A. Kouris, F. Dimeas, and N. Aspragathos. A frequency domain approach for contact type distinction in human–robot collaboration. *IEEE Robot. Autom. Lett.*, 3(2):720–727, Jan 2018.

[15] G. Hu, C. Makkar, and W. E. Dixon. Energy-based nonlinear control of underactuated euler–lagrange systems subject to impacts. *IEEE Trans. Autom. Control*, 52(9):1742–1748, Sept 2007.

[16] S. Haddadin, A. Albu-Schaffer, A. De Luca, and G. Hirzinger. Collision detection and reaction: A contribution to safe physical human-robot interaction. In *Proc. IEEE Int. Conf. Robot. Syst.*, pages 3356–3363, Nice, France, Sept 2008.

[17] O. Khatib. Real-time obstacle avoidance for manipulators and mobile robots. In *Autonomous robot vehicles*, pages 396–404. Springer, 1986.

[18] M. Kimmel and S. Hirche. Active safety control for dynamic human-robot interaction. In *Proc. IEEE Intell. Robot. Syst.*, pages 4685–4691, Hamburg, Germany, Sept 2015.

[19] M. S. Wiig, K. Y. Pettersen, and T. R. Krogstad. Collision avoidance for underactuated marine vehicles using the constant avoidance angle algorithm. *IEEE Transactions on Control Systems Technology*, 2019.

[20] W. E. Dixon, I. D. Walker, D. M. Dawson, and J. P. Hartranft. Fault detection for robot manipulators with parametric uncertainty: A prediction-error-based approach. *IEEE Transactions on Robotics and Automation*, 16(6):689–699, 2000.

[21] M. Geravand, F. Flacco, and A. De Luca. Human-robot physical interaction and collaboration using an industrial robot with a closed control architecture. In *2013 IEEE International Conference on Robotics and Automation*, pages 4000–4007. IEEE, 2013.

[22] Z. Kingston, M. Moll, and L. E. Kavraki. Sampling-based methods for motion planning with constraints. *Annual review of control, robotics, and autonomous systems*, 1:159–185, 2018.

[23] Y. Huang, H. Ding, Y. Zhang, H. Wang, D. Cao, N. Xu, and C. Hu. A motion planning and tracking framework for autonomous vehicles based on artificial potential field elaborated resistance network approach. *IEEE Transactions on Industrial Electronics*, 67(2):1376–1386, 2019.

[24] J. Mareczek, M. Buss, and M. W. Spong. Invariance control for a class of cascade nonlinear systems. *IEEE Transactions on Automatic Control*, 47(4):636–640, 2002.

[25] J. Wolff and M. Buss. Invariance control design for nonlinear control affine systems under hard state constraints. *IFAC Proceedings Volumes*, 37(13):555–560, 2004.

[26] S. Norouzzadeh, T. Lorenz, and S. Hirche. Towards safe physical human-robot interaction: an online optimal control scheme. In *2012 IEEE RO-MAN: The 21st IEEE International Symposium on Robot and Human Interactive Communication*, pages 503–508. IEEE, 2012.

[27] J. Wilson, M. Charest, and R. Dubay. Non-linear model predictive control schemes with application on a 2 link vertical robot manipulator. *Robotics and Computer-Integrated Manufacturing*, 41:23–30, 2016.

[28] F. Guo, Y. Liu, and F. Luo. Adaptive stabilisation of a flexible riser by using the lyapunov-based barrier backstepping technique. *IET Control Theory & Applications*, 11(14):2252–2260, 2017.

[29] K. B. Ngo, R. Mahony, and Z.-P. Jiang. Integrator backstepping using barrier functions for systems with multiple state constraints. In *Proceedings of the 44th IEEE Conference on Decision and Control*, pages 8306–8312. IEEE, 2005.

[30] B. Niu and J. Zhao. Barrier lyapunov functions for the output tracking control of constrained nonlinear switched systems. *Systems & Control Letters*, 62(10):963–971, 2013.

[31] J.-H. Shin and J.-J. Lee. Fault detection and robust fault recovery control for robot manipulators with actuator failures. In *Proceedings 1999 IEEE International Conference on Robotics and Automation (Cat. No. 99CH36288C)*, volume 2, pages 861–866. IEEE, 1999.

[32] T. S. Wikman, M. S. Branicky, and W. S. Newman. Reflex control for robot system preservation, reliability and autonomy. *Computers & electrical engineering*, 20(5):391–407, 1994.

[33] R. Isermann. Process fault detection based on modeling and estimation methods—a survey. *automatica*, 20(4):387–404, 1984.

[34] K. Suita, Y. Yamada, N. Tsuchida, K. Imai, H. Ikeda, and N. Sugimoto. A failure-to-safety" kyozon" system with simple contact detection and stop capabilities for safe human-autonomous robot coexistence. In *Proceedings of 1995 IEEE International Conference on Robotics and Automation*, volume 3, pages 3089–3096. IEEE, 1995.

[35] M. Thirumarimurugan, N. Bagyalakshmi, and P. Paarkavi. Comparison of fault detection and isolation methods: A review. In *2016 10th International Conference on Intelligent Systems and Control (ISCO)*, pages 1–6. IEEE, 2016.

[36] J. Gertler. Analytical redundancy methods in fault detection and isolation-survey and synthesis. *IFAC Proceedings Volumes*, 24(6):9–21, 1991.

[37] M. Basseville. Information criteria for residual generation and fault detection and isolation. *Automatica*, 33(5):783–803, 1997.

[38] W. Brockmann and N. Rosemann. Instantaneous anomaly detection in online learning fuzzy systems. In *2008 3rd International Workshop on Genetic and Evolving Systems*, pages 23–28. IEEE, 2008.

[39] K. Smarsly and K. H. Law. Decentralized fault detection and isolation in wireless structural health monitoring systems using analytical redundancy. *Advances in Engineering Software*, 73:1–10, 2014.

[40] S. Anwar and L. Chen. An analytical redundancy-based fault detection and isolation algorithm for a road-wheel control subsystem in a steer-by-wire system. *IEEE Transactions on Vehicular Technology*, 56(5):2859–2869, 2007.

[41] F. Yamaoka, T. Kanda, H. Ishiguro, and N. Hagita. A model of proximity control for information-presenting robots. *IEEE Transactions on Robotics*, 26(1):187–195, 2009.

[42] K. Dautenhahn, M. Walters, S. Woods, K. L. Koay, C. L. Nehaniv, A. Sisbot, R. Alami, and T. Siméon. How may i serve you? a robot companion approaching a seated person in a helping context. In *Proceedings of the 1st ACM SIGCHI/SIGART conference on Human-robot interaction*, pages 172–179, 2006.

[43] A. D. Dragan, K. C. Lee, and S. S. Srinivasa. Legibility and predictability of robot motion. In *2013 8th ACM/IEEE International Conference on Human-Robot Interaction (HRI)*, pages 301–308. IEEE, 2013.

[44] T. Kanda, H. Ishiguro, T. Ono, M. Imai, and R. Nakatsu. Development and evaluation of an interactive humanoid robot" robovie". In *Proceedings 2002 IEEE International Conference on Robotics and Automation (Cat. No. 02CH37292)*, volume 2, pages 1848–1855. IEEE, 2002.

[45] A. Colomé, D. Pardo, G. Alenya, and C. Torras. External force estimation during compliant robot manipulation. In *2013 IEEE International Conference on Robotics and Automation*, pages 3535–3540. IEEE, 2013.

[46] F. Caccavale and I. D. Walker. Observer-based fault detection for robot manipulators. In *Proceedings of International Conference on Robotics and Automation*, volume 4, pages 2881–2887. IEEE, 1997.

[47] C. C. De Wit and J.-J. Slotine. Sliding observers for robot manipulators. *Automatica*, 27(5):859–864, 1991.

[48] C. Edwards, S. K. Spurgeon, and R. J. Patton. Sliding mode observers for fault detection and isolation. *Automatica*, 36(4):541–553, 2000.

[49] L. M. Capisani, A. Ferrara, A. F. De Loza, and L. M. Fridman. Manipulator fault diagnosis via higher order sliding-mode observers. *IEEE Transactions on Industrial Electronics*, 59(10):3979–3986, 2012.

[50] G. Antonelli, F. Caccavale, S. Chiaverini, and L. Villani. Tracking control for underwater vehicle-manipulator systems with velocity estimation. *IEEE Journal of Oceanic Engineering*, 25(3):399–413, 2000.

[51] R.-J. Wai. Tracking control based on neural network strategy for robot manipulator. *Neurocomputing*, 51:425–445, 2003.

[52] S. Mobayen, F. Tchier, and L. Ragoub. Design of an adaptive tracker for n-link rigid robotic manipulators based on super-twisting global nonlinear sliding mode control. *International Journal of Systems Science*, 48(9):1990–2002, 2017.

[53] Y. Kali, M. Saad, and K. Benjelloun. Optimal super-twisting algorithm with time delay estimation for robot manipulators based on feedback linearization. *Robotics and Autonomous Systems*, 108:87–99, 2018.

[54] A. H. Khan, S. Li, and X. Luo. Obstacle avoidance and tracking control of redundant robotic manipulator: An rnn-based metaheuristic approach. *IEEE Transactions on Industrial Informatics*, 16(7):4670–4680, 2019.

[55] B. Siciliano and O. Khatib. *Handbook of Robotics*. Springer, Berlin and Heidelberg, 2007.

[56] V. Utkin, J. Guldner, and J. Shi. *Sliding mode control in electro-mechanical systems*. Taylor & Francis, 1999.

[57] P. A. Hancock, D. R. Billings, K. E. Schaefer, J. Y. Chen, E. J. De Visser, and R. Parasuraman. A meta-analysis of factors affecting trust in human-robot interaction. *Human factors*, 53(5):517–527, 2011.

[58] M. Salem, G. Lakatos, F. Amirabdollahian, and K. Dautenhahn. Would you trust a (faulty) robot? effects of error, task type and personality on human-robot cooperation and trust. In *2015 10th ACM/IEEE International Conference on Human-Robot Interaction (HRI)*, pages 1–8. IEEE, 2015.

[59] C. Bartneck and J. Forlizzi. A design-centred framework for social human-robot interaction. In *RO-MAN 2004. 13th IEEE international workshop on robot and human interactive communication (IEEE Catalog No. 04TH8759)*, pages 591–594. IEEE, 2004.

[60] C. L. Bethel, K. Salomon, R. R. Murphy, and J. L. Burke. Survey of psychophysiology measurements applied to human-robot interaction. In *RO-MAN 2007-The 16th IEEE International Symposium on Robot and Human Interactive Communication*, pages 732–737. IEEE, 2007.

[61] P. A. Lasota and J. A. Shah. Analyzing the effects of human-aware motion planning on close-proximity human–robot collaboration. *Human factors*, 57(1):21–33, 2015.

[62] T. Kruse, P. Basili, S. Glasauer, and A. Kirsch. Legible robot navigation in the proximity of moving humans. In *2012 IEEE Workshop on Advanced Robotics and its Social Impacts (ARSO)*, pages 83–88. IEEE, 2012.

[63] M. S. Khireddine, K. Chafaa, N. Slimane, and A. Boutarfa. Sensor and actuator fault diagnosis based on soft computing techniques. *Journal of Intelligent Systems*, 24(1):1–21, 2015.

[64] W.-H. Chen, D. J. Ballance, P. J. Gawthrop, and J. O'Reilly. A nonlinear disturbance observer for robotic manipulators. *IEEE Transactions on industrial Electronics*, 47(4):932–938, 2000.

[65] W. Chen and M. Saif. Robust fault detection and isolation in constrained nonlinear systems via a second order sliding mode observer. *IFAC Proceedings Volumes*, 35(1):269–274, 2002.

[66] B. Bona and M. Indri. Analysis and implementation of observers for robotic manipulators. In *Proceedings. 1998 IEEE International Conference on Robotics and Automation (Cat. No. 98CH36146)*, volume 4, pages 3006–3011. IEEE, 1998.

[67] W. Kim, D. Shin, D. Won, and C. C. Chung. Disturbance-observer-based position tracking controller in the presence of biased sinusoidal disturbance for electrohydraulic actuators. *IEEE Transactions on Control Systems Technology*, 21(6):2290–2298, 2013.

[68] A. De Luca and R. Mattone. Actuator failure detection and isolation using generalized momenta. In *2003 IEEE International Conference on Robotics and Automation (Cat. No. 03CH37422)*, volume 1, pages 634–639. IEEE, 2003.

[69] K. Narukawa, T. Yoshiike, K. Tanaka, and M. Kuroda. Real-time collision detection based on one class svm for safe movement of humanoid robot. In *Proc. IEEE Humanoid Robotics*, pages 791–796, Birmingham, United Kindom, Nov 2017.

[70] S. Golz, C. Osendorfer, and S. Haddadin. Using tactile sensation for learning contact knowledge: Discriminate collision from physical interaction. In *2015 IEEE International Conference on Robotics and Automation (ICRA)*, pages 3788–3794. IEEE, 2015.

[71] D. Kulić and E. A. Croft. Safe planning for human-robot interaction. *Journal of Robotic Systems*, 22(7):383–396, 2005.

[72] A. Chakraborty, P. Seiler, and G. J. Balas. Nonlinear region of attraction analysis for flight control verification and validation. *Control Engineering Practice*, 19(4):335–345, 2011.

[73] F. Berkenkamp, R. Moriconi, A. P. Schoellig, and A. Krause. Safe learning of regions of attraction for uncertain, nonlinear systems with gaussian processes. In *2016 IEEE 55th Conference on Decision and Control (CDC)*, pages 4661–4666. IEEE, 2016.

[74] A. Guendouzi, A. Boubakir, and M. Hamerlain. Higher order sliding mode control of robot manipulator. In *Proceedings of the 9th International Conference on Autonomic and Autonomous Systems*, pages 61–66, 2013.

[75] A. Ferrara and G. P. Incremona. Design of an integral suboptimal second-order sliding mode controller for the robust motion control of robot manipulators. *IEEE Transactions on Control Systems Technology*, 23(6):2316–2325, 2015.

[76] P. M. Frank. Fault diagnosis in dynamic systems using analytical and knowledge-based redundancy: A survey and some new results. *automatica*, 26(3):459–474, 1990.

[77] C. L. Bethel and R. R. Murphy. Review of human studies methods in hri and recommendations. *International Journal of Social Robotics*, 2(4):347–359, 2010.

[78] A. K. Akametalu, J. F. Fisac, J. H. Gillula, S. Kaynama, M. N. Zeilinger, and C. J. Tomlin. Reachability-based safe learning with gaussian processes. In *53rd IEEE Conference on Decision and Control*, pages 1424–1431. IEEE, 2014.

[79] B. Jiang, M. Staroswiecki, and V. Cocquempot. Fault accommodation for nonlinear dynamic systems. *IEEE Transactions on automatic Control*, 51(9):1578–1583, 2006.

[80] A. De Luca and L. Ferrajoli. Exploiting robot redundancy in collision detection and reaction. In *2008 IEEE/RSJ International Conference on Intelligent Robots and Systems*, pages 3299–3305. IEEE, 2008.

[81] T. Lau, S. A. Wolfman, P. Domingos, and D. S. Weld. Programming by demonstration using version space algebra. *Machine Learning*, 53(1-2):111–156, 2003.

[82] S. Calinon and A. Billard. Statistical learning by imitation of competing constraints in joint space and task space. *Advanced Robotics*, 23(15):2059–2076, 2009.

[83] G. Charalambous, S. Fletcher, and P. Webb. The development of a scale to evaluate trust in industrial human-robot collaboration. *International Journal of Social Robotics*, 8(2):193–209, 2016.

[84] I. Gaudiello, E. Zibetti, S. Lefort, M. Chetouani, and S. Ivaldi. Trust as indicator of robot functional and social acceptance. an experimental study on user conformation to icub answers. *Computers in Human Behavior*, 61:633–655, 2016.

[85] K. Hoang Dinh, O. S. Oguz, M. Elsayed, and D. Wollherr. Adaptation and transfer of robot motion policies for close proximity human-robot interaction. *Frontiers in Robotics and AI*, 6:69, 2019.

[86] A. Crespi, K. Karakasiliotis, A. Guignard, and A. J. Ijspeert. Salamandra robotica ii: an amphibious robot to study salamander-like swimming and walking gaits. *IEEE Transactions on Robotics*, 29(2):308–320, 2013.

[87] H. Wei, Y. Cai, H. Li, D. Li, and T. Wang. Sambot: A self-assembly modular robot for swarm robot. In *2010 IEEE International Conference on Robotics and Automation*, pages 66–71. IEEE, 2010.

[88] Mining robots in the future. [EB/OL]. `https://blog.robotiq.com/discussing-the-future-of-mining-robots-with-prof.-jung` Accessed Aug 26, 2020.

[89] S. L. Anderson. Asimov's "three laws of robotics" and machine metaethics. *Ai & Society*, 22(4):477–493, 2008.

[90] Principles of robotics. [EB/OL]. `https://epsrc.ukri.org/research/ourportfolio/themes/engineering/activities/principlesofrobotics/` Accessed May 30, 2020.

[91] Iso/ts 15066:2016. [EB/OL]. `https://www.iso.org/standard/62996.html/` Accessed May 30, 2020.

[92] E. Bekele and N. Sarkar. Psychophysiological feedback for adaptive human–robot interaction (hri). In *Advances in physiological computing*, pages 141–167. Springer, 2014.

[93] B. R. Donald. A geometric approach to error detection and recovery for robot motion planning with uncertainty. Technical report, Cornell University, 1988.

[94] R. Ross, R. Collier, and G. M. O'Hare. Demonstrating social error recovery with agentfactory. In *Proceedings of the Third International Joint Conference on Autonomous Agents and Multiagent Systems-Volume 3*, pages 1424–1425, 2004.

[95] T. Takeda, Y. Hirata, and K. Kosuge. Hmm-based error recovery of dance step selection for dance partner robot. In *Proceedings 2007 IEEE International Conference on Robotics and Automation*, pages 1768–1773. IEEE, 2007.

[96] A. Nakamura, K. Nagata, K. Harada, N. Yamanobe, T. Tsuji, T. Foissotte, and Y. Kawai. Error recovery using task stratification and error classification for manipulation robots in various fields. In *2013 IEEE/RSJ International Conference on Intelligent Robots and Systems*, pages 3535–3542. IEEE, 2013.

[97] J. Carlson, R. R. Murphy, and A. Nelson. Follow-up analysis of mobile robot failures. In *IEEE International Conference on Robotics and Automation, 2004. Proceedings. ICRA'04. 2004*, volume 5, pages 4987–4994. IEEE, 2004.

[98] T. Uchida, T. Minato, T. Koyama, and H. Ishiguro. Who is responsible for a dialogue breakdown? an error recovery strategy that promotes cooperative intentions

from humans by mutual attribution of responsibility in human-robot dialogues. *Frontiers in Robotics and AI*, 6:29, 2019.

[99] Y. Ting, S. Tosunoglu, and D. Tesar. A control structure for fault-tolerant operation of robotic manipulators. In *[1993] Proceedings IEEE International Conference on Robotics and Automation*, pages 684–690. IEEE, 1993.

[100] M. L. Visinsky, I. D. Walker, and J. R. Cavallaro. Layered dynamic fault detection and tolerance for robots. In *[1993] Proceedings IEEE International Conference on Robotics and Automation*, pages 180–187. IEEE, 1993.

[101] R. Isermann and P. Balle. Trends in the application of model-based fault detection and diagnosis of technical processes. *Control engineering practice*, 5(5):709–719, 1997.

[102] R. Canham, A. H. Jackson, and A. Tyrrell. Robot error detection using an artificial immune system. In *NASA/DoD Conference on Evolvable Hardware, 2003. Proceedings.*, pages 199–207. IEEE, 2003.

[103] O. Pettersson. Execution monitoring in robotics: A survey. *Robotics and Autonomous Systems*, 53(2):73–88, 2005.

[104] J. Hutchinson, M. J. Kaiser, and H. M. Lankarani. The head injury criterion (hic) functional. *Applied mathematics and computation*, 96(1):1–16, 1998.

[105] H.-W. Henn. Crash tests and the head injury criterion. *Teaching mathematics and its applications*, 17(4):162–170, 1998.

[106] S. Haddadin, A. Albu-Schäffer, and G. Hirzinger. Safety evaluation of physical human-robot interaction via crash-testing. In *Robotics: Science and Systems*, volume 3, pages 217–224. Citeseer, 2007.

[107] S. Haddadin, A. Albu-Schaffer, M. Strohmayr, M. Frommberger, and G. Hirzinger. Injury evaluation of human-robot impacts. In *2008 IEEE International Conference on Robotics and Automation*, pages 2203–2204. IEEE, 2008.

[108] F. Lin. Diagnosability of discrete event systems and its applications. *Discrete Event Dynamic Systems*, 4(2):197–212, 1994.

[109] A. Schicketmueller, J. Lamprecht, M. Hofmann, M. Sailer, and G. Rose. Gait event detection for stroke patients during robot-assisted gait training. *Sensors*, 20(12):3399, 2020.

[110] J. K. Mills and D. M. Lokhorst. Control of robotic manipulators during general task execution: A discontinuous control approach. *Int J Robotics Research*, 12(2):146–163, Apr 1993.

[111] Z. Wang, A. Peer, and M. Buss. An hmm approach to realistic haptic human-robot interaction. In *World Haptics 2009-Third Joint EuroHaptics conference and Symposium on Haptic Interfaces for Virtual Environment and Teleoperator Systems*, pages 374–379. IEEE, 2009.

[112] L. T. Kohn, J. M. Corrigan, M. S. Donaldson, T. McKay, and K. Pike. To err is human. *building a safer health system*, 600:2000, 2000.

[113] Y. Kobayashi, M. Onishi, S. Hosoe, and Z. Luo. Multi-tasking arbitration and behaviour design for human-interactive robots. *International journal of systems science*, 44(5):795–811, 2013.

[114] A. Swein and H. Guttmann. Handbook of human reliability analysis with emphasis on nuclear power plant application. *NUREG/CR-1278*, 1983.

[115] A. Rizzo, S. Bagnara, and M. Visciola. Human error detection processes. *International journal of man-machine studies*, 27(5-6):555–570, 1987.

[116] Y. Yamada, T. Morizono, Y. Umetani, and T. Yamamoto. Human error recovery for a human/robot parts conveyance system. In *Proceedings 2002 IEEE International Conference on Robotics and Automation (Cat. No. 02CH37292)*, volume 2, pages 2004–2009. IEEE, 2002.

[117] D. A. Norman. Categorization of action slips. *Psychological review*, 88(1):1, 1981.

[118] E. Dale and J. S. Chall. The concept of readability. *Elementary English*, 26(1):19–26, 1949.

[119] P. Kember and D. Varley. The legibility and readability of a visual display unit at threshold. *Ergonomics*, 30(6):925–931, 1987.

[120] J. Collins and R. Hall. Legibility and readability of light refecting matrix variable message road signs. *Lighting Research & Technology*, 24(3):143–148, 1992.

[121] L. Takayama, D. Dooley, and W. Ju. Expressing thought: improving robot readability with animation principles. In *Proceedings of the 6th international conference on Human-robot interaction*, pages 69–76, 2011.

[122] T. Chakraborti, A. Kulkarni, S. Sreedharan, D. E. Smith, and S. Kambhampati. Explicability? legibility? predictability? transparency? privacy? security? the emerging landscape of interpretable agent behavior. In *Proceedings of the international conference on automated planning and scheduling*, pages 86–96, 2019.

[123] A. D. Dragan, S. Bauman, J. Forlizzi, and S. S. Srinivasa. Effects of robot motion on human-robot collaboration. In *2015 10th ACM/IEEE International Conference on Human-Robot Interaction (HRI)*, pages 51–58. IEEE, 2015.

[124] C. Breazeal and B. Scassellati. Robots that imitate humans. *Trends in cognitive sciences*, 6(11):481–487, 2002.

[125] F. Yamaoka, T. Kanda, H. Ishiguro, and N. Hagita. " lifelike" behavior of communication robots based on developmental psychology findings. In *5th IEEE-RAS International Conference on Humanoid Robots, 2005.*, pages 406–411. IEEE, 2005.

[126] P. Liu, D. F. Glas, T. Kanda, H. Ishiguro, and N. Hagita. How to train your robot-teaching service robots to reproduce human social behavior. In *The 23rd IEEE International Symposium on Robot and Human Interactive Communication*, pages 961–968. IEEE, 2014.

[127] A. Sciutti, M. Mara, V. Tagliasco, and G. Sandini. Humanizing human-robot interaction: On the importance of mutual understanding. *IEEE Technology and Society Magazine*, 37(1):22–29, 2018.

[128] J. Bütepage, H. Kjellström, and D. Kragic. Anticipating many futures: Online human motion prediction and generation for human-robot interaction. In *2018 IEEE international conference on robotics and automation (ICRA)*, pages 1–9. IEEE, 2018.

[129] J. Mainprice and D. Berenson. Human-robot collaborative manipulation planning using early prediction of human motion. In *2013 IEEE/RSJ International Conference on Intelligent Robots and Systems*, pages 299–306. IEEE, 2013.

[130] E. Nakano, H. Imamizu, R. Osu, Y. Uno, H. Gomi, T. Yoshioka, and M. Kawato. Quantitative examinations of internal representations for arm trajectory planning: minimum commanded torque change model. *Journal of Neurophysiology*, 81(5):2140–2155, 1999.

[131] X. Broquere, D. Sidobre, and K. Nguyen. From motion planning to trajectory control with bounded jerk for service manipulator robots. In *2010 IEEE International Conference on Robotics and Automation*, pages 4505–4510. IEEE, 2010.

[132] T. Morita, K. Shibuya, and S. Sugano. Design and control of mobile manipulation system for human symbiotic humanoid: Hadaly-2. In *Proceedings. 1998 IEEE International Conference on Robotics and Automation (Cat. No. 98CH36146)*, volume 2, pages 1315–1320. IEEE, 1998.

[133] F. D. Davis. Perceived usefulness, perceived ease of use, and user acceptance of information technology. *MIS quarterly*, pages 319–340, 1989.

[134] D.-H. Shin and H. Choo. Modeling the acceptance of socially interactive robotics: Social presence in human–robot interaction. *Interaction Studies*, 12(3):430–460, 2011.

[135] V. Venkatesh, M. G. Morris, G. B. Davis, and F. D. Davis. User acceptance of information technology: Toward a unified view. *MIS quarterly*, pages 425–478, 2003.

[136] A. Weiss, R. Bernhaupt, M. Tscheligi, D. Wollherr, K. Kuhnlenz, and M. Buss. A methodological variation for acceptance evaluation of human-robot interaction in public places. In *RO-MAN 2008-The 17th IEEE International Symposium on Robot and Human Interactive Communication*, pages 713–718. IEEE, 2008.

[137] A. Kupferberg, S. Glasauer, M. Huber, M. Rickert, A. Knoll, and T. Brandt. Biological movement increases acceptance of humanoid robots as human partners in motor interaction. *AI & society*, 26(4):339–345, 2011.

[138] R. Kirby, R. Simmons, and J. Forlizzi. Companion: A constraint-optimizing method for person-acceptable navigation. In *RO-MAN 2009-The 18th IEEE International Symposium on Robot and Human Interactive Communication*, pages 607–612. IEEE, 2009.

[139] V. M. Olivera and R. Simmons. Implementing human-acceptable navigational behavior and a fuzzy controller for an autonomous robot. In *Proceedings WAF: 3rd workshop on physical agents*, pages 113–120, 2002.

[140] M. Itoh and K. Tanaka. Mathematical modeling of trust in automation: Trust, distrust, and mistrust. In *Proceedings of the human factors and ergonomics society annual meeting*, volume 44, pages 9–12. SAGE Publications Sage CA: Los Angeles, CA, 2000.

[141] A. Freedy, E. DeVisser, G. Weltman, and N. Coeyman. Measurement of trust in human-robot collaboration. In *2007 International Symposium on Collaborative Technologies and Systems*, pages 106–114. IEEE, 2007.

[142] R. E. Yagoda and D. J. Gillan. You want me to trust a robot? the development of a human–robot interaction trust scale. *International Journal of Social Robotics*, 4(3):235–248, 2012.

[143] A. Bruce, I. Nourbakhsh, and R. Simmons. The role of expressiveness and attention in human-robot interaction. In *Proceedings 2002 IEEE international conference on robotics and automation (Cat. No. 02CH37292)*, volume 4, pages 4138–4142. IEEE, 2002.

[144] E. A. Sisbot, L. F. Marin, and R. Alami. Spatial reasoning for human robot interaction. In *2007 IEEE/RSJ International Conference on Intelligent Robots and Systems*, pages 2281–2287. IEEE, 2007.

[145] M. Giuliani, M. E. Foster, A. Isard, C. Matheson, J. Oberlander, and A. Knoll. Situated reference in a hybrid human-robot interaction system. In *Proceedings of the 6th international natural language generation conference*, pages 67–75. Association for Computational Linguistics, 2010.

[146] M. K. Lee and M. Makatchev. How do people talk with a robot? an analysis of human-robot dialogues in the real world. In *CHI'09 Extended Abstracts on*

Human Factors in Computing Systems, pages 3769–3774, New York, NY, USA, 2009. Association for Computing Machinery.

[147] M. Giersich, P. Forbrig, G. Fuchs, T. Kirste, D. Reichart, and H. Schumann. Towards an integrated approach for task modeling and human behavior recognition. In *International Conference on Human-Computer Interaction*, pages 1109–1118. Springer, 2007.

[148] C. Lenz, S. Nair, M. Rickert, A. Knoll, W. Rosel, J. Gast, A. Bannat, and F. Wallhoff. Joint-action for humans and industrial robots for assembly tasks. In *RO-MAN 2008-The 17th IEEE International Symposium on Robot and Human Interactive Communication*, pages 130–135. IEEE, 2008.

[149] A. Stewart, M. Cao, A. Nedic, D. Tomlin, and N. Leonard. Towards human–robot teams: Model-based analysis of human decision making in two-alternative choice tasks with social feedback. *Proceedings of the IEEE*, 100(3):751–775, 2011.

[150] R. G. Meulenbroek, J. Bosga, M. Hulstijn, and S. Miedl. Joint-action coordination in transferring objects. *Experimental Brain Research*, 180(2):333–343, 2007.

[151] E. C. Grigore, K. Eder, A. G. Pipe, C. Melhuish, and U. Leonards. Joint action understanding improves robot-to-human object handover. In *2013 IEEE/RSJ International Conference on Intelligent Robots and Systems*, pages 4622–4629. IEEE, 2013.

[152] S. Nikolaidis, R. Ramakrishnan, K. Gu, and J. Shah. Efficient model learning from joint-action demonstrations for human-robot collaborative tasks. In *2015 10th ACM/IEEE International Conference on Human-Robot Interaction (HRI)*, pages 189–196. IEEE, 2015.

[153] T. Flash and N. Hogan. The coordination of arm movements: an experimentally confirmed mathematical model. *Journal of neuroscience*, 5(7):1688–1703, 1985.

[154] A. Mörtl, T. Lorenz, B. N. Vlaskamp, A. Gusrialdi, A. Schubö, and S. Hirche. Modeling inter-human movement coordination: synchronization governs joint task dynamics. *Biological cybernetics*, 106(4-5):241–259, 2012.

[155] Y. Li, K. P. Tee, W. L. Chan, R. Yan, Y. Chua, and D. K. Limbu. Role adaptation of human and robot in collaborative tasks. In *2015 IEEE International Conference on Robotics and Automation (ICRA)*, pages 5602–5607. IEEE, 2015.

[156] A. Mörtl, M. Lawitzky, A. Kucukyilmaz, M. Sezgin, C. Basdogan, and S. Hirche. The role of roles: Physical cooperation between humans and robots. *The International Journal of Robotics Research*, 31(13):1656–1674, 2012.

[157] T. Sato, M. Hashimoto, and M. Tsukahara. Synchronization based control using online design of dynamics and its application to human-robot interaction. In *2007 IEEE International Conference on Robotics and Biomimetics (ROBIO)*, pages 652–657. IEEE, 2007.

[158] M. Giuliani, N. Mirnig, G. Stollnberger, S. Stadler, R. Buchner, and M. Tscheligi. Systematic analysis of video data from different human–robot interaction studies: a categorization of social signals during error situations. *Frontiers in psychology*, 6:931, 2015.

[159] A. H. Mason and C. L. MacKenzie. Grip forces when passing an object to a partner. *Experimental brain research*, 163(2):173–187, 2005.

[160] W. P. Chan, C. A. Parker, H. M. Van der Loos, and E. A. Croft. Grip forces and load forces in handovers: implications for designing human-robot handover controllers. In *Proceedings of the seventh annual ACM/IEEE international conference on Human-Robot Interaction*, pages 9–16, 2012.

[161] Z. Wang, A. Peer, and M. Buss. Fast online impedance estimation for robot control. In *2009 IEEE International Conference on Mechatronics*, pages 1–6. IEEE, 2009.

[162] R. S. Dahiya, G. Metta, M. Valle, and G. Sandini. Tactile sensing—from humans to humanoids. *IEEE transactions on robotics*, 26(1):1–20, 2009.

[163] E. I. Barakova and T. Lourens. Expressing and interpreting emotional movements in social games with robots. *Personal and ubiquitous computing*, 14(5):457–467, 2010.

[164] Y. Xiao, J. Yuan, and D. Thalmann. Human-virtual human interaction by upper body gesture understanding. In *Proceedings of the 19th ACM symposium on virtual reality software and technology*, pages 133–142, 2013.

[165] D. E. Cahya, R. Ramakrishnan, and M. Giuliani. Static and temporal differences in social signals between error-free and erroneous situations in human-robot collaboration. In *Social Robotics*, pages 189–199, Cham, 2019. Springer International Publishing.

[166] T. Kanda, H. Ishiguro, M. Imai, and T. Ono. Body movement analysis of human-robot interaction. In *IJCAI*, volume 3, pages 177–182. Citeseer, 2003.

[167] M. Huber, A. Knoll, T. Brandt, and S. Glasauer. Handing over a cube. *Annals of the New York Academy of Sciences*, 1164(1):380–382, 2009.

[168] A. Koene, A. Remazeilles, M. Prada, A. Garzo, M. Puerto, S. Endo, and A. M. Wing. Relative importance of spatial and temporal precision for user satisfaction in human-robot object handover interactions. In *Third International Symposium on New Frontiers in Human-Robot Interaction*, 2014.

[169] H. Kazerooni. Human-robot interaction via the transfer of power and information signals. *IEEE Transactions on systems, Man, and Cybernetics*, 20(2):450–463, 1990.

[170] T. Baur, G. Mehlmann, I. Damian, F. Lingenfelser, J. Wagner, B. Lugrin, E. André, and P. Gebhard. Context-aware automated analysis and annotation of social human–agent interactions. *ACM Transactions on Interactive Intelligent Systems (TiiS)*, 5(2):1–33, 2015.

[171] A. Vinciarelli, M. Pantic, D. Heylen, C. Pelachaud, I. Poggi, F. D'Errico, and M. Schroeder. Bridging the gap between social animal and unsocial machine: A survey of social signal processing. *IEEE Transactions on Affective Computing*, 3(1):69–87, 2011.

[172] M. Joosse, A. Sardar, and V. Evers. Behave: A set of measures to assess users' attitudinal and non-verbal behavioral responses to a robot's social behaviors. In *International Conference on Social Robotics*, pages 84–94. Springer, 2011.

[173] E. T. Hall. *The hidden dimension*, volume 609. Garden City, NY: Doubleday, 1966.

[174] J. Rios-Martinez, A. Spalanzani, and C. Laugier. From proxemics theory to socially-aware navigation: A survey. *International Journal of Social Robotics*, 7(2):137–153, 2015.

[175] D. Helbing and P. Molnar. Social force model for pedestrian dynamics. *Physical review E*, 51(5):4282, 1995.

[176] M. P. Michalowski, S. Sabanovic, and R. Simmons. A spatial model of engagement for a social robot. In *9th IEEE International Workshop on Advanced Motion Control, 2006.*, pages 762–767. IEEE, 2006.

[177] G. Ferrer, A. Garrell, and A. Sanfeliu. Robot companion: A social-force based approach with human awareness-navigation in crowded environments. In *2013 IEEE/RSJ International Conference on Intelligent Robots and Systems*, pages 1688–1694. IEEE, 2013.

[178] C. Wang, Y. Li, S. S. Ge, and T. H. Lee. Adaptive control for robot navigation in human environments based on social force model. In *2016 IEEE International Conference on Robotics and Automation (ICRA)*, pages 5690–5695. IEEE, 2016.

[179] A. K. Pandey and R. Alami. A framework for adapting social conventions in a mobile robot motion in human-centered environment. In *2009 International Conference on Advanced Robotics*, pages 1–8. IEEE, 2009.

[180] D. Carton, A. Turnwald, D. Wollherr, and M. Buss. Proactively approaching pedestrians with an autonomous mobile robot in urban environments. In *Experimental Robotics*, pages 199–214. Springer, 2013.

[181] X. Wang and S. Wang. New approach of friction identification for electro-hydraulic servo system based on evolutionary algorithm and statistical logics with experiments. *Journal of Mechanical Science and Technology*, 30(5):2311–2317, 2016.

[182] R. Baddoura and G. Venture. Social vs. useful hri: experiencing the familiar, perceiving the robot as a sociable partner and responding to its actions. *International Journal of Social Robotics*, 5(4):529–547, 2013.

[183] T. Minato, M. Shimada, H. Ishiguro, and S. Itakura. Development of an android robot for studying human-robot interaction. In *International conference on Industrial, engineering and other applications of applied intelligent systems*, pages 424–434. Springer, 2004.

[184] M. Scheutz, P. Schermerhorn, J. Kramer, and D. Anderson. First steps toward natural human-like hri. *Autonomous Robots*, 22(4):411–423, 2007.

[185] K. Hayashi, M. Shiomi, T. Kanda, N. Hagita, and A. Robotics. Friendly patrolling: A model of natural encounters. In *Proc. RSS*, page 121, 2012.

[186] Y. Yamada, Y. Hirasawa, S. Huang, Y. Umetani, and K. Suita. Human-robot contact in the safeguarding space. *IEEE/ASME transactions on mechatronics*, 2(4):230–236, 1997.

[187] J. Scholtz. Theory and evaluation of human robot interactions. In *36th Annual Hawaii International Conference on System Sciences, 2003. Proceedings of the*, pages 10–pp. IEEE, 2003.

[188] W. T. Townsend and J. K. Salisbury. Mechanical design for whole-arm manipulation. In *Robots and Biological Systems: Towards a New Bionics?*, pages 153–164. Springer, 1993.

[189] A. Bicchi and G. Tonietti. Fast and" soft-arm" tactics [robot arm design]. *IEEE Robotics & Automation Magazine*, 11(2):22–33, 2004.

[190] M. Zinn, O. Khatib, B. Roth, and J. K. Salisbury. Playing it safe [human-friendly robots]. *IEEE Robotics & Automation Magazine*, 11(2):12–21, 2004.

[191] G. Tonietti, R. Schiavi, and A. Bicchi. Design and control of a variable stiffness actuator for safe and fast physical human/robot interaction. In *Proceedings of the 2005 IEEE international conference on robotics and automation*, pages 526–531. IEEE, 2005.

[192] C. Loughlin, A. Albu-Schäffer, S. Haddadin, C. Ott, A. Stemmer, T. Wimböck, and G. Hirzinger. The dlr lightweight robot: design and control concepts for robots in human environments. *Industrial Robot: an international journal*, 34(5):376–385, 2007.

[193] S. Wolf and G. Hirzinger. A new variable stiffness design: Matching requirements of the next robot generation. In *2008 IEEE International Conference on Robotics and Automation*, pages 1741–1746. IEEE, 2008.

[194] M. Zinn, B. Roth, O. Khatib, and J. K. Salisbury. A new actuation approach for human friendly robot design. *The international journal of robotics research*, 23(4-5):379–398, 2004.

[195] M. C. F. Castro and A. Cliquet. A low-cost instrumented glove for monitoring forces during object manipulation. *IEEE Transactions on Rehabilitation Engineering*, 5(2):140–147, 1997.

[196] Z. Wang, J. Hoelldampf, and M. Buss. Design and performance of a haptic data acquisition glove. In *Proceedings of the 10th Annual International Workshop on Presence*, pages 349–357, 2007.

[197] E. Magrini, F. Flacco, and A. De Luca. Control of generalized contact motion and force in physical human-robot interaction. In *2015 IEEE international conference on robotics and automation (ICRA)*, pages 2298–2304. IEEE, 2015.

[198] A. Cherubini, R. Passama, A. Crosnier, A. Lasnier, and P. Fraisse. Collaborative manufacturing with physical human–robot interaction. *Robotics and Computer-Integrated Manufacturing*, 40:1 – 13, 2016.

[199] S. Thrun. Toward a framework for human-robot interaction. *Human–Computer Interaction*, 19(1-2):9–24, 2004.

[200] Z. Wang, J. Yuan, and M. Buss. Modelling of human haptic skill: A framework and preliminary results. *IFAC Proceedings Volumes*, 41(2):14761–14766, 2008.

[201] F. D'Ippolito, F. Alonge, and E. Cucco. Contact estimation in robot interaction. *International Journal of Advanced Robotic Systems*, 11(7):96, 2014.

[202] R. Muradore and P. Fiorini. A pls-based statistical approach for fault detection and isolation of robotic manipulators. *IEEE Transactions on Industrial Electronics*, 59(8):3167–3175, 2011.

[203] M. Dev Anand, T. Selvaraj, and S. Kumanan. Fault detection and fault tolerance methods for industrial robot manipulators based on hybrid intelligent approach. *Advances in Production Engineering & Management*, 7(4), 2012.

[204] I. Agriomallos, S. Doltsinis, I. Mitsioni, and Z. Doulgeri. Slippage detection generalizing to grasping of unknown objects using machine learning with novel features. *IEEE Robot. Autom. Lett.*, 3(2):942–948, Apr 2018.

[205] A.-N. Sharkawy, P. N. Koustoumpardis, and N. A. Aspragathos. Manipulator collision detection and collided link identification based on neural networks. In *International Conference on Robotics in Alpe-Adria Danube Region*, pages 3–12. Springer, 2018.

[206] R. J. Patton, C. Lopez-Toribio, and F. Uppal. Artificial intelligence approaches to fault diagnosis for dynamic systems. *International Journal of applied mathematics and computer science*, 9(3):471–518, 1999.

[207] D. Brambilla, L. M. Capisani, A. Ferrara, and P. Pisu. Fault detection for robot manipulators via second-order sliding modes. *IEEE Transactions on Industrial Electronics*, 55(11):3954–3963, 2008.

[208] D. Shi, E. G. Collins Jr, B. Goldiez, A. Donate, X. Liu, and D. Dunlap. Human-aware robot motion planning with velocity constraints. In *2008 International Symposium on Collaborative Technologies and Systems*, pages 490–497. IEEE, 2008.

[209] A. Pentland and A. Liu. Modeling and prediction of human behavior. *Neural computation*, 11(1):229–242, 1999.

[210] A. Yokoyama and T. Omori. Modeling of human intention estimation process in social interaction scene. In *International Conference on Fuzzy Systems*, pages 1–6. IEEE, 2010.

[211] Y. Li and S. S. Ge. Human–robot collaboration based on motion intention estimation. *IEEE/ASME Transactions on Mechatronics*, 19(3):1007–1014, 2013.

[212] A. Dragan and S. Srinivasa. Integrating human observer inferences into robot motion planning. *Autonomous Robots*, 37(4):351–368, 2014.

[213] G. Ferrer and A. Sanfeliu. Bayesian human motion intentionality prediction in urban environments. *Pattern Recognition Letters*, 44:134–140, 2014.

[214] A. Turnwald, D. Althoff, D. Wollherr, and M. Buss. Understanding human avoidance behavior: interaction-aware decision making based on game theory. *International Journal of Social Robotics*, 8(2):331–351, 2016.

[215] T. Kruse, A. K. Pandey, R. Alami, and A. Kirsch. Human-aware robot navigation: A survey. *Robotics and Autonomous Systems*, 61(12):1726–1743, 2013.

[216] A. De Santis, B. Siciliano, A. De Luca, and A. Bicchi. An atlas of physical human–robot interaction. *Mechanism and Machine Theory*, 43(3):253–270, 2008.

[217] J. J. Gertler. Survey of model-based failure detection and isolation in complex plants. *IEEE Control systems magazine*, 8(6):3–11, 1988.

[218] F. Flacco and A. De Luca. Safe physical human-robot collaboration. In *2013 IEEE/RSJ International Conference on Intelligent Robots and Systems*, pages 2072–2072. IEEE, 2013.

[219] S. Yousefizadeh and T. Bak. Unknown external force estimation and collision detection for a cooperative robot. *Robotica*, pages 1–17, 2020.

[220] W.-H. Chen. Disturbance observer based control for nonlinear systems. *IEEE/ASME transactions on mechatronics*, 9(4):706–710, 2004.

[221] V. I. Utkin and H.-C. Chang. Sliding mode control on electro-mechanical systems. *Mathematical problems in Engineering*, 8(4-5):451–473, 2002.

[222] T. Floquet and J.-P. Barbot. Super twisting algorithm-based step-by-step sliding mode observers for nonlinear systems with unknown inputs. *International journal of systems science*, 38(10):803–815, 2007.

[223] C. Edwards and S. K. Spurgeon. Sliding mode stabilization of uncertain systems using only output information. *International Journal of Control*, 62(5):1129–1144, 1995.

[224] V. Utkin and J. Shi. Integral sliding mode in systems operating under uncertainty conditions. In *Proceedings of 35th IEEE conference on decision and control*, volume 4, pages 4591–4596. IEEE, 1996.

[225] Y. Niu, D. W. Ho, and J. Lam. Robust integral sliding mode control for uncertain stochastic systems with time-varying delay. *Automatica*, 41(5):873–880, 2005.

[226] S. Laghrouche, F. Plestan, and A. Glumineau. Higher order sliding mode control based on integral sliding mode. *Automatica*, 43(3):531–537, 2007.

[227] G. P. Incremona, A. Ferrara, and L. Magni. Mpc for robot manipulators with integral sliding modes generation. *IEEE/ASME Transactions on Mechatronics*, 22(3):1299–1307, 2017.

[228] M. Rubagotti, A. Estrada, F. Castaños, A. Ferrara, and L. Fridman. Integral sliding mode control for nonlinear systems with matched and unmatched perturbations. *IEEE Transactions on Automatic Control*, 56(11):2699–2704, 2011.

[229] J.-X. Xu, Z.-Q. Guo, and T. H. Lee. Design and implementation of integral sliding-mode control on an underactuated two-wheeled mobile robot. *IEEE Transactions on industrial electronics*, 61(7):3671–3681, 2014.

[230] J.-W. Zhu, G.-H. Yang, H. Wang, and F. Wang. Fault estimation for a class of nonlinear systems based on intermediate estimator. *IEEE Transactions on Automatic Control*, 61(9):2518–2524, 2015.

[231] C. P. Tan and C. Edwards. Sliding mode observers for detection and reconstruction of sensor faults. *Automatica*, 38(10):1815–1821, 2002.

[232] Y. Zhang and Q. Xu. Adaptive sliding mode control with parameter estimation and kalman filter for precision motion control of a piezo-driven microgripper. *IEEE transactions on control systems technology*, 25(2):728–735, 2016.

[233] Z. Gao and S. X. Ding. State and disturbance estimator for time-delay systems with application to fault estimation and signal compensation. *IEEE Transactions on Signal Processing*, 55(12):5541–5551, 2007.

[234] C. Wang, L. Quan, Z. Jiao, and S. Zhang. Nonlinear adaptive control of hydraulic system with observing and compensating mismatching uncertainties. *IEEE Transactions on Control Systems Technology*, 26(3):927–938, 2017.

[235] T. Fong, I. Nourbakhsh, and K. Dautenhahn. A survey of socially interactive robots. *Robotics and autonomous systems*, 42(3-4):143–166, 2003.

[236] M. Böhm, J.-U. Pott, M. Kürster, O. Sawodny, D. Defrere, and P. Hinz. Delay compensation for real time disturbance estimation at extremely large telescopes. *IEEE Transactions on Control Systems Technology*, 25(4):1384–1393, 2016.

[237] J. Qin, Q. Ma, H. Gao, and W. X. Zheng. Fault-tolerant cooperative tracking control via integral sliding mode control technique. *IEEE/ASME Transactions on Mechatronics*, 23(1):342–351, 2017.

[238] M. Bodson and S. C. Douglas. Adaptive algorithms for the rejection of sinusoidal disturbances with unknown frequency. *Automatica*, 33(12):2213–2221, 1997.

[239] M. Van. An Enhanced Robust Fault Tolerant Control Based on an Adaptive Fuzzy PID- Nonsingular Fast Terminal Sliding Mode Control for Uncertain Nonlinear Systems. *IEEE/ASME Transactions on Mechatronics*, 23(3):1362–1371, 2018.

[240] Y. Wan and T. Keviczky. Real-time fault-tolerant moving horizon air data estimation for the reconfigure benchmark. *IEEE Transactions on Control Systems Technology*, 27(3):997–1011, 2018.

[241] A. De Luca, A. Albu-Schaffer, S. Haddadin, and G. Hirzinger. Collision detection and safe reaction with the dlr-iii lightweight manipulator arm. In *Intelligent Robots and Systems, 2006 IEEE/RSJ International Conference on*, pages 1623–1630. IEEE, 2006.

[242] H. K. Khalil and J. W. Grizzle. *Nonlinear systems*, volume 3. Prentice hall Upper Saddle River, NJ, 2002.

[243] S. Haddadin, A. Albu-Schäffer, and G. Hirzinger. Safe physical human-robot interaction: measurements, analysis and new insights. In *Robotics research*, pages 395–407. Springer, 2010.

[244] D. Althoff, J. J. Kuffner, D. Wollherr, and M. Buss. Safety assessment of robot trajectories for navigation in uncertain and dynamic environments. *Autonomous Robots*, 32(3):285–302, Apr 2012.

[245] B. Schuller, S. Steidl, A. Batliner, E. Bergelson, J. Krajewski, C. Janott, A. Amatuni, M. Casillas, A. Seidl, M. Soderstrom, et al. The interspeech 2017 computational paralinguistics challenge: Addressee, cold & snoring. In *ComParE, Interspeech 2017*, pages 3442–3446, 2017.

[246] K. Qian, C. Janott, Z. Zhang, D. Jun, A. Baird, C. Heiser, W. Hohenhorst, M. Herzog, W. Hemmert, and B. Schuller. Teaching machines on snoring: a benchmark on computer audition for snore sound excitation localisation. *Archives of Acoustics*, 43(3):465–475, 2018.

[247] K. Qian, Z. Zhang, A. Baird, and B. Schuller. Active learning for bird sound classification via a kernel-based extreme learning machine. *The Journal of the Acoustical Society of America*, 142(4):1796–1804, Sept 2017.

[248] R. Yan, R. X. Gao, and X. Chen. Wavelets for fault diagnosis of rotary machines: A review with applications. *Signal processing*, 96:1–15, Mar 2014.

[249] D. Verstraete, A. Ferrada, E. L. Droguett, V. Meruane, and M. Modarres. Deep learning enabled fault diagnosis using time-frequency image analysis of rolling element bearings. *Shock and Vibration*, 2017.

[250] A. Rahimi, K. D. Kumar, and H. Alighanbari. Fault detection and isolation of control moment gyros for satellite attitude control subsystem. *Mechanical Systems and Signal Processing*, 135:106419, 2020.

[251] F. Karim, S. Majumdar, H. Darabi, and S. Chen. Lstm fully convolutional networks for time series classification. *IEEE Access*, 6:1662–1669, 2017.

[252] S.-Y. Shao, W.-J. Sun, R.-Q. Yan, P. Wang, and R. X. Gao. A deep learning approach for fault diagnosis of induction motors in manufacturing. *Chin. J. Mech. Eng.*, 30(6):1347–1356, Oct 2017.

[253] H. Wu, D. Liu, S. Duan, Y. Guan, and J. Rojas. Multimodal sparse representation for anomaly classification in a robot introspection system. In *2018 IEEE International Conference on Robotics and Biomimetics (ROBIO)*, pages 1594–1600. IEEE, 2018.

[254] S. Luo, H. Wu, H. Lin, S. Duan, Y. Guan, and J. Rojas. Fast, robust, and versatile event detection through hmm belief state gradient measures. In *2018 27th IEEE International Symposium on Robot and Human Interactive Communication (RO-MAN)*, pages 1–8. IEEE, 2018.

[255] D. Romeres, D. K. Jha, W. Yerazunis, D. Nikovski, and H. A. Dau. Anomaly detection for insertion tasks in robotic assembly using gaussian process models. In *2019 18th European Control Conference (ECC)*, pages 1017–1022. IEEE, 2019.

[256] E. Di Lello, M. Klotzbücher, T. De Laet, and H. Bruyninckx. Bayesian time-series models for continuous fault detection and recognition in industrial robotic tasks. In *2013 IEEE/RSJ International Conference on Intelligent Robots and Systems*, pages 5827–5833. IEEE, 2013.

[257] D. Park, H. Kim, Y. Hoshi, Z. Erickson, A. Kapusta, and C. C. Kemp. A multimodal execution monitor with anomaly classification for robot-assisted feeding. In *2017 IEEE/RSJ International Conference on Intelligent Robots and Systems (IROS)*, pages 5406–5413. IEEE, 2017.

[258] J. Rojas, S. Luo, D. Zhu, Y. Du, H. Lin, Z. Huang, W. Kuang, and K. Harada. Online robot introspection via wrench-based action grammars. In *Proc. IEEE Intell. Robot. Syst.*, pages 5429–5436, Vancouver, Canada, Sept 2017.

[259] T. G. Puranik and D. N. Mavris. Identification of instantaneous anomalies in general aviation operations using energy metrics. *Journal of Aerospace Information Systems*, 17(1):1–17, 2019.

[260] L. Wellhausen, R. Ranftl, and M. Hutter. Safe robot navigation via multi-modal anomaly detection. *IEEE Robotics and Automation Letters*, 5(2):1326–1333, 2020.

[261] S. Yahaya, A. Lotfi, and M. Mahmud. A framework for anomaly detection in activities of daily living using an assistive robot. In *Proceedings of the 2nd UK-RAS Robotics and Autonomous Systems Conference, Loughborough, 24 January 2019*, pages 131–134. UK-RAS Network, London, January 2019.

[262] R. Bischoff, J. Kurth, G. Schreiber, R. Koeppe, A. Albu-Schäffer, A. Beyer, O. Eiberger, S. Haddadin, A. Stemmer, G. Grunwald, et al. The kuka-dlr lightweight robot arm-a new reference platform for robotics research and manufacturing. In *Robotics (ISR), 2010 41st international symposium on and 2010 6th German conference on robotics (ROBOTIK)*, pages 1–8. VDE, 2010.

[263] sklearn.org. [EB/OL]. `https://scikit-learn.org/stable/` Accessed Sept 1, 2020.

[264] K. Qian, C. Janott, Z. Zhang, C. Heiser, and B. Schuller. Wavelet features for classification of vote snore sounds. In *Proc. IEEE Int. Conf. ICASSP.*, pages 221–225, Shanghai, China, Mar 2016.

[265] K. Qian, C. Janott, V. Pandit, Z. Zhang, C. Heiser, W. Hohenhorst, M. Herzog, W. Hemmert, and B. Schuller. Classification of the excitation location of snore sounds in the upper airway by acoustic multifeature analysis. *IEEE Trans. Biomed. Eng.*, 64(8):1731–1741, Oct 2017.

[266] M. D. Prieto, G. Cirrincione, A. G. Espinosa, J. A. Ortega, and H. Henao. Bearing fault detection by a novel condition-monitoring scheme based on statistical-time features and neural networks. *IEEE Trans. Ind. Electron.*, 60(8):3398–3407, Aug 2013.

[267] S. Mazilu, M. Hardegger, Z. Zhu, D. Roggen, G. Troster, M. Plotnik, and J. M. Hausdorff. Online detection of freezing of gait with smartphones and machine learning techniques. In *Proc. IEEE PervasiveHealth*, pages 123–130, San Diego, California USA, May 2012.

[268] K. Qian, C. Janott, J. Deng, C. Heiser, W. Hohenhorst, M. Herzog, N. Cummins, and B. Schuller. Snore sound recognition: on wavelets and classifiers from deep nets to kernels. In *Conf Proc IEEE Eng. Med. Biol. Soc.*, pages 3737–3740, Jeju Island, Korea, July 2017.

[269] J. M. Taylor. Kendall's and spearman's correlation coefficients in the presence of a blocking variable. *Biometrics*, pages 409–416, 1987.

[270] K. Kira, L. A. Rendell, et al. The feature selection problem: Traditional methods and a new algorithm. In *Aaai*, volume 2, pages 129–134, 1992.

[271] I. Kononenko, E. Šimec, and M. Robnik-Šikonja. Overcoming the myopia of inductive learning algorithms with relieff. *Applied Intelligence*, 7(1):39–55, 1997.

[272] B. Brogliato, S.-I. Niculescu, and P. Orhant. On the control of finite-dimensional mechanical systems with unilateral constraints. *IEEE Transactions on Automatic Control*, 42(2):200–215, 1997.

[273] F. Blanchini. Set invariance in control. *Automatica*, 35(11):1747–1767, 1999.

[274] D. Wollherr, J. Mareczek, M. Buss, and G. Schmidt. Rollover avoidance for steerable vehicles by invariance control. In *2001 European Control Conference (ECC)*, pages 3522–3527. IEEE, 2001.

[275] M. Sobotka, J. Wolff, and M. Buss. Invariance controlled balance of legged robots. In *2007 European Control Conference (ECC)*, pages 3179–3186. IEEE, 2007.

[276] M. Scheint, J. Wolff, and M. Buss. Invariance control in robotic applications: Trajectory supervision and haptic rendering. In *2008 American Control Conference*, pages 1436–1442. IEEE, 2008.

[277] M. Kimmel and S. Hirche. Invariance control for safe human–robot interaction in dynamic environments. *IEEE Transactions on Robotics*, 33(6):1327–1342, 2017.

[278] J. H. Park and H. C. Cho. An online trajectory modifier for the base link of biped robots to enhance locomotion stability. In *Proceedings 2000 ICRA. Millennium Conference. IEEE International Conference on Robotics and Automation. Symposia Proceedings (Cat. No. 00CH37065)*, volume 4, pages 3353–3358. IEEE, 2000.

[279] N. Y. Ko, R. G. Simmons, and D. J. Seo. Trajectory modification using elastic force for collision avoidance of a mobile manipulator. In *Pacific Rim International Conference on Artificial Intelligence*, pages 190–199. Springer, 2006.

[280] C. Rösmann, W. Feiten, T. Wösch, F. Hoffmann, and T. Bertram. Trajectory modification considering dynamic constraints of autonomous robots. In *ROBOTIK 2012; 7th German Conference on Robotics*, pages 1–6. VDE, 2012.

[281] M. Bernardes, B. V. Adorno, P. Poignet, and G. Borges. Robot-assisted automatic insertion of steerable needles with closed-loop imaging feedback and intraoperative trajectory replanning. *Mechatronics*, 23(6):630–645, 2013.

[282] V. Usenko, L. von Stumberg, A. Pangercic, and D. Cremers. Real-time trajectory replanning for mavs using uniform b-splines and a 3d circular buffer. In *2017 IEEE/RSJ International Conference on Intelligent Robots and Systems (IROS)*, pages 215–222. IEEE, 2017.

[283] A. Pokle, R. Martín-Martín, P. Goebel, V. Chow, H. M. Ewald, J. Yang, Z. Wang, A. Sadeghian, D. Sadigh, S. Savarese, et al. Deep local trajectory replanning and control for robot navigation. In *2019 International Conference on Robotics and Automation (ICRA)*, pages 5815–5822. IEEE, 2019.

[284] V. I. Utkin and A. S. Poznyak. Adaptive sliding mode control with application to super-twist algorithm: Equivalent control method. *Automatica*, 49(1):39–47, 2013.

[285] H. Richter. A multi-regulator sliding mode control strategy for output-constrained systems. *Automatica*, 47(10):2251–2259, 2011.

[286] G. Bartolini, A. Ferrara, and E. Punta. Multi-input second-order sliding-mode hybrid control of constrained manipulators. *Dynamics and Control*, 10(3):277–296, 2000.

[287] G. P. Incremona, M. Rubagotti, and A. Ferrara. Sliding mode control of constrained nonlinear systems. *IEEE Transactions on Automatic Control*, 62(6):2965–2972, June 2017.

[288] K. Youcef-Toumi and S. Wu. Input/output linearization using time delay control. In *1991 American Control Conference*, pages 2601–2606. IEEE, 1991.

[289] C.-S. Jeong, J.-S. Kim, and S.-I. Han. Tracking error constrained super-twisting sliding mode control for robotic systems. *International Journal of Control, Automation and Systems*, 16(2):804–814, 2018.

[290] X. Yu and M. Ö. Efe. *Recent advances in sliding modes: from control to intelligent mechatronics*, volume 24. Springer, 2015.

[291] B. Draženović. The invariance conditions in variable structure systems. *Automatica*, 5(3):287–295, 1969.

[292] H. Lee, E. Kim, H.-J. Kang, and M. Park. A new sliding-mode control with fuzzy boundary layer. *Fuzzy Sets and Systems*, 120(1):135–143, 2001.

[293] M.-L. Tseng and M.-S. Chen. Chattering reduction of sliding mode control by low-pass filtering the control signal. *Asian Journal of control*, 12(3):392–398, 2010.

[294] A. Levant. Principles of 2-sliding mode design. *automatica*, 43(4):576–586, 2007.

[295] L. Fridman, J. Moreno, and R. Iriarte. Sliding modes after the first decade of the 21st century. *Lecture notes in control and information sciences*, 412:113–149, 2011.

[296] M. Rubagotti, M. L. Della Vedova, and A. Ferrara. Time-optimal sliding-mode control of a mobile robot in a dynamic environment. *IET control theory & applications*, 5(16):1916–1924, 2011.

[297] E. Alpaydin. *Introduction to machine learning*. MIT press, 2020.

[298] S. Balakrishnama and A. Ganapathiraju. Linear discriminant analysis-a brief tutorial. In *Institute for Signal and information Processing*, volume 18, pages 1–8, 1998.

[299] sklearn.lda. [EB/OL]. `https://scikit-learn.org/0.16/modules/generated/sklearn.lda.LDA.html` Accessed Sept 1, 2020.

[300] sklearn.svm. [EB/OL]. `https://scikit-learn.org/stable/modules/generated/sklearn.svm.SVC.html` Accessed Sept 1, 2020.

[301] sklearn.fnn. [EB/OL]. `https://scikit-learn.org/stable/modules/generated/sklearn.neural_network.MLPClassifier.html` Accessed Sept 1, 2020.

[302] W. Schiffmann, M. Joost, and R. Werner. Optimization of the backpropagation algorithm for training multilayer perceptrons. *University of Koblenz: Institute of Physics*, 1994.

Own Publications

[303] Y. Sun, Z. Zhang, M. Leibold, R. Hayat, D. Wollherr, and M. Buss. Protective control for robot manipulator by sliding mode based disturbance reconstruction approach. In *2017 IEEE International Conference on Advanced Intelligent Mechatronics (AIM)*, pages 1015–1022. IEEE, 2017.

[304] Z. Zhang, M. Leibold, and D. Wollherr. Integral sliding-mode observer-based disturbance estimation for euler-lagrangian systems. *IEEE Transactions on Control Systems Technology*, 2019.

[305] Z. Zhang, K. Qian, B. W. Schuller, and D. Wollherr. An online robot collision detection and identification scheme by supervised learning and bayesian decision theory. *IEEE Transactions on Automation Science and Engineering*, pages 1–13, 2020.

[306] Z. Zhang, Y. Wang, and D. Wollherr. Safe tracking control of euler-lagrangian systems based on a novel adaptive super-twisting algorithm. *Accepted to IFAC 2020 World Congress*.